UNIVERSITÀ
DEGLI STUDI
FIRENZE

DOTTORATO DI RICERCA IN SCIENZE CHIMICHE

CICLO XXVIII

COORDINATORE Prof. ANDREA GOTI

CANTILEVER TORQUE MAGNETOMETRY: A POWERFUL TOOL TO INVESTIGATE MAGNETIC ANISOTROPY IN CRYSTALS AND THIN FILMS

Settore Scientifico Disciplinare CHIM/03

Dottorando
Dott. Mauro Perfetti

_____
(firma)

Tutore
Prof. Roberta Sessoli

_____
(firma)

Coordinatore
Prof. Andrea Goti

_____
(firma)

Anni 2012/2015

Contents

List of the main Acronyms

Acronym	Definition
AC	Alternating Current
CF	Crystal Field
CTM	Cantilever Torque Magnetometry
DC	Direct Current
EPR	Electronic Paramagnetic Resonance
LF	Ligand Field
Ln	Lanthanide Ion
QT	Quantum Tunneling
rf	Reference Frame
RS	Russell-Saunders
TM	Transition Metal Ion
SIM	Single Ion Magnet
SMM	Single Molecule Magnet
SOC	Spin Orbit Coupling
ZFS	Zero Field Splitting

1 Organization of the Thesis

This PhD Thesis is the result of the work of the author as well as of many other collaborators.

Since the field of molecular magnetism is a very specific interdisciplinary area that lies between solid state physics and chemistry, we decided to organize this Thesis starting with an **Introduction** (Chapter 2) that can help any reader to understand the main concepts that constitute the basis on which all the experiments and simulations performed here are grounded. Besides a brief history of magnetism (Section 2.1), we treated the modelling of magnetic anisotropy both in bulk (Section 2.2.1) and in molecular materials (Section 2.2.2), with a particular attention for molecular systems containing lanthanide ions.

Indeed, the main purpose of this PhD Thesis is to study anisotropic systems, so we devoted a Chapter to explain the main sources of **Non-collinearity** (Chapter 3) in molecular materials, focusing on the ones arising from ligand geometry and crystal packing.

The systems that are reported here were characterized using several techniques that are commonly used in molecular magnetism like EPR, AC and DC susceptometry, however the leading technique that was used for all the systems reported here is the **Cantilever Torque Magnetometry** (Chapter 4), that is treated in details both from a theoretical and from an experimental point of view, focusing on the type of measurements that can be performed and thus the physical quantities on which we can have information. A Section was also devoted to describe the basic program (that was modified *ad hoc* as a function of the studied system) that was written by the author with the assistance of Prof. Roberta Sessoli to fit and simulate the torque curves.

The Chapters were organized in an increasing complexity fashion with four steps. From **Collinear systems** (Chapter 5), where all the anisotropy tensors are isooriented, we pass to **Intermolecular noncollinear systems** (Chapter 6), that contains more than one molecule that is not simply reported by an inversion centre. The next step was to study **Intramolecular noncollinear systems** (Chapter 7), where the more than one anisotropic ion is present inside the molecule, thus adding a remarkable intricacy in the disentanglement of the single contributions. As a pioneer approach, we reported the investigation of **Films** of magnetic molecules on different substrates (Chapter 8), where the order is not in principle established, and could, up to now, being studied only using expensive techniques based on synchrotron light.

Finally, we also included an **Appendix** where we attached all the articles already published by the Author and others on some results discussed in this Thesis.

2 Introduction

2.1 Magnetism: an ancient story

The discover of magnetism is deeply rooted in ancient times. According to Pliny The Elder, the word *magnetism* derives its etymology from the shepherd *Magnes* who first realized that iron was attracted by lodestone because the nails in his boots remained stuck into a mysterious stone when he was grazing the flock. More likely, the word is originated from the city of Magnesia, surrounded by tens of lodestone mines. Moreover there are evidences that when the Han dynasty ruled in China (300-200 BC), a rudimentary compass made of lodestone was fashioned (Figure 2.1).

Figure 2.1: Reconstruction of the Chinese compass

Since that period, many notorious personalities of science (*e.g.* Galilei, Bacon, Descartes) studied phenomena related to magnetism, but a huge progress has to be attributed to Coulomb, that in 1789 wrote a paper called: *Du magnètisme*. In this work he finally point out that magnetism and electricity are two distinct but strictly related phenomena, that sometimes are ruled by similar laws. Several years later (1830) Oersted discovered that electrical currents (and thus electrons) flowing into a wire can influence the

orientation of a compass needle. Also Ampere gave a massive contribution in understanding the origin of magnetism: he realized that magnetism is a microscopic phenomenon, that only in some cases can result into a macroscopic property of matter. However the concept of field was introduced only several years later by Faraday and supported by Maxwell that also identified light as an electromagnetic oscillatory field. In 1905 Langevin elaborated a theory that explained the dependence of the magnetic properties of some classes of substances. This theory was extended by Weiss that formulated the Molecular (or Mean) Field Theory. The further connection of magnetism with quantum physics pioneered by Debye, allowed the opening of a new scientific path that is currently studied.

Today magnetism is a very vast field that comprises a lot of sub-fields very different from each other. Just to have a general idea, the magnetic moments that originates inside materials can be used for several applications ranging from magnetic resonance imagining (MRI) to microphones, from levitating trains to data record and storage.

2.2 Magnetic anisotropy

Before starting to briefly explain the theory that lies beneath the experiments and calculations described in this Thesis, it can be useful to recall some basic concepts related to the origin of magnetic anisotropy in materials based on organic or inorganic structures. The word *anisotropy* has Greek etymology, and can be literally translated as: not-equally-turned, meaning that a property of matter changes if the direction along which it is observed is changed. The adjective *magnetic* means that the property that is not equally distributed in space is the magnetization ($\boldsymbol{M}$), defined as:

$$\boldsymbol{M} = \sum_{i=1}^{n} \boldsymbol{m}_i \tag{2.1}$$

where the sum runs over all the $\boldsymbol{m}_i$ microscopic magnetic moments inside the material. If at some instant the magnetization in an anisotropic material is not one of the lowest energy direction, some energy is *stored* inside the

material. This energy, that can be physically defined as the work that has to be done to magnetize the sample along a certain direction, is called anisotropy energy (E_{ani}) and it contains several contributions that are analysed in this section.

It is also important to point out that a precise knowledge of the magnetic anisotropy can be useful to obtain a complete picture of the magnetic behaviour of a material. In this way it is also possible to predict if a system is a suitable candidate for a certain application, ans also address the synthetic efforts to the more convenient route toward the research of high performance materials.

2.2.1 Bulk materials

In this Thesis the main topic is the study of the magnetic anisotropy in molecular-based materials, however it is useful to briefly explain how magnetic anisotropy is normally rationalized in bulk materials because, as we will see later, the parallelism will be discussed.

We will proceed here using an intuitive approach. The anisotropy energy must contains a series of powers of the direction cosines of the magnetization unit vector ($\boldsymbol{w}$). The quantity E_{ani} is invariant under time reversal whereas $\boldsymbol{M}$ is not, hence it is straightforward that E_{ani} must be expressed with an even function of the components of $\boldsymbol{w}$. We explicit here the simplest case (and often also most relevant) of uniaxial crystals, *e.g.* $\boldsymbol{w}$ has only two independent components, namely w_x (or w_y) and w_z. Since $\boldsymbol{w}$ is a unitary vector, $w_x^2 + w_y^2 + w_z^2 = 1$, thus the expansion begins with the square component:

$$E_{\text{ani}} = K(w_x^2 + w_y^2) = K(\cos^2\varphi \sin^2\vartheta + \sin^2\varphi \sin^2\vartheta) = K\sin^2\vartheta \quad (2.2)$$

where K is called anisotropy constant and have the dimension of an energy density. The angles ϑ and φ are the polar angles with respect to the xyz reference frame where z is the unique axis. Note that Equation 2.2 can be

equivalently written as:

$$E_{\text{ani}} = -Kw_z^2 = -K\cos^2\vartheta \tag{2.3}$$

The two notations differ for a factor K that is independent on the direction, hence when a change in notation is done, one must include this constant in the isotropic part of the potential. It is worth noticing that E_{ani} is correctly dependent *only* on the ϑ angle in a uniaxial anisotropy model. The sign of K is determinant for the resultant anisotropy shape, in fact if $K>0$ then $\vartheta = 0$ is an energy minimum and the anisotropy is called *easy axis* type, while if $K<0$ the energy minimum occurs for $\vartheta = \pi/2$, and the anisotropy is called *easy plane* type. In Figure 2.2 we represent $|E_{\text{ani}}|$ in the *xyz* reference frame to easily visualize the difference between this two limits.

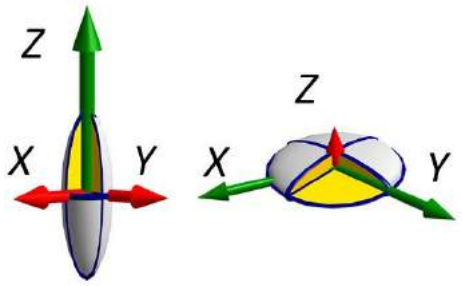

Figure 2.2: Three dimensional plot of $|E_{\text{ani}}|$ for the two limits: easy axis (left) and easy plane (right).

The anisotropy constant K must encase all the possible sources of anisotropy: shape, surface, interactions, and crystal structure. Also other external causes (*e.g.* stress, irradiation, annealing, deformation) may origin magnetic anisotropy, but are generally weak effects compared to the ones mentioned above.

The shape of the sample can produce anisotropy due to the demagnetizing field that is created inside the material when an external applied field is switched on. The demagnetizing field is stronger along a short axis then along a long axis, so that any shape that deviates from the spherical one

can induce anisotropy and thus contributes to E_{ani} with a demagnetizing energy $E_{\text{D}} = -M^2/(2\mu_0)$ [1] where μ_0 is the permeability of vacuum. To calculate the shape anisotropy contribution it is common to refer to the Stoner-Wohlfarth model [2].

Also the surface of materials is a source of anisotropy. This can be easily understood from a chemical point of view: the atoms on the surface have incomplete coordination sphere, meaning that the chemical interactions are not the same as bulk atoms, thus generating anisotropy. This contribution is generally very difficult to estimate but is of paramount importance in thin films because the surface-induced generation of anisotropy is responsible of magnetic order in 2D lattices as stated by the Mermin Wagner theorem [3]. Many works have been done on this topic, clarifying that in some films the order is established by stripe domains [4] that can be even modified with a rise in temperature [5, 6].

Also interactions between magnetic ions play a crucial role in the definition of the anisotropy, and they will be discussed in details in Section 3.1. The last contribution that has to be considered is the magnetocrystalline one, that derives from the disposition of the atoms in the solid. It is generally small in bulk ferromagnets but plays a crucial role in molecular-based materials, for this reason it will be treated in detail in Section 2.2.2. Here we just recall that the contribution arising from the crystal structure is due to the SOC, as firstly suggested by Van Vleck [7]. It is generally difficult to evaluate also in highly symmetric structures such as cubic crystals and, even if models to calculate this contribution have been suggested [8], to obtain reliable results it is often necessary to calculate a huge number of k-points in the Brillouin zone [9, 10].

2.2.2 Molecular materials

Molecular-based anisotropic materials have become an hot topic in magnetism since the discover of the first Single Molecule Magnet (SMM) in 1993 by Sessoli *et al.* [11]. After this first derivative, based on a cluster of transition metal ions (TM), a real revolution in this field was provided by Ishikawa *at al.* in 2002, when a family of Single Ion Magnets (SIM)

based on lanthanide ions (Ln) [12] was characterized. The most exciting derivative of this family, Terbium Phtalocyanine ($TbPc_2$), is a sandwich-like compound containing a Tb^{3+} ion surrounded by two phtalocyaninate ligands. The peculiarity of this class of molecules is exhibiting slow relaxation of the magnetization (from milliseconds up to several hours) and magnetic hysteresis at low temperature [13]. This materials have been intensively studied with a number of different experimental techniques and theoretical methods because a rational design of their magnetic properties is mandatory to precisely address the synthetic efforts in the direction of developing materials more and more useful. In fact the most intriguing application for this materials could be the storage of data at the molecular level [14].

Despite in bulk ferromagnets, this peculiar features are no longer connected to long order interactions, but are characteristic of the single molecule. A necessary, but not sufficient, requirement that a molecule must fulfil to behave as a SMM is to have a preferential direction on which the magnetization tends to lie, that is, magnetic anisotropy.

To deeply understand the origin of magnetocrystalline anisotropy, that is the dominant term in this compounds, one must start from the free ion Hamiltonian that contains three major contributions, namely the kinetic energy ($\mathcal{H}_{\text{kin}}$), the electron-electron repulsion ($\mathcal{H}_{\text{ee}}$) and the spin-orbit coupling ($\mathcal{H}_{\text{SOC}}$):

$$\mathcal{H}_{\text{free}} = \mathcal{H}_{\text{kin}} + \mathcal{H}_{\text{ee}} + \mathcal{H}_{\text{SOC}} = \sum_i \left(\frac{\boldsymbol{p}_i^2}{2m} - \frac{Ze^2}{r_i}\right) + \sum_{i<j} \frac{e^2}{|\boldsymbol{r}_i - \boldsymbol{r}_j|} + \sum_i \xi_i \boldsymbol{l_i} \cdot \boldsymbol{s_i} \tag{2.4}$$

where the indices i and j refer to the ith and jth electron, respectively. The other quantities are: the linear momentum operator ($\boldsymbol{p}_i$) , the electron mass (m), the electron charge (e), the nuclear charge in unit of e (Z), the position vector ($\boldsymbol{r}_i$), the Spin-Orbit Coupling (SOC) strenght (ξ_i), the orbital angular momentum ($\boldsymbol{l}_i$) and the spin angular momentum ($\boldsymbol{s}_i$). Note that the strength of the SOC is dependent on the element and, more in detail, on the partially filled valence orbitals. Hereafter we will discuss the

treatment that is commonly employed for Ln because in this Thesis we will present measurements and calculations on highly anisotropic molecular materials, that often contains Ln. For TM the order of the perturbations is different because the effect of the ligands around the d-orbitals of the TM has the consequence to "quench" the orbital momentum, reducing the contribution of the SOC to the energy. On the contrary, the inner nature of the partially filled f-orbitals of Ln assures a large unquenched orbital contribution. The first two terms of Equation 2.4 that describes the motions of the electrons, defines as a consequence the effective spatial region where the electrons can be found: the orbitals. From this point it is possible to define the orbital angular momentum of the single electron that enters inside the SOC term.

The intrinsic property of the electrons that is responsible of magnetic behaviour is the *spin*. As fermions, the electrons must obey to the Pauli exclusion principle and possess semi-integer spin with absolute value equal to 1/2 (the sign can be either positive/negative or up/down, respectively). In case of elements that have more than one unpaired electron, we define the total spin (S) as:

$$S = \sum_{i=1}^{n} s_i \tag{2.5}$$

where the sum runs over all the i-unpaired electrons. Moreover considering degenerate orbitals (like d and f orbitals), the Hund's rule and the Pauli exclusion principle, may give rise to a total orbital momentum defined as:

$$L = \sum_{i=1}^{n} l_i \tag{2.6}$$

If the interaction with the ligand field is smaller than the SOC (that is the case of Ln), the energy terms that possess a different relative orientation of L and S have very different energy and are usually labelled as ${}^{2S+1}L_J$ using a formalism known as Russell-Saunders coupling [15]. The symbol J is defined as the total angular momentum, and can assume different values depending on the relative orientation of the total orbital momentum with

respect to the total spin angular momentum as follows:

$$J = |L - S|, \cdots, L + S \tag{2.7}$$

We will now propose a semi-classical treatment of the interaction between the spin and the orbital momentum of a single electron to describe the origin of the magnetocrystalline anisotropy. If an external magnetic field ($\boldsymbol{B}$) is applied on a paramagnetic substance, the spins align their directions parallel to $\boldsymbol{B}$. This comes directly from the definition of energy of a magnetic dipole ($\boldsymbol{m}$) in a field, that has a minimum for $\varphi = 0$, where φ is the angle between $\boldsymbol{B}$ and $\boldsymbol{m}$:

$$E = -\boldsymbol{m} \cdot \boldsymbol{B} = -mBcos\varphi \tag{2.8}$$

However this is straightforward only if no orbital contribution is present (isotropy).

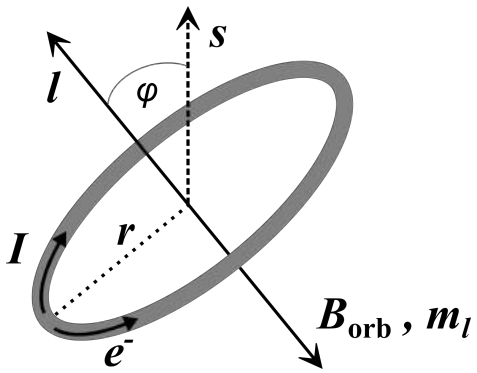

Figure 2.3: Sketch of the spin-orbit interaction.

To fully understand the role of the orbital contribution in magnetic anisotropy, it is useful to start writing the classical magnetic moment for a circulating electron with charge $q = -e$:

$$\boldsymbol{m}_l = -\frac{e\mu_0}{2}(\boldsymbol{r} \times \boldsymbol{v}) \tag{2.9}$$

where μ_0 is the permeability of vacuum, $\boldsymbol{r}$ is the position vector and $\boldsymbol{v}$ is

the tangential velocity.

Using the classical definition of angular momentum of an electron with mass m_e, $\boldsymbol{l} = m_e(\boldsymbol{r} \times \boldsymbol{v})$, we can now rewrite Equation 2.9 as:

$$\boldsymbol{m}_l = -\frac{e\mu_0}{2m_e}\,\boldsymbol{l} \tag{2.10}$$

Equation 2.10 can be used to write in a similar way, except a constant, the magnetic spin moment of a single electron:

$$\boldsymbol{m}_s = -\frac{e\mu_0}{m_e}\,\boldsymbol{s} \tag{2.11}$$

Lets now consider a single electron orbital motion. According to Figure 2.3, we can write the modulus of the magnetic field generated by this motion in a classical way, as $B_{\text{orb}} = I/2r$, where I is the current and r is the radius. Moreover the magnetic dipole moment of a current loop is $m = \mu_0 I \pi r^2$. Taking also advantage from Equation 2.10, we can write:

$$\boldsymbol{B}_{\text{orb}} = \frac{-e}{4\pi m_e r^3}\,\boldsymbol{l} \tag{2.12}$$

We can finally calculate the magnetostatic energy of a spin moment immersed into an orbitally generated magnetic field as:

$$E = -\boldsymbol{m}_s \cdot \boldsymbol{B}_{\text{orb}} = -\frac{e^2\mu_0}{4\pi m_e^2 r^3}\,\boldsymbol{l} \cdot \boldsymbol{s} \tag{2.13}$$

Now it is clear that if in a solid the orbital moment prefers to lie along a specific direction, Equation 2.13 is exactly the energy difference between the favoured ($\boldsymbol{l}$ and $\boldsymbol{s}$ parallel) and the unfavoured ($\boldsymbol{l}$ and $\boldsymbol{s}$ perpendicular) direction, that is the magnetocrystalline anisotropy. In the aforementioned demonstration we did not assume any preferential direction for the orbital momentum, so at the single ion level all directions will provide the same magnetostatic energy. However the word *magnetocrystalline* reminds that the single ion is far from being isolated, and that the electrostatic potential generated by the surrounded atoms will break the spherical symmetry identifying some preferred directions on which the orbital momentum tends

to lie. Indeed, the main conclusion of this demonstration is that in solids the magnetocrystalline anisotropy comes from the SOC, but only if the electrostatic potential around it deviates from a spherical one.

The description of this electrostatic potential generated by the surrounded atoms or groups called *ligands*, tightly bounded to the metal by chemical bonds, is usually presented using Crystal Field (CF) operators. Various notations have been developed to take into account the effect of the ligands on the electronic structure of the metal, here we present the Wybourne one:

$$\mathcal{H}_{\mathrm{CF}} = \sum_{k,q} B_k^q \boldsymbol{C}_k^q \tag{2.14}$$

where $k = 2, 4, 6$ and $-k \leq q \leq k$, so that to describe a completely non-symmetrical system one needs 27 CF parameters. The CF operators can be obtained starting from a combination of spherical harmonics $Y_k^q(r, \vartheta, \varphi)$, and a generic $\boldsymbol{C}_k^q$ operator of order q is written with a sum of terms that contain operators of power up to q so every parameter with $q = 0$ depends on operators like $\boldsymbol{J}_z^k$, meaning that it is diagonal in the J manifold. If one or more symmetry elements are present, some CF parameters automatically vanish, thus simplifying the description.

If one takes into account only the ground multiplet, that in Ln can be easily obtained by the Hund's rules, it can be convenient to use a different notation proposed by Stevens:

$$\mathcal{H}_{\mathrm{CF},J} = \sum_{k=2,4,6} \rho(k) \sum_{q=-k}^{k} b_k^q \boldsymbol{O}_k^q(\boldsymbol{J}) \tag{2.15}$$

where $\rho(k)$ is a parameter (different for each f^n configuration and k value) which accounts for the proportionality between the spherical harmonic of order k and the corresponding operator equivalent for that configuration. It is common to rename $\rho(k)$ in three different ways as a function of k as follows: $\rho(2) = \alpha$, $\rho(4) = \beta$ and $\rho(6) = \gamma$. If one takes into account only the ground state, the Stevens parameters are simply related to the Wybourne ones by some tabulated coefficients [15, 16, 17]. The effect of

the CF can be summarized in the splitting of the $2J+1$ degeneracy of the Russell-Saunders terms as a function of the value of the projection of J on the z -axis, $J_z\,|m_J, J\rangle = m_J\,|m_J, J\rangle$. In the case of non-Kramers ions (even number of f electrons) this degeneracy can be completely removed, while for Kramers ions (odd numbers of f electrons) the degeneracy of the m_J sublevels, often called Stark sublevels, has to remain *at least* 2 (Kramers theorem [18]). Moreover CF operators with $q \neq 0$ (called transverse, rhombic or non-diagonal terms) mix the m_J states creating a set of levels that can be expressed as a linear combination of pure m_J states.

Since in this Thesis a particular attention will be devoted to describe systems containing Ln, we want to stress here the physical meaning of the CF term in the Hamiltonian to make a parallelism between the bulk and molecular treatment of materials containing Ln. In the following we will demonstrate that the shape of the anisotropy of Ln can be in most cases efficiently predicted by using a simple model that combines the electron charge density around the metal ion and the charge density of the ligands. We anticipate now that this is possible due to the peculiar small extension of the f orbitals (radius, $r_{4f} \sim 0.5\,\text{Å}$) compared to some of the other filled orbitals in Ln. The charge density ($\rho^{J,m_J}(\boldsymbol{r})$) around a Ln can be calculated knowing the number of f electrons around the ion, their spin $\boldsymbol{s}_i$ and their position $\boldsymbol{r}_i$ as follows:

$$\rho^{J,m_J}(\boldsymbol{r}) = \int d\boldsymbol{r}_1 \ldots d\boldsymbol{r}_n \sum_{s_\nu} \sum_{\nu=1}^{n} |\Psi_{J,m_J}(\boldsymbol{r}_1 s_1 \ldots \boldsymbol{r}_n s_n)|^2 \sum_{i=1}^{n} \delta(\boldsymbol{r} - \boldsymbol{r}_i) \tag{2.16}$$

This equation can be reduced to a relatively simple summation of one particle contributions $\varphi^2(\boldsymbol{r})|Y_3^{m_J}(\vartheta,\varphi)|^2$, so it is possible to expand the charge density as a sum of spherical harmonics. It is also worth noticing that the one particle contributions are dependent on $|Y_3^{m_J}|^2$, so the spherical harmonics that must be used in the expansions should have $k \leq 6$ and $q = 0$ (due to the rotational symmetry imposed along the z axis). Moreover the parity of Y_k^q allows only terms with even values of k. For these reasons,

we can rewrite Equation 2.16 as:

$$\rho^{J,m_J}(\boldsymbol{r}) = \varphi^2(\boldsymbol{r}) \sum_{k=0,2,4,6} c_k(J, m_J, L, n) Y_k^0(\vartheta) \tag{2.17}$$

The coefficients c_k can be evaluated by taking advantage from the Wigner-Eckart theorem [19, 20]. We are not going to enter into details of complicated calculations on this topic, but we just report the approximation of the angular dependence of the total $4f$ charge density for the largest value of m_J of the ground J multiplet. Since for *all* Ln the largest coefficient in Equation 2.17 is c_2, that is the one originating the quadrupole moment, its sign is the one responsible for the alignment of the charge perpendicular (oblate ions, $c_2 < 0$) or parallel (prolate ions, $c_2 > 0$) to the z axis. Even if the coefficient c_2 is not exactly the coefficient $\rho(2) = \alpha$ defined in Equation 2.15, the two values are related and, more importantly, their sign is *the same*.

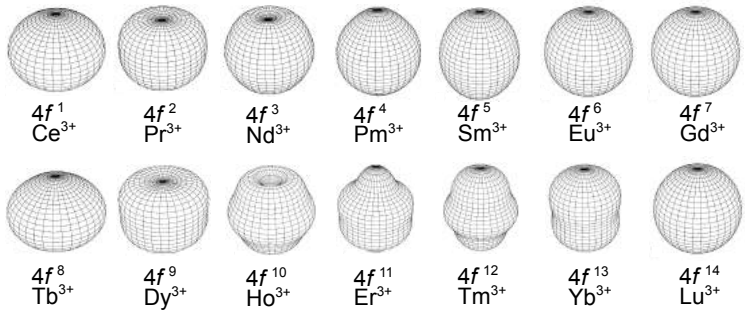

Figure 2.4: Approximation of the angular dependence of the total $4f$ charge density for the largest value of m_J of the ground J multiplet. Oblate ions: Ce^{3+}, Pr^{3+}, Nd^{3+}, Tb^{3+}, Dy^{3+} and Ho^{3+}; prolate ions: Pm^{3+}, Sm^{3+}, Er^{3+}, Tm^{3+} and Yb^{3+}. Ions with filled (Lu^{3+}) and half-filled (Gd^{3+}) f-shell as well as Eu^{3+} that stabilized the $J = 0$, $m_J = 0$ ground state can be represented as spheres. Figure adapted from ref. [19].

In molecular magnetism it is often desirable to have easy axis anisotropy because it enhance the possibility to observe slow relaxation of the magnetization, that is obtained if the coefficient of the $\boldsymbol{O}_2^0$ operator is

negative (strictly speaking if one considers all the CF operators, this is not straightforward, but is often a very good approximation). Considering that $\boldsymbol{O}_2^0 |J, m_J\rangle = 3J_z^2 - J(J+1) |J, m_J\rangle$, if we assume to stabilize the largest projection of $J_z = J$, the eigenvalue of the operator becomes $3J^2 - J(J+1) = J(2J-1)$ and is *always positive*, so it does not change the sign of the coefficient. Since this coefficient is obtained as $\alpha \cdot b_2^0$, to obtain negative values the sign of the Stevens coefficient must be opposite to the one of the charge density. For an equatorial distribution of the negative charges of the ligands, we obtain $b_2^0 > 0$, while opposite values are obtained for an axial distribution of the ligands' charges. For this reason, oblate ions ($\alpha < 0$) will generate Ising type anisotropy with axial ligands while prolate ions ($\alpha > 0$) will do that if coordinated to equatorial ligands [21].

All the aforementioned considerations can be applied also in bulk materials containing Ln [22], *e.g.* $Nd_2Fe_{14}B$ of SmCo magnets, where the Ln is inserted in a little percentage inside the lattice. As already seen in Section 2.2.1, the anisotropy of bulk materials is often expressed with the value of the anisotropy constant K, defined in Equation 2.2. This constant can be conveniently written in terms of Stevens coefficients as:

$$K = -\frac{3}{2}\alpha r_{4f}^2 b_2^0 J(2J-1) \tag{2.18}$$

where r_{4f} is the radius of the f orbitals. It is useful to recall here that easy axis anisotropy is obtained for *positive* values of K.

The body-centered cubic environment of Nd^{3+} inside a NdFeB permanent magnet act as an axial ligand ($b_2^0 > 0$), thus the replacement of Nd^{3+} with other prolate ions like Dy^{3+} or Pr^{3+} can maintain the Ising anisotropy that allows the employment of this materials as a permanent magnet. Another interesting material is Sm_2Fe_{17}, because the diffusion of nitrogen atoms in the structure define an equatorial disposition of the negative charges around the Ln, generating Ising anisotropy when oblate ions, like Sm^{3+} are present in the structure.

This simple model, based essentially on electrostatic considerations is generally well suited to describe bulk and molecular structures containing

Ln, however it suffers of some major limitations. The weakest points in the model are the complete absence of covalency, that can be sometimes crucial to describe molecular systems like DyDOTA [23], and also the neglect of the mixing of the m_J states that can be also produced by small distortions of the ligand geometry.

An alternative notation to describe the effect of the ligands is provided by the angular overlap model [24, 25, 26] in which the parameters are obtained in a chemically more intuitive way, using effects of covalency.

Finally, it is important to notice that often in molecular magnetism it is common to use the Spin-Hamiltonian formalism that considers the effect of the ligand as a *zero-field* splitting (ZFS). This term can be written as:

$$\mathcal{H}_{\mathrm{ZFS}} = \boldsymbol{J} \cdot \boldsymbol{D} \cdot \boldsymbol{J} \tag{2.19}$$

where $\boldsymbol{D}$ is the real, symmetric zero-field splitting tensor. A proper rotation of the reference frame to make $\boldsymbol{D}$ diagonal, and the subtraction of a constant (that gives only an offset in the energy), make possible to decompose the tensor into two distinct contributions: a diagonal one (D) and an off-diagonal one (E). The ZFS term of the Hamiltonian looks like:

$$\mathcal{H}_{\mathrm{ZFS}} = D[J_z^2 - \frac{1}{3}J(J+1)] + E(J_x^2 + J_y^2) \tag{2.20}$$

Of course the notation of Equation 2.20 takes into account only the first order term in the expansion (the one proportional to J^2), but more terms can be added, if required. The ZFS approach and the CF approach are thus equivalent in the limit of considering only $\boldsymbol{O}_2^0$ and $\boldsymbol{O}_2^2$ operators. If only the ground multiplet is taken into account, the relation between ZFS and CF coefficients are: $D = 3b_2^0$ and $E = b_2^2$.

When a magnetic field is applied, a further term, called "Zeeman" term, in honour to the 1902 Nobel Prize Pieter Zeeman (1865-1943) must be added at the Hamiltonian. This term can be written in the form:

$$\mathcal{H}_{\mathrm{Zeeman},J} = [\frac{3}{2} + \frac{S(S+1) - L(L+1)}{2J(J+1)}]\mu_B \boldsymbol{J} \cdot \boldsymbol{B} = g_J \mu_B \boldsymbol{J} \cdot \boldsymbol{B} \tag{2.21}$$

where g_J is the Landé factor and μ_B is the Bohr magneton. This perturbation removes the $\pm m_J$ degeneracy whatever the parity of the spin, thus selectively populating the ground state with a defined sign of m_J. While the entity of the Zeeman splitting is generally limited to tens of cm^{-1}, its effect can have a major role in determining the magnetic properties of the system, *e.g.* a SMM can pass from a QT regime to a thermally activated one.

Since the magnetic anisotropy of most molecular compounds (especially based on Ln) are dominated by the ground state, it is often convenient, in terms of dimension of the Hamiltonian matrix, to write the Zeeman term substituting the the total angular momentum operator with an effective spin $S = 1/2$ and an anisotropic $\boldsymbol{g}$ tensor (formally only $\boldsymbol{g}^2$ should be considered a second-rank tensor). Of course this is only possible with Kramers' ions because the minimum degeneracy of the levels must be at least two. The corresponding Hamiltonian term takes the form:

$$\mathcal{H}_{\mathrm{Zeeman},S_{\mathrm{eff}}} = \mu_B \boldsymbol{S}_{\mathrm{eff}} \cdot \boldsymbol{g} \cdot \boldsymbol{B} \tag{2.22}$$

The reference frame in which $\boldsymbol{g}$ is diagonal provides the orientation of the magnetic anisotropy, and the relative magnitude of the components give an idea of the shape ($g_z \gg g_x = g_y$ - easy axis, $g_z \ll g_x = g_y$ - easy plane). The *effective spin* description must furnish the same information of Equation 2.21 considering only the ground doublet ($g_J J = g_z S_{\mathrm{eff}}$), thus if there is no mixing between states, the value of g_J is simply proportional to m_J of the pure ground doublet. The upper limit of g_z is thus equal to $2g_J J$.

Finally also the interaction between electronic and nuclear spins (*hyperfine* term) may play a role if the considered metal has one or more isotopes with a non-zero nuclear spin. Let us suppose for the sake of simplicity that inside a molecule is present only one magnetic ion, with a single isotope of nuclear spin I. The hyperfine term is then:

$$\mathcal{H}_{\mathrm{hyp}} = \boldsymbol{J} \cdot \boldsymbol{A} \cdot \boldsymbol{I} \tag{2.23}$$

where $\boldsymbol{A}$ is a tensor that couples the electronic spin operator with the nuclear one. It is generally complex to calculate because it contains several contributions (contact, dipolar and pseudocontact). However this interaction is generally weak for heavy elements and it is often neglected for Ln.

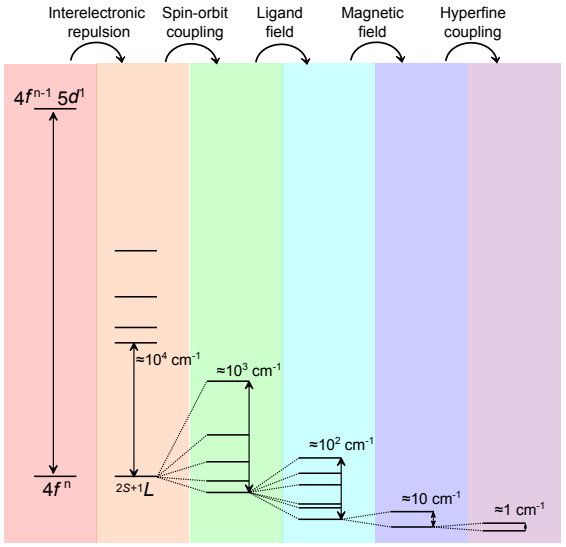

Figure 2.5: Energy diagram of the electronic structure of Ln.

All the contributions mentioned in this Section play a role in the definition of the energy of the system, anyhow the two that are responsible for magnetic anisotropy are the SOC and the CF. In an intuitive way we can say that while the SOC of the single ion defines the energetically more stable relative orientation between L and S, the CF orients the anisotropy in a certain spatial direction, as a function of the surrounded atoms. We can finally summarize that the Hamiltonian that must be used to obtain an accurate description of the energy of an atom is a sum of 4 terms:

$$\mathcal{H}_{\text{tot}} = \mathcal{H}_{\text{free}} + \mathcal{H}_{\text{CF}} + \mathcal{H}_{\text{Zeeman}} + \mathcal{H}_{\text{hyp}} \tag{2.24}$$

An energy diagram that summarizes the relative strength (considering Ln) of all the contributions mentioned in this Section is reported in Figure 2.5.

3 Noncollinearity

In Section 2.2.2 it was pointed out that a precise knowledge of the CF originated by the ligands is a mandatory requirement to correctly describe the anisotropy of molecules containing a metal centre. However it is not common to deal with crystals, or films, formed by molecules equally oriented in space and containing only one metal centre. More likely crystals are complex structures which can contain poly-nuclear clusters with interacting metals and/or molecules that are not equally oriented, thus exhibiting noncollinear magnetic structure. There are several sources of noncollinearity: some of them arises from interactions between centres such as the *Dzyaloshinskii-Moriya* term (Section 3.1.1) or frustration (Section 3.1.2) while others are related by crystal symmetry or molecular structures (Section 3.2).

3.1 Interactions

3.1.1 Antisymmetric interactions

Let us suppose to have a couple of interacting spins, namely $\boldsymbol{S}_1$ and $\boldsymbol{S}_2$. The useful Hamiltonian to describe this system is composed by three additive terms: the Hamiltonian for $\boldsymbol{S}_1$, the Hamiltonian for $\boldsymbol{S}_2$ (that can be both written as Equation 2.24) and an exchange term ($\mathcal{H}_{\text{exc}}$):

$$\mathcal{H}_{\text{exc}} = \boldsymbol{S}_1 \cdot \boldsymbol{J}_{\text{exc}} \cdot \boldsymbol{S}_2 = -J_{12}\boldsymbol{S}_1 \cdot \boldsymbol{S}_2 + \boldsymbol{S}_1 \cdot \boldsymbol{D}_{12} \cdot \boldsymbol{S}_2 + \boldsymbol{d}_{12}\boldsymbol{S}_1 \times \boldsymbol{S}_2 \quad (3.1)$$

The matrix $\boldsymbol{J}_{\text{exc}}$ describes the interaction between centres and it is not subject to any restriction. It is generally helpful to decompose $\mathcal{H}_{\text{exc}}$ into three contributions as in Equation 3.1: a scalar one, a vectorial one and

a tensorial one.

The scalar contribution is called *isotropic* or *Heisenberg* due to the absence of directional features. It tends to align the spins parallel ($J_{12} > 0$) or antiparallel ($J_{12} < 0$) and it is generally the biggest. If it dominates, the others can be treated as perturbations and the total spin $S_{\text{tot}} = S_1 + S_2$ is a good quantum number. In this regime the energies of the states can be easily obtained as:

$$\mathrm{E}(S) = -(J_{12}/2)[S(S+1) - S_1(S_1+1) - S_2(S_2+1)] \qquad (3.2)$$

The second contribution is called *anisotropic* because the matrix D_{12} is responsible of the alignment of the spins along a certain direction. It has also the same form of the ZFS term of the Spin Hamiltonian (Equation 2.19), and in fact it has the same effect on the spins, *e.g.* the canting toward a certain direction that is imposed by the $\boldsymbol{D}_{12}$ matrix. If the molecular symmetry is high, a number of constrains can be imposed on the orientation of this matrix thus helping to obtain a quantitative estimation of this contribution [27].

The third contribution is called *antisymmetric* or *Dzyaloshinskii-Moriya*. This is due to the fact that the existence of this part of the interaction was firstly pointed out by Dzyaloshinskii in 1958 [28] and theoretically justified two years later by Moriya [29, 30]. Moriya showed that that this term can be obtained by the second order perturbation theory with respect to spin-orbit interaction and isotropic interatomic exchange interaction and it has approximately magnitude of the order $d_{12} \sim \lambda I_0/\Delta E_{12}$, where λ is the spin-orbit parameter, I_0 is the exchange interaction integral that connects the ground state of 1 with an excited state of 2 and ΔE_{12} is the energy gap between these two states. It can be shown [31] that two atoms antiferromagnetically (AFM) coupled exhibit a canting angle with respect to the direction of the AFM alignment $\alpha = \arctan(D_{12}/(2\sqrt{6}J_{\text{exc}}))$ that leads to weak magnetization perpendicular to the alignment. A detailed review of some examples of antisymmetric interactions can be found in ref. [32].

3.1.2 Frustration

Starting from Equation 3.1, and supposing to be in the strong exchange limit (the anisotropic and antisymmetric part of the interaction are perturbations compared to the isotropic one), one can think that all the interactions between spins in the considered molecule are fulfilled. However sometimes it is geometrically impossible to accommodate all this interactions, leading to a phenomenon called *spin frustration*.

The simplest model to understand frustration is reported in Figure 3.1: a triangle with AFM interactions (coupling constant $J_{ex} < 0$) between its vertexes. There are several approaches to frustration well-explained by Schnack [33], and a number of books have been written on this topic [34, 35], so in this Section we just recall some systems where frustration is present and the major effects that it produces. The phenomenon of

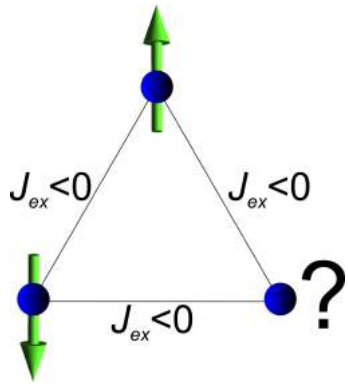

Figure 3.1: Sketch of a frustrated triangular spin system, which possess ambiguity about the direction of the third spin.

frustration is known since 1977 when was for the first time applied to spin-ice systems [36, 37]. Later, it was identified as the major responsible of the exotic magnetic behaviour of some complex oxides such as pyrochlore systems containing Ln as $Ln_2Ti_2O_7$ (Ln=Ho,Dy) [38, 39, 40, 41].

Later, frustration was also found in some molecular magnets, such as odd-membered spin rings [42] or Ln-based chains [43, 44] or triangular structures [45]. Clearly some requirements must be fulfilled to efficiently obtain this

class of molecules: the spins must interact but remain localized, so in this vision Ln are good candidates due to their large unquenched orbital moments, but also complex architectures of TM ions can be employed, even if proper spacers must be used.

3.2 Crystal structure and ligand geometry

In this Section we will analyse how the crystal habit of some compounds as well as the ligand geometry can reflect in noncollinear anisotropy axes. There are 7 crystal systems, each one characterized by three direction vectors (a, b, c) and three angles (α, β, γ), as reported in Table 3.1.

Crystal system	Vectors	Angles	Typical operation
Triclinic	$a \neq b \neq c$	$\alpha, \beta, \gamma \neq 90°$	None
Monoclinic	$a \neq b \neq c$	$\alpha = \gamma = 90°, \beta \neq 90°$	C_2 or σ
Orthorombic	$a \neq b \neq c$	$\alpha = \beta = \gamma = 90°$	3 C_2 or C_2 & 2 σ
Tetragonal	$a = b \neq c$	$\alpha = \beta = \gamma = 90°$	C_4
Trigonal	$a = b \neq c$	$\alpha = \beta = 90°, \gamma = 120°$	C_3
Hexagonal	$a = b \neq c$	$\alpha = \beta = 90°, \gamma = 120°$	C_6
Cubic	$a = b = c$	$\alpha = \beta = \gamma = 90°$	4 C_3

Table 3.1: Angles and vectors characteristic of the seven crystal systems.

If inside the unit cell of the crystal more than one molecule is present (molecules reported by an inversion centre do not count, due to the symmetry of the anisotropy), there will be noncollinearity between the anisotropy axis and thus the anisotropy of the crystal will be a geometrical sum of all the inequivalent contributions. This point is crucial, because the most sensitive technique used to determine the anisotropy of crystals, the Single Crystal Magnetometry, has the major disadvantage to be sensitive only to a fixed component of the magnetization, so that the results obtained using this technique cannot be easily interpreted if more than one contribution is present. Moreover this technique requires a huge amount of material, which means massive crystals, that usually have plenty of defects and are thus very difficult to obtain with a high degree of crystallinity. The only

structures that can be successfully analysed with this technique must have a molecular symmetry *at least equal* than the crystal symmetry. This is straightforward only in the triclinic space group where no symmetry operation are present and it is extremely rare in all other cases. A textbook example that will be discussed in this thesis is the LnDOTA family [46, 23].

However a proper choice of the ligands can efficiently compensate the presence of crystal symmetry operation, or *viceversa* can favour a certain spin structure. For the first case we can cite the LnTRENSAL family that crystallizes in a hexagonal space group $P\bar{3}c1$: the molecular symmetry of this derivatives (C_3) can be treated at a first approximation as uniaxial thus the contributions arising from the two not isooriented molecules in the cell can be treated as one [47]. Obviously, the ligand structure can also force a molecular structure that favours particular spin configuration such as in the helix analysed in Section 7.3 and for this reason a lot of synthetic efforts are devoted to the chemical design of ligands; a detailed discussion about the more successful synthetic strategies is reported in ref. [48].

4 Cantilever Torque Magnetometry

The present Chapter is devoted to describe the technique that will be the cornerstone of this Thesis: Cantilever Torque Magnetometry (CTM). After an overview of the main theoretical concepts (Section 4.1) and of the experimental setup (Section 4.2) that is necessary for a satisfactory comprehension of the technique and its results, in Section 4.3 we will describe all the possible physical quantities that can be varied during a measurement, and which information they can provide. Finally a comparison between this technique and few others will be presented in Section 4.4.

4.1 Theoretical background

The capacitance of an ideal parallel plate capacitor is given by:

$$C = \frac{\varepsilon A}{d} \tag{4.1}$$

Where ε is the permittivity of the dielectric that separates the plates, A is the area of the cantilever and d is the separation between the plates. The relation between C and a change in the separation Δd can be obtained starting from the Taylor series of the function $F(x) = 1/(x + \delta)$:

$$\frac{1}{x+\delta} = \frac{1}{n!} \sum \frac{\mathrm{d}^n f}{\mathrm{d}\delta^n}\bigg|_{\delta=0} \delta^n \tag{4.2}$$

The capacitance without any applied force is $C_0 = \varepsilon A/d_0$. Using Equation 4.2 we can expand the capacitance, and we can further obtain the difference of capacitance (ΔC) as:

$$\Delta C = C(d_0 + \delta d) - C_0 = -\frac{C_0}{d_0}\Delta d + \frac{C_0}{d_0^2}\Delta d^2 - \frac{C_0}{d_0^3}\Delta d^3 + \cdots \tag{4.3}$$

From Equation 4.3, we see that the capacitance is directly proportional to Δd, which in turn is directly proportional to the applied torque. A calibration of the system is possible using gold micro tracks, but for the results discussed in this thesis it was not necessary. We just taken into account the different intensity of the resultant signal due to the different mass of the samples using a scale factor (f_{sc}).

The relation between magnetic torque ($\boldsymbol{\tau}$) and magnetic anisotropy is a little more tricky to find, but can be derived starting from the definition of torque, that is, the derivative of the energy with respect to the angle. We have already seen in Equation 2.8 that a magnetic moment $\boldsymbol{m}_i$ inside a magnetic field $\boldsymbol{B}$ gains a potential energy that is a function of the angle φ between $\boldsymbol{m}_i$ and $\boldsymbol{B}$. If we derive this equation with respect to this angle, we obtain the torque acting on $\boldsymbol{m}_i$ as:

$$\tau_i = \frac{\mathrm{d}E}{\mathrm{d}\varphi} = m_i B \sin\varphi \tag{4.4}$$

If we now consider a magnetized permanent magnet containing n equal magnetic moments, we can rewrite Equation 4.4 obtaining the macroscopic torque $\boldsymbol{\tau}$ as follows:

$$\boldsymbol{\tau} = \sum_{i=1}^{n} (\boldsymbol{m}_i \times \boldsymbol{B}) = \boldsymbol{M} \times \boldsymbol{B} \tag{4.5}$$

Nevertheless, if we consider a paramagnet one may think that $\boldsymbol{M}$ and $\boldsymbol{B}$ are always parallel, and $\boldsymbol{\tau}$ should be identically zero at any moment. This is true *only* in the case of a purely isotropic paramagnet but it fails as more as the molecule is anisotropic. Indeed, for low values of B, the anisotropy of the sample imposes that $\boldsymbol{M}$ should lie along a specific direction, thus creating a non-zero torque. It is now useful to define the symmetric magnetic susceptibility tensor as:

$$\boldsymbol{\chi}_{ij} = \frac{\partial M_j}{\partial B_i} \tag{4.6}$$

Where $i, j = x, y, z$. For low values of B (which means $k_B T \gg g\mu_B B$), M increases linearly with the field and the susceptibility is field independent. If we place both $\boldsymbol{B}$ and $\boldsymbol{M}$ in the same plane (say, xz), $M_\alpha = \chi_{\alpha\alpha} B_\alpha + \chi_{\beta\alpha} B_\beta$ (where $\alpha = z$ and $\beta = x$ or *viceversa*). Defining η the angle between the $\boldsymbol{B}$ and the z-axis in the plane, we can rewrite Equation 4.5 as:

$$\begin{aligned} \tau_y &= M_z B_x - M_x B_z = (\chi_{zz} - \chi_{xx}) B_x B_z + (B_x^2 - B_z^2)\chi_{xz} \\ &= B^2(\chi_{zz} - \chi_{xx}) \cos\eta \sin\eta + B^2 \chi_{xz}(1 - 2\sin^2\eta) \end{aligned} \tag{4.7}$$

It is always possible to set the term χ_{xz} to zero by a proper shift of reference frame, so from now on we will always write τ_y as:

$$\tau_y = B^2(\chi_{zz} - \chi_{xx}) \cos\eta \sin\eta \tag{4.8}$$

From Equation 4.8 it is clear that the torque of an anisotropic paramagnet *does not* have the typical $k\pi$ periodicity of a vector product, but it goes to zero at least every 90°. Recalling that the angle η is the one between the easy direction and $\boldsymbol{B}$, it is clear that with this technique it is particularly easy to detect the orientation of the anisotropy axis. Moreover in a typical measurement $\boldsymbol{B}$ and η are known quantities, so torque can be considered a *direct* measurements of the anisotropy character $(\chi_{zz} - \chi_{xx})$ of the system. Neverthenless normally $\boldsymbol{M}$ does not lie in the plane of rotation, so what can be detected is only the torque generated by the component of $\boldsymbol{M}$ in the plane.

4.2 Experimental setup

The experimental setup used for measuring magnetic torque *via* capacitive detection is quite simple to achieve. The core of the instrument is the capacitor sketched in Figure 4.1, that has a fixed copper base plate (thickness $\sim 300\,\text{nm}$) separated by $\sim 1\,\text{mm}$ from an upper plate (the cantilever)

that can be deflected elastically if a torque is acting on the sample that is fixed on top of it. The upper plate has a thickness of about 25 µm and it is made of copper-beryllium alloy (∼2% of Be). The choice of CuBe has several advantages with respect to other metallic alloys: first of all it is diamagnetic, then it has a linear expansion coefficient that is almost independent on temperature [49, 50], and has a high elastic and fatigue strengths. The support, as well as the spacer, are made of Epoxy and have the function of establishing a well-defined parallelism and distance (∼ 100 µm) between the two plates. A gear wheel is connected to the core of the instrument and allows a complete clockwise rotation around the Y-axis in the laboratory rf. In this reference frame the Z-axis corresponds to the direction of $\boldsymbol{B}$ and the rotation angle (ϑ) is defined between the upper plate of the cantilever and -Z (see Figure 4.1 b).

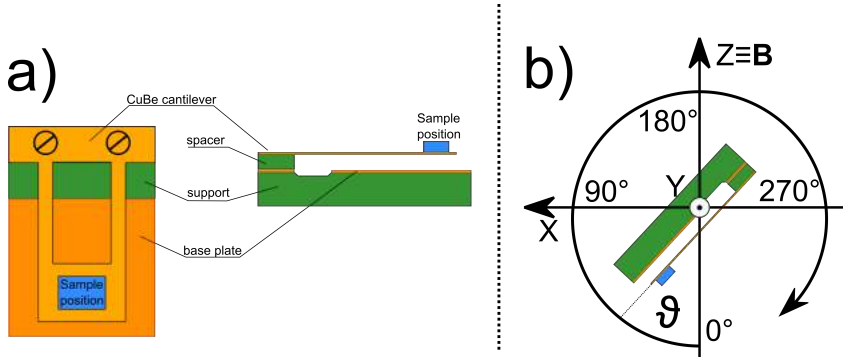

Figure 4.1: a) Top (left) and side (right) view of the main part of a capacitive torque meter. b) Basic operation mode of the instrument, with rotation angle and laboratory XYZ reference frame on it.

The sample can be either a single crystal or a thin film evaporated on a support of glass or other inert material. In the case of single crystals the sample is glued or fixed on a square acetate foil with two distinguishable sides. Before doing the measurements, all the crystal samples were indexed with an X-rays diffractometer to know exactly which crystallographic plane will be investigated during the experiment.

Even if there are several ways to detect the magnetic torque acting on

a sample, *e.g.* optical [51, 52], piezoresistive [53, 54] piezoelectric [55] and capacitive [56, 57, 58], in this Thesis the detection is always capacitive (Andeen-Hagerling 2550A automatic capacitance bridge), due to the sensitivity and simplicity of this method.

4.3 Type of measurements

The physical quantities that can be varied during a measurement with a cantilever magnetometer are: the temperature (T), the angle (ϑ) between sample and magnetic field and the intensity of the magnetic field (B). The most common measurement with a cantilever magnetometer is to fix all the variables except the angle, because an angle scan provides data on the orientation of the magnetic anisotropy of the sample. A simulated curve is reported for three different values of the magnetic field in Figure 4.2 for uniaxial anisotropy. While for low fields the angular dependence of the torque is the one described in Equation 4.8, increasing the field the curves are progressively warped. In particular, when $\boldsymbol{M}$ is perpendicular to $\boldsymbol{B}$ ($\vartheta = \pi/2 + n\pi$ in Figure 4.2), we observe the maximum slope in the torque curve.

In Figure 4.3 we reported $\partial\tau/\partial\vartheta$ to emphasize the deviation from Equation 4.8 when the field increases. First of all we notice that the values and shape of maxima and minima of the derivative are not symmetric, due to the effect of non-symmetric depopulation of $\boldsymbol{M}$ as a function of the angle. As expected this asymmetry is more pronounced for high values of $\boldsymbol{B}$. As a consequence, also the zero-derivative points are *different* for all curves, and they are more close to the angle at which the field is parallel to the hard direction ($\vartheta = 90°$) the more $\boldsymbol{B}$ is high. This peculiarity makes CTM particularly suitable for identifying the anisotropy shape.

The temperature dependence of the torque (Figure 4.4) is principally related to the population of the levels inside the ground J manifold that is of course connected to the relative weight of the thermal energy (k_BT) compared to the intensity of the field perturbation ($g\mu_B B$). In fact, a uniform population of the levels inside the ground multiplet must mirror

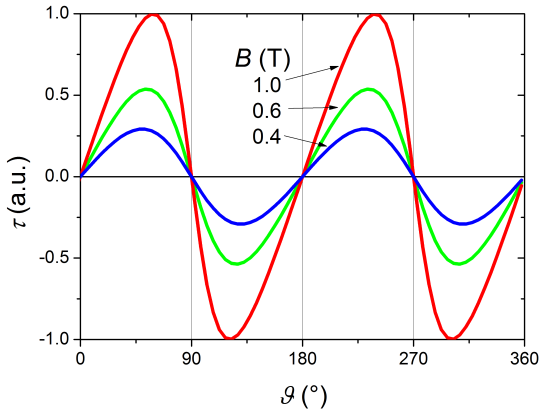

Figure 4.2: Simulated torque for a Dy^{3+} ion with uniaxial anisotropy ($b_2^0 = -0.035$) at fixed temperature ($T = 2\,\mathrm{K}$). The angle $\vartheta = 0°$ corresponds to the easy axis of the molecule being parallel to the field.

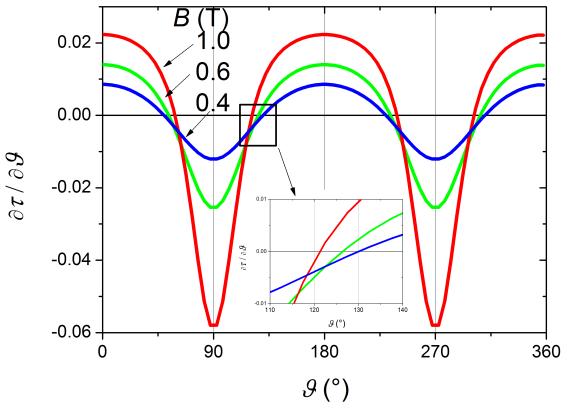

Figure 4.3: First derivative of the curves reported in Figure 4.2.

in a perfect spatial magnetic isotropy, thus in this limit no resulting torque is expected. Due to the fact that a measure of magnetic torque is not sensitive to the isotropic part of the magnetization, if the crystal contains a suitable number of magnetic moments, a study in temperature can provide access to the CF parameters [15] or to the ZFS parameter [13].

Similar information can also be extracted fixing the angle and the temperature, while the field is varied. In this way the torque, near the hard direction ($\vartheta = 89°$ in Figure 4.5) increase quadratically with the field at low fields (when $\boldsymbol{M}$ is linear with $\boldsymbol{B}$, thus $\chi = M/B$), and then passes through a maximum before reaching the saturation value $-2DJ[J - 0.5]\sin\vartheta\cos\vartheta$ (in this case $D = b_2^0$, see also Section 2.2.2). The field at which the maximum is observed is called *breaking field* [59], and it represents the minimum value of the magnetic field that is able to overcome the anisotropy of the sample, thus canting the magnetization toward an unfavoured direction. Of course, the breaking field is related to the spin multiplicity of the sample: for this reason heavy Ln, that have high anisotropy, are characterized by values of breaking field generally higher than TM. Unfortunately this kind of measurements can be performed only if T and ϑ are known with great accuracy, and even so the maximum of the torque obtained with this type of measurements is often very broadened so that this measurements can only provide an initial estimation of the ZFS value, but must be flanked by other type of experimental evidences.

If the sample retains its magnetization over a period of time and under a certain T (that is, exhibit *magnetic hysteresis*), the measurement with fixed T and ϑ and B varied from negative to positive and *viceversa* are not superimposable. This means that also CTM is able to detect if a sample possess magnetic hysteresis, but with a limitation: at zero field the torque is forced to vanish (Equation 4.5), so it is impossible to detect remnant magnetization. Nevertheless samples that are commonly studied in molecular magnetism are often characterized by butterfly hysteresis curves, so in this cases the only difference between the CTM and the DC hysteresis loop is that the torque do not change sign upon inversion of $\boldsymbol{B}$ because in the low field limit also $\boldsymbol{M}$ is reversed, while the DC loop does.

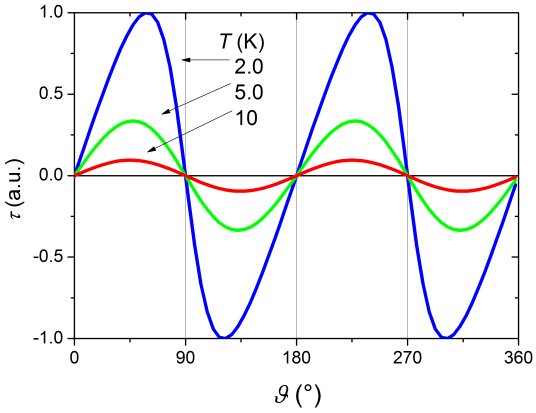

Figure 4.4: Simulated torque for a Dy^{3+} ion with uniaxial anisotropy ($b_2^0 = -0.035$) at fixed field $B = 1\,\mathrm{T}$. The angle $\vartheta = 0°$ corresponds to the easy axis of the molecule being parallel to the field.

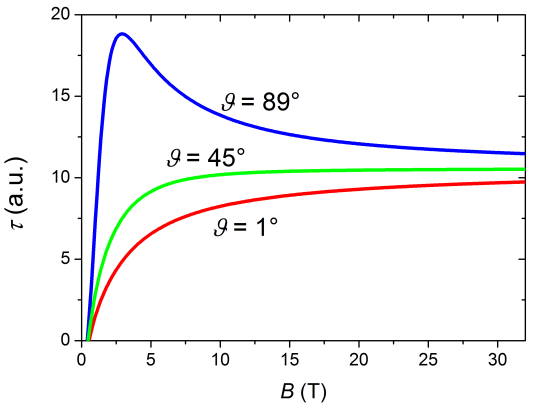

Figure 4.5: Simulated torque for a Dy^{3+} ion with uniaxial anisotropy ($b_2^0 = -0.035$) at fixed field $T = 2\,\mathrm{T}$ and various ϑ angles. All the curves were normalize for a factor $\sin\vartheta\cos\vartheta$, to obtain the same saturation value (straight line) for all the angles.

4.4 Comparison with other techniques

As we pointed out in Section 4.3, CTM can extract precious information about the direction of the anisotropy of molecular systems. The other technique that is usually employed for this type of measurements is Angular Resolved Single Crystal Magnetometry. This is a powerful tool that can be employed to obtain accurate values of the susceptibility tensor of indexed single crystals. The basic principle is to rotate the crystal inside a weak magnetic field and detecting the component of the magnetization that is aligned with the field, in this way the detection of the easy and hard directions of anisotropy is very easy because they can be observed as a maximum or a minimum (respectively) of the signal. Unfortunately, the anisotropic contribution at the signal is summed to a huge isotropic one, so it is often very difficult to isolate the desired signal. Moreover when the field is increased not only the anisotropic, but also the absolute value of the diamagnetic contribution increases, so the effect of increasing the field *does not* increase the sensitivity. Finally, the technique is often time consuming.

Another technique that is widely used to investigate single crystals of magnetic molecules is the Electronic Paramagnetic Resonance (EPR). The high sensitivity and versatility place this technique in a privileged position when an evaluation of anisotropy is needed. EPR can in fact extract the principal components of the $\boldsymbol{g}$ tensor from powder experiments and also determine the orientation of the anisotropy axis performing single crystal measurements. This can be done fixing a certain frequency and varying uniformly the magnetic field since a transition is observed. The first limitation is to have an observable transition inside the range of the fields experimentally achievable: for this reason Kramers' ions are generally less complicated because of the degeneracy of the ground state. However it is also important to consider that some selection rules are active as a function of the experimental setup, so the composition of the ground state strongly influences the transition probability, and thus the intensity of the detected signal. For all this reasons it is not uncommon to study systems

that do not possess any EPR signal especially strongly axial molecules. A particularly difficult case of study in EPR are the Ln because they generally have very fast spin-lattice relaxation times (that causes a broadening of the line) and the separation of the first excited state is often one order of magnitude larger than the one experimentally accessible.

The other spectroscopic technique that is used to study magnetic systems is Luminescence. If the experimental setup is properly equipped, the levels that can be detect can arise both from the ground or from excited multiplets; this designate luminescence as the most powerful technique to obtain the CF splitting parameters. The main limitations are instead the fact that the investigated ion must be exhibit energy differences between levels that can be detected with the experimental setup and that if more than one not equivalent ion is present inside the crystal, it is possible to have superposition of the absorption/emission line, making the spectra impossible to unequivocally interpret.

Compared to this two techniques, CTM has some useful advantages as well as some limitations. To detect a torque signal it is not necessary to use big crystals, because the capacitive detection is extremely sensitive and also because the signal does not contain any isotropic part (see Equation 4.8). Moreover, as we have seen in Section 4.3, the detection of the anisotropy orientation is very easy and fast and can be done for *all* the crystallographic systems and *all* magnetic ions, even if in some cases the results need to be flanker with other experimental or theoretical data to distinguish between more than one possible solution. The temperature range of the measurements is about $2 - 300\,\mathrm{K}$, so the only levels that contributes to the signal are those significantly populated at this temperatures, however CTM data are extremely sensitive to the low energy levels, that are the ones involved in the mechanism of slow magnetic relaxation of Single Molecule Magnets.

4.5 Program

In this Section we will analyse the program that we used for all the fits and simulations reported in this thesis. The program, wrote in FORTRAN 90 programming language, was conceived to calculate the magnetic torque experienced by a sample formed by an arbitrary number of noncollinear magnetic moments inside a magnetic field that rotates in an arbitrary number of different planes.

Before entering into the details of the program we briefly present all the rf used in the program, to clarify the convention and the notation used in the rest of the Thesis. The laboratory XYZ rf has *always* the static magnetic field parallel to the Z axis, and the sample rotating in the XZ plane. The Y axis is the only direction in which we can experimentally register the torque acting on the sample. The crystallographic rf abc was always abandoned before starting the calculations to pass to the more convenient orthogonal $ab'c^*$ rf. Finally the xyz molecular rf is defined as the rf of the principal magnetic axis of the molecule (*e.g.* the rf in which the $\boldsymbol{g}$ tensor is diagonal).

The first input of the program is build up with several data: the director cosines of Y and of Z in the $ab'c^*$ rf, the Euler angles (ρ, ξ, ψ) that connect $ab'c^*$ to xyz, a scale factor (f_{sc}), the CF parameters, the principal values of the $\boldsymbol{g}$ tensor, the ZFS parameters or any other quantity that can enter inside the Hamiltonian that we want to use to describe the system. Of course all this quantities can be varied or fixed during the calculation (particular attention needed to be devoted to avoid overparametrization problems).

The initial values of the Euler angles were used to build up the Euler rotation matrix ($\mathrm{E_M}$, see Equation 4.9) that connects two rf.

$$\begin{pmatrix} \cos\psi\cos\rho - \sin\psi\cos\xi\sin\rho & \cos\psi\sin\rho + \sin\psi\cos\xi\cos\rho & \sin\psi\sin\xi \\ -\cos\rho\sin\psi - \cos\psi\cos\xi\sin\rho & -\sin\rho\sin\psi + \cos\xi\cos\rho\cos\psi & \cos\psi\sin\xi \\ \sin\rho\sin\xi & -\sin\xi\cos\rho & \cos\xi \end{pmatrix} \tag{4.9}$$

In the program, we used the extrinsic x-convention, which means that

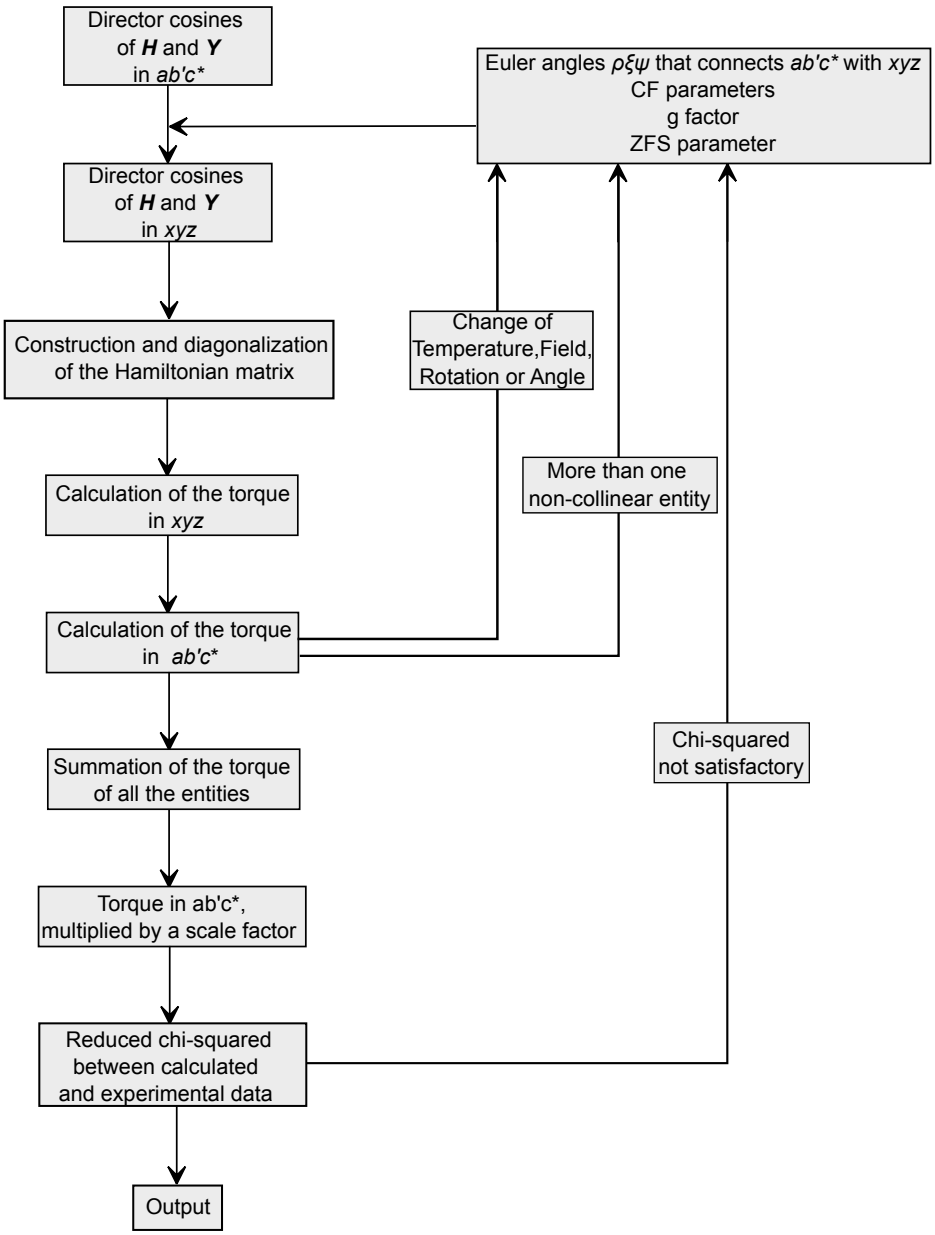

Figure 4.6: Block diagram of the program used for the torque simulations and fits.

the first rotation of an angle ψ must be performed using the initial z axis as rotation axis (that is the c^* axis), the second rotation of angle ξ using the initial x-axis as rotation axis and the last one of an angle ρ using again z-axis as rotation axis. A model picture of an intrinsic rotation is reported in Figure 4.7. Once the program has calculated the director cosines of the

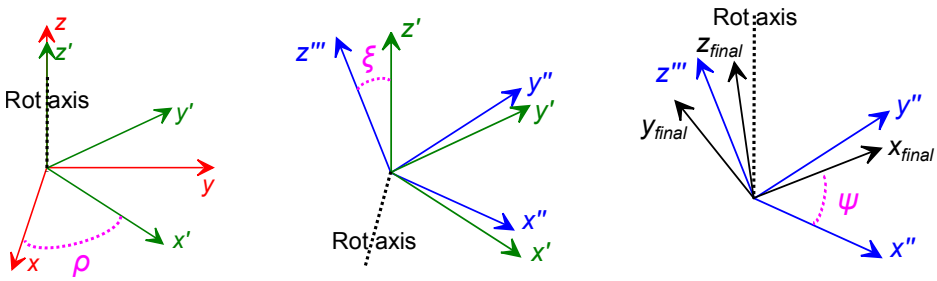

Figure 4.7: Extrinsic rotation using the x-convention of the original (red) rf using three angles ρ, ξ, ψ to obtain the final (black) rf passing through two intermediate (green and blue) rf.

direction of the field (Z) and of the rotation axis (Y) in the initial xyz rf, we used a simple rotation matrix to reproduce the components of the field at any ϑ angle in the xyz rf. In the following matrix we will use the notation $\sin(\vartheta) = S$ and $\cos(\vartheta) = C$:

$$\begin{pmatrix} Y_a^2 + (1 - Y_a^2)C & (1 - C)Y_aY_b - Y_cS & (1 - C)Y_aY_c + Y_bS \\ (1 - C)Y_aY_b + Y_cS & Y_b^2 + (1 - Y_b^2)C & (1 - C)Y_bY_c - Y_aS \\ (1 - C)Y_aY_c - Y_bS & (1 - C)Y_bY_c + Y_aS & Y_c^2 + (1 - Y_c^2)C \end{pmatrix} \quad (4.10)$$

In this way, we can insert the director cosines of the field in the construction of the Hamiltonian matrix to calculate the Zeeman contribution that, summed with all the other desired terms, constitute the Hamiltonian matrix of the system. This matrix is diagonalized to obtain eigenvectors and eigenvalues that provides the energies of the system. Moreover in this way it is also possible to obtain the magnetic torque acting on the sample in the xyz rf taking advantage of Equation 4.5.

If more than one noncollinear contribution is present inside the structure, we can easily find the orientation of the i-th molecular rf simply modifying

the Euler angles of the first rf following the symmetry operation of the group. In this way we can calculate, and sum, all the torque moments acting on the sample, obtaining the resultant torque. At this point a simple scalar product between the extracted torque and the rotation axis Y provides a quantity that, multiplied by a scale factor to take into account the amount of magnetic material, can be directly compared to the experimental data. A calculation of the χ^2 coefficient discriminates if the fitting values should be refined or the program can exit with the output. The obtained errors were estimated using a MINUIT subroutine (version 94.1).

5 Collinear systems

The correlation between anisotropy and magnetic relaxation is, up to now, a field with a lot of open questions in molecular magnetism. The rush to obtain the SMM with the highest barrier for the relaxation of the magnetization as well as the increasing number of experimental studies devoted to the construction of spintronic devices based on single molecules must be flanked by a rational understanding of the role that magnetic anisotropy plays for these systems. Even if more than one published papers individuated some "golden rules" that can often provide a good starting point to synthesise promising materials, it is common to read articles where this rules are violated.

To shed light on the interplay between magnetic anisotropy and magneto-structural properties, we initially studied simple systems containing only collinear contributions. In particular we focused on Ln based mononuclear complexes because they are a class of molecules that possess high anisotropy and that already find lots of uses in different fields ranging from spintronics to biophysics. As already explained in Section 2.2.2 models based on point charge interactions are often used to predict the shape and direction anisotropy of systems containing Ln [60, 21, 61] but can often fail. In this Chapter we will analyse two systems: the first one is the complex formed by Ln with the TRENSAL ligand; a family of molecules that crystallizes in the hexagonal space group and have been already intensively studied *via* luminescent measurements. The second one is the LnDOTA family, that crystallizes in the triclinic space group. For the sake of simplicity in this two sections the compounds will be called with the Ln element that they contain in bold.

5.1 LnTRENSAL

Papers in Appendix

Beyond the anisotropy barrier: slow relaxation of the magnetization in both easy-axis and easy-plane Ln(trensal) complexes.
E. Lucaccini, L. Sorace, M. Perfetti, J.P. Costes and R. Sessoli.
Chemical Communications, **2014**, 50(14), 1648-1651.

Determination of Magnetic Anisotropy in the LnTRENSAL Complexes (Ln = Tb, Dy, Er) by Torque Magnetometry
M. Perfetti, E. Lucaccini, L. Sorace, J.P. Costes and R. Sessoli.
Inorganic Chemistry, **2015**, 54(7), 3090-3092

The H_3TRENSAL ligand (2,2',2"- Tris(salicylideneimino)triethylamine) is an heptacoordinate coordination agent (it contains 4 Nitrogens and 3 Oxygens free to coordinate a metal ion) that can efficiently encapsulate any Ln. In literature is present more than one synthetic strategy to obtain this compounds [62, 63, 64, 65, 66] because they were initially studied in coordination chemistry as a rare example of heptacoordinates Ln complexes [67] and, more recently, the functionalization and interaction between ErTRENSAL and a metallic surface was also investigated [68, 69]. All this isomorphous compounds crystallizes in the trigonal $P\bar{3}c1$ space group, with the C_3 axis passing through the Ln ion. A molecule belonging to this family is reported in Figure 5.1.

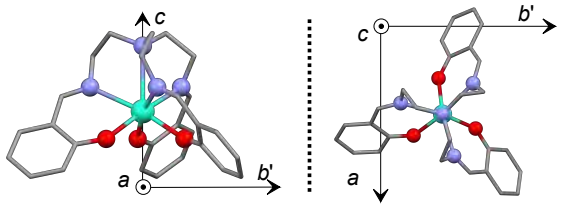

Figure 5.1: Two different views of the LnTRENSAL structure in the orthogonal $ab'c$ rf. Color code: grey-Carbon, green-Lanthanide, blue-Nitrogen, red-Oxygen, Hydrogen atoms were omitted for clarity.

In the first work that we have published on these systems (see Appendix), we have found that the **Er** and **Dy** derivatives showed easy-axis and easy-plane anisotropy, respectively, but surprisingly they both exhibit slow relaxation of the magnetization. This phenomenon is commonly associated with a magnetic bistability, practically realized when the spins are "trapped" inside a well with an assigned sign of m_J, and they can populate the other degenerate (without applied field) ground Stark sublevel *via* quantum tunneling (QT), thermal activated (Orbach) process, two phonon process or Raman process. The appearance of magnetic bistability was retained to be possible *only* when the magnetization tends to lie along an axis, that is, when Ising anisotropy is present (a detailed discussion about this topic can be found in ref. [13]). Our work clearly showed, with a multitechnique approach (EPR, standard magnetometry), that this is not generally true because the easy plane **Dy** relaxes slowly even in zero applied field. To investigate the role of the relaxation processes and their relative weight in this compounds, we diluted our samples in a diamagnetic isostructural matrix of **Y** (dilution $\sim$ 95 % **Y**). In Figure 5.2 we reported the field

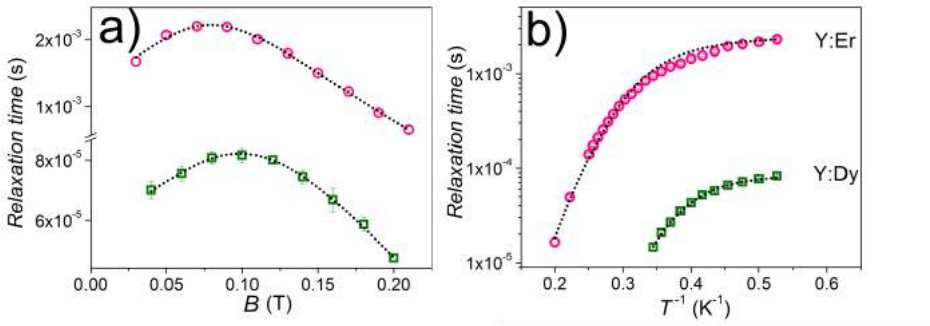

Figure 5.2: Field (panel a) and temperature (panel b) dependence of the relaxation times of **YEr** (circles) and **YDy** (squares) and best fit curves obtained by using Equation 5.1 and 5.2.

(panel a, $T = 1.8\,\mathrm{K}$) and temperature (panel b, $B = 0.08\,\mathrm{T}$ for **Dy** and $B = 0.09\,\mathrm{T}$ for **Er**) dependence of the relaxation time that we extracted from AC susceptibility data (see Appendix). The analysis of the relaxation

	Dy	**Er**
$A_1(\mathrm{s^{-1}\,K^{-1}\,T^{-4}})$	$(2.0 \pm 1.8) \times 10^4$	$(3 \pm 2) \times 10^5$
$A_2(\mathrm{s^{-1}\,K^{-1}\,T^{-2}})$	$(1.4 \pm 0.1) \times 10^4$	$(2.0 \pm 0.1) \times 10^1$
$B_1(\mathrm{s^{-1}})$	$(71 \pm 4) \times 10^1$	$(158 \pm 2) \times 10^2$
$B_2(\mathrm{T^{-2}})$	$(2.7 \pm 0.4) \times 10^2$	$(9.2 \pm 0.7) \times 10^1$

Table 5.1: Best fit parameters obtained using Equation 5.1

times ($\mathcal{T}$) in field was tentatively performed using the following equation:

$$\mathcal{T}^{-1} = \frac{B_1}{1 + B_2 B^2} + A_1 B^4 T + A_2 B^2 T \tag{5.1}$$

where the first term represents the field dependence of QT process [70], the second one the direct process for a Kramers ion without hyperfine interactions, and the third one is the direct process for a Kramers ion in the presence of hyperfine interaction [15]. The obtained results, summarized in Table 5.1, where successively used to fit temperature dependence of $\mathcal{T}$ as follows:

$$\mathcal{T}^{-1} = \frac{B_1}{1 + B_2 B^2} + A_1 B^4 T + A_2 B^2 T + C T^n + \frac{1}{\mathcal{T}_0} e^{-\Delta / k_B T} \tag{5.2}$$

where the first three terms are the same as in Equation 5.1, the fourth is the Raman one, and the fifth is the Orbach one. To avoid overparametrization we fixed the coefficients B_1, B_2, A_1, A_2 to the values extracted from Equation 5.2. For none of the two derivatives reasonable fits could be obtained by including Orbach processes in addition to the direct and QT ones, while a Raman process, with variable exponent n, provided reasonable reproduction of the data (best fit values $n = 9$ for **Dy** and $n = 11$ for **Er**). The main conclusions of this work were to establish that the slow relaxation of the magnetization can take place also in compounds with easy plane anisotropy and to invalidate the general assumption that the Orbach process is the main relaxation pathway for an easy axis SMM.

At the end of this first study two major questions were yet unsolved: we wanted to obtain a reliable set of CF parameters that can reproduce

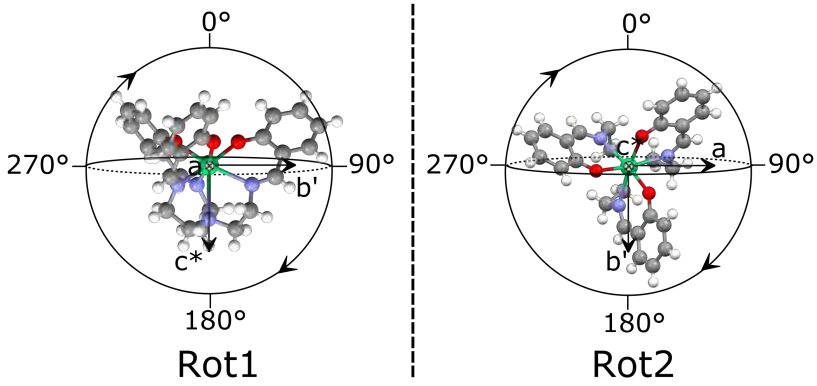

Figure 5.3: Graphical representation of Rot1 (from C_3 axis to ab plane) and Rot2 (in-plane). The reported angle is ϑ. Color code: grey-carbon, white-hydrogen, red-oxygen, blue-nitrogen, green-rare earth.

at least the splitting of the ground multiplet, in particular the energy gap between ground and first excited Stark level, and we also wanted some information about **Tb** that exhibited an unexpected EPR signal. To answer this questions we indexed single crystals of **Tb**,**Dy** and **Er** glued with grease to a square acetate foil with two distinguishable faces (details about the synthesis and on the indexing can be found in Appendix). For all the studied crystals the unit cell corresponded to the one reported in literature [62]. The indexing was necessary to connect the chosen orthogonal crystallographic rf $(ab'c)$ to the laboratory rf XYZ, where the torque is measured along Y and the applied field is always parallel to Z. Figure 5.3 shows the two rotations that have been performed for each derivative: the first (Rot1) having Y lying in the ab plane, and Z coincident with -c, while the second (Rot2) scanning the ab plane, *ergo* during Rot2 the rotation axis was the c crystallographic axis.

In Figure 5.4 we reported the angular dependence of the torque signal for the three studied systems (Rot1) at fixed field ($B = 12\,\mathrm{T}$) and temperature ($T = 5\,\mathrm{K}$). As we already mentioned, in the high field limit the quantity $\partial\tau/\partial\vartheta$ is extremely different if the easy axis is parallel or perpendicular to

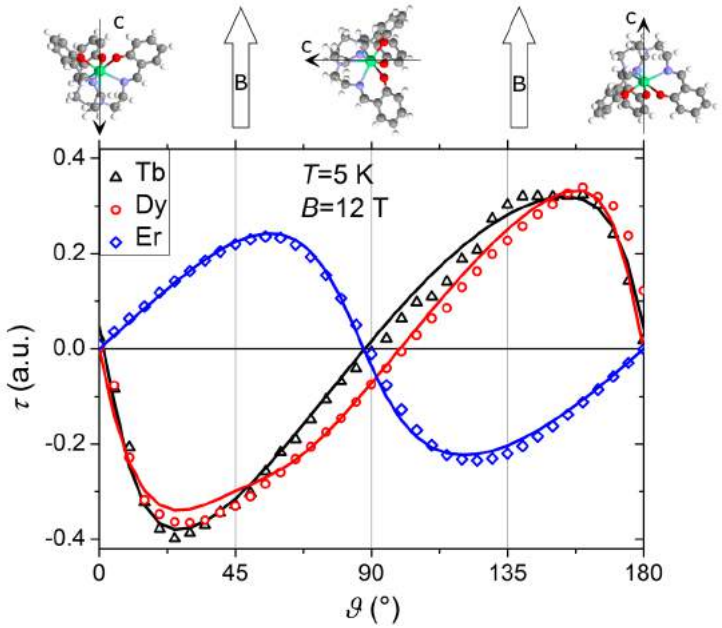

Figure 5.4: Torque signals for **Tb**, **Dy**, and **Er** obtained at 5 K and 12 T. The solid lines are the best-fit curves.

the field (see Figure 4.3). The upper part of Figure 5.4 relates the angle ϑ with the orientation of the molecule with respect to $\boldsymbol{B}$, it is thus evident that c is an easy direction for **Er** while it is an hard direction for **Tb** and **Dy**. Rot2 was performed to scan the effective in-plane anisotropy but none of the derivatives showed any signal (see Appendix): this means that for the sensitivity of these measurements the ab plane has to be considered isotropic. The strong axial character of all the derivatives of this family well justify the description of the system as formed by isooriented molecules, thus neglecting the small difference between the disposition of the donor atoms in the ab plane arising from the presence of two glide planes. Collecting the information coming from the two rotations, we can thus assert that the shape of anisotropy in **Er** is easy axis, while it is easy plane for **Tb** and **Dy**. This conclusion is coherent with the previous study [71], and it also add a precious information on **Tb** that was impossible to study only with EPR. Indeed, the powder X-band EPR spectrum of **Tb** at 5 K showed an

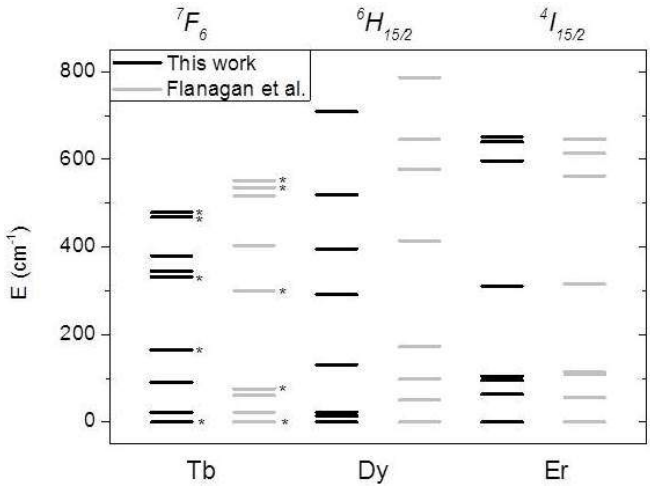

Figure 5.5: Energy patterns calculated using the CF parameters for the ground-state manifolds $J = 6$, 15/2,and 15/2 of **Tb**, **Dy**, and **Er**, respectively, obtained by CTM (black) and luminescence (grey). All of the levels are doublets, except for the ones indicated with black stars, which are singlets.

hyperfine split transition with isotropic line shape at about zero field, in both the perpendicular and parallel polarization modes (see Appendix).

The high anisotropy of this derivatives allowed also a study varying the temperature from 2 K up to 100 K, where the excited levels of the ground J multiplet can be also populated. For the C_3 symmetry, the correct Hamiltonian to describe the torque data must contain a Zeeman term and a CF term of the form (Wybourne's notation):

$$\begin{aligned}\mathcal{H} = {} & B_0^2\boldsymbol{C_0^2} + B_0^4\boldsymbol{C_0^4} + B_0^6\boldsymbol{C_0^6} + B_3^4(\boldsymbol{C_{-3}^4} - \boldsymbol{C_3^4}) + B_3^6(\boldsymbol{C_{-3}^6} - \boldsymbol{C_3^6}) \\ & + iB_3'^6(\boldsymbol{C_{-3}^6} + \boldsymbol{C_3^6}) + B_6^6(\boldsymbol{C_{-6}^6} - \boldsymbol{C_6^6}) + iB_6'^6(\boldsymbol{C_{-6}^6} + \boldsymbol{C_6^6})\end{aligned} \tag{5.3}$$

To avoid the inclusion of the term $B_3^{4'}$ without any loss of generality [62], all the parameters must be expressed in a precise molecular rf xyz, that can be connected to $ab'c$ by a trivial rotation (see Appendix for further details). Small misalignements of the crystals were taken into account using two polar angles ($\delta = \widehat{Zc}$ and $\alpha = \widehat{Ya}$). While α was fixed at the value obtained

by the indexing due to the isotropy of the ab plane, δ was found to be slightly different from zero only for **Tb** ($\delta = (0.3 \pm 0.1)^\circ$). The extracted values of the CF parameters are reported in table 5.2, together with the composition of m_J sublevels of the ground J multiplets for all derivatives. Note that some errors are huge: this is both due to the strong correlation between them and the low weight of some of them in the determination of the anisotropy.

Parameter (cm^{-1})	**Tb**	**Dy**	**Er**
B_2^0	-562 ± 152	-710 ± 38	-726 ± 115
B_4^0	40 ± 36	-274 ± 80	-81 ± 162
B_6^0	-1410 ± 2115	1309 ± 183	952 ± 88
B_4^3	1344 ± 520	-1406 ± 98	-2401 ± 233
B_6^3	712 ± 498	674 ± 69	366 ± 69
$B_6'^3$	420 ± 420	-760 ± 344	300 ± 900
B_6^6	1137 ± 877	935 ± 187	490 ± 157
$B_6'^6$	840 ± 840	0 ± 1	120 ± 360

Table 5.2: Best fit parameters obtained using Hamiltonian 5.3.

The evaluation of the CF parameters for this derivatives from a magnetometric technique may seem to be inappropriate since for this derivatives the same parameters were extracted from a spectroscopic method (luminescence, ref [62]), however the transitions that involve the ground multiplet were not observed for **Tb** and **Dy**. The extracted set of parameters is thus more accurate in the description of the low energy levels, that are the ones involved in the magnetic behaviour of the lanthanide-based compunds. Figure 5.5 compares the levels extracted from the two measurements. It is evident that for **Er** the agreement between the two techniques is almost perfect: this is due to the fact that for this derivatives all the transitions involving the low levels were experimentally observed [72].

To evaluate the accuracy of the extracted parameters, we also simulated the χT curves for all derivatives (see Appendix) and compared them with the ones present in literature [62, 68]. This is a mandatory but not sufficient test, in fact the magnetic susceptibility behaviour can be easily reproduced

by a number of different CF sets.

With these two studies we have accurately determined the nature of the anisotropy of 3 derivatives of a family of mononuclear neutral Ln-based compounds. Surprisingly **Dy** showed slow relaxation of the Magnetization even exhibiting easy plane anisotropy, thus invalidating the general assumption that the slow relaxation is associated to magnetic anisotropy of Ln complexes. We have also determined which contributions to the relaxation mechanism are the most relevant finding that Raman and QT plays a major role in these compounds. The CTM study was instead useful to determine a set of CF parameters that efficiently predicted the energy splitting of the ground multiplet, proving that CTM can flank spectroscopic techniques in the modelling of magnetic anisotropy of Ln-based compounds.

AUTHOR CONTRIBUTIONS JPC synthesized all the derivatives. EL (with assistance of MP) performed all the *AC* measurements and the treatment of data. LS and EL performed the EPR characterization. MP measured and treated the torque data and wrote the program (with assistance of RS) to fit the data. The first paper was written by EL (with assistance of MP) and revised by all the authors while the second one was written by MP (with assistance of EL) and revised by all the authors.

5.2 LnDOTA

Manuscript in preparation

Complete determination of magnetic anisotropy in the LnDOTA series: a combined theoretical and experimental approach.
M. Briganti, F. Totti, R. Sessoli and M. Perfetti.

The DOTA ligand (H_4DOTA=1,4,7,10-tetraazacyclododecane-N,N',N",N"'-tetraacetic acid) is a macrocyclic molecule that is able to form complexes with a huge amount of metal ions, with all possible external configurations [73]. The 4 Nitrogen of the cycle and 4 Carboxylate moieties can efficiently

bind also metals that usually exhibit high coordination numbers like lanthanides or actinides, however for the majority of these complexes the first coordination sphere is completed by a solvent molecule, in most cases water, that can be considered labile in solution. This peculiar property makes these complexes suitable for application in Magnetic Resonance Imagining, in particular GdDOTA is one of the most powerful positive contrast agents and DyDOTA has turned to be useful as negative contrast agent at high magnetic fields [74]. Moreover the four N atoms in the cycle can be easily attached to a variety of different organic molecules to change the type and number of donor atoms of this versatile class of ligands [75]. The eventual balance of the charge can be done by a number of different cations, ranging from alkali metals to hindered organic molecules, thus allowing a fine tuning of the distance between the coordinated metals. Focusing on the complexes with Ln, a lot of papers have been published. The dimension of the Ln was nicely investigated to detect fine structural variations, especially in solution [76], but in some cases it is possible to obtain the same coordination sphere as well as the same crystal packing for all the Ln ions. The possibility to encapsulate all possible Ln was also found suitable to study the luminescent properties of these complexes, that can be tuned using chemical design [77, 75, 78].

In this Chapter we will focus on derivatives of formula $Na[Ln(DOTA)(H_2O)]\cdot 4\,H_2O$ (see Figure 5.6, where we reported a simplified structure), hereafter called with the name of Ln in bold. The magnetic properties of these systems started to be studied in 2011 when we discovered an unusual field dependence of more than six order of magnitude of the relaxation time in **Dy** as a function of the applied magnetic field. The magnetic anisotropy of this system, studied with Single Crystal Magnetometry, was found out to be markedly easy axis with the unique axis pointing almost orthogonal to the direction that connects the oxygen of the water molecule and the Ln (hereafter called $Ln{-}O_{water}$) [46]. This is surprising because the Dy^{3+} ion has a prolate electron density that is expected to generate easy plane magnetic anisotropy in combination with an equatorial ligand like DOTA [21], and also because point charge symmetry of the coordination sites allows

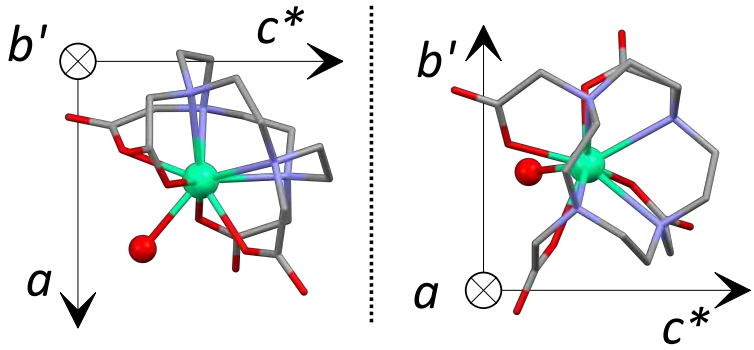

Figure 5.6: Two different orientation of the LnDOTA structure in the $a'bc^*$ rf. Color code: grey-Carbon, green-Lanthanide, blue-Nitrogen, red-Oxygen, Hydrogen and Sodium atoms were omitted for clarity. The left panel corresponds to the angle $\vartheta = 0°$ of Rot1 for all derivatives when the field is vertical.

the presence of an easy axis only along the C_4 axis. The inclusion of other atoms like hydrogen atoms of the water and Na^+ atoms in the *ab-initio* calculations was indeed able to justify the orientation of the unique axis. We thus decided to proceed in the study of all the derivatives belonging to the second half of the series (that stabilizes the maximum projection of $\boldsymbol{J}$). While experimental studies were limited to few derivatives (**Tb**, **Dy**, **Er**, **Yb**), theoretical calculations were performed for all the complexes of the second half of the series. All the studied compounds were observed and calculated to be easy axis, whatever the number of the f-electrons, but a gradual rotation of the easy axis from perpendicular to parallel to the $Ln{-}O_{water}$ direction was predicted. We thus decided to investigate these compounds using CTM to have a complete experimental determination of the orientation of the magnetic anisotropy, thus producing a milestone report on such a studied family.

The adopted synthetic procedure as well as the crystallization method, were described in our previous work [23]. All the compounds of the series are isostructural and crystallize in the triclinic $P\bar{1}$ space group, so all the molecules must be considered perfectly collinear in terms of anisotropy (structural data are reported in Table 5.3). All the paramagnetic ions of the

Ln	a	b	c	α	β	γ
Ce	8.697(16)	9.239(13)	15.77(3)	83.41(15)	85.63(15)	81.39(16)
Pr	8.719(4)	9.179(5)	15.860(4)	82.71(3)	84.98(3)	80.86(4)
Nd	8.65(2)	9.23(2)	15.55(4)	82.99(19)	84.6(2)	80.4(2)
Eu	8.705(10)	9.123(7)	15.787(9)	82.57(8)	85.36(10)	81.36(8)
Gd	8.719(3)	9.110(6)	15.707(10)	82.79(5)	85.47(4)	81.43(4)
Tb	8.77(2)	9.12(2)	15.69(2)	83.02(16)	85.34(16)	81.4(2)
Dy	8.724(10)	9.046(16)	15.599(13)	83.04(11)	85.73(9)	81.66(12)
Ho	8.87(6)	9.12(3)	15.72(3)	83.2(2)	86.3(3)	81.9(4)
Er	8.697(13)	9.011(13)	15.568(17)	83.20(10)	86.30(11)	82.10(12)
Tm	8.806(10)	8.898(13)	15.74(2)	82.70(11)	85.31(10)	81.22(11)
Yb	8.738(16)	9.16(3)	15.599(18)	83.65(15)	85.88(12)	81.84(19)

Table 5.3: Cell parameters for all the investigated LnDOTA derivatives.

series were characterized with only two exceptions: radioactive Prometium and Samarium, for which it was not possible to isolate single crystals.

The CTM characterization was performed starting from the rotation along b' (Rot1, see Figure 5.6, left): in this way the plane of rotation almost contains the Ln$-$O$_{\text{water}}$ bond (the angle between this plane and the bond is about 6°). It is therefore easy to appreciate if that direction is a principal direction of anisotropy simply looking at the angles at which τ vanishes. In Figure 5.7 we plotted the normalized τ recorded during Rot1 for all the measured derivatives. Even if the determination of the direction of the projection of the easy axis on the plane of rotation can be visually determined simply observing the different slope of the curves near the zeroes, also the sign of τ can be used, in fact a positive torque at $\vartheta = 0°$ means that the easy axis is closer to the Ln$-$O$_{\text{water}}$ bond than to the plane orthogonal to it. Indeed, the curves can be well-divided into two categories, as a function of their sign. It is worth noticing that the angular range at which the curves vanish is very narrow along the series (ϑ =37° to 57° and ϑ =127° to 147°) pointing out that along the series a dramatic change in the orientation of the easiest axis is observed. To have a more precise idea of the position of easy and hard directions, we

fitted the curves using the usual f_{sc}, an axial parameter b_2^0 (with negative sign, arbitrarily assigned) and only one Euler angle (ξ). The other Euler angle was fixed to 90° because the rotation axis was b': in this way the second Euler angle is exactly the angle between the easy axis and the c^* axis. For all derivatives we just considered the ground state, except Eu^{3+} ($J = 0$), for which we consider the first excited state $J = 1$ as ground state (the ground state, as long as it remains unmixed, should not contribute to the anisotropy of the system). In Table 5.4 we reported the obtained best fit parameters. Note that the value of b_2^0 has no real physical meaning because an accurate description of the anisotropy of this complexes needs all the 27 CF parameters [23]; for this reason we did not evaluate the error on these parameters.

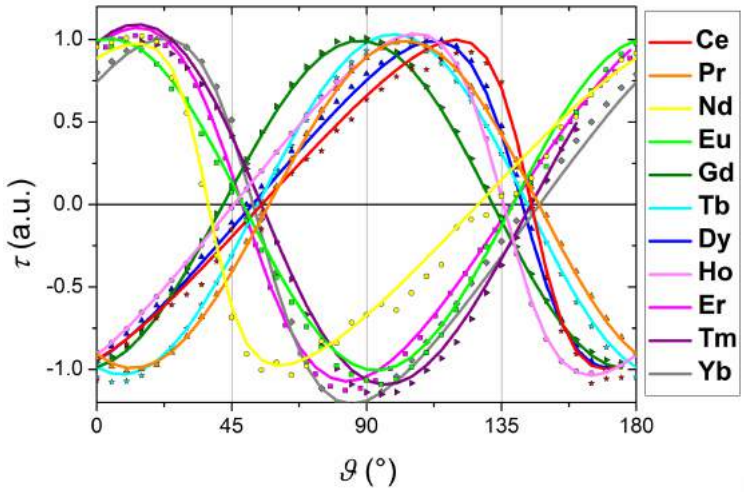

Figure 5.7: Normalized experimental (points) and fitted (lines) data recorded during Rot1 for all the studied LnDOTA derivatives. Magnetic field and best fitted parameters are reported in Table 5.4.

Since we know that the angle between the c^* axis and the projection of the $Ln-O_{water}$ bond is 130°, we can also calculate the angle (η) between that projection and the easy molecular axis as reported in Figure 5.8, that is comparable with the one reported in ref. [23], and also listened in Table

5.4 (together with the experimental and the calculated values). Rigurously, the angle η is really comparable only if it is near 90° (because only that angle is the same for all the possible projections of the easy axis in the plane of rotation). Nevertheless none of the derivatives with low values of η have been found to have easy axis far from the plane of rotation (see ref. [23] for **Er** and **Yb**, and after for **Tm**, **Nd** and **Eu**). Since the error on our estimation is both affected by the visual crystal alignment and by the small angle between the scanned plane and the Ln−O_{water} bond, we estimated that it does not exceed 10°.

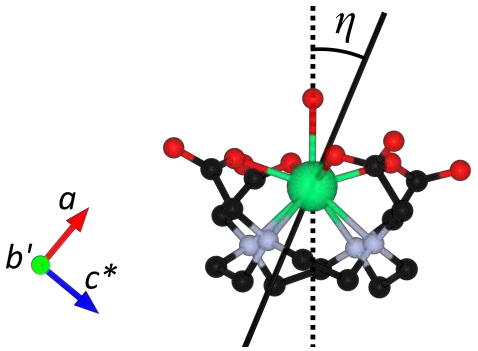

Figure 5.8: Graphical visualization of the angle η between the Ln−O_{water} direction (dotted line) and the easy axis (black) in the ac^* plane.

All values of η, experimentally determined in ref. [23] are comparable, within the experimental error, with those extracted by CTM, except **Er** and **Ho**, for which the theoretical values of ref. [23] differs significantly. This discrepancy was already attributed to the large influence of the dynamic electronic correlation correction (CASPT2) [79] for **Er**, while **Ho** was never experimentally determined, but it is worth noticing that the electron density of this ion is only slightly prolate (the change in shape for the second half of the series occurs indeed between Ho and Er, see Figure 2.4).

The first rotation, performed on all the derivatives, can give an idea of the deviation between the easy axis and the bond with the apical water, however for all the derivatives that were not previously experimentally determined, we also performed a second rotation orthogonal to Rot1. In

Ln	ξ	b_2^0	B(T)	T(K)	η	η,Boulon et al.
Ce	35	-0.4	12	2	85	no data
Pr	32	-0.003	9	2	82	no data
Nd	142	-0.2	12	2	12	no data
Eu	131	-0.06	9	2	1	no data
Gd	48	-0.006	3	2	82	no data
Tb	36	-0.06	3	2	84	85/86
Dy	38	-0.04	2	2	88	84/78
Ho	44	-0.03	2	2.3	86	-/58
Er	132	-0.04	5	5	2	6/48
Tm	125	-0.01	1.5	2	5	-/9
Yb	126	-0.1	3	2.3	4	12/7

Table 5.4: Best fit parameters and experimental conditions of Figure 5.7.

this case we fitted the two rotations simultaneously using a f_{sc}, b_2^0, b_2^2 and three relevant Euler angles (ρ, ξ and ψ). The results are summarized in Table 5.5 and reported graphically in Figure 5.9. For **Nd** the signal during Rot2 was too low to be detected and that the rotation axis of Rot2 was approximately the Ln$-$O$_{\mathrm{water}}$ bond, so we took the position of the axis found fitting only Rot1.

While also in this case the value of the CF parameters are not relevant due to the low symmetry of the complex, a major indication of the type of anisotropy arises from the sign of b_2^0, in fact only in the case of **Ce**, **Pr** and **Gd** the best fit axial parameter was positive. This means that, neglecting the b_2^2 parameter, the anisotropy of these derivatives can be rationalized as easy plane.

In Figure 5.9 we reported a graphical view of the minimum energy direction of the magnetization (we reported it as a vector to facilitate the reader) on the molecular structure for all the investigated derivatives. A sudden change of orientation from perpendicular to parallel (and *viceversa*) is always observed when a change in the shape of the electron density is observed (see also Figure 2.4). The low symmetry of the complex inevitably bring the simple treatment of Rinehart and Long [21] to fail

in the prediction of the anisotropy shape for some derivatives, indeed according to this model all the oblate ions should have an easy axis parallel to the Ln−O_{water} direction while all the prolate ions should have an easy plane perpendicular to it.

Now we will examine all the orientations starting from the electronic density of the Ln. Complexes formed by oblate ions (**Er**, **Tm** and **Yb**) have an easy axis pointing approximately along the Ln−O_{water} direction, as expected also from electrostatic considerations. This model also predict almost correctly the anisotropy of molecules containing the strongly prolate ions **Ce** and **Pr** while in all the other cases the prediction of the model is not verified. **Tb** and **Dy** have a marked easy axis anisotropy, with the easy axis pointing almost perpendicular to the Ln−O_{water} direction. It is interesting to notice that ions with intermediate electron density (**Nd** and **Ho**) have the easy direction tilted by $\sim 75°$ between each other, and behave as a prolate (**Ho**) and oblate (**Nd**) ion, respectively. Two exceptions are of course constituted by **Eu** ($J = 0$) and **Gd** (isotropic at the first order), that however showed a detectable anisotropy, with the easy axis pointing parallel (**Eu**) or perpendicular (**Gd**) to the Ln−O_{water} bond. Finally, we can also try to predict the anisotropy orientation for the two derivatives that were not studied, **Sm** and **Pm**, that should exhibit an easy axis parallel to the Ln−O_{water} direction.

Concluding, we have successfully obtained the orientation of the easiest anisotropy axis for all the LnDOTA complexes (except **Pm** and **Sm**). These data are a useful library for theoreticians that wants to validate methods

Ln	ρ	ξ	ψ	b_2^0	b_2^2
Ce	77	125	0	0.3	0.3
Pr	66	114	107	0.085	0.067
Eu	83	130	0	-0.13	0
Gd	144	133	0	0.013	0.008
Ho	75	46	0	-0.03	0
Tm	87	125	0	-0.01	0

Table 5.5: Best fit parameters of Figure 5.9.

to predict the orientation of anisotropy on low-symmetry compounds based on Ln ions.

AUTHOR CONTRIBUTIONS MP synthesised all the complexes and performed measurements and simulation of torque data. RS supervised all work.

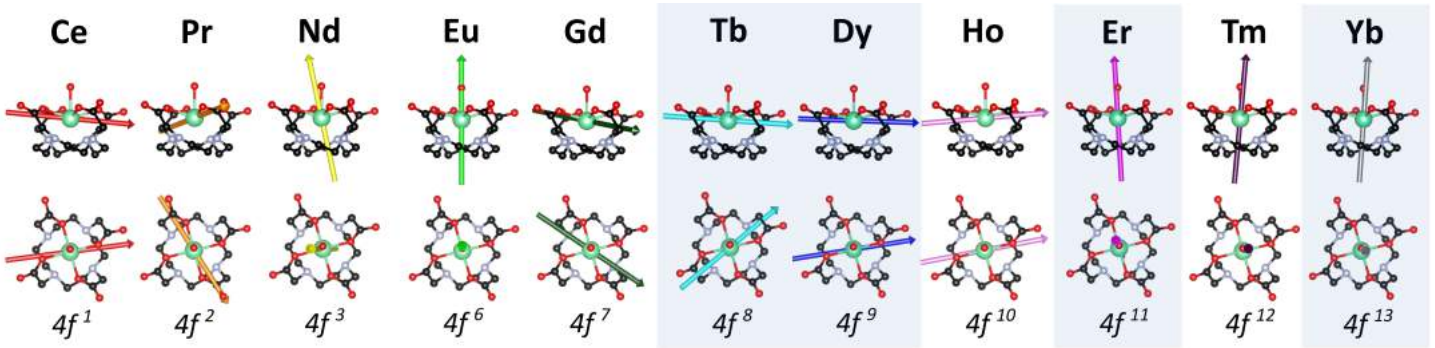

Figure 5.9: Orientation of the easiest direction of the magnetization for all the investigated LnDOTA derivatives. For **Tb**, **Dy**, **Er** and **Yb** we used the data from ref. [23], while all the others were experimentally determined *via* CTM (see text).

6 Intermolecular noncollinear systems

The presence of symmetry operations that generate other molecules inside the unit cell complicates markedly the treatment of the data. The major experimental problem is that, once achieved the direction cosines for the principal axes, one has to attribute these cosines to a certain molecular entity, inside the cell. An high symmetry of the molecule can help to solve this problem (*e.g.* Cp*ErCOT and Ni(TMC)N_3) but in some cases the ambiguity can only be solved flanking theoretical calculations to the experimental evidences (*e.g.* Dy$(LH)_3$ and Co(TMC)N_3). The results are presented in an increasing-complexity way, that is, increasing the number of noncollinear molecules in the unit cell. Indeed the this number is two for Cp*ErCOT (Section 6.1), $DyLH_3$ (Section 6.2 and Ni(TMC)N_3 (Section 6.3), but it increases to four in the case of Co(TMC)N_3 (Section 6.3).

6.1 Cp*ErCOT

Paper in Appendix

*Angular-Resolved Magnetometry Beyond Triclinic Crystals Part II: Torque Magnetometry of Cp*ErCOT Single-Molecule Magnets.*
M. Perfetti, G. Cucinotta, M.E. Boulon, F. El Hallak, S. Gao and R. Sessoli.
Chemistry, a European Journal, **2014**, 20(43), 14051-14056.

It is known from decades that the chemistry of Ln includes the possibility coordinate them with carbon atoms belonging to organic electron-reach

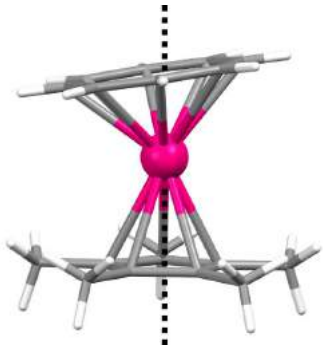

Figure 6.1: Cp*ErCOT structure. Color code: grey-Carbon, pink-Erbium, blank-Hydrogen. The dotted line represents the pseudo C_∞ rotation axis.

donors [80]. This was recently found to be interesting in the field of molecular magnetism because several organometallic complexes based on f elements exhibit SMM behaviour. The choice to use cyclic organic ligands is principally related to their capability of generating high order uniaxial local symmetry, due to the delocalized π electrons. Up to now in literature are present several examples of organometallic SIM based on both actinides [81, 82] and on lanthanides [83, 84], and they all exhibit high barrier for the relaxation of the magnetization. The derivative that will be described in this section is reported in Figure 6.1 and it is based on an Er^{3+} ion, coordinated to the pentamethylcyclopentadiene anion (Cp*) and to the cyclooctatetraene dianion (COT); it crystallizes in the orthorombic *Pnma* space group with two almost orthogonal families of molecules. This compound has attracted much interest because of its high barrier for the reversing of the magnetization ($\simeq 272\,\mathrm{K}$) and it was nicely studied in an out-of-equilibrium regime (under hysteresis) with Single Crystal Magnetometry (SCM) to obtain the anisotropy orientation of the single centres [85]. This is thus, at the best of our knowledge, the unique example of noncollinear anisotropic structure that could be solved with SCM. For this reasons this system can be considered a textbook example to exploit at best the sensitivity of CTM.

First of all, it is interesting to show here the information on magnetic

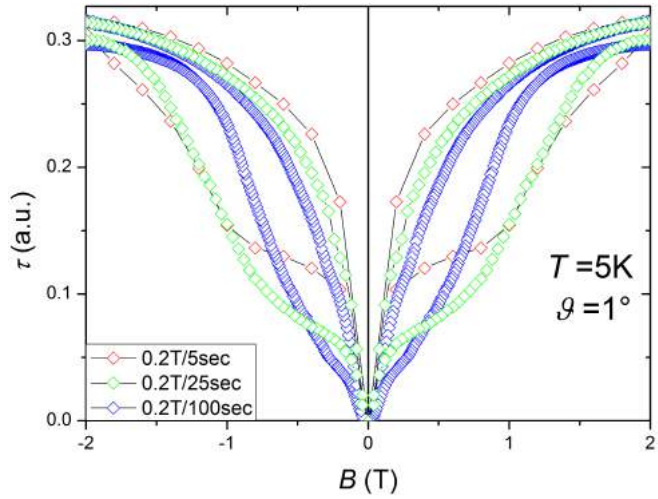

Figure 6.2: Hysteresis loops recorded at $T = 5\,\mathrm{K}$ and $\vartheta = 1°$. The legend refers to the velocity at which the magnetic field is varied.

bistability that can be provided by CTM [86]. With this aim we recorded hysteresis loops at a fixed temperature and angular position, varying the sweeping rate of the applied magnetic field, as reported in Figure 6.2. Irreversibility is clearly observed at 5 K and the dynamic origin of the hysteresis is well evidenced by the differences upon changing the sweeping rate. A relevant feature to be stressed is that, according to Equation 4.5, the magnetic torque always vanishes at zero applied field. Torque magnetometry is, therefore, unable to detect remnant magnetization. However, it is important to notice that, referring to a standard hysteresis loop, the magnetization curve goes through the II and IV quadrants if the remnant magnetization is not zero. In these regions the magnetization and the external field have different polarity and torque is expected to change sign in comparison with the I and III quadrants. In Figure 6.2 the torque has the same sign over the entire loop, thus indicating that this system presents no remnant magnetization, and is actually characterized by a butterfly hysteresis cycle as observed by standard magnetometry [85].

In Figure 6.3 we reported the simulation of two orthogonal Ising contributions ($S = 1/2$ and $g_{\mathrm{eff}} = 18$): for low fields Equation 4.8 holds, and the

resultant signal is identically zero for any angle (panel a), while for high fields the contributions *do not* cancel out (panel b). As already pointed out in Section 4.4, this peculiarity makes CTM a suitable technique to study more than one noncollinear contribution.

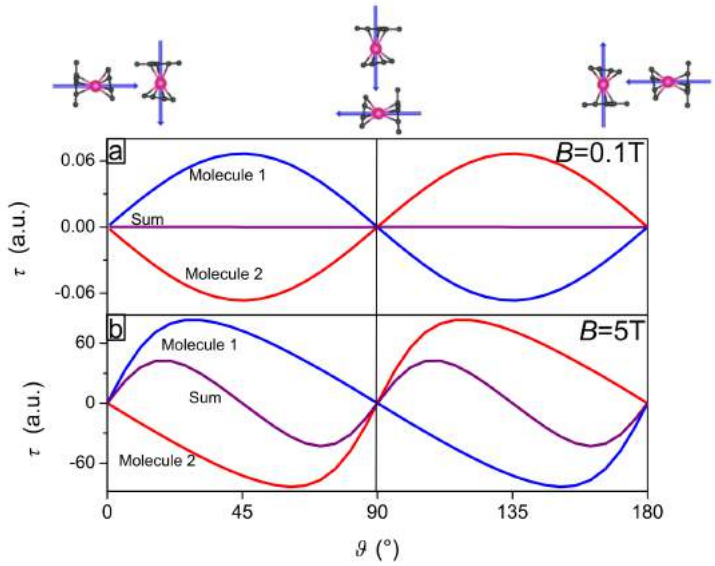

Figure 6.3: Calculated magnetic torque resulting from two orthogonal Ising spins at $T = 10\,\mathrm{K}$ and at two different magnetic fields: a) 0.1 T and b) 5 T). The individual contributions are shown as blue and red, and the resultant signal is drawn in purple. The position of the axes is reported is reported on top of the graph, considering the field always vertical.

A single indexed crystal was mounted with its (101) face stuck to the cantilever. In this way, it was possible to adjust the b crystallographic axis as the rotation axis and thus the scanned crystallographic plane was ac (see Figure 6.4). This rotation was chosen for several reasons: first of all the ideal symmetry of the complex force the anisotropy to be, at a first approximation, uniaxial with the easy (or hard) direction parallel to the C_∞ axis, that is, in the ac plane. Moreover this rotation corresponds to Rot2 of the SCM in ref. [85], so the recorded data can be more easily compared to the ones previously reported.

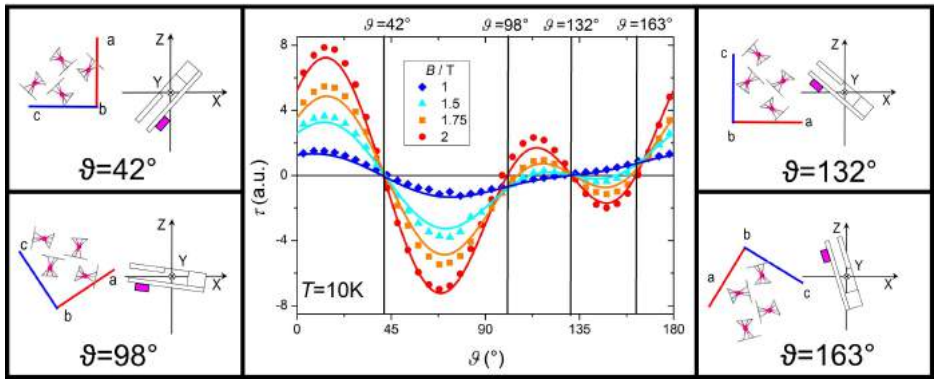

Figure 6.4: Rotation performed at $T = 10\,\mathrm{K}$ and various fields (dots are experimental points, lines are fits). In the left and right panels is evidenced the position of the molecules with respect to the vertical magnetic field. While 42° and 132° correspond to symmetry-imposed zero torque, 98° and 163° correspond to "accidental" zeroes.

The experimental data in Figure 6.4, show oscillations with different amplitude in contrast to the regular features of Figure 6.3. This is a clear indication that the two families of molecules are not oriented with their easy axis exactly at 90°. The experimental data are in fact well reproduced (solid lines), with an Ising model assuming the same angle (95°) between the two Ising directions as in ref. [85] and the effective g-factor (g_{eff}) free to adjust (more fits can be found in Appendix). A scale factor has been introduced, given the incertitude on the mass of the sample and on the elastic constant of the cantilever; the latter has been assumed to be temperature independent because the Young modulus of CuBe varies only 6% over the entire investigated range of temperatures (from 2 K up to 150 K) [87]. The best fit of g_{eff} value at 10 K, $g_{\mathrm{eff}} = 19.4(2)$ is in reasonable agreement with the value expected for Er^{3+} ions in the easy-axis limit ($g_{\mathrm{eff}} = 18$).

For this derivative, another independent fit was performed, as reported in Figure 6.5 (more fittings in Appendix), using a restricted set of axial CF operators ($\boldsymbol{O}_2^0$ and $\boldsymbol{O}_4^0$) to avoid overparametrization problems. In

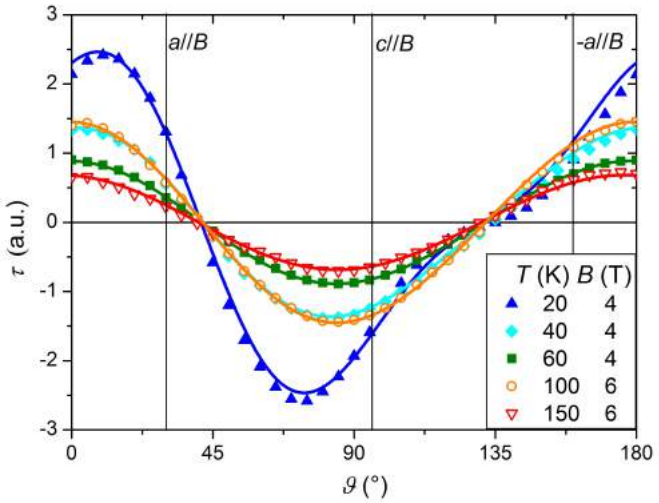

Figure 6.5: Angular dependence of the magnetic torque at variable temperature and applied fields. The lines correspond to the simulations performed by using an axial CF Hamiltonian. See text for best fit parameters.

principle one should also include many transverse terms of the CF because even small deviations from a perfect axial symmetry can produce non-negligible contributions. However, the small tilt angle between the organic rings that act as ligands suggests that transverse terms can be neglected at first approximation. The choice to avoid transverse terms was well-justified by the *ab initio* calculations of ref. [85] that showed a strong axial character for the complex. Moreover, the inclusion of the operator $\boldsymbol{O}_6^0$ did not give any significant improvement on the quality of the fit, so it was neglected. The best fit values, reported in the Stevens formalism: $b_2^0 = (-1.3 \pm 0.1)\,\mathrm{cm}^{-1}$ and $b_2^0 = (-0.003 \pm 0.001)\,\mathrm{cm}^{-1}$. The sign and magnitude of the parameters unequivocally determine the easy axis nature and the strength of the anisotropy of the molecule. To prove the high sensitivity of the torque to the angle, we also fitted the tilt angle between the axis of the two molecules, finding the same value of ref [85], that is $(95 \pm 1)^\circ$.

Combining the information coming from the two fits, we can plot the

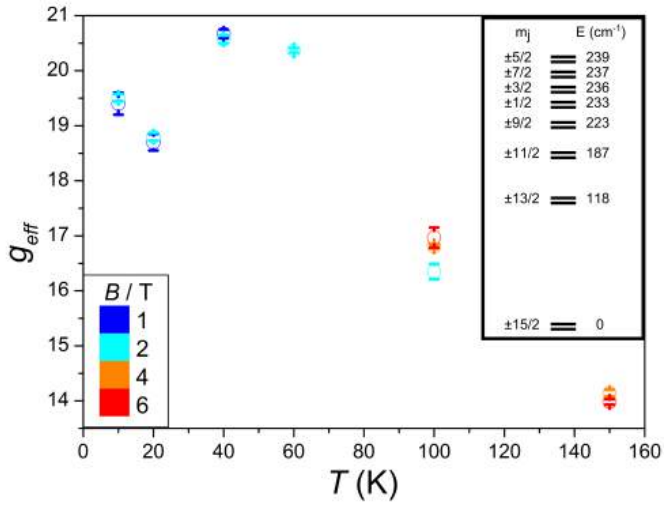

Figure 6.6: Values obtained for the g_{eff} factor at different temperatures and fields. Inset shows the doublets pattern of the $J = 15/2$ ground multiplet calculated with the best fit CF parameters reported in the text.

g_{eff} value as a function of temperature and qualitatively compare its trend with the level structure extracted from the best fit CF parameters, as reported in Figure 6.6. As expected, we can observe a *strong axiality zone* below 60 K with high values of g_{eff}, that progressively decrease when the excited levels begin to be populated. The energy of the first excited doublet ($118\,\text{cm}^{-1}$) is in excellent agreement with the one extracted from *ab initio* calculations [85].

Finally, as a comparison between CTM and SCM, we report in Figure 6.7 the polar plot of the magnetization and of the torque. The anisotropic part of the magnetization signal coming from SCM measurements has to be extracted from a huge isotropic contribution so one has to isolate the deviation of the polar plot from a perfect circle. On the contrary CTM is uniquely sensitive to the anisotropy, so all the torque signal refers to the anisotropy of the system.

In conclusion we have determined, without ambiguity, the anisotropy orientation of the Cp*ErCOT SMM, where two almost orthogonal entities

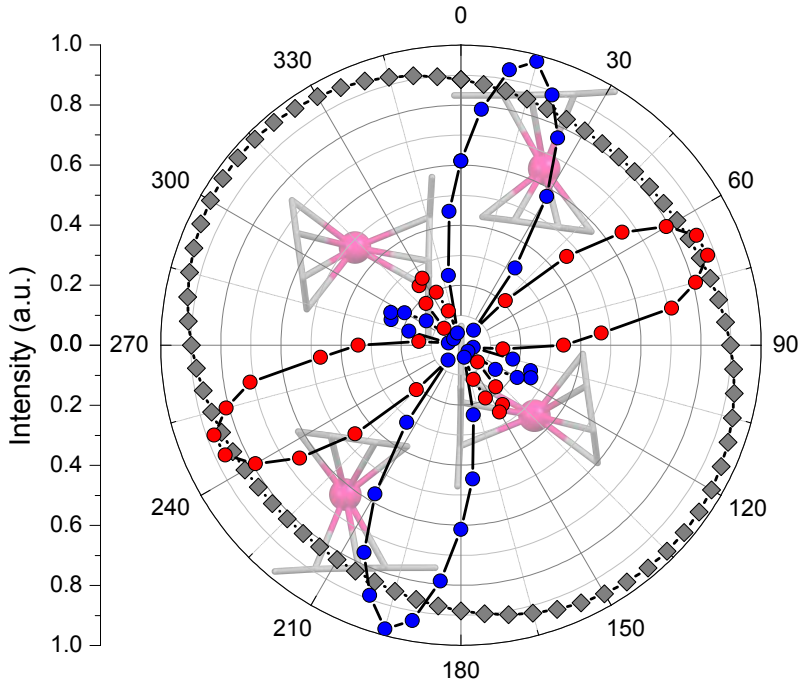

Figure 6.7: Polar plot (angle vs intensity) of SCM from ref. [85] (grey squares, $T = 5\,\mathrm{K}$ and $H = 0.1\,\mathrm{T}$) and of CTM (dots, positive values are blue while negative values are red, $T = 10\,\mathrm{K}$ and $H = 2\,\mathrm{T}$) for Cp*ErCOT.

are present, thus proving that CTM can be successfully used to map the anisotropy of crystals containing noncollinear anisotropy tensors. Our estimation of the energy difference between the ground and the first excited Stark level, obtained by two different fitting procedures, resulted to be in good agreement with *ab initio* calculations.

AUTHOR CONTRIBUTIONS SG synthesise the complex that MEB and GC analysed and indexed. The torque measurements were performed by MP (with assistance of RS) and the treatment of the data by MP (CF parameters, energies, orientation) and GC (g-components). The paper was written by MP and RS and revised by all the authors.

6.2 Dy(LH)$_3$

Paper Submitted

Magnetic anisotropy and relaxation dynamics in a low symmetry Dy(III) complex.
E. Lucaccini, M. Briganti, M. Perfetti, L. Vendier, J.P. Costes, F. Totti, R. Sessoli and L. Sorace.

The investigation and understanding of complexes exhibiting low symmetry environment around a Ln is a hot topic in molecular magnetism, not only to support and validate theoretical investigations, but also to establish a more direct channel between pure science and applications. It is quite clear that to correctly describe the relaxation processes in these systems a detailed picture of the electronic structure of the Ln and its relation to the molecular structure is needed. The strategy that is increasingly employed for this purpose is to use a combined approach of experimental characterization and theoretical studies to interpret the result of the magnetization dynamics analysis. In this approach single crystal measurements have a major role, even if they are still not widespread despite they can cast light on the magnetic anisotropy by providing access to the preferred orientations of magnetization and, on the degree of axiality of the low lying levels of the J multiplet. In this Chapter we will deal with a mononuclear system containing Dy^{3+}, that do not sit on any symmetry element inside the crystal, that is therefore a good candidate to compare the experimental and theoretical results.

In Figure 6.8 we reported the molecular structure of the Dy(LH)$_3$ compound (hereafter **Dy**), where LH_2 is the 2-Hydroxy-N'-[(E)-(2-hydroxy-3-methoxyphenyl)methylidene] benzhydrazide ligand. Three molecules of this potentially pentadentate ligand in its monoanionic state can coordinate Ln, to form neutral complexes. The Ln exhibit thus a coordination number 9 with 6 Nitrogen and 3 Oxygen as donor atoms. Sometimes, as in the case of **Dy**, also some solvent molecules (dimethylformamide, dmf) can crystallize in the unit cell.

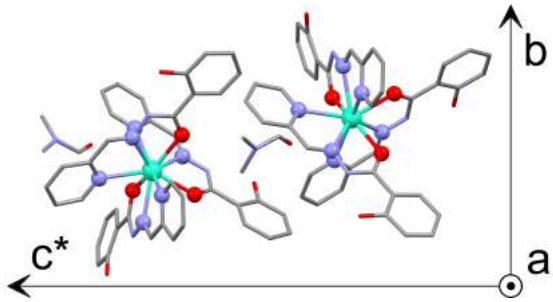

Figure 6.8: $Dy(LH)_3$ structure, with the two noncollinear molecules inside the unit cell. Color code: grey-Carbon, red-Oxygen, blue-Nitrogen, green-Dysprosium, Hydrogen atoms were omitted for clarity. The *ac* plane is a glide plane while *b* is a C_2 axis.

At the best of our knowledge this compound was never reported in literature, so we proceeded with an accurate structure determination, and then with a classical magnetic characterization. The compound showed a χT vs T curve that saturates at high temperature at a value ($\chi T = 13.97\,\mathrm{emuKmol^{-1}}$) close to the one expected for a free Dy^{3+} ion ($^6H_{15/2}$, $g_L = 4/3$, $\chi T = 14.17\,\mathrm{emuKmol^{-1}}$), as reported in Figure 6.9. If the temperature is lowered we observe only a smooth decrease of the χT product, in agreement with the calculated energy level diagram (*vide infra*). We also synthesized the analogue compound doped with Yttrium (diluition $\sim 10\%$ Dy, hereafter **YDy**) to magnetically isolate the Dy^{3+} centres and avoid any interaction. As already mentioned in Section 5.2, Y is a suitable metal to magnetically dilute Ln because it generally forms isostructural compounds with diamagnetic behaviour (Y^{3+}: $S = 0$, $L = 0$). The χT curve of this compound shows similar trend with respect to the pure complex, but it saturates at a slightly lower value ($\chi T = 13.71\,\mathrm{emuKmol^{-1}}$, Figure 6.9). The small observable offset is probably due to the presence of a small amount of diamagnetic impurities (not detectable from the X-rays Diffraction pattern). The little jump in the magnetization curve near 45 K has to be attributed to saturation effects due to the change of the field (normally χT vs T curves are recorded using $H = 0.1$ T from 2 K to 45 K and $H = 1$ T from 40 K to 300 K), however it is also present in the

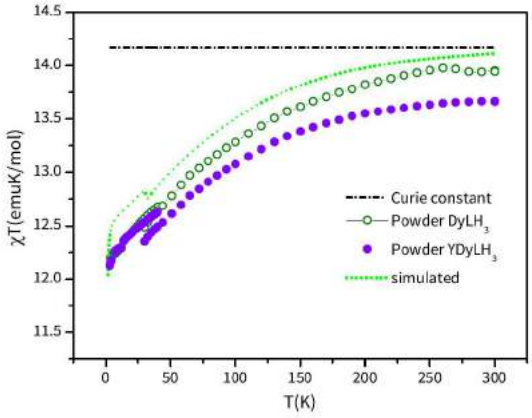

Figure 6.9: Temperature dependence of the χT product for **Dy** (empty circles) and **YDy** (full circles) along with theoretical curves (dotted line) calculated by using CF parameters derived from *ab-initio* calculations. The dashed line corresponds to the expected free-ion χT value.

simulation (obtained with home-made software EVALUCF [71]) performed using the 27 CF parameters derived from *ab initio* calculations (*vide infra*). Moreover the M vs H curves, recorded with a SQUID magnetometer at $T = 5\,\mathrm{K}$ and $T = 10\,\mathrm{K}$, could be correctly simulated using the computed CF parameters.

To study magnetic anisotropy of this system, we proceeded with a multi technique approach. EPR investigation with an X-band ($\nu \sim 9.4\,\mathrm{GHz}$) spectrometer revealed that the complex was silent. This could be attribute either to fast relaxation or to a low intradoublet transition probability due to the composition of the ground state, and the excited ones being too high in energy to be observed. The latter explanation is in agreement with a strong axiality of the ground Kramers doublet. To investigate more in detail the direction of the anisotropy of this system, we indexed a crystal of **DyY** to avoid interactions and we performed two orthogonal rotations using CTM. The compound crystallizes in the $P2_1/n$ monoclinic space group, ans, besides the inversion, possess two symmetry operations: the crystallographic b axis is a C_2 axis and the ac plane is a glide plane, for

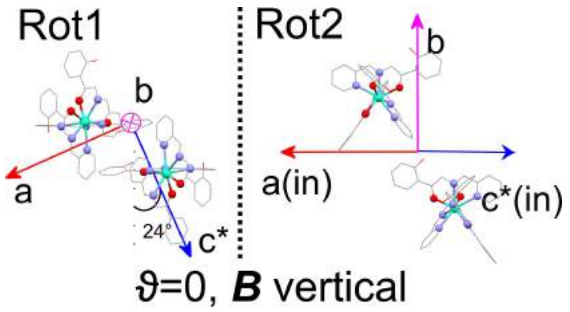

Figure 6.10: Position of the crystals at $\vartheta = 0$. Since ac is a mirror plane, Rot1 gave only one contribution, while Rot2 gave two different contributions. Same color code of Figure 6.8.

this reason only two noncollinear contributions are present in the crystal structure. The chosen orthogonal crystallographic reference frame was abc^*. As reported in Figure 6.10, the first rotation (Rot1) had b as rotation axis, while in the second rotation (Rot2) the rotation axis was in the ac plane. The first rotation turned out to be extremely useful because in virtue of the symmetry operation of the crystal, Rot1 gave only one contribution to the torque (we recall that the contribution to the torque arises only from the projection of the magnetization vectors in the plane orthogonal to the rotation axis). The fit was performed with a Spin Hamiltonian of the form:

$$\mathcal{H}_S = \mu_B \boldsymbol{S}_{\text{eff}} \cdot \boldsymbol{g} \cdot \boldsymbol{B} \tag{6.1}$$

where $\boldsymbol{g}$ is the g-tensor, μ_B is the Bohr magneton and $\boldsymbol{S}_{\text{eff}}$ is an effective spin operator (see also Section 2.2.2). To reproduce the torque shape, other three parameters were taken into account: the usual scale factor (f_{sc}) and two Euler angles (ρ and ξ, the x-convention was used) that connects the abc^* crystallographic rf to the xyz molecular rf. It is important to notice that the third Euler angle was neglected because we assumed uniaxial anisotropy. For both rotations small offsets (less than 5°) where taken into account to correctly fit the zero-torque angles. In Figure 6.11 we reported the curves detected at $T = 5\,\text{K}$ and $B = 7\,\text{T}$. The fitting procedure for the parameters gave: $g_x = g_y = 0.010 \pm 0.005$, $g_z = 16 \pm 1$, $\rho =$

$(212 \pm 1)^\circ$, $\xi = (71 \pm 1)^\circ$ and $f_{sc} = (2.6 \pm 0.3) \times 10^{-2}$. The components of $\boldsymbol{g}$ clearly indicates that the complex is strongly axial ($g_{\max} = 20$ for Dy^{3+}) as suggested by the absence of EPR signal. From the Euler angles we can extract the angles of the z axis in abc^*: $\alpha_1 = 120^\circ$, $\alpha_2 = 37^\circ$, $\alpha_3 = 71^\circ$. However since there are two noncollinear molecules in the unit cell, and the complex has zero symmetry, it is in principle possible to identify two possible orientation of the easy axis of the molecule with respect to the atomic coordinates. This experimental result was then flanked by a detailed

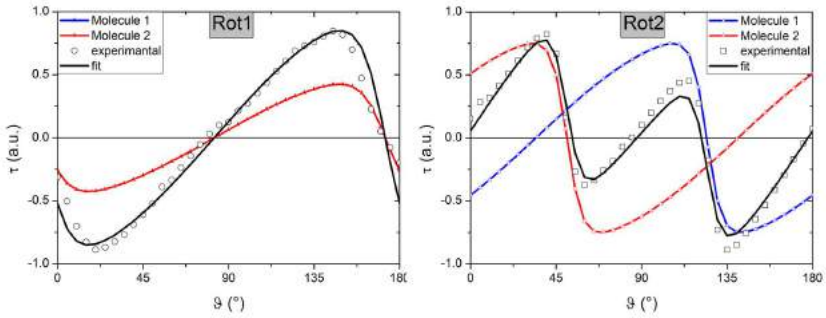

Figure 6.11: Torque curves recorded at $T = 5\,\mathrm{K}$ and $B = 7\,\mathrm{T}$ for Rot1 (empty circles, left) and Rot2 (empty squares, right). Black lines are the fit, obtained as sum of the different contributions coming from the two noncollinear molecules (red and blue triangles).

theoretical analysis to deeply understand the electronic structure of **Dy**. In good agreement with the experimental evidences, the ground Kramers doublet was identified as an almost a pure $m_J = \pm 15/2$ with $g_z = 19.8$, with the first and the second excited doublets at $195\,\mathrm{cm}^{-1}$ and $237\,\mathrm{cm}^{-1}$, respectively. In Table 6.1, we reported the complete energy splitting of the ground ${}^6H_{15/2}$ multiplet of Dy obtained by *ab initio* methods.

Nevertheless the most relevant test about the correct reproduction of the anisotropy of this system was the direct comparison of the anisotropy axis orientation, graphically reported in Figure 6.12: the calculation found $\alpha_1 = 122^\circ$, $\alpha_2 = 38^\circ$, $\alpha_3 = 72^\circ$ as angles of z in abc^*, in perfect agreement with the experimental results (angle between the theoretical and the

	Energy Levels	(cm^{-1})	g_x	g_y	g_z
$^6H_{\frac{15}{2}}$	E_0	0	0.0	0.0	19.8
	E_1	195	0.5	1.8	14.9
	E_2	237	0.1	2.2	14.3
	E_3	289	1.5	3.7	12.1
	E_4	324	0.6	2.8	13.8
	E_5	371	2.6	4.5	8.8
	E_6	430	3.4	4.1	7.4
	E_7	478	1.1	4.7	15.9

Table 6.1: Results of the calculations with RCC basis sets for $Dy(LH)_3$: energy splitting of the ground $^6H_{\frac{15}{2}}$ and main values of the main magnetic axes for each Kramers' doublet

experimental orientation $\sim 5°$).

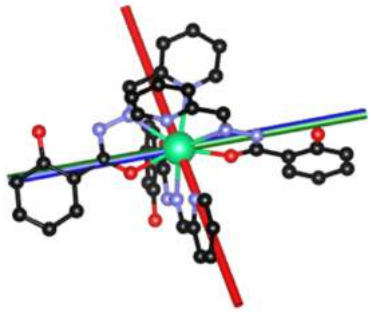

Figure 6.12: Theoretical direction of magnetic anisotropy for the ground state (blue) compared with with the two possible experimental direction (red and green). The angle between blue and green axes is only 5°.

With a detailed description of the level structure of this compound, we proceeded in the study of the AC susceptibility as a function of temperature ($T = 2 - 20\,\mathrm{K}$), frequency ($\nu = 0.02 - 10\,000\,\mathrm{Hz}$) and applied field ($B = 0 - 0.1\,\mathrm{T}$). The pure compound showed two different relaxation channels in zero and non-zero magnetic field, and the application of a crescent field suppress progressively one of the two channels, as reported in Figure 6.13. This behaviour is not unusual in SMM, and it was already observed in

another derivative analyzed in this Thesis [88]. The field scan revealed an *optimum* field of 0.1 T, so we proceeded with a study in temperature and we extract the relaxation time for both **Dy** and **YDy** at $B = 0\,\mathrm{T}$ and $B = 0.1\,\mathrm{T}$. Here we only report the evolution of the relaxation time for the diluted compound (Figure 6.14). We performed a fit of the relaxation time of **YDy** including two contributions, a Raman and an Orbach process:

$$\mathcal{T}_1^{-1} = CT^n + \mathcal{T}_0^{-1} e^{(-\Delta/T)} \tag{6.2}$$

where C and $\mathcal{T}_0^{-1}$ are empirical factors and Δ is the energy barrier for the reversal of the magnetization. A first attempt was made fixing the energy barrier at $270\,\mathrm{K} \sim 195\,\mathrm{cm}^{-1}$, that is the calculated energy for the first excited state. With this assumption we obtained: $\mathcal{T}_0 = (1.6 \pm 0.5) \times 10^{-10}\,\mathrm{s}$, $n = 6.20(6)$, $C = (4.9 \pm 0.7) \times 10^{-5}\,\mathrm{s}^{-1}\ \mathrm{K}^{-\mathrm{n}}$. On the contrary, if we let the fit free, we obtain $\Delta = (330 \pm 80)\,\mathrm{K}$, $\mathcal{T}_0 = (5 \pm 20) \times 10^{-12}\,\mathrm{s} \sim 230\,\mathrm{cm}^{-1}$, while the Raman contribution was substantially unaffected.

Conversely, the green line in Figure 6.14 was obtained considering the master matrix equation [13]: this approach allows the calculation of the relaxation rate from a state $|q\rangle$ (eigenstate of the Hamiltonian that describes the system) to another state $|p\rangle$ and to extract the relaxation time. Using an Hamiltonian with a Zeeman and a CF contribution built from the *ab initio* calculations, it was possible to reconstruct the master matrix for all temperatures and thus obtain the relaxation time ($\mathcal{T}$) from the first non vanishing eigenvalue of the master matrix (λ_1) as:

$$\mathcal{T} = -\frac{1}{\lambda_1} \tag{6.3}$$

The extracted $\mathcal{T}$ are influenced only by the coupling with phonons, so they can provide an indication of the temperature from which the system start to relax with an Orbach process. This temperature was found to be about 15 K (green line in Figure 6.14) but experimentally it is possible to follow the relaxation time only up to 20 K, so the points in Figure 6.14 that can be attributed to an Orbach relaxation are few. The relaxation barrier obtained with this approach (320 K) nicely reproduces the high temperature

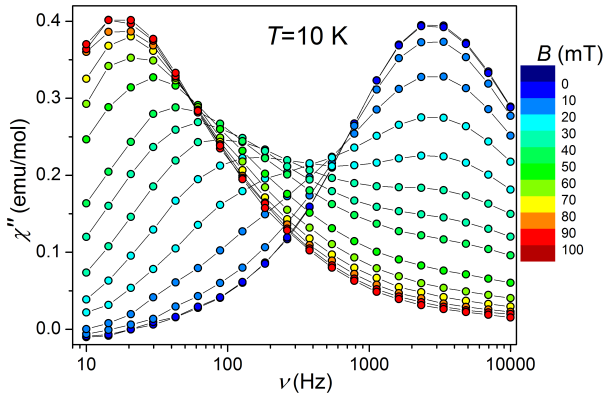

Figure 6.13: Imaginary susceptibility of **Dy** at 10 K as a function of the applied field.

dependence of $\mathcal{T}$ but it overestimates its value at low temperature. This is clearly due to interactions which are not taken into account by this model, such as residual dipolar intermolecular interactions and hyperfine interactions, with the isotopes of Dy with a magnetic nuclear momentum. These open the possibility of relaxation via QT, which is strictly forbidden for a simple seminteger spin, and might also change the expected field and temperature dependence of direct processes. In this framework, the Raman term, which was found necessary to nicely reproduce our low temperature data has to be considered as purely phenomenological, since a real Raman process should be more effective at high temperature than at lower ones.

Concluding, we have fully characterized the anisotropy of a mononuclear Dy-based complex with marked Ising character and high barrier for the reversal of the magnetization. The interplay between CTM and theoretical calculations resulted to be very efficient in this regard, even in absence of spectroscopic data. Moreover the high temperature behaviour could be correctly interpreted using the master matrix approach. On the contrary, the low temperature region appeared to be much more sensitive to other effects (*e.g.* hyperfine or dipolar interactions) that are reduced, but not completely quenched at the level of dilution used here.

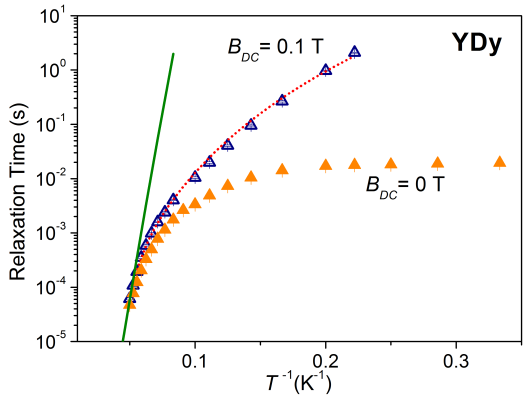

Figure 6.14: $\mathcal{T}$ versus $1/T$ for compound **YDy**, in zero (full orange triangles) and applied static field (empty blue squares). The red dotted line represents the fit of the relaxation time including Raman and Orbach processes with $\Delta = 270\,\mathrm{K}^{-1}$ while the green full circles are the relaxation times simulated using the master matrix equation(see also text).

AUTHOR CONTRIBUTIONS JPC synthesised the complexes that LV characterize by X-ray diffraction. MP carried out the torque measurements as well as the treatment of the data and modified the program. EL characterized the complex *via* *DC* and *AC* magnetometry and EPR (with LS). MB and FT performed the theoretical calculations. RS supervised all the work. All the authors wrote the manuscript.

6.3 M(TMC)N_3 M=Co,Ni

Manuscript in preparation

Influence of the ligand geometry in the anisotropy of Cobalt(II) and Nickel (II) penta-coordinate complexes.
G. Zakhia, B. Cahier, N. Guihéry, M. Perfetti, R. Sessoli, A.L. Barra and T. Mallah

The research of highly axial systems based on mononuclear TM complexes is a hot topic in molecular magnetism, and the main efforts are devoted to synthetize and study coordination compounds with tetrahedral or octahedral symmetry. Systems of lower symmetry are in general less investigated because their anisotropy is strongly dependent on the nature of the metal ion, as we have already discussed in Section 5.2. However the isostructural character often exhibited by Ln compounds is not straightforward for TM complexes, in which the external configuration of the metal can drive the geometry of the ligand. This is the case of pentacoordinate complexes of Co^{2+} and Ni^{2+} with modifications of the Tris-(2-aminoethyl)amine (tren) ligand that exhibited giant Ising anisotropy [89] and revealed to be a suitable system to tune by chamical design [90, 91].

Here we report two pentacoordinated complexes containing a TM (Ni^{2+} or Co^{2+}) that crystallizes in the orthorhombic space group and thus have unit cells with more than one noncollinear entity. The complexes, reported in Figure 6.15, contains the bipositive metal ion encapsulated in the neutral 1,4,8,11-tetramethyl 1,4,8,11-tetraazacyclotetradecane (TMC) macrocyclic ligand that coordinates the metal with the four nitrogen atoms, the coordination number 5 is reached by the addition of an azide (N_3^-) anion. To balance the charge a perchlorate anion has also to be included in the formula. The synthesis and characterization can be found in literature [92, 93]. The resolution of the crystal structure, as well as preliminary *ab initio* calculations evidenced that the geometry around the TM ion is almost trigonal bipyramidal for the Co derivative and square pyramidal

for the Ni derivative, as indeed expected for a d^7 and a d^8 TM ion, respectively. An EPR characterization performed at the CNRS, revealed that both complexes are strongly easy plane and that the Co derivative also exhibit a strong rhombic distortion with best fitted ZFS parameters: $D_{Co} = 40\,\mathrm{cm}^{-1}$, $E_{Co} = 7.7\,\mathrm{cm}^{-1}$, $D_{Ni} = 22\,\mathrm{cm}^{-1}$, $E_{Ni} = 0.3\,\mathrm{cm}^{-1}$. For the sake of simplicity, we will call the Co and Ni derivatives as Co(TMC)N_3 and Ni(TMC)N_3, respectively.

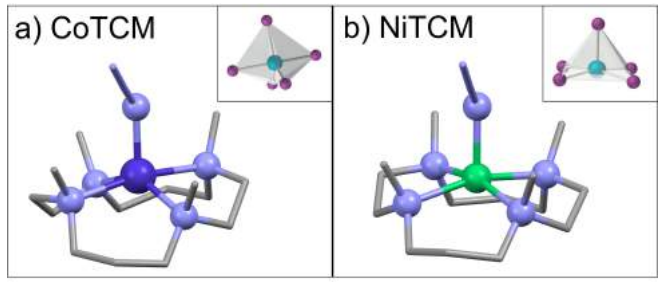

Figure 6.15: Structure of Co(TMC)N_3 (panel a) and of Ni(TMC)N_3 (panel b). Color code: dark blue-Cobalt, pale blue-Nickel, grey-Carbon, blue-Nitrogen, Hydrogen atoms and ClO_4^- ions were omitted for clarity. The insets show the closest ligand geometry: trigonal bipyramidal for CoTCM and square pyramidal for NiTCM.

Both crystals belongs to the orthorhombic space group, however there is a major difference in the symmetry operation of the group: the cobalt complex crystallizes in the $Pna2_1$ space group while the nickel one in the $Pmnb$ space group. In both complexes c is a C_2 axis and the ac plane is a glide plane, nevertheless only the Ni complex possess a mirror plane (bc) that contains the Ni atom and the azide ion. For this reason the number of noncollinear molecules in the cell, that is 4 in the case of Co(TMC)N_3, is reduced to 2 in Ni(TMC)N_3. This structural feature turned out to be very useful for the rotations performed using CTM (see after).

For each derivative we performed two orthogonal rotations. The position of the crystals during the rotations can be found in the middle of Figure 6.16 and Figure 6.17. Let us examine the single rotations starting from Ni(TMC)N_3. From a qualitative point of view we can firstly assume that

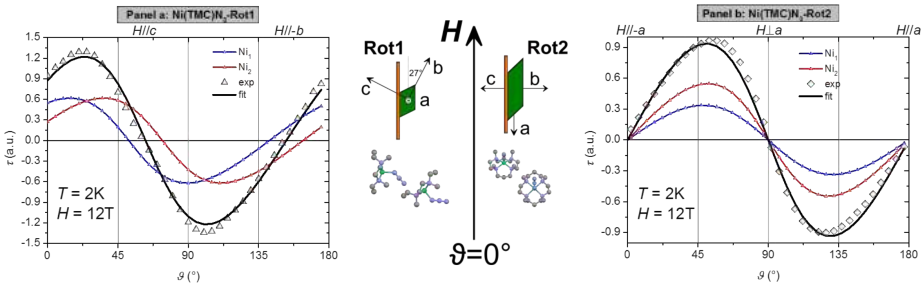

Figure 6.16: Experimental data (black symbols) and best fit (black lines) of Rot1 (panel a) and Rot2 (panel b) for $Ni(TMC)N_3$ (see legend for temperature and fields). Red and blue curves are the simulated contributions of the single noncollinear sites (see text). Middle: Position of the crystal at $\vartheta = 0°$ for the two rotations.

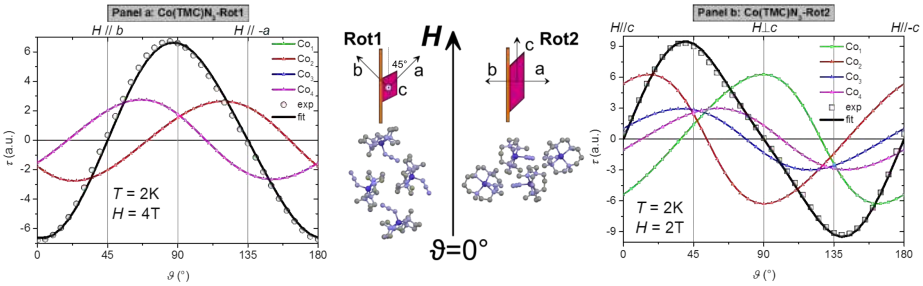

Figure 6.17: Experimental data (black symbols) and best fit (black lines) of Rot1 (panel a) and Rot2 (panel b) for $Co(TMC)N_3$ (see legend for temperature and fields). Red, blue, magenta and green curves are the simulated contributions of the single noncollinear sites (see text). Middle: Position of the crystal at $\vartheta = 0°$ for the two rotations.

the geometry around the metal ion is approximately square planar, with the Ni−N_3 bond in the apical position. It is of paramount importance to recall that with this assumption, the Ni−N_3 bond must be a principal axis of anisotropy for the molecule. The first rotation, panel a of Figure 6.16, was conducted using a as rotation axis and at $\vartheta = 0°$ the field was at 63° from the c axis. Indeed we observe two zero points in the $0 - 180°$ angular range corresponding to the magnetic field being parallel to c (63°) and to b (153°). This is expected because the ac and ab planes are glide planes of the molecular structure. When the field begins to approach the c axis, the torque exhibit the usual rapid variation, indicating that the hard axes of the two noncollinear molecules lie close to the magnetic field direction. Indeed, the axial bonds of the two molecules are tilted of 25° (we recall that ac is a glide plane) from the c axis, so the Ni−N_3 direction for this molecule results to be an hard direction and, as a consequence, the anisotropy of the system must be easy plane at a first approximation. Curves obtained during Rot2 (Figure 6.16, panel b) that was performed with the rotation axis lying in the bc plane, exhibit zeroes at $\vartheta = 0°$ and 180°, and have the easy direction when a is parallel to the field, confirming that the Ni−N_3 bond is an hard direction of anisotropy for the complex.

The case of Co(TMC)N_3 was complicated by the lack of mirror planes. Rot1 for Co(TMC)N_3 was performed using c as rotation axis to be as coherent as possible with Rot1 of Ni(TMC)N_3, in this way the 4 contributions can be reunited in two couples that give a signal shifted by 54°, that is two times the angle between the Co−N_3 bond and the bc plane. Moreover the angle between the magnetic field and the a-axis is 45° at $\vartheta = 0°$, so the resulting torque is expected to vanish at 45° and 135°, coherently with the experimental evidences. Finally, Rot2 of Co(TMC)N_3 contains four independent contributions that, due to the fact that at $\vartheta = 0°$ the c axis was parallel to the field, should vanish at 0° and 90°. Analysing the shape of the torque for the two rotations we can preliminarily conclude that if the Co−N_3 bond is a principal axis of anisotropy it must not be an hard axis in this complex, differently from the case of Ni(TMC)N_3. However only an accurate fit of the experimental data can provide more useful

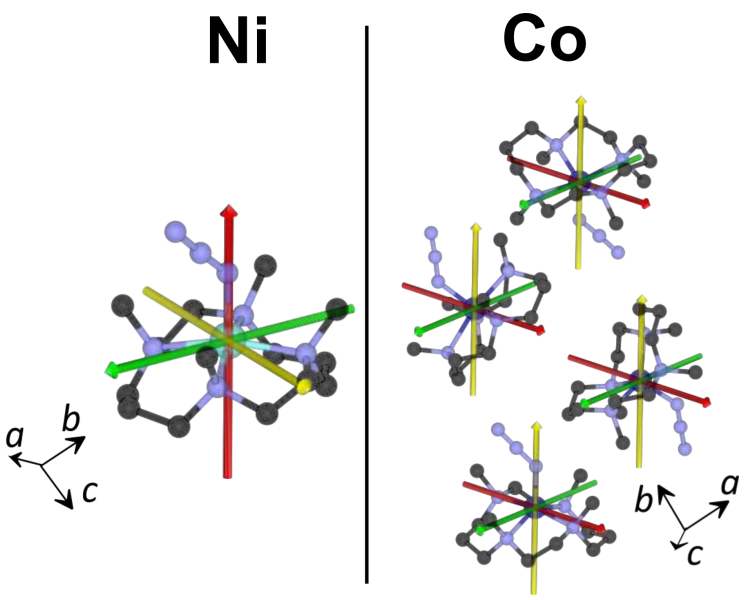

Figure 6.18: Principal anisotropy axis of Ni(TMC)N_3 (left) and Co(TMC)N_3 (right). x-yellow (intermediate), y-green (easy) and z-red (hard). For Ni(TMC)N_3 the solution is unique, while for Co(TMC)N_3 there is ambiguity.

information about this system that in principle could have any orientation of the molecular reference frame.

The fit of the two rotations for each compound was performed leaving free to adjust four parameters: the usual scale factor and three Euler angles (ρ, ξ, ψ). The torque was then obtained using a Spin Hamiltonian of the form:

$$\mathcal{H} = g\mu_B \boldsymbol{S} \cdot \boldsymbol{B} + D[\boldsymbol{S}_z^2 - \frac{1}{3}S(S+1)] + E(\boldsymbol{S}_x^2 - \boldsymbol{S}_y^2) \qquad (6.4)$$

where all the quantities were already defined in Section 2.2.2. To avoid overparametrization, the values of the ZFS parameters were fixed from the ones extracted from EPR measurements.

We obtained $\rho = 0.0(2)°$, $\xi = 10.8(5)°$ and $\psi = 4.0(7)°$ for Ni(TMC)N_3 while $\rho = 250.0(1)°$, $\xi = 55.1(1)°$ and $\rho = 348.69(1)°$ for Co(TMC)N_3. The results of the fit, reported as black solid lines in Figure 6.16 and 6.17, are in excellent agreement with the experimental data. Figure 6.18 is a graphical

view of the molecular reference frame on the chemical structure, obtained from the Euler matrix elements. As anticipated, while for Ni(TMC)N_3 the apical bond must be a principal axis so the solution obtained from torque data is unique, this is not true for Co(TMC)N_3, because the found solution can be in principle arise from one of the four noncollinear molecules in the unit cell that we reported. However it is worth noticing that preliminary theoretical calculations support one of the found solutions (that is the lowest reported in Figure 6.18).

In conclusion we can assert that both compounds showed an easy plane anisotropy, the hard axis being almost coincident with the M$-N_3$ bond for Ni(TMC)N_3 but tilted by 90° passing to Co(TMC)N_3 (considering the solution coincident to the *ab initio* calculations). It is also interesting to notice that the M$-N_3$ axis remains a principal axis for both derivatives.

AUTHOR CONTRIBUTIONS GZ synthetized the complexes and performed the standard magnetic characterization, BC and NG performed all the calculations, MP characterized the complex *via* cantilever torque magnetometry and performed the experimental fits (with assistance of RS). ALB performed the EPR measurements. TM coordinated all the work.

7 Intramolecular noncollinear systems

This chapter is devoted to the description of systems in which the noncollinearity of magnetic moments arises at the single molecule level, such as in clusters containing metal ions with different coordination environment. In the field of molecular magnetism it is very useful to obtain molecules with easy axis anisotropy, because they can exhibit a barrier for the relaxation of the magnetization at sufficiently low temperature [13]. This can be achieved combining approximately collinear easy axis contributions, such as in Mn_6 [94] and Mn_{12} [11, 95, 96, 97] clusters, or assembling easy and hard axis metal ions with their unique axis approximately parallel and perpendicular to a molecular axis, respectively. This last situation finds a practical realization in the family of the Fe_4 propeller-like complexes, that have inspired Section 7.1 and Section 7.2 of this Chapter. The four Fe^{3+} ions that constitute the core of all the molecules of the Fe_4 family are arranged in a centred triangular fashion and are connected by bridges containing oxygen atoms; due to the strongly hard donor atoms all the metal ions are in their high spin state $s = 5/2$. A characteristic of all this derivatives is the strong antiferromagnetic coupling between the central ion and the peripheral ones that gives rise to a well defined total spin quantum number $S = (3 - 1)(5/2) = 5$. This class of derivatives is particularly interesting because they possess a barrier for the relaxation of the magnetization that amounts about 13-15 K [98, 99, 100], however only the central ion has an Ising type anisotropy, while the three peripheral have a positive ZFS parameter, clearly shown by dilution experiments [101] and confirmed by theoretical predictions [102, 103]. This "strong

exchange" regime allows the description of the magnetic anisotropy of each multiplet with a tensor $\boldsymbol{D}(S)$, which can be expressed as a linear combination, with proper coefficients (d), of contributions arising from the single site anisotropy ($\boldsymbol{D}_i$) and from spin-spin interactions between centres ($\boldsymbol{D}_{i,j}$) [104]:

$$\boldsymbol{D}(S) = \sum_i d_i(S)\boldsymbol{D}_i + \sum_{i,j} d_{i,j}(S)\boldsymbol{D}_{i,j} \tag{7.1}$$

Luckily, in most of the clusters investigated in molecular magnetism, the second term is small compared to the first one and can be safely neglected: this is the case of Fe_4Ag (Section 7.2). The strong exchange limit can be a precious tool to calculate the magnetic properties of these clusters in a computational achievable way, however it is fundamental to deeply investigate the magnetic properties of these systems also at a single ion level (Section 7.1) because a comprehension of the role of the local magnetic anisotropy tensors with respect to the global behaviour of the molecule can address the synthesis of new derivatives with enhanced desirable properties.

Nevertheless, in literature are reported also exotic arrangements such as toroidal [105, 106] or helical [107, 108] spin structures. Indeed, in Section 7.3 we describe a chiral spin structure arrangement in a chain formed by Dy complexes.

7.1 Fe_3La

Paper in Appendix

Mapping of single-site magnetic anisotropy tensors in weakly coupled spin clusters by torque magnetometry.
L. Rigamonti, A. Cornia, A. Nava, M. Perfetti, M.E. Boulon, A.L. Barra, X. Zhong, K. Park and R. Sessoli.
Physical Chemistry Chemical Physics, **2014**, 16(32), 17220-17230.

The most commonly employed techniques in magnetism allow only the observation of the global zero-field splitting tensor $\boldsymbol{D}(S)$, so the effect of noncollinearities inside the molecules is expected to appear only with

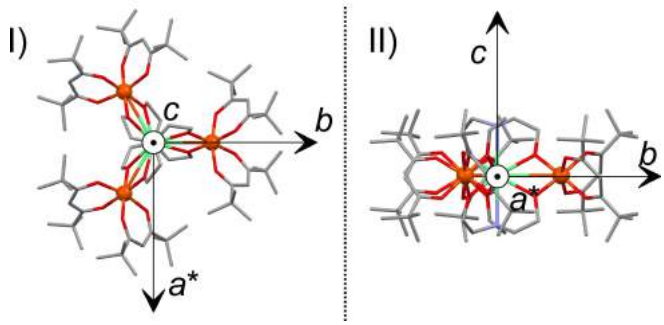

Figure 7.1: Fe_3La structure in the a^*bc rf. Panel a shows the view along the trigonal axis while panel b shows the view along the a^* axis. Color code: green-Lanthanum (taken as the origin of the reference frames), grey-Carbon, orange-Iron, blue-Nitrogen, red-Oxygen, Hydrogen atoms were omitted for clarity.

extremely sensitive techniques, such as CTM. The conditions at which one has to operate to appreciate the single contributions are low temperatures and high fields, that is, the "weak-exchange" limit where the equation that relates the anisotropy tensor to the field and the magnetization (Equation 4.6) breaks down.

To deeply investigate the single contributions coming from the peripheral Fe^{3+} ions, we synthesizes a derivative that has a La^{3+} ions that substitutes the central Fe^{3+} ion (hereafter Fe_3La), so that the ideal D_3 symmetry of the complex can be maintained. This replacement strongly reduces the communication between the magnetic centres, allowing the study of the magnitude and orientation of the single-site anisotropies in unprecedented detail. A specific description of the synthesis, structural characterization and instrumentation used for the characterization can be found in Appendix. In Figure 7.1 we reported the molecular structure of the complex in the a^*bc orthogonal rf used for all the calculations.

The static magnetic properties of the complex in form of a fine pressed powder pellet were investigated from 1.9 to 240 K finding a high temperature value of the χT product of 13.2 emu K mol^{-1}, close to the expectation value for three independent Fe^{3+} ions (13.13 emu K mol^{-1}, with $g = 2$), as reported in Appendix. The plot of $1/\chi$ *vs.* T is linear in the whole

temperature range explored and can be fitted obtaining a Curie constant $C = (13.264 \pm 0.005)\,\mathrm{emu\,K\,mol^{-1}}$ and a Curie-Weiss temperature $T_{C-W} = -(0.90 \pm 0.03)\,\mathrm{K}$. A negative value of T_{C-W} indicates three substantially independent ions, exhibiting weak magnetic anisotropy and/or AFM interactions among each other. This is confirmed by the M vs B curves that exhibit significat nesting when plotted against B/T. To have an idea of the values of the ZFS if the single ions ($\boldsymbol{D}_i$) and of the coupling constant (J), we firstly fit the DC data assuming isotropic super-exchange interactions, thus neglecting the antisymmetric and anisotropic part of the exchange; this was justified *a posteriori* by the fact that the single-site anisotropies so determined are much larger than isotropic coupling constant. Neglecting terms of the fourth order and assuming $g = 2$, the spin Hamiltonian written as a function of the individual spin operators ($\boldsymbol{s}_i$) takes the form:

$$\begin{aligned}\mathcal{H} = {} & J(\boldsymbol{s}_1 \cdot \boldsymbol{s}_2 + \boldsymbol{s}_2 \cdot \boldsymbol{s}_3 + \boldsymbol{s}_3 \cdot \boldsymbol{s}_1) + g\mu_B \boldsymbol{S} \cdot \boldsymbol{B} \\ & + \boldsymbol{s}_1 \cdot \boldsymbol{D}_1 \cdot \boldsymbol{s}_1 + \boldsymbol{s}_2 \cdot \boldsymbol{D}_2 \cdot \boldsymbol{s}_2 + \boldsymbol{s}_3 \cdot \boldsymbol{D}_3 \cdot \boldsymbol{s}_3 + \mathcal{H}_{dip}\end{aligned} \tag{7.2}$$

here $\mathcal{H}_{dip}$ accounts for dipolar interactions. The molecular rf (xyz) adopted in this case was coincident with the a^*bc crystallographic rf, in particular z coincident with the trigonal axis c, $y$along the b axis which is parallel to $\mathrm{La_1}\cdots\mathrm{Fe_1}$ direction and coincides with a twofold symmetry axis and x along a^*, as reported in Figure 7.1. The symmetry of the complex constrains the $\boldsymbol{D}_i$ tensors to be related by a threefold rotation around c, moreover the traceless nature of the tensor and the chosen rf give rise to only three independent non-zero values of the tensor elements, say $\boldsymbol{D}_i(xx)$, $\boldsymbol{D}_i(zz)$, $\boldsymbol{D}_i(xz)$. Using axial tensors for simplicity, data could be fitted with comparable accuracy for any angle β between the z molecular axis and the z_i axis of the tensors, but only using a positive ZFS, in agreement with literature and with HF-EPR measurements (see Appendix). In Figure 7.3 is reported the molecular structure of $\mathrm{Fe_3La}$ where the iron atoms are replaced by single-site susceptibility tensors. The angle β is the one between the hard axis of the tensors (red arrows) and the z molecular axis, that in this system corresponds to the c axis.

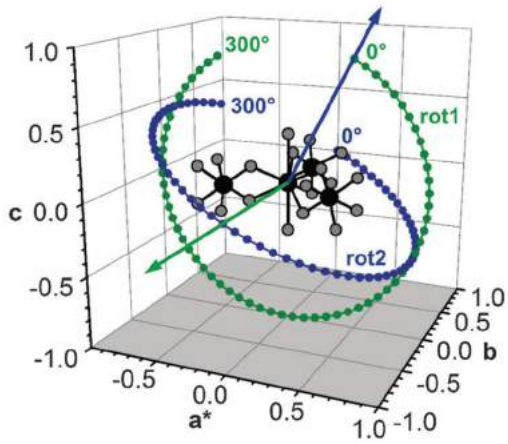

Figure 7.2: Direction cosines of the magnetic field in the a^*bc rf for the two performed rotations (rot1 and rot2), with the initial and final setting angles (0° and 300°). For each rotation, an arrow perpendicular to the field trajectory indicates the direction along which the torque signal has been measured. The molecular structure of Fe_3La is also included in the graph, omitting for clarity carbon and hydrogen atoms. Colour code: La, Fe = large black spheres, N, O = grey spheres.

This results clearly indicates that standard magnetic measurements are not sufficient to precisely characterize the anisotropy of this system, so we proceeded with CTM measurements on an indexed single crystal at $T = 2.3\,\mathrm{K}$ and $T = 5.5\,\mathrm{K}$ with B =1 T to 7 T. We performed two rotations, as reported in Figure 7.2.

Data recorded at $T = 2.3\,\mathrm{K}$ for rot1 are reported in Figure 7.4. Beyond the trivial 180° periodicity expected for any paramagnetic system, we can notice that around 0° the torque has negative sign, indicating that the sample has a tendency to rotate so as to bring the c axis closer to $\boldsymbol{B}$, *i.e.* the trigonal axis is an easy magnetization direction. This is also proven by the vanishing torque signal at 155°, when the c axis is parallel to the field. However the other zero torque angles (51-63° and 231-243°, depending on the magnitude of the field) are not evenly spaced, meaning that Equation 4.8 is not valid anymore and the main requisite for our analysis is fulfilled.

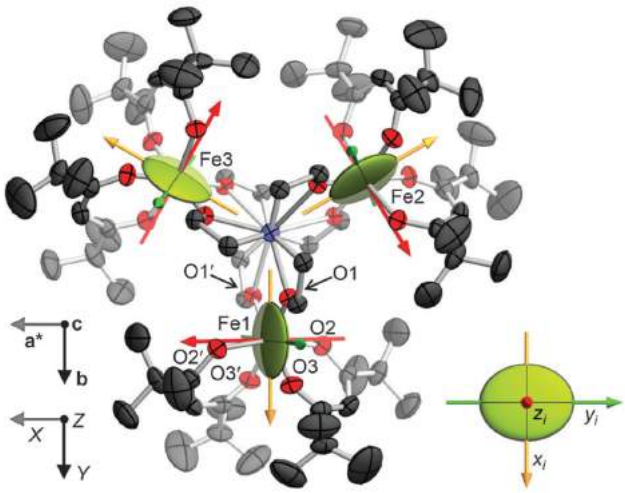

Figure 7.3: Molecular structure of Fe_3La where the iron thermal ellipsoids are replaced by single-site susceptibility tensors, calculated in the high temperature limit and drawn at an arbitrary scale. The hard, intermediate and easy magnetic directions are depicted using red, yellow and green arrows, respectively. A view of the susceptibility tensor along its hard axis is shown in the lower-right part of the figure.

It is possible to explain this features starting from the symmetry of the free energy surface, because, as reported in Equation 4.4, the torque is the derivative of the energy with respect to the angle. The free energy surface is in fact expected to exhibit D_{3d} symmetry (that is the point group symmetry D_3 of the molecule *plus* and inversion centre), and a section along the mirror plane perpendicular to b will display twofold symmetry. The second rotation, rot2, is reported in Figure 7.5 for $T = 2.3\,\mathrm{K}$. In this case we can notice that the torque dependence is considerably more complex than in rot1, and that around $\vartheta = 0°$ the torque change sign. Also this feature can be reconstructed starting from the symmetry of the free energy, that in a plane containing b axis will display $2mm$ point-group symmetry, with mirror lineas directed along b and perpendicular to it. As a consequence $\vartheta = 0°$ corresponds to a free energy extremes and the torque component perpendicular to the section must then vanish. All the aforementioned

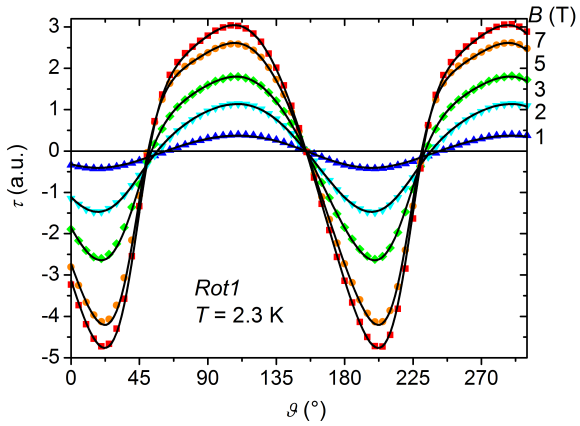

Figure 7.4: Torque signal of Fe_3La measured at 2.3 K and for different values of the applied field during rot1. The cantilever was sensitive to the torque component along the green arrow in Figure 7.2. The solid curves provide the best fit to experimental data.

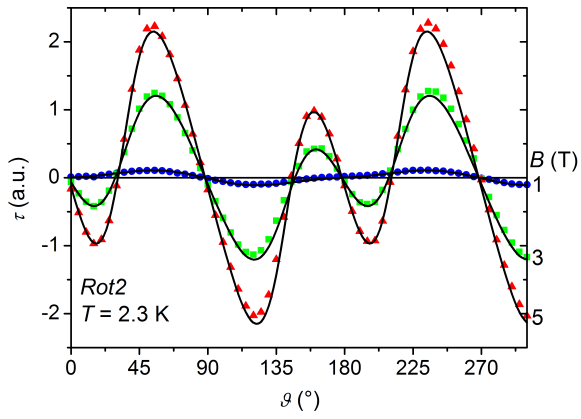

Figure 7.5: Torque signal of Fe_3La measured at 2.3 K and for different values of the applied field during rot2. The cantilever was sensitive to the torque component along the blue arrow in Figure 7.2. The solid curves provide the best fit to experimental data.

anomalies in the torque shape, signals of the dominant magnetic anisotropy effects over superexchange interactions, are considerably dumped when the temperature is increased to 5.5 K, meaning that the torque approaches the low field limit described by Equation 4.8.

For this system we performed detailed simulations of the torque data neglecting the dipolar and the superexchange terms in Equation 7.2 and considering $\boldsymbol{D}_i$ to be axial. Here, the value of β becomes critical, because it determines if the c axis will correspond to a global easy or hard axis of the molecule. Even more importantly, setting $\beta = 90°$ introduces extra mirror lines in the free energy surface, not observable in the torque curves (especially in rot1), proving that the rhombic distortion is weak or negligible and that the hard axis of the tensors are neither exactly parallel nor perpendicular to the c axis. Furthermore it is important to notice that adding superexchange or dipolar interactions do not change our conclusions that are based on symmetry arguments.

As already pointed out for Ln in Equation 2.20, also for TM ions it is common to decompose the $\boldsymbol{D}_i$ tensor into two distinct contributions, namely D_i and E_i. The torque signal was recorded in a.u., so we introduced a scale factor (f_{sc1} and f_{sc2}) and an angular offsets to take into account small misalignments (ϑ_1 and ϑ_2) for each rotation. The best fit was than obtained using the 8 aforementioned adjustable parameters with the values of: $J = (0.0783 \pm 0.0019)\,\mathrm{cm}$, $D_1 = (0.989 \pm 0.009)\,\mathrm{cm}$, $E_1 = (0.0517 \pm 0.0019)\,\mathrm{cm}$, $\beta = (68.89 \pm 0.08)°$, $\vartheta_1 = -(2.36 \pm 0.07)°$, $\vartheta_2 = (1.78 \pm 0.08)°$, $f_{\mathrm{sc1}} = 0.650 \pm 0.009$ and $f_{\mathrm{sc2}} = 0.696 \pm 0.009$. This results are in agreement to the precision of the technique, in fact the two scale factors differs of less than 7% and the angular offsets are extremely good, considering the precision of a visual crystal alignment. The local anisotropies are not far from being axial ($|E/D| = 0.05$) and the intermediate magnetic axis of $\boldsymbol{D}_1$ is directed along the $\mathrm{La}_1 \cdots \mathrm{Fe}_1$ direction, in close agreement with previous works [98, 99, 100, 101]. The free energy surface computed at $T = 2.3$ and 5.5 K and $B = 3\,\mathrm{T}$ with best-fit spin Hamiltonian parameters is reported in Figure 7.6: as the temperature is raised the D_{3d} symmetry is replaced by a more cylindrical shape along

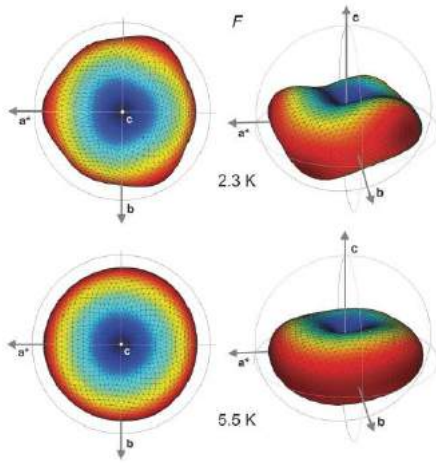

Figure 7.6: Free energy surfaces computed with the set of best-fit spin Hamiltonian parameters for different orientations of a 3 T magnetic field at 2.3 and 5.5 K. The distance from the centre of the diagram is proportional to $F - F_{\min}$, where $F_{\min}$ is the minimum value of the free energy, which is found when the field is applied along c. The angular dependence of F is also displayed using a colour scale (from blue to red).

c. Note also that during Rot1 we scanned the a^*c plane, the position of the free enery maximum is close to the orientation of the local hard axis, therefore the shape of the free energy surface is a direct measurement of the single tensors arrangement (computed energy surfaces for very low temperatures can be found in Appendix).

HF-EPR spectra (240 GHz) could be simulated with a reasonable agreement using parameters with values similar to the one extracted with CTM and provided a precise picture of the energy level structure of the system due to the observation of the transition from $m_S = -3/2$ to $-1/2$ (at $B = 10.7$ and 11.2 T) and of $m_S = -5/2$ to $-3/2$ (at $B = 12.6$ and 13.5 T).

Finally, also DFT calculations supported the experimental results, calculating $D_i = 1.094\,\mathrm{cm}^{-1}$, $E_i = 0.034\,\mathrm{cm}^{-1}$, $\beta = 72.7^\circ$ and the intermediate axis exactly along the $\mathrm{La}_1 \cdots \mathrm{Fe}_1$ direction.

Concluding, we have efficiently provided a complete picture of the local

anisotropy tensors of the peripheral atoms of a Fe_4 cluster that resulted to be hard axis type and, more importantly, they are strongly noncollinear, forming an angle of 70° with the threefold molecular axis which becomes an easy magnetic direction for the molecule. This study was possible only due to the presence of a La^{3+} atom in the middle, that efficiently quenches the interactions between magnetic ions. The key technique was once again CTM, that turned out to be extremely sensitive also in detecting small anisotropy components.

AUTHOR CONTRIBUTIONS LR and AN synthesized and characterized the complex. MEB and MP worked on the crystallographic indexing. MP (with the assistance of RS) performed the torque measurements. AC wrote the program and fitted the experimental data. ALB carried out the EPR measurements, while KP and XZ worked on the theoretical calculations. The paper was written by AC and revised by all the authors.

7.2 Fe_4Ag

Manuscript in preparation

Diamond-Shaped Metal Organic Framework of Fe_4 Single-Molecule Magnets.
L. Rigamonti, C. Cotton, A. Nava, T. Rüffer, R. Sessoli, L. Sorace, M. Perfetti, W. Wernsdorfer, Y. Lanf and A. Cornia.

In this Section we will focus on the magnetic analysis on a system containing SMMs of the family of Fe_4 connected in a porous 3D network, forming a structure that is commonly called Metal Organic Framework (MOF). Up to date, the scientific community express a growing interest about the rational design, experimental characterization, theoretical study and applications of new MOFs because this kind of systems can be very versatile and find applications ranging from catalysis [109], to gas storage [110, 111], from bio-mimetism [112] to quantum dot semiconductors [113].

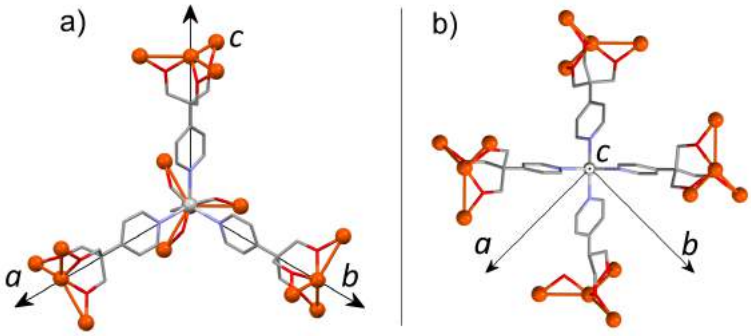

Figure 7.7: Fe_4Ag structure in the *abc* rf. Panel I and Panel II refers to the position $\vartheta = 0°$ for rot1 and rot2 of the CTM measurements when the field is vertical (see text), respectively. Color code: light grey-Silver, grey-Carbon, orange-Iron, blue-Nitrogen, red-Oxygen, surrounding ligands of the Fe_4 moieties and hydrogen atoms were omitted for clarity and because the structure is not entirely solved yet.

The synthesis of structures containing SMM organized in 3D network is already known in literature [114, 115, 116, 117, 118, 119], however the supramolecular organization are often serendipitous.

A recent work [120] showed the synthesis and 1D organization of a new derivative of the Fe_4 family as a chain magnet, $Fe_4(pPy)_2(dpm)_6$ (where H_3pPy is the 2-(hydroxymethyl)-2-(pyridin-4-yl)propane-1,3-diol and Hdpm is the dipivaloylmethane, hereafter Fe_4pPy). The compound that will be described is a MOF obtained by the use of Fe_4pPy as a ditopic supramolecular synthon that is able to connect Ag^+ ions. The tendency of Ag^+ to form tetrahedral complexes is able to temple the entire structure in a diamond-like fashion, so that we can imagine that the Ag^+ atoms are the carbon atoms of a diamond structure and the Fe_4pPy are the axis of the directional bonds of the architecture. As a consequence, the easy axis of the giant ground state $S = 5$ characteristic of the Fe_4 core, that is known to be orthogonal to the plane on which the 4 Fe^{3+} ions lie [121], are forced to be noncollinear by the structure. Indeed, by simple symmetry consideration we can consider the easy direction of the magnetization

forming a sort of "symmetry frustrated" structure with disposition of the magnetic moments similar of that present in the spin ice compounds. This MOF, hereafter called Fe_4Ag can be isolated in a crystalline form with a cubic $Fd\bar{3}c$ unit cell. The 3D structure of this derivative, not entirely solved yet, is very complicated, due to either inclusion of solvent molecules inside the pores and local disorder. Also for this reason, CTM has to be considered a powerful technique to investigate this system because the complete identification of the magnetic structure of the MOF must mirrors in a precise spatial organization of the atoms. In Figure 7.7 we reported a view of the structure along the S_3 (panel a) and along the C_4 (panel b) molecular axis that where chosen as rotation axis for the CTM measurements (*vide infra*).

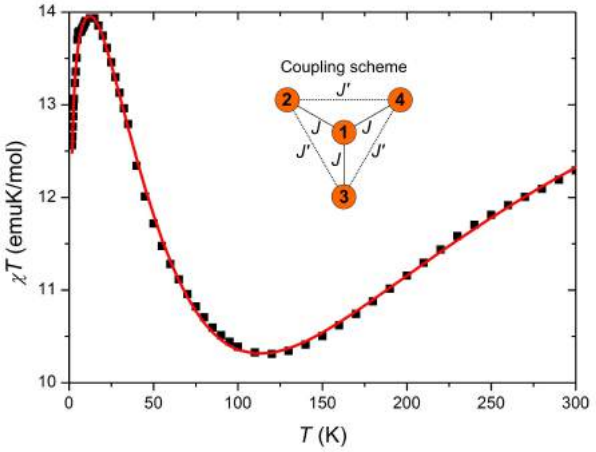

Figure 7.8: χT vs T plot of Fe_4Ag. The red line is the best fit (parameters reported in the text) of the experimental points (black squares). The inset is the adopted coupling scheme for the magnetic interactions.

The magnetic properties of the complex were initially characterized by *DC* magnetic measurements. The χT vs T plot (Figure 7.8) shows typical features of the Fe_4 systems [100, 120, 98] exhibiting a decrease when the temperature is lowered, as a consequence of the antiferromagnetic coupling

between the central and peripheral ions of the Fe_4 cluster, until a minimum at 120 K. Further cooling causes an increase due to selective population of the $S = 5$ ground manifold. The drop below 5 K may arise from magnetic saturation, anisotropy effects or intermolecular interactions. The χT vs T data were fitted using a Hamiltonian containing a Heisenberg plus a Zeeman contribution, assuming three-fold molecular symmetry, to evaluate the magnetic exchange interactions between centres:

$$\mathcal{H} = J(\boldsymbol{S}_1 \cdot \boldsymbol{S}_2 + \boldsymbol{S}_1 \cdot \boldsymbol{S}_3 + \boldsymbol{S}_1 \cdot \boldsymbol{S}_4) + J'(\boldsymbol{S}_2 \cdot \boldsymbol{S}_3 + \boldsymbol{S}_3 \cdot \boldsymbol{S}_4 + \boldsymbol{S}_2 \cdot \boldsymbol{S}_4) + g\mu_B \boldsymbol{S} \cdot \boldsymbol{B} \tag{7.3}$$

where $\boldsymbol{S}_i$ is the spin vector referring to the i-th centre and J and J' are the nearest-neighbour and the next-nearest neighbour exchange coupling constants, respectively, following the simple scheme reported in the inset of Figure 7.8. A Curie-Weiss correction, $T_{\text{C-W}}$, was applied to the equation in order to account for the drop of the χT curve after 5 K, as commonly used for other Fe_4 systems [101, 121]. The results are the following: $g = 1.9560(14)$, $J = (16.41 \pm 0.06)\,\text{cm}^{-1}$, $J' = (0.035 \pm 0.036)\,\text{cm}^{-1}$, $T_{\text{C-W}} = (-0.284 \pm 0.006)\,\text{K}$. As expected for this system, the next-nearest neighbour constant is essentially zero and the Curie-Weiss temperature is of the same order of magnitude of the ones commonly found in these systems.

From literature we know that the ZFS parameter of the family of Fe_4 is $D \sim -0.4\,\text{cm}^{-1}$, but it changes slightly as a function of the chemical structure. To have an estimation of this value for the studied system, we fitted the M vs B/T curves recorded at three temperatures with a Spin Hamiltonian of the form:

$$\mathcal{H} = \boldsymbol{S} \cdot D \cdot \boldsymbol{S} + g\mu_B \boldsymbol{S} \cdot \boldsymbol{B} \tag{7.4}$$

The best fit curves, also reported on the experimental points in Figure 7.9, gave: $D = -(0.411 \pm 0.006)\,\text{cm}^{-1}$ and $g = 1.9093 \pm 0.0016$. The value of g is really close to the free electron value ($g_e \simeq 2$), while the value of D must

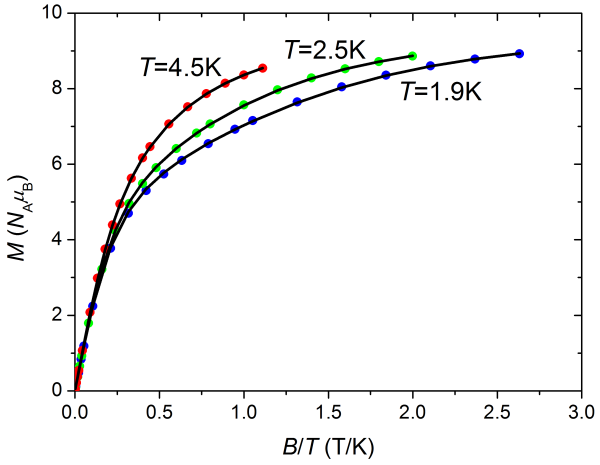

Figure 7.9: Magnetization vs field over temperature curves recorded at three different temperatures. The black lines are the best fit curves (see text).

be compared to the one extracted by CTM measurements (*vide infra*).

To have a more precise idea of the entity of the ZFS, we performed detailed CTM measurements mounting an indexed single crystal of Fe_4Ag on the cantilever magnetometer. For this system we decided to carry out two rotations (see also Figure 7.7): for rot1 the rotation axis was the diagonal of the crystal cubic cell (S_3 axis), while for rot2 it was the side of the cube, that is a C_4 axis. We already know from literature, as well as for the study of Section 7.1, that in the strong exchange limit, the Fe_4 cluster can be considered as a unique magnetic entity with negative ZFS with the easy axis parallel to the local pseudo C_3 axis. For this reason we could consider three noncollinear contributions in rot1 and two noncollinear contributions in rot2.

The torque signal recorded at $T = 2\,\mathrm{K}$ and variable field of rot1 is reported in Figure 7.10. The first thing that has to be noticed is that we observe three peaks in the angular range from $0°$ to $180°$, meaning that if we use CTM on a system with more than one noncollinear Fe_4 system, we can only appreciate the noncollinearity of the $S = 5$ giant spins, not the

one inside the atoms of a cluster. This is somehow expected because, as we already pointed out in Section 7.1, to observe single site anisotropy in this class of molecules, we need to decouple the peripheral Fe atoms to the one in the middle, and this is not the case. The polar plot in Figure 7.10, realized in the entire polar range taking advantage of the 180° periodicity, can give a clearer idea of the shape of anisotropy on the molecular structure. Nevertheless, the values of the torque at the maxima are not the same for all the peaks: this has to be attributed to small misalignments in the process of fixing the crystal on the cantilever. The molecular rf was fixed to have the z axis parallel to the diagonal of the cube using two Euler angles $\rho = 45°$ and $\xi = 54.7°$ (the third angle is not relevant if we describe the system as uniaxial). The signals arising from the other three Fe_4 cores can be easily reproduced by proper symmetry operations. To avoid overparametrization, we firstly fixed the D value to the one extracted by the M vs B curves ($D = -0.411\,\mathrm{cm}^{-1}$) and we fitted the usual scale factor, three Euler angles (α, β, γ) to identify small misalignment in the position of the rotation axis, and an offset to identify the direction of the field in the plane perpendicular to the rotation axis (the offset refers to the angle of which one has to rotate in the plane perpendicular to the rotation axis to obtain $\boldsymbol{B}$ perpendicular to the a axis). The results were: $\alpha = (6.7 \pm 0.6)°$, $\beta = (4.5 \pm 0.8)°$, $\gamma = (9.8 \pm 0.2)°$, offset $= (44 \pm 1)°$, $f_{\mathrm{sc}} = 1.27 \pm 0.02$. From this results we can calculate the angle between the predicted (Y) and the effective (Y') rotation axis: $\widehat{YY'}_{\mathrm{rot1}} = 4.4°$. As expected, the value is compatible with a visual crystal alignment. Moreover the offset is really close to the one expected from the position of the crystal (45°).

The same procedure was adopted for rot2, that is reported in Figure 7.11. For this rotation we observe only two peaks from 0° to 180°, because the projection of the anisotropy axis of the four Fe_4 cores are parallel in pairs (see polar plot of Figure 7.11). Despite the maxima in the curve were rather symmetric for this rotation, we adopted the same fitting procedure that we used for rot1. In this case we obtained: $\alpha = (2.9 \pm 0.5)°$, $\beta = (1.6 \pm 0.5)°$, $\gamma = (2.5 \pm 0.9)°$, offset$=(30 \pm 1)°$, $f_{\mathrm{sc}} = 1.26 \pm 0.02$. This means that the misalignment angle for this rotation is only $\widehat{YY'}_{\mathrm{rot2}} = 2.4°$, in agreement

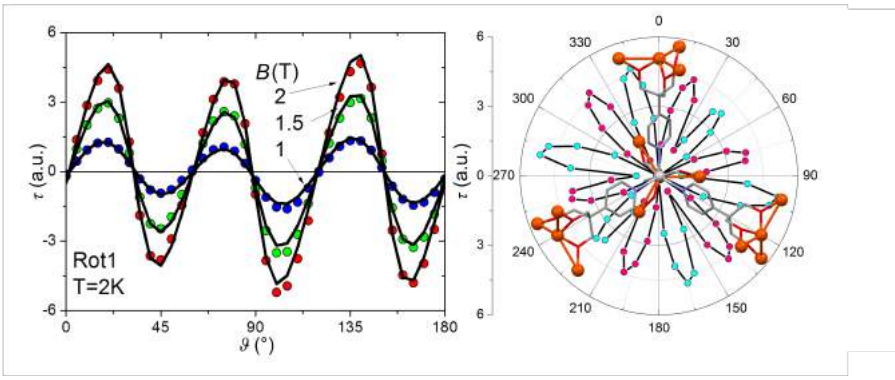

Figure 7.10: Left: Torque signal of Fe_4Ag measured at 2 K and for different values of the applied field during rot1. The solid black curves provide the best fit to experimental data. Right: Polar plot of the the absolute value of the torque for rot1, $T = 2\,\mathrm{K}$, $B = 2\,\mathrm{T}$ (pink-positive values, cyan-negative values) plotted on the molecular structure.

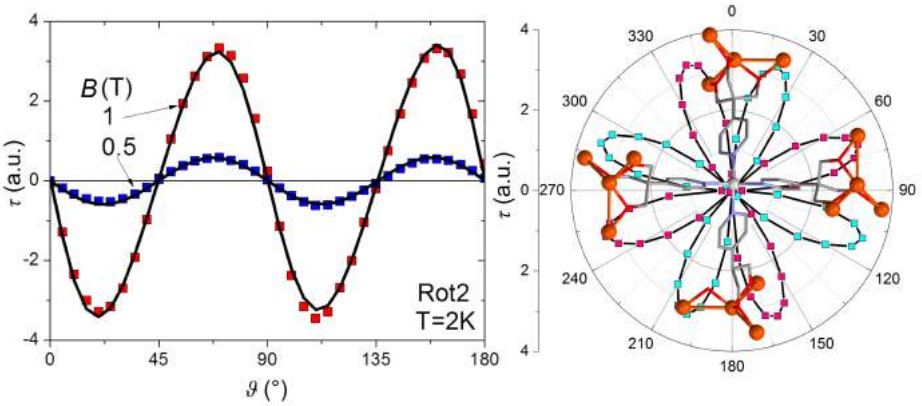

Figure 7.11: Left: Torque signal of Fe_4Ag measured at 2 K and for different values of the applied field during rot2. The solid black curves provide the best fit to experimental data. Right: Polar plot of the the absolute value of the torque for rot2, $T = 2\,\mathrm{K}$, $B = 1\,\mathrm{T}$ (pink-positive values, cyan-negative values) plotted on the molecular structure.

with the more symmetric shape of the curves. Also in this case the offset is exactly the one expected (30°).

Once obtained the real position of the laboratory rf with respect to the crystallographic one, we reunited all the data of the two rotations and we fitted one scale factor and the D parameter, obtaining $f_{sc} = 1.25 \pm 0.02$ and $D = -(0.426 \pm 0.006)\,\mathrm{cm}^{-1}$ (the black lines in Figure 7.10 as well as in Figure 7.11 refer to this fit). First of all we notice that the scale factor differs of only few percent from the ones obtained by fitting the single rotations, moreover the value of the ZFS is in really good agreement to the one obtained by DC magnetic measurements.

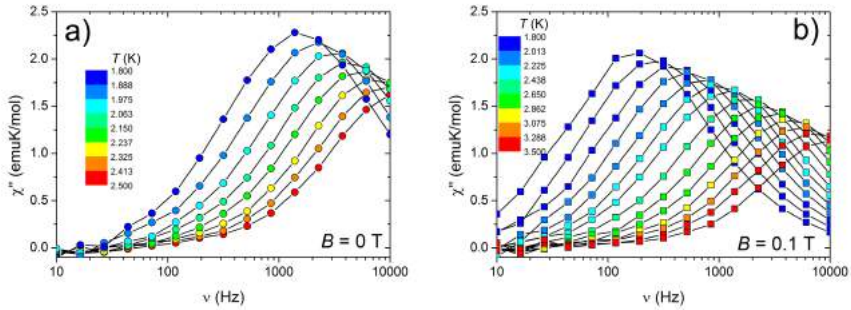

Figure 7.12: Imaginary part of the magnetic susceptibility for Fe_4Ag in zero (left, $T = 1.8 - 2.5\,\mathrm{K}$) and 0.1 T (right, $T = 1.8 - 3.5\,\mathrm{K}$) applied field.

The value and sign of the ZFS parameter are compatible with the possibility to have slow relaxation of the magnetization for this system. Indeed, a field scan at $T = 1.8\,\mathrm{K}$, reveals that Fe_4Ag exhibit a peak in χ'' both in zero field and with an optimum applied field of 0.1 T, as reported in Figure 7.12. The Casimir and Du Pré formula [122] was used to fit χ'' obtaining the dependence of the relaxation time as a function of the temperature (Figure 7.13). For the Fe_4 family the fit using only an Orbach process seems appropriate, so we used the formula:

$$ln(\mathcal{T}) = ln(\mathcal{T}_0) - \Delta/T \tag{7.5}$$

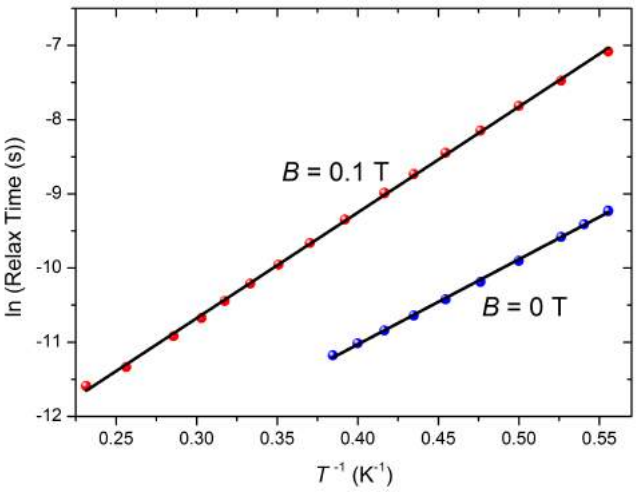

Figure 7.13: Temperature dependence of the relaxation time for Fe_4Ag at zero (blue) and 0.1 T (red) applied field.See text for results of the fit.

where all the symbols were already defined in Equation 6.2. For $B = 0\,\mathrm{T}$ we obtained $\mathcal{T}_0 = (1.65 \pm 0.08) \times 10^{-7}\,\mathrm{s}$ and $\Delta = (11.46 \pm 0.10)\,\mathrm{K}$, while for $B = 0.1\,\mathrm{T}$ we obtained $\mathcal{T}_0 = (3.21 \pm 0.11) \times 10^{-7}\,\mathrm{s}$ and $\Delta = (14.25 \pm 0.08)\,\mathrm{K}$. These value of the barrier is comparable to others extracted from Fe_4 systems in crystals [123] and also in 3D architectures such as gold nanoparticles connected by Fe_4 SMM [124].

Concluding, in this Section we have analysed a magnetic MOF that is formed by the link of Fe_4 cores thanks to organic ligand and Ag^+ atoms that acts as templating agents forming a diamond-like 3D structure. Taking advantage on the structural constrains, we have analysed the system using CTM to extract the value of the ZFS parameter that resulted to be in good agreement with the one obtained from *DC* magnetometry measurements. The CTM signals turned out to be precious to testify the goodness of the structure, that was difficult to solve due to solvent molecules inside the pores and local disorder. Also in this case the extreme sensitivity of CTM to anisotropy, as well as its insensitivity to isotropic contributions, resulted to be the key properties to map this system. This results open the

possibility to extend the CTM characterization to 3D extended molecular systems containing magnetic ions.

AUTHOR CONTRIBUTIONS AN, LR and CC synthesized the complex. CC fitted the experimental data of *DC* and *AC* magnetometry. MP (with the assistance of RS) performed the torque measurements and the fitting of the data. TR solved the structure, LS performed the EPR measurements, while WW and YL performed Micro SQUID measurements (not described in this Thesis). AC supervised the whole work.

7.3 Dy_6

Manuscript in preparation

Mapping a chiral spin structure using Cantilever Torque Magnetometry
M. Perfetti, I. Mihalcea, C. Anson and R. Sessoli

In this Chapter we will discuss the role of noncollinearity inside chain structures. We can consider a structure as a chain when the magnetic entities are connected by interactions (that in general are the chemical bonds) which define a direction in space. This does not mean that all the bonds must be parallel, but only that the structure develops on a certain spatial direction, so also zig-zag or helical structures must be included in this definition. As far as the chain is isolated, the system can be considered 1D, while if other chain are sufficiently close to interact, the system assumes a 2D or a 3D character, depending on the type of interactions. From the last decade, this class of materials attracted a growing interest mostly because the relaxation of the magnetization is normally less efficient than in 3D or 2D molecular magnets: the reason is that in a 1D system the spins have only one way to communicate. Nevertheless, this is true only for ideal chains, because defects and breaks in the chain act as crucial points for the relaxation [125, 126]. However, the slow relaxation of the magnetization is

not the only phenomenon that can attract interest in these materials, in fact it is possible to observe the so-called magnetochiral effect (MChE).

The interplay between chirality and magnetism is studied since the XXIX century [127] but is still a hot topic in solid state physics [128] because it is connected to a number of exotic phenomena such as magneto structural conductance [129] and skyrmions [130, 131]. To have the chance to observe MChE one must measure a compound that simultaneously breaks the parity (spatial) and the time reversal symmetry, that is in general possible either in magnetoelectrical media and multiferroics [132, 133] and in paramagnetic and diamagnetic systems if an external magnetic field is applied. Indeed the chirality is obviously parity ODD but time EVEN and the generation of a magnetic moment is parity EVEN and time ODD because angular momenta are characterized by a handed temporal motion, but reflections do not affect the sense of rotation. In literature are present only few studies on magnetic 2D and 3D structures [134, 135] and molecules [136, 137] that exhibit this behaviour and, at the best of our knowledge, only one report on a 1D system [138]. This last paper clearly confirms that in a chain the MChE is observable thanks to the measurement of two isostructural compounds containing Mn^{2+} and Co^{2+} ions spaced out by nitronyl-nitroxide radical ligands (MnPhOMe and CoPhOMe, respectively). It is interesting to notice here that the ligands that connects the metal ions *are not* chiral, but the interchain and intrachain interactions in CoPhOMe and MnPhOMe drive the packing to the chiral $P3_1/P3_2$ space groups. The major difference between these two systems is that Mn^{2+} is a d^5 ion (at the first order it has no orbital contribution) so that the spins must align with an external applied field while Co^{2+} has a d^7 external configuration (high magnetic anisotropy) that is mirrored in a noncollinear spin structure. This peculiarity makes MnPhOMe a suitable "blank" if the effect is observed by hard X-rays techniques that need an orbital contribution. As expected only CoPhOMe showed MChE, however it was not clear if the spin chirality played a significant role in the rising of the effect, or if it is dominated by structural chirality. This would require to investigate other model systems where the orbital contribution is present and can be tuned. In this regard

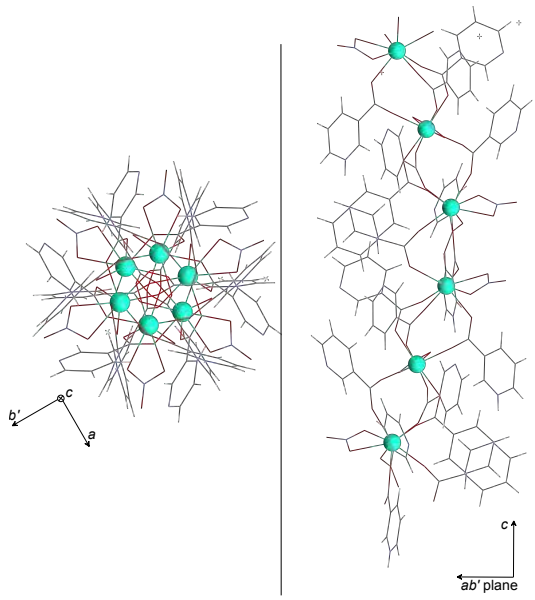

Figure 7.14: Position of the crystal at $\vartheta = 0°$ ($\boldsymbol{B}$ vertical, rotation clockwise) for Rot1 (left) and Rot2 (right). Green-Dysprosium, red-Oxygen, blue-Nitrogen, grey-Carbon, white-Hydrogen.

the Ln offer a sound alternative to TM ions because their compounds are often isostructural but the different electronic density around the metal mirrors in completely different magnetic anisotropy. In this way it is possible to vary the degree of spin chirality of the chain to investigate its role in the magnetochiral effect.

To investigate the role of spin chirality, is required a technique that can efficiently map the spin structure of a chain system. A previous estimation of the presence/absence of chirality can be obtained using a simple single crystal measurement using standard magnetometry because if the structure is collinear the value of the magnetization when the field is applied parallel to the chain axis is expected to be maximum and, conversely, is expected to be minimum if the field is applied perpendicular to the axis. In all the other cases a chiral structure is present, but the presence of more than one magnetic centre reported by symmetry (the exact number is related to the symmetry of the chain) complicates the interpretation of the results. In

this scenario CTM represents a useful technique for this kind of systems because with two convenient rotations it can provide a complete picture of the spin structure of the chain, even if definitive results can be obtained only if this analysis is flanked by theoretical calculations. Moreover it is important to remark that CTM exploits its maximum sensitivity for high magnetic fields, thus studies on chains can be performed only if the anisotropy is large enough to produce a detectable magnetic torque acting on the sample. This condition is hard to fulfil in chains formed by TM because the quenching of the orbital momentum due to the CF and the high values of the coupling constant between centres often produces zero-torque measurements. On the contrary, Ln-based magnet chains are very good systems to study, because of their electronic structure (see Section 2.2.2), but up to now the literature on this system is still scarce and mostly based on the chemical modification of the nitronyl-nitroxide ligand [139, 140, 141, 142, 143, 144, 145, 146, 147].

The compound analysed in this Section is a chain formed by ligands that coordinates Dy^{3+} ions: its formula can be described as $[Dy(HNA)(NA)_2(NO_3)]n$ where HNA is the nicotinic acid. Details about the synthesis, that was adapted from the previously reported analogues of Eu^{3+}, Gd^{3+} and Tb^{3+}, can be found in ref. [148]. Nevertheless to have a precise idea of the magnetic behaviour of this system it is mandatory to precisely describe, from a chemical point of view, the entire structure, that is reported in Figure 7.14. The metal ions are coordinated by 8 oxygen atoms (2 from the nitrate anion and 6 from the NA^- ligands) forming a triangular dodecahedral geometry with quasi-D_{2d} symmetry (best fit polyhedron obtained by Shape 2.0 [149]). The bridge between metal centres is provided by the 1,3 carboxylic moieties of the NA^- ligands that fix the distance between Dy^{3+} ions to ~ 4.8 Å. This is however not sufficient to completely suppress ferromagnetic interactions that were evidenced by *DC* measurements [150], that are anyway expected to be weak.

The hexagonally shaped crystals (dimension about $1 \times 0.1 \times 0.1$ mm) belong to the chiral $P6_1/P6_5$ space group and possess a C_6 axis parallel to the crystallographic c axis. Since the coordination sphere is exactly the

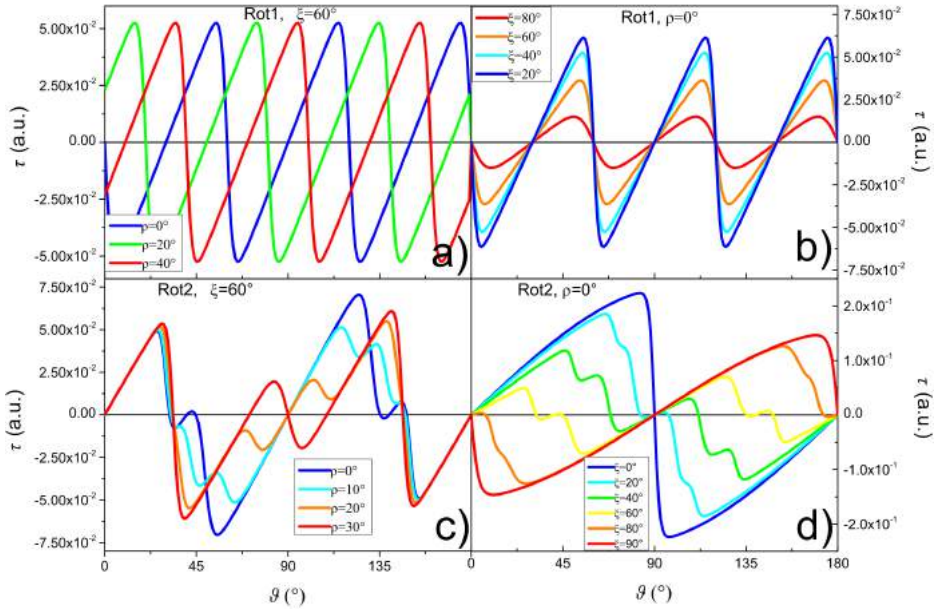

Figure 7.15: Simulations of the fitting curves for Rot1 (panel a and b) and for Rot2 (panel c and d) varying the two relevant Euler angles. In all graphs $T = 2\,\mathrm{K}$ and $B = 7\,\mathrm{T}$.

same for all the metal ions the chain can be considered formed by only six independent Dy atoms, that are related by the C_6 axis of the helix. The smartest way to map this spin structure using CTM is to perform two rotations: Rot1 using the c axis as rotation axis and Rot2 othogonal to Rot1 (see Figure 7.14).

Since the final goal of the measurements was to map the spin structure, we decided to use the Y-doped analogue of Dy_6, with nominal formula $Y_{0.82}Dy_{0.18}$ (hereafter $(DyY)_6$), in this way all the interactions between centres are reasonably quenched. Before entering into the details of the shape and intensity of the curves, we need to explain the adopted fitting procedure, that is based on the simple Hamiltonian:

$$\mathcal{H} = g_L \mu_B \boldsymbol{J} \cdot \boldsymbol{B} + b_2^0 \boldsymbol{O}_2^0 \tag{7.6}$$

The parameters that we let free to adjust are four: two Euler angles (ρ

and ξ) that connects the crystallographic rf to the molecular one, an axial CF parameter (b_2^0, using the Stevens notation) and the usual scale factor (f_{sc}) necessary to take into account the number of spins inside the crystals. Note that we used only one CF parameter to avoid overparametrization, so its value must be carefully taken as a qualitative estimation, in particular we will focus on its sign, that determines the shape of anisotropy (easy axis or easy plane).

In Figure 7.15, we reported the simulated torque curves for Rot1 (panel a and b) and Rot2 (panel c and d) fixing $f_{\mathrm{sc}} = 0.001$ and $b_2^0 = -0.635$: in this way we only focused on the role of the Euler angles during the two rotations. The angle ρ is the one between the a axis and the projection of the unique axis of the spins in the ab plane, while the angle ξ is the one between the chain axis and the direction of the spins.

Panel a indicates the role of the angle ρ during Rot1 when ξ is fixed, that is the shifting of the entire curve (that always exhibit three peaks in the 0-180° angular range), moreover panel b testifies that a variation of ξ if ρ is fixed does not affect the shape of the curve but only its intensity. As a consequence, the angle at which the curves go to zero for the first time is directly the angle ρ of the fit (formally it is $\rho + 60°$ but due to the C_6 symmetry of the molecule this two values are equivalent), that in fact refers to a rotation along the c axis (see Section 4.5).

Panel c and d indicates instead the role of the angles ρ and ξ on Rot2, respectively. However, since ρ can be fixed using Rot1, Rot2 becomes sensitive only to ξ that can assume values between 0° (spins parallel to the chain axis) and 90° (spins perpendicular to the chain axis). It is important to notice that, besides 0° and 90° that remains zeroes in any case, the other angles at which the torque changes sign and also the intensity of the peaks is dependent on the value of b_2^0, but the relative height of the peaks in this rotation is directly related to ξ.

In Figure 7.16 we reported the experimental data obtained during each rotation. The structure of the curves recorded during Rot1, that exhibit 3 equivalent maxima (minima) in the 0-180° angular range is clearly indicative that the rotation axis is indeed a C_6 axis, as expected. Conversely, Rot2

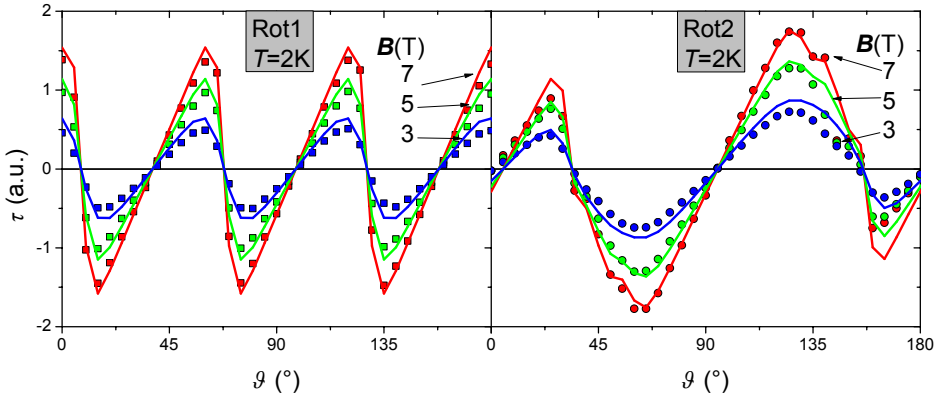

Figure 7.16: Experimental data (squares or circles) and fits (lines) obtained in Rot1 (left) and Rot2 (right) at $T = 2\,\mathrm{K}$.

exhibit two distinct maxima of different intensity. This is indicative of the fact that the spins inside the chain are not pointing along the chain axis (already proven by Rot1), neither perpendicular to it, which means that the spin structure is chiral. The obtained best fit parameters were: $\rho = 8(1)^\circ$, $\xi = 61(1)^\circ$, $b_2^0 = -0.292(3)\mathrm{cm}^{-1}$, $f_{\mathrm{sc}} = 0.028(5)$. It is important to notice that, while the angle ξ is unique for all the spins, there are six possibilities for the angle ρ, related by the C_6 symmetry of the chain. This leads to an unsolvable ambiguity in the assignment of the director cosines for each spin, however it does not affect the conclusion that the chain is indeed chiral, because it is strictly dependent only on the value of the angle ξ.

To estimate the goodness of our results we have performed two independent checks: the experimental measurement of M vs B curves of a single crystal with the field parallel and perpendicuar to the chain axis and a simple theoretical calculation based on the sofware MAGELLAN [60]. The experimental curves obtained on a single crystal of Dy_6 are reported in Figure 7.17. The magnetization recorded with the field perpendicular to the chain axis has slightly higher values then the other, as expected for an angle between c and spins moderately larger than the magic angle (54.7°). Moreover, the simple calculation based on electrostatic considerations per-

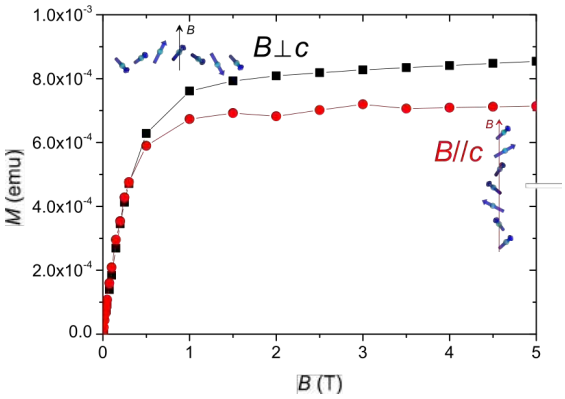

Figure 7.17: M vs B curves recorded at $T = 2\,\mathrm{K}$ on a single crystal of Dy_6.

formed by the sofware MAGELLAN [60], provides the director cosines of the easy axis of the Dy^{3+} ions, and thus the Euler angles associated to them. The result of the calculation, when transformed to Euler angles, gave: $\rho_{\mathrm{Mag.}} = 0°$ and $\xi_{\mathrm{Mag.}} = 57°$, in good agreement with the ones extracted by CTM. Finally, in Figure 7.18 we graphically report the results obtained with CTM selecting the solution more similar to the one extracted by MAGELLAN [60].

Concluding, we have correctly obtained for the first time the orientation of the easy axis of a chiral chain formed by Dy^{3+} atoms using CTM. The results obtained by CTM where validated thanks to *DC* standard measurements and theoretical calculations. The technique was therefore proved to be useful to obtain information at the single ion level also in extended structures containing Ln. The ensemble of these results drew a precise picture that labels the spin structure of this system as chiral, nominating this molecule as a promising candidate to investigate the presence of magnetochiral effect in Ln compounds.

AUTHOR CONTRIBUTIONS IM and CA synthetized the complex. MP performed the torque measurements and wrote the program to fit the data with assistance of RS.

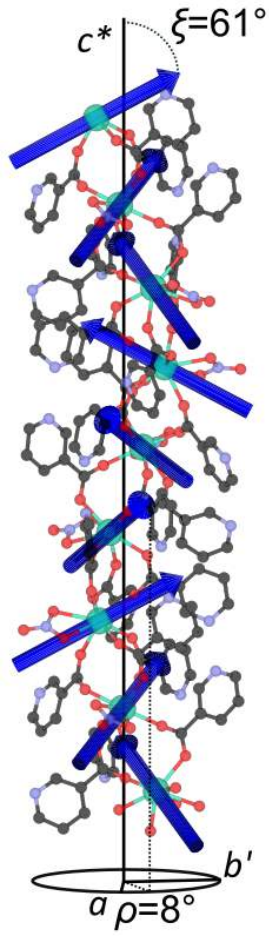

Figure 7.18: Relevant Euler angles found for $(DyY)_6$. Color code: Dysprosium-green, Carbon-black, Oxygen-red, Nitrogen-blue, Hydrogen atoms were omitted for clarity. The easy axis are presented as blue arrows to facilitate the reader.

8 Films

Manuscript in preparation

Molecular order detected on a film of $TbPc_2$ by torque magnetometry
M. Perfetti, M. Serri, L. Poggini, M. Mannini, S. Heutz, P. Sainctavit and R. Sessoli

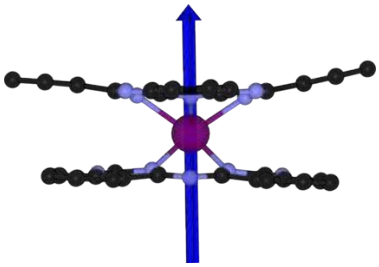

Figure 8.1: $TbPc_2$ structure. The blue axis refers to the easy anisotropy axis of the molecule, that is approximately orthogonal to the planes of the phtalocyanine ligands. Color code: violet-terbium, black-carbon, light blue-nitrogen, hydrogens were omitted for clarity.

As already mentioned in Section 2.2.2, the discovery of the high barrier for the reversal of the magnetization ($\sim 400\,\mathrm{K}$) of Terbium Bis-Phtalocyaninate ($TbPc_2$) has to be considered a real revolution in the field of molecular magnetism and because of that tens of papers have been published on similar derivatives. The structure of $TbPc_2$ is reported in Figure 8.1: a central Tb^{3+} ion is surrounded by two phtalocyaninato ligands that are able to complex the metal using the 4 Nitrogen atoms of the ring [151] forming a double decker complex. The Nitrogen of the rings that coordinates the metal are in an staggered configuration, thus the 8-fold

coordinated geometry around the Ln can be approximate to a D_{4d} local symmetry, very useful to reduce the number of CF parameters involved in the description of the magnetic behaviour of this system, that behaves as a strongly Ising system with the unique axis parallel to the pseudo C_4 axis. Even if historically the first studied form of the complex was the monoanionic, the charge of the complex can be easily varied using electrochemical techniques [152, 153]. In particular the degree of magnetic axiality of the neutral form is expected to be similar (slightly higher) than the monoanionic form [154]. This is extremely useful for any application involving this complex [155] because the neutral form can be evaporated allowing deposition on a large number of different substrates ranging from metals [156, 157, 158], to organic molecules [159] and to oxides [158, 157].

The organization of molecules on a surface is ruled by a number of different factors (interaction with the substrate, intermolecular interactions, rate and method of deposition, etc.) that can be often difficult to predict, even if their knowledge is a mandatory requirement for the implementation of these molecules inside any device. Up to now it is known that $TbPc_2$ *does not* assume the same orientation on all the substrates. This can be justified by a simple chemical analysis: an electron reach (*e.g.* metals) or highly conjugated (*e.g.* graphene) surface can efficiently interact with the planes of the phtalocyanine rings, forcing the molecules to assume a *flat* configuration (easy anisotropy axis perpendicular to the substrate), while oxides have only a minor interaction with the molecules that tend to interact via π-π stacking, assuming a stand configuration (easy anisotropy axis parallel to the plane of the substrate).

In Figure 8.2 we reported the simulation of the torque for a film of collinear $TbPc_2$ molecules in a stand (black line) and in a flat configuration (grey line). The curves, that were reported in a 0° to 180° angular range because of the typical periodicity of torque measurements, vanish at 0° and 90° as expected for paramagnets with the easy direction parallel or perpendicular to the surface. Moreover the variation of the torque is more rapid near 0° for the flat configuration and near 90° for the stand configuration, according to the theory (see Section 4.1). The simulations

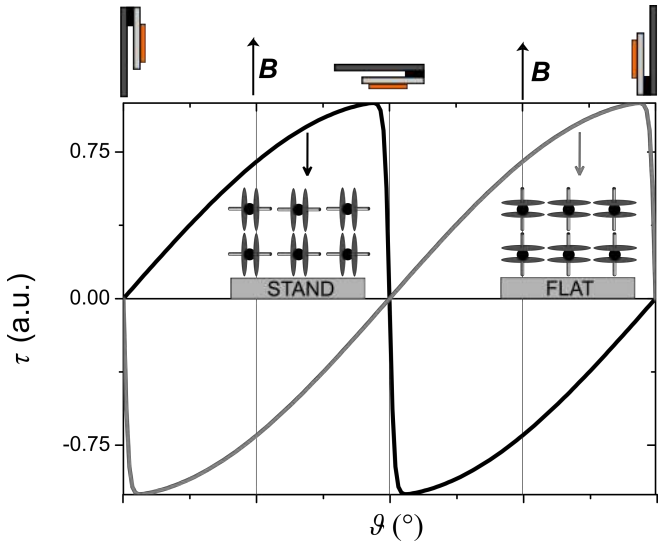

Figure 8.2: Normalized simulation of the torque profile of a $TbPc_2$ film in a perfectly stand (black line) and perfectly flat (grey line) orientation. The upper part indicates the position of the sample (orange slab) during the rotation.

were obtained using a Spin Hamiltonian that includes the Zeeman term and three diagonal CF parameters taken from ref. [151]. As discussed before, the use of parameters that refer to the anionic form of the complex ($TbPc_2^-$) is well-justified by the strong axiality of the complex in all its oxidation states and by the low temperature conditions of our experiments, however to prove that we have performed some simulations varying the used set of diagonal Stevens parameters (±50% from ref. [151]) obtaining in all cases almost superimposable curves.

Reuniting all the data reported in literature, we can thus conclude that $TbPc_2$ is the ideal candidate for a study with the purpose to determine the preferential orientation of the molecules evaporated on different surfaces. We choose three substrates that can be considered representative of the most investigated class of surfaces: gold (Au) for metals, glass (SiO_2) for oxides and perylene-3,4,9,10-tetracarboxylic dianhydride (PTCDA) for conjugated organic molecules.

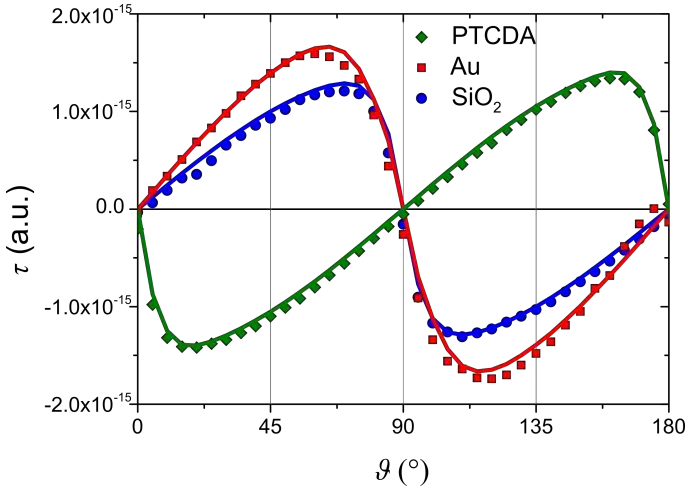

Figure 8.3: Experimental (symbols) and fitted (lines) curves for a film of $\sim 100\,\mathrm{nm}$ of $TbPc_2$ on different substrates (see legend). All the simulations and experiments where performed at $T = 2\,\mathrm{K}$ and $B = 12\,\mathrm{T}$. The experimental data are rescaled for a cube of volume $= 1\,\mathrm{nm}^3$.

In Figure 8.3 we reported the experimental data recorded at $T = 2\,\mathrm{K}$ and $B = 12\,\mathrm{T}$ for films of $TbPc_2$ evaporated on the chosen substrates: Au (red), glass (blue) and PTCDA (green). The height of the film, estimated by Atomic Force Microscopy measurements, was 80(2)nm on Au and SiO_2 and 105(10)nm on PTCDA. Comparing the experimental data in Figure 8.3 with the simulations in Figure 8.2 it is trivial to identify at a first glance that the preferential order of the molecules is flat on PTCDA and stand both on SiO_2 and Au. This is a clear indication of a different influence of Au and PTCDA as substrates, indeed the interaction between molecules and Au is not sufficient to maintain the flat orientation for high thickness, while the templating effect of PTCDA revealed to be far more powerful, influencing the order of the molecules even after hundreds of layers. The shape of the simulated curves in Figure 8.2 *is not* the same as the measured ones, indeed the variation around the hard zero is less abrupt in the experimental curves, indicating a the presence of a partial noncollinearity in the orientation of the molecules in the films.

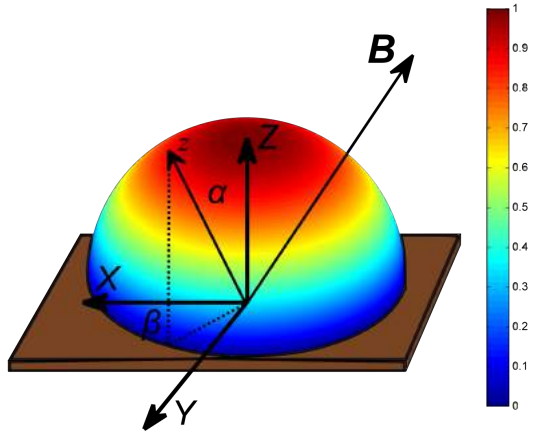

Figure 8.4: Definition of the components of a general vector (z) identifying the easy axis of a molecule using two polar angles α, β. The color scale is a guide for the eye and defines the probability (centred in this case on a perfectly flat molecule) to find a molecule in a certain orientation.

To have a quantitative estimation of the degree of the disorder we assumed isotropy in the plane of the film so that the normal to the substrate is a symmetry axis. In Figure 8.4 we have reported a hemisphere to represent all possible orientations of the anisotropy axes of the molecules on the substrate (note that a complete sphere would be redundant due to the symmetry of the anisotropy tensor). The color scale is useful to recall that the probability to find a molecule has to fulfil the symmetry of the system. According to this model, the angular distribution of the molecules on the substrate can be described using a polar angle, α, and an azimuthal one, β, that take into account for all possible orientations of a uniaxial system like $TbPc_2$ with respect to the magnetic field. Note that, for a fixed α the calculation *must* include all the orientations with $0° \leq \beta \leq 180°$ because molecules with values of β wich differ by 90° *do not* give the same torque signal (see also panel c of Figure 8.5). For a fixed couple of polar angles, we calculated the torque curve that was then multiplied by a weight factor that depends only on the angle that the easy axis of

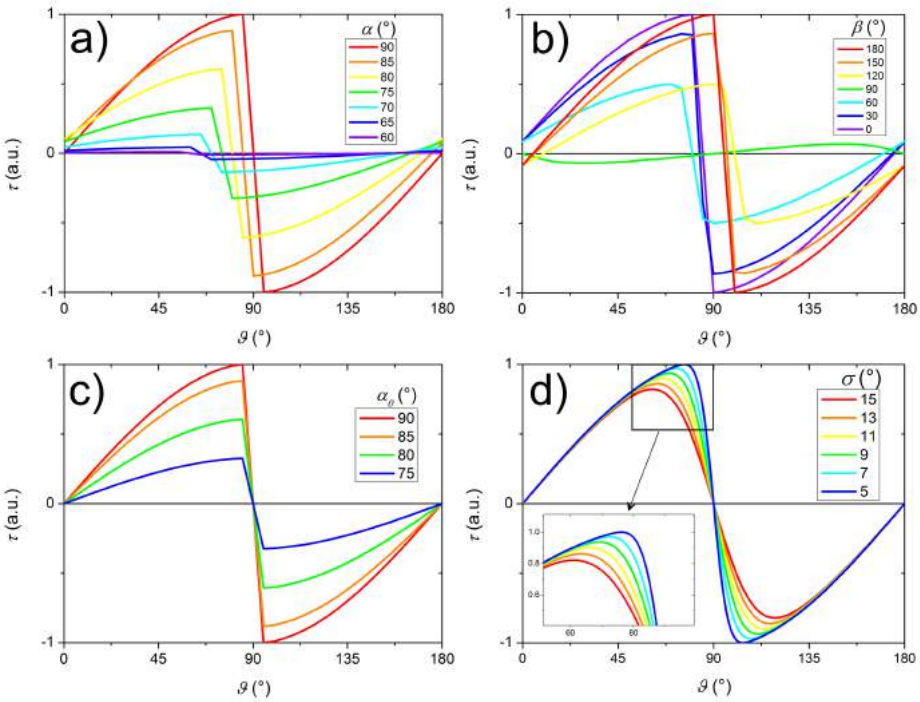

Figure 8.5: Influence of the different angular parameters on the shape of the torque curves. Panel a): α =60° to 90°, $\beta = 0°$, $\sigma = 7°$, $\alpha_0 = 90°$. Panel b) $\alpha = 90°$, $\beta = 0°$ to 90°, $\sigma = 7°$, $\alpha_0 = 90°$. Panel c): $\alpha = 90°$, $\beta = 0°$, $\sigma = 7°$, $\alpha_0 = 75°$ to 90°. Panel d): $\alpha = 90°$, $\beta = 0°$, $\sigma = 5°$ to 15°, $\alpha_0 = 90°$.

that sampled molecule makes with the preferred direction. This factor was identified as the width (σ) of a simple Gaussian distribution centred on the most probable orientation (α_0). The fitting of this last parameter is particularly important for very thin films (see after) because studies on free phtalocyanine [160] and on complexes with TM ions of general formula MPc [161, 162] revealed a small tilting angle between the surface and the plane of the phtalocyanine ring (about 7° for metal surfaces). Besides α_0 and σ, we fitted also the usual scale factor (f_{sc}) that was necessary to reproduce the intensity of $\boldsymbol{\tau}$.

In Figure 8.5 we have simulated the effect of all the quantities that can be varied during the fit (except the trivial f_{sc}). Panel a and b refer to the

variation of the polar angle (α) when all the other quantities are constant. In this particular case we choose a relatively narrow distribution (that well fits with the real samples, see after) $\sigma = 7°$ centred on a molecule with the easy axis parallel to the surface ($\alpha_0 = 90°$) and to the field (β =0°) at the beginning of the rotation. The most relevant effects are the shift of the entire curve, indeed the value of α determines the angle at which the field is parallel to the easy axis of the molecule, and a strong damping, due to the low probability to find molecules with orientation very different from the central one. This last factor was taken into account by multiplying the curves by the value of the Gaussian distribution as a function of the solid angle between the considered easy axis and the central one, and is strongly dependent on the value of the width of the distribution. In panel b we represented the effect of a variation of β on a molecule with $\alpha_0 = 85°$ and $\sigma = 7°$. The effect of the azimuthal angle is to damp, shift and deform the curves (some of these effect can be partially or totally quenched for particular values of α). For values β near 90°, the curves begin to be strongly damped and deformed. When this angle is exactly 90° the torque curve has opposite trend comparing to the others, however this effect is only poorly relevant due to the low weight of these contributions. Due to the symmetry of the system, values of $\beta \geq 90°$ must be taken into account because they have opposite effect on the curves with respect to values $\leq$ 90°. Panel c and d refer to the parameters that were effectively fitted. As reported in panel c the *only* influence of a distribution not centred on molecules perfectly stand is to damp the curve (same conclusion can be obtained for molecules perfectly flat). This is of paramount importance for our fits because it warns about the possibility to have a collective tilt of the molecules. Finally, panel d casts light on the influence of the width of the distribution, that is to damp and to deform the curves shifting the maximum toward 45° (and the minimum toward 135°). This last characteristic is peculiar of σ, and gives an estimation of the degree of disorder in the film.

The shape of the curves reported in Figure 8.3 gives a preliminary indication concerning the values of α_0 that is expected to be near 0° for

the sample on PTCDA and near 90° for the sample on Au and SiO_2. The obtained fits are reported as solid lines in Figure 8.3. As expected, the most probable orientation of the molecules is almost flat for the sample on PTCDA and almost stand in the other two cases, with relatively narrow distributions in all the samples. The scale factor is of the order of the unit for all samples. It should be noted that the unavoidable incertitude on the mass of measured samples could hamper the detection of a fraction of molecules that are not oriented at all and therefore do not contribute to the magnetic torque. As discussed later, synchrotron investigations performed to validate our CTM method allow to exclude the occurrence of a significant fraction of disordered molecules.

After the successful characterization of layers of $TbPc_2$, we decided to fully exploit the high sensitivity of CTM to magnetic anisotropy to study the order of the molecules as a function of the growth of the film. In practice, we evaporated a layer of $TbPc_2$ at a certain height on a film formed by YPc_2, its isostructural and isotropic analogue. In fact, even if YPc2 carries an unpaired electron, no torque was detected on films of 85 nm on Au. In this way we were able to efficiently map the order of the molecules at different positions from the surface, using the anisotropy of $TbPc_2$ as a local probe. We analyzed four samples, named in relation to the position of the $TbPc_2$ layer: TOP (~ 10 nm of $TbPc_2$ on top of ~ 50 nm of YPc_2), MIDDLE (~ 10 nm of $TbPc_2$ between two layers of ~ 20 nm of YPc_2), BOTTOM (~ 5 nm of $TbPc_2$ covered by ~ 50 nm of YPc_2) and ULTRA BOTTOM (~ 2 nm of $TbPc_2$ covered by ~ 50 nm of YPc_2). A sketch of the composition of the samples is reported inside each graph of Figure 8.6, while the best fit results for all the samples are reported in Figure 8.7.

Summing up all the information we can extract from Figure 8.6, it is possible to reconstruct the preferential order of the molecules on the three investigated substrates. Considering all the samples grown on SiO_2, we can argue that on this substrate the molecules assume an almost stand configuration that is maintained from few nm up to 80 nm as reported in literature. The values of the best fit parameters clearly show that the

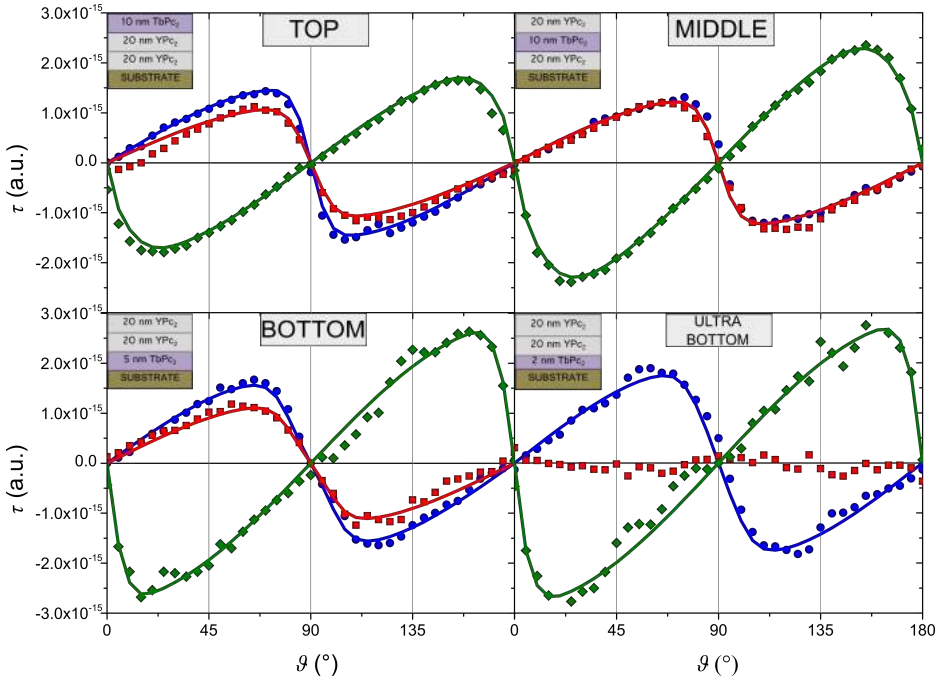

Figure 8.6: Torque signal obtained for three different position of the layer of $TbPc_2$ with respect to the YPc_2 (TOP, MIDDLE and BOTTOM). The ULTRA BOTTOM sample is a very thin layer ($\sim 2\,nm$) of $TbPc_2$ covered by YPc_2. All the data were rescaled for a volume of $1\,nm^3$.

molecules near the surface are more disordered than at high distance, as testify by the decreasing values σ (and the values of α_0 that became closer to 90°) going from ULTRA BOTTOM to TOP samples, probably because the interaction between the molecules and the surface atoms is not sufficiently strong to efficiently order the molecules. Conversely, at high distances the π-π stacking interactions between rings are the only relevant forces that can act between molecules, adding order to the film. The stand configuration is also characteristic of molecules on Au for all the investigated samples, except for the ULTRA BOTTOM that had no signal at all. This is not surprising because many reports have shown that $TbPc_2$ on Au assumes a flat configuration for few layers and the

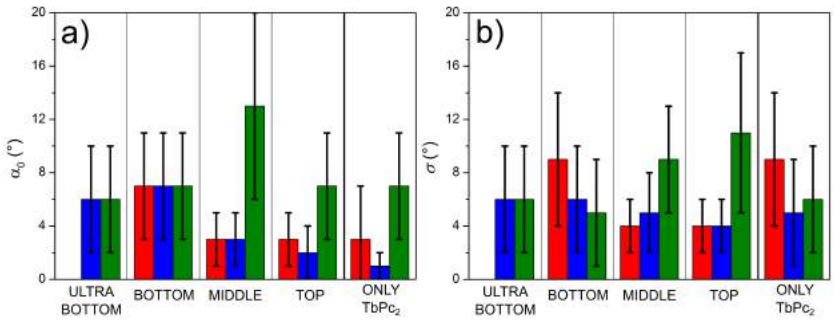

Figure 8.7: Graphical view of the extracted best fit parameters for all the measured samples. Panel a): α_0, panel b): σ. To compare all the values of α_0, for Au and SiO_2 we plotted in panel a) the deviation from a "perfectly stand" molecules $(90 - \alpha_0)$.

stand configuration for high thickness. Since the BOTTOM sample has a low signal, and its shape indicates a preferential stand configuration, we can argue that the reorientation process of the molecules on Au occurs in very few layers, so that the layers comprised in a film of thickness of 2 nm result to be completely disordered. Also σ of the fits support this conclusion since it decreases for the samples with the $TbPc_2$ layer very far from the surface, as in the case of SiO_2. The order of molecules has an opposite trend for PTCDA, going from $\alpha_0 = 6°$ and $\sigma = 6°$ of the ULTRA BOTTOM sample to $\alpha_0 = 7°$ and $\sigma = 11°$ of the TOP sample (the spike of the MIDDLE sample in the centre position, that is in any case inside the trend considering the error bar, can be attributed to experimental problems in the deposition). This indicates that the templating effect of PTCDA is only modestly perturbed even for films of ~ 100 nm. In Figure 8.8 we draw two hemispheres to graphically represent the orientation of the molecules on Au or SiO_2 (left) or on PTCDA (right). We choose a medium value between all the investigated samples (that are however very similar between them), using $\alpha_0 \sim 7°/83°$ and $\sigma \sim 7°$. Note that the highest probability *is* near, but not exactly, at the pole or at the equator of the hemispheres due to the value of α_0. Moreover the low value of the width assures to find the molecules with high probability in a very tiny region of

the space, that is near the equator (quasi-stand configuration) for Au and SiO_2 and near the pole (quasi-flat configuration) for PTCDA.

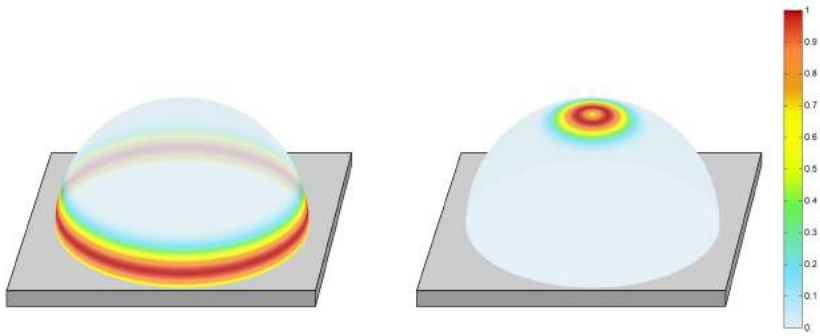

Figure 8.8: Preferential order of $TbPc_2$ on SiO_2 and Au (left) and on PTCDA (right). The color scale refers to the weight that has been assigned to a certain orientation of the easy axis of the molecule.

To have a further confirmation of the results that we obtained using CTM, we characterized some selected samples using synchrotron radiation. Even if this synchrotron characterization was not the subject of this Thesis, it is interesting to anticipate here some results for a quick comparison. At the ID32 beamline in ESRF we recorded the X-ray Natural Linear Dichroism (XNLD) at the $M_{4,5}$ edge of Tb. XNLD is a powerful element-selective tool to investigate the environment of the probed chemical species and, if associated to the Total Electron Yield detection mode, it is also sensitive to the upper few nm of the material [163]. Moreover XNLD signal can be renormalized to the isotropic X-ray absorption (Aiso). In this way significant fraction of fully disordered species can be easily detected through a decrease of the XNLD/Aiso ratio. A sample of the TOP category, i.e. constituted by ∼10 nm of $TbPc_2$ deposited on ∼50 nm of YPc_2 using PTCDA on Si as a substrate presented a XNLD/Aiso of 53 % (measured with the sample at 45° from the X-rays beam). The sign and shape of the XNLD signal well compares with that calculated for lying $TbPc_2$ molecules. From a quantitative point of view the value of 53% has to be compared to the theoretical one estimated for an ideal flat orientation of

$TbPc_2$ molecules (69%) and with the experimental one (54%) measured in a monolayer of $TbPc_2$ deposited on Au [157]. This rough preliminary analysis of the synchrotron data fully confirms the reliability of the CTM in detecting the orientation of the MPc_2 molecules in evaporated films.

This study clearly testifies that using CTM the anisotropy of the single molecule can be used as a local probe to investigate the orientation of the molecules in contact with a surface and as a function of the thickness of the film. This work, performed on $TbPc_2$ due to its well-known magnetic properties, can be easily extend to other systems containing anisotropic metal ions. It is important to remark that not only Ln can be used [164], but also TM if the anisotropy (both easy axis or easy plane) is strong enough: in this regard a good candidate could be the FePc complex [165]. The study can be also extended to materials containing more than one layer of molecules (*e.g.* spin transistors), even if a simple treatment can be used only if just one type of anisotropic molecule is present. Finally, CTM measurements on oriented films of systems could efficiently flank other magnetic measurements, like AC measurements, to investigate the influence of the collinearity of anisotropy on the dynamics of the relaxation of the magnetization.

AUTHOR CONTRIBUTIONS MS and SH prepared all the samples that MP measured using CTM. MP and RS wrote the program to fit the data. PS, LP, MM, RS and MS performed the synchrotron characterization.

9 Conclusion

The main purpose of this Thesis was to deeply investigate the presence of magnetic anisotropy in molecular systems containing magnetic metal ions. In this regard we found the Cantilever Torque Magnetometry experimental technique particularly suitable because of its extreme sensitivity to the presence of anisotropic sources inside a sample. This last feature allowed to investigate the magnetic anisotropy of lanthanide ions up to room temperature allowing not only to characterize the magnetic anisotropy of the lowest states of the J manifold but to gain precious information on the Crystal Field splitting. Moreover the different response of anisotropic paramagnetic materials in the low and high field regimes was precious to examine systems containing more than one contribution to magnetic anisotropy. For systems with a large number of noncollinear contributions the interpretation of the data is far more complicated, but we have developed a code that is able to simultaneously take into account all the entities, related by the crystal symmetry. Despite a definite identification of the principal direction of anisotropy is straightforward only for collinear systems, we have proven that in several cases, adding simple geometrical constrains, it is possible to reach the correct solution. Anyhow, if this ambiguity cannot be solved only with Cantilever Torque Magnetometry, a number of different theoretical approaches can efficiently lead to a certain answer. Concerning the nature of the investigated metal ions, we have revealed that all the magnetic ions can be investigated without any exception, even if highly anisotropic complexes of lanthanides and clusters of metal ions with high value of the total spin are particularly suitable to fully exploit all the advantages of this technique. This peculiar characteristic opens the perspective to investigate magnetic samples that are also useful for a fan of applications ranging from

catalysis and gas storage (e.g. Metal Organic Frameworks) to quantum computation and spintronics (e.g. Spin Qubits, Single Molecule Magnets). In our study we also overreached the common use of the technique, that in molecular magnetism is limited to single crystals, investigating the anisotropy of thin films evaporated on different substrates. Besides the successful characterization of a film composed by only magnetic molecules, we pushed the sensitivity of the technique at its limit using magnetic anisotropy as a local probe to monitor the orientation of molecules on a surface as a function of the thickness of the film. This last study opens the possibility to use this technique to investigate the growth of films of anisotropic molecules (and also of similar isotropic/non magnetic species) as well as to probe the orientation of these molecules inside multilayers or devices. We expect that this thesis work, where the potentialities of this simple but powerful technique have been explored on a wide range of molecular materials, and the related publications will boost its diffusion among the molecular magnetism community. A careful characterization of the magnetic anisotropy of these materials is necessary to design successful strategies to improve the performances of molecular materials and make them really competitive in a wide range of applications.

Appendix - Published papers

ChemComm

COMMUNICATION

View Article Online
View Journal | View Issue

Cite this: *Chem. Commun.*, 2014, **50**, 1648

Received 20th November 2013,
Accepted 5th December 2013

DOI: 10.1039/c3cc48866g

www.rsc.org/chemcomm

Beyond the anisotropy barrier: slow relaxation of the magnetization in both easy-axis and easy-plane Ln(trensal) complexes†

Eva Lucaccini,[a] Lorenzo Sorace,*[a] Mauro Perfetti,[a] Jean-Pierre Costes[b] and Roberta Sessoli[a]

We present a spectroscopic and magnetic (both static and dynamic) characterization of two isostructural Dy and Er complexes evidencing that, despite the different types of magnetic anisotropy, the two molecules show similar slow relaxation of the magnetization in a static magnetic field.

The number of mononuclear lanthanide complexes reported to show slow relaxation of the magnetization at low temperature has increased very rapidly after the seminal report of Ishikawa on terbium-phthalocyaninate,[1] making this one of the most studied subjects in molecular magnetism.[2] Despite the efforts and the achievements obtained to date, many open questions remain on the behaviour of these molecules, which need to be rationalized if one wishes to improve their properties in term of the blocking temperature. In particular, the relaxation processes characterizing these systems are often more complex than assumed. With the exception of few reports,[3,4] the slow relaxation of the magnetization is usually attributed to an Orbach mechanism[5] even if further experimental or theoretical confirmation is not available. However, the clarification of the different dynamics reported so far and the exploration of the different pathways for magnetic relaxation require a detailed picture of the electronic structure of these systems. Experimentally, this can only be obtained by using a combined spectroscopic and magnetic characterization of structurally simple systems.[6]

Following this approach, we present here the results obtained by a combined magnetic, Electron Paramagnetic Resonance (EPR) and Crystal Field (CF) analysis, on mononuclear lanthanide complexes having the formula Ln(trensal) (where H_3trensal = 2,2′,2″-Tris-(salicylideneimino)triethylamine) which feature crystallographically imposed trigonal symmetry (Fig. 1, inset and Fig. S1 and S2, ESI†).[7] This series represents an ideal system for correlating the magnetization dynamics with the magnetic anisotropy because C_3 symmetry, preserved at liquid helium temperature,[7b] reduces the number of CF parameters to be determined to describe their electronic structure. These are known with great accuracy thanks to the high quality luminescence spectra which were previously analysed and reproduced for most of the derivatives in the series.[7b] In the following we will focus on Er^{III} (**1**) and Dy^{III} (**2**) derivatives, since both these ions show a ground $J = 15/2$ state but, according to phenomenological approach popularized by Long, should behave differently in terms of the low temperature dynamics.[2b]

We first analyzed the χT *vs.* T curves (Fig. 1): the room temperature values are in agreement with those expected for the $^4I_{15/2}$ and $^6H_{15/2}$ multiplets of Er^{III} and Dy^{III}, while the observed temperature dependence can be attributed to the progressive depopulation of the excited sublevels. To evaluate if this behaviour is in agreement with the CF parameters reported in ref. 7*b* (Table S1, ESI†) we used the home-developed software EVALUCF.[8] Here the effect of the CF over the different multiplets, arising from the spin–orbit splitting of the ground term of each rare-earth, is calculated

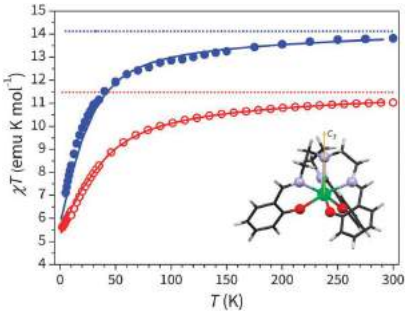

Fig. 1 Temperature dependence of the χT product for **1** (empty circles) and **2** (full circles), along with theoretical curves calculated by using the CF parameters reported in ref. 7*b*. Dashed lines correspond to the expected free-ion χT values. In the inset the molecular structure of Ln(trensal) is sketched, evidencing the trigonal symmetry.

[a] *Dipartimento di Chimica "U. Schiff" and UdR INSTM, Università di Firenze, Via della Lastruccia 3-13, Sesto Fiorentino(FI), Italy. E-mail: lorenzo.sorace@unifi.it; Fax: +39 0554573372; Tel: +39 0554573336*

[b] *Laboratoire de Chimie de Coordination 205, route de Narbonne 31077 Toulouse, Cedex 4, France*

† Electronic supplementary information (ESI) available: Synthetic procedure; experimental setup; Powder X-ray diffractograms; EPR spectra; isothermal magnetization curves, original *ac* susceptibility data. See DOI: 10.1039/c3cc48866g

using the appropriate Hamiltonian in the Wybourne formalism,[9] which for C_3 symmetry is:†

$$\hat{H}_{CF} = B_0^2\boldsymbol{C}_0^2 + B_0^4\boldsymbol{C}_0^4 + B_3^4\left(\boldsymbol{C}_{-3}^4 - \boldsymbol{C}_3^4\right) + B_0^6\boldsymbol{C}_0^6 + B_3^6\left(\boldsymbol{C}_{-3}^6 - \boldsymbol{C}_3^6\right) + iB_3'^6\left(\boldsymbol{C}_{-3}^6 + \boldsymbol{C}_3^6\right) + B_6^6\left(\boldsymbol{C}_{-6}^6 + \boldsymbol{C}_6^6\right) + iB_6'^6\left(\boldsymbol{C}_{-6}^6 - \boldsymbol{C}_6^6\right) \quad (1)$$

The energy difference between the different multiplets was phenomenologically adjusted to correctly reproduce the results reported in ref. 7*b*, and the final diagonalization provided the eigenvalues and eigenvectors in terms of the $|J, M_J\rangle$ components. The effect of a magnetic field was then evaluated over a 55 point grid to obtain the powder average susceptibility at different temperatures.[8] This approach, without any free parameters, reproduced very well the experimental curves for both derivatives, lending further support to the correctness of the parameter set.

The resulting energy patterns for the two ground multiplets are reported in Table 1: a gap of 54 and 50 cm^{-1} is calculated between the ground and first excited doublets for **1** and **2**, respectively. The corresponding ground state wavefunctions are characterized in both cases by large mixing of different $|M_J\rangle$ (Table 1 and Fig. S3, ESI†). By calculating the effect of the magnetic field over the energy levels of the two complexes we could calculate the effective *g* values for the ground doublets of the two derivatives as $g_\perp^{eff} = 1.2$, $g_\parallel^{eff} = 13$ for **1** and $g_\perp^{eff} = 9.6$, $g_\parallel^{eff} = 2.6$ for **2**. Experimental confirmation of this estimate could be obtained by EPR spectroscopy on microcrystalline powder samples, both at X- and W- band (Fig. 2 and Fig. S4, ESI†), which confirmed the expected trend, with **1** being the easy axis ($g_\parallel = 11.8 \pm 0.4 > g_\perp = 3.6 \pm 0.1$) and **2** the easy plane ($g_\perp = 9.4 \pm 0.5 > g_\parallel = 1.8 \pm 0.1$). The observed *g* values for **1** are also in agreement with the saturation value of the *M vs. H* curve, slightly higher than the calculated one (Fig. S5, ESI†). At any rate, the combined luminescence, EPR and *dc* magnetic analysis provided a sound quantitative description of the electronic structure of these systems, evidencing the different character of the magnetic anisotropy of the two derivatives, as expected on the basis of the prolate and oblate charge distribution of the two ions.[2b,10] Since **1** is an easy axis system with a non-negligible gap between the ground and the first excited doublet, it may be expected to show slow relaxation of the magnetization at low temperature with an Arrhenius like dependence of the relaxation rate, while **2** should not.

Table 1 Energies of the 8 doublets of the $J = 15/2$ multiplets calculated with the CF parameters reported in ref. 7*b*, and corresponding composition of ground doublets. Contributions lower than 5% are not reported. See ESI for more details

Energies (cm^{-1})								
1	0	54	102	109	321	568	619	651
2	0	50	98	172	414	577	645	787

Amplitude of $\|M_J\rangle$ contributing to ground doublets	
1	$68.4\%\left\|\pm\frac{13}{2}\right\rangle, 5\%\left\|\pm\frac{7}{2}\right\rangle, 10.4\%\left\|\pm\frac{1}{2}\right\rangle, 11.6\%\left\|\mp\frac{13}{2}\right\rangle$
2	$8.7\%\left\|\pm\frac{13}{2}\right\rangle, 24.3\%\left\|\pm\frac{7}{2}\right\rangle, 33.1\%\left\|\pm\frac{1}{2}\right\rangle, 20.2\%\left\|\mp\frac{5}{2}\right\rangle, 5.3\%\left\|\mp\frac{11}{2}\right\rangle$

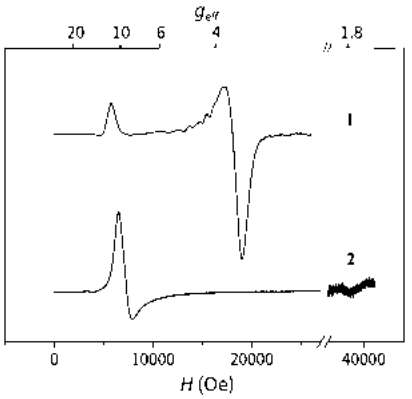

Fig. 2 W-band (94.3 GHz) spectra of microcrystalline powder samples of **1** and **2**, recorded at 5 K.

To investigate this point, variable frequency *ac* magnetic susceptibility experiments were performed for complexes **1** and **2** as a function of temperature, with and without applied *dc* field. In the absence of the *dc* field, none of the two complexes showed out-of phase magnetic susceptibility, χ''. This is not surprising, since quantum tunneling (QT) of magnetization[11] is expected to play a relevant role due to the mixture of different $|J, M_J\rangle$ characterizing the ground doublets of the two derivatives. However, when applying *dc* fields in the range of 200–2400 Oe at 1.9 K, a clear slow relaxation process is unexpectedly observed for both complexes, the maximum of the relaxation time being observed at an applied field of about 800 Oe and 900 Oe for **1** and **2**, respectively (Fig. S6, ESI†).

The Arrhenius plot of the temperature dependence of the relaxation times, obtained by fitting the χ'' *vs.* ν curves to a Debye model (Fig. S7 and S8, ESI†),[12] evidences quite a similar trend for the two derivatives, with large deviation from linear behaviour at lower temperatures. A tentative fit of the high temperature region results in the following parameters: $\tau_0 = (2.7 \pm 0.5) \times 10^{-8}$ s, $\Delta = 22 \pm 1$ cm^{-1} for **1**, and $\tau_0 = (5 \pm 2) \times 10^{-7}$ s, $\Delta = 7 \pm 1$ cm^{-1} for **2**. The two estimated barriers are clearly in contrast to the energy difference between the ground and the first excited doublet obtained by the luminescence data, indicating that the outcome of the phenomenological fit to the Arrhenius law has no physical meaning in this case, thus excluding that the observed barrier is connected to an Orbach process. Since both the easy axis **1** and the easy-plane **2** complexes show slow relaxation of the magnetization, it is quite clear that other mechanisms should account for the observed slow relaxation.

To analyse this issue in more detail we performed experiments on a isomorphous Y(trensal) complex doped with 5.8% and 3.1% of Er^{III} and Dy^{III}, respectively (see ESI†) to rule out the possibility of effects due to intermolecular interactions. These are indeed known to play a relevant role in the magnetic relaxation of single-molecule magnets, especially in mononuclear and f-element systems.[13]

Both systems showed field and temperature dependences of the dynamic susceptibility which are largely similar to those of the pure samples (Fig. S9 and S10, ESI†). The analysis of the relaxation rate as a function of the field at low temperature ($T = 1.8$ K) is reported in the upper panel of Fig. 3 and points to a competition between

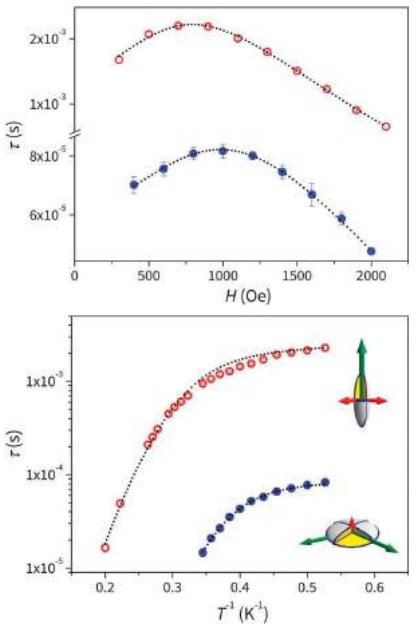

Fig. 3 Field (upper) and temperature (lower) dependence of the relaxation times of Y:Er(trensal) (empty circles) and Y:Dy(trensal) (full circles) and best fit curves obtained by using eqn (2) and (3). The ellipsoids in lower panel graphically represent the anisotropy of the susceptibility tensors of the ground doublet of the two derivatives.

two different field dependent relaxation processes. The increase in relaxation time observed in lower fields indicates that, on applying the field, QT processes are reduced, while the decrease observed at higher fields should be attributed to the increased relevance of the direct process. On these grounds, we tentatively analyzed the observed behaviour using eqn (2):

$$\tau^{-1} = \frac{B_1}{1 + B_2 H^2} + A_1 H^4 T + A_2 H^2 T \qquad (2)$$

where the first term represents the field dependence of QT process,[14] the second one the direct process for a Kramers ion without hyperfine interactions, and the third one is the direct process for a Kramers ion in the presence of hyperfine interaction.[15] Indeed, both samples contain magnetic and non-magnetic nuclei. The best fit curves provided in both cases very small values for the direct process not involving hyperfine interaction (parameters: $A_1 = (2.0 \pm 1.8) \times 10^{-12}$ s^{-1} K^{-1} Oe^{-4}, $A_2 = (1.4 \pm 0.1) \times 10^{-4}$ s^{-1} K^{-1} Oe^{-2}, $B_1 = (71 \pm 4) \times 10$ s^{-1}, $B_2 = (2.7 \pm 0.4) \times 10^{-6}$ Oe^{-2} for **1**; $A_1 = (3 \pm 2) \times 10^{-11}$ s^{-1} K^{-1} Oe^{-4}, $A_2 = (2.0 \pm 0.1) \times 10^{-3}$, s^{-1} K^{-1} Oe^{-2} $B_1 = (158 \pm 2) \times 10^2$ s^{-1}, $B_2 = (9.2 \pm 0.7) \times 10^{-7}$ Oe^{-2} for **2**). The temperature dependence of the relaxation time for the diluted systems are reported in the lower panel of Fig. 3: the weak temperature dependence of τ observed at low temperature suggests a contribution by the QT process, whereas the temperature dependence observed at higher T indicates that relaxation proceeds by exchange of energy with lattice vibrations. The observed curvature of the Arrhenius plot indicates a non-negligible influence of direct and/or Raman processes in determining the relaxation rate,[15,16] the former having been confirmed using the field dependent measurements. On these grounds we analysed the temperature dependence of the relaxation rates for diluted samples by using eqn (3):

$$\tau^{-1} = \frac{B_1}{1 + B_2 H^2} + A_1 H^4 T + A_2 H^2 T + C T^n + \tau_0^{-1} \exp(-\Delta / kT) \qquad (3)$$

where the first three terms are the same as in eqn (2), the fourth is the Raman one, and the fifth is the Orbach one. Due to the large number of parameters involved we fixed the first three to the values obtained by the analysis of the field dependent relaxation rate. For none of the two derivatives reasonable fits could be obtained by including Orbach processes in addition to the direct and QT ones, while a Raman process, with variable exponent n, provided reasonable reproduction of the data (best fit values $n = 9$ for **1** and $n = 11$ for **2**). Therefore it is evident that the relaxation is not occurring *via* the first excited doublet in any of the two derivatives.

In summary we conclude that, despite Er(trensal) being an easy axis type complex and Dy(trensal) an easy plane one, the two molecules show slow relaxation of the magnetization, both as a function of temperature and of the field. This observation invalidates the general assumption that the slow dynamics of magnetization is associated with the magnetic anisotropy in lanthanide complexes, and stresses the absolute importance of complementing the magnetic characterization of these systems with spectroscopic techniques.[17] It is clear that only a multitechnique approach allows us to understand the factors affecting the magnetization dynamics and relaxation mechanisms in these systems and can provide a valuable feedback to develop new synthetic strategies.

We acknowledge the financial support of MIUR through the project Futuro in Ricerca 2012 (RBFR12RPD1) and of EC through ERC-AdG MolNanoMas (267746).

Notes and references

1 N. Ishikawa, M. Sugita, T. Ishikawa, S. Koshihara and Y. Kaizu, *J. Am. Chem. Soc.*, 2003, **125**, 8694.
2 (*a*) D. N. Woodruff, R. E. P. Winpenny and R. A. Layfield, *Chem. Rev.*, 2013, **113**, 5110; (*b*) J. D. Rinehart and J. C. Long, *Chem. Sci.*, 2011, **2**, 2078; (*c*) L. Sorace, C. Benelli and D. Gatteschi, *Chem. Soc. Rev.*, 2011, **40**, 3092; (*d*) M. A. AlDamen, S. Cardona-Serra, J. M. Clemente-Juan, E. Coronado, C. Martì-Gastaldo, A. Gaita-Arino, F. Luis and O. Montero, *Inorg. Chem.*, 2009, **48**, 3467.
3 (*a*) G. Cucinotta, M. Perfetti, J. Luzon, M. Etienne, P. E. Car, A. Caneschi, G. Calvez, K. Bernot and R. Sessoli, *Angew. Chem., Int. Ed.*, 2012, **51**, 1606; (*b*) M.-E. Boulon, G. Cucinotta, J. Luzon, C. Degl'Innocenti, M. Perfetti, K. Bernot, G. Calvez, A. Caneschi and R. Sessoli, *Angew. Chem., Int. Ed.*, 2013, **52**, 350.
4 (*a*) R. J. Blagg, L. Ungur, F. Tuna, J. Speak, P. Comar, D. Collison, W. Wernsdorfer, E. J. L. McInnes, L. F. Chibotaru and R. E. P. Winpenny, *Nat. Chem.*, 2013, **5**, 673; (*b*) K. Bernot, J. Luzon, L. Bogani, M. Etienne, C. Sangregorio, M. Shanmugam, A. Caneschi, R. Sessoli and D. Gatteschi, *J. Am. Chem. Soc.*, 2009, **131**, 5573; (*c*) H. L. C. Feltham, Y. Lan, F. Klöwer, L. Ungur, L. F. Chibotaru, S. Brooker and A.K. Powell, *Chem.–Eur. J.*, 2011, **17**, 4362.
5 R. Orbach, *Proc. R. Soc. London, Ser. A*, 1961, **264**, 458.
6 (*a*) J. D. Rinehart and J. R: Long, *Dalton Trans.*, 2012, **41**, 13572; (*b*) N. Magnani, R. Caciuffo, E. Colineau, F. Wastin, A. Baraldi, E. Buffagni, R. Capelletti, S. Carretta, M. Mazzera, D. T. Adroja, M. Watanabe and A. Nakamura, *Phys. Rev. B*, 2009, **79**, 104407.

7 (*a*) P. V. Bernhardt, B. M. Flanagan and M. J. Riley, *Aust. J. Chem.*, 2000, **53**, 229; (*b*) B. M. Flanagan, P. V. Bernhardt, E. R. Krausz, S. R. Lüthi and M. J. Riley, *Inorg. Chem.*, 2002, **41**, 5024.
8 E. Lucaccini, Master thesis, Univ. of Florence, 2013.
9 C. Görller-Walrand and K. Binnemans, in *Handbook on the Physics and Chemistry of Rare Earths*, ed. K. A. Gschneidner Jr and L. Eyring, 1996, vol. 23, p. 121.
10 J. Sievers, *Z. Phys. B: Condens. Matter Quanta*, 1982, **45**, 289.
11 D. Gatteschi, R. Sessoli and J. Villain, *Molecular nanomagnets*, Oxford University Press, Oxford, 2006.
12 H. B. J. Casimir and F. K. Du Pré, *Physica*, 1938, **5**, 507.
13 K. Meihaus, J. Rinehart and J. R. Long, *Inorg. Chem.*, 2011, **50**, 8484.
14 A. Fort, A. Rettori, J. Villain, D. Gatteschi and R. Sessoli, *Phys. Rev. Lett.*, 1998, **80**, 612.
15 A. Abragam and B. Bleaney, *Electron Paramagnetic Resonance of Transition Ions*, Dover, New York, 1986.
16 (*a*) J. M. Zadrozny, M. Atanasov, A. M. Bryan, C.-Y. Lin, B. D. Rekken, P. P. Power, F. Neese and J. R. Long, *Chem. Sci.*, 2013, **4**, 125; (*b*) J.-L. Liu, K. Yuan, J.-D. Leng, L. Ungur, W. Wernsdorfer, F.-S. Guo, L. F. Chibotaru and M.-L. Tong, *Inorg. Chem.*, 2012, **51**, 8538.
17 During the submission of this manuscript we were informed that another group is currently working on the magnetic characterization of Er(trensal): J. Dreiser, private communication.

ELECTRONIC SUPPLEMENTARY INFORMATION

Beyond anisotropy barrier: slow relaxation of the magnetization in both easy-axis and easy-plane Ln(trensal) complexes

Eva Lucaccini,[a] Lorenzo Sorace,[a*] Mauro Perfetti,[a] Jean-Pierre Costes,[b] and Roberta Sessoli[a]

[a] *Department of Chemistry "Ugo Schiff" and INSTM Research Unit, University of Florence, Via della Lastruccia 3, 50019 Sesto Fiorentino, Italy. E-mail:* lorenzo.sorace@unifi.it

[b] *Laboratoire de Chimie de Coordination du CNRS, 205, route de Narbonne, BP 44099, 31077 Touluse Cedex 4, France.*

1 Synthesis

Powder microcrystalline samples of Er(trensal) and Dy(trensal) were obtained by the synthetic procedure reported in ref. (*1*). Yttrium diluted samples were obtained by adding the desired molar ratio of Y(trensal) and Er(trensal) or Dy(trensal) in MeOH, refluxing for 30 min and cooling at room temperature. After filtration under vacuum the solid was washed with MeOH and dried under nitrogen flux. The obtainment of the correct $P\bar{3}c1$ phase was checked by powder X-ray diffractograms (figure S1). All the patterns are superimposable to the one obtained from the crystallographic information file (.cif) of the solved molecular structure (Er derivative) (*2*).
Extremely diluted samples (0.5 %) were obtained for Dy derivative, but this did not result in any detectable change of the magnetic properties, except an increased signal-to-noise ratio due to the lower amount of material probed, so we chose the few percent dilution.

2 Experimental setup

X-ray powder diffraction patterns of both pure and Y-diluted samples were measured with a Bruker D8 Advance powder diffractometer equipped with a Cu source (K_α, $\lambda = 1.54$ Å).
Dc magnetic measurements were performed by using a Quantum Design MPMS SQUID magnetometer on powders pressed in a pellet to avoid field induced orientation of the crystallites. The concentration of Dy and Er in Y diluted samples was estimated by treating the corresponding magnetic data as if the samples contained only Y and then comparing the residual room temperature χT with that of the pure sample from Curie law (14.17 emu K mol^{-1} for Dy and 11.48 emu K mol^{-1} for Er).
Ac susceptibility was measured using Quantum Design PPMS in *ac* mode for the frequency range $1 \div 10^4$ Hz. The Quantum Design MPMS SQUID magnetometer was used for low frequencies ($0.1 \div 10^3$ Hz).
EPR spectra were recorded at 5 K and 10 K with a E500 Bruker spectrometer for the X band ($\nu \sim 9.4$ GHz) and a E600 Bruker spectrometer for the W band ($\nu \sim 94$ GHz).

3 Computation

The CF hamiltonian for a C_3 point symmetry is:

$$\begin{aligned} V_c(C_3) = {} & B_0^2\mathbf{C}_0^2 + B_0^4\mathbf{C}_0^4 + B_3^4(\mathbf{C}_{-3}^4 - \mathbf{C}_3^4) + \mathrm{i}B'^4_3(\mathbf{C}_{-3}^4 + \mathbf{C}_3^4) + B_0^6\mathbf{C}_0^6 \\ & + B_3^6(\mathbf{C}_{-3}^6 - \mathbf{C}_3^6) + \mathrm{i}B'^6_3(\mathbf{C}_{-3}^6 + \mathbf{C}_3^6) + B_6^6(\mathbf{C}_{-6}^6 + \mathbf{C}_6^6) + \mathrm{i}B'^6_6(\mathbf{C}_{-6}^6 - \mathbf{C}_6^6) \end{aligned} \quad (1)$$

In this symmetry one can always choose an orientation of xy axes such that $B'^4_3 = 0$ so to minimize the number of CF parameters (see table S1). The energy levels, the wavefunction composition and the corresponding g_{eff} expected on the basis of the reported CF parameters (table S1) were calculated using a home-developed software which allowed to include the effect of mixing of the higher lying multiplets arising form the same spectroscopic term of the ground one. The composition of the

ground multiplet of Dy(trensal) was calculated including $J = \frac{13}{2}$ and $J = \frac{11}{2}$ but no major effects were noticed on considering the two excited multiplets. On the contrary for Er(trensal) inclusion of excited multiplets ($J = \frac{13}{2}, \frac{11}{2}, \frac{9}{2}$) results in an increased admixing of $|JM_J\rangle$ components contributing to the ground state wavefunction.

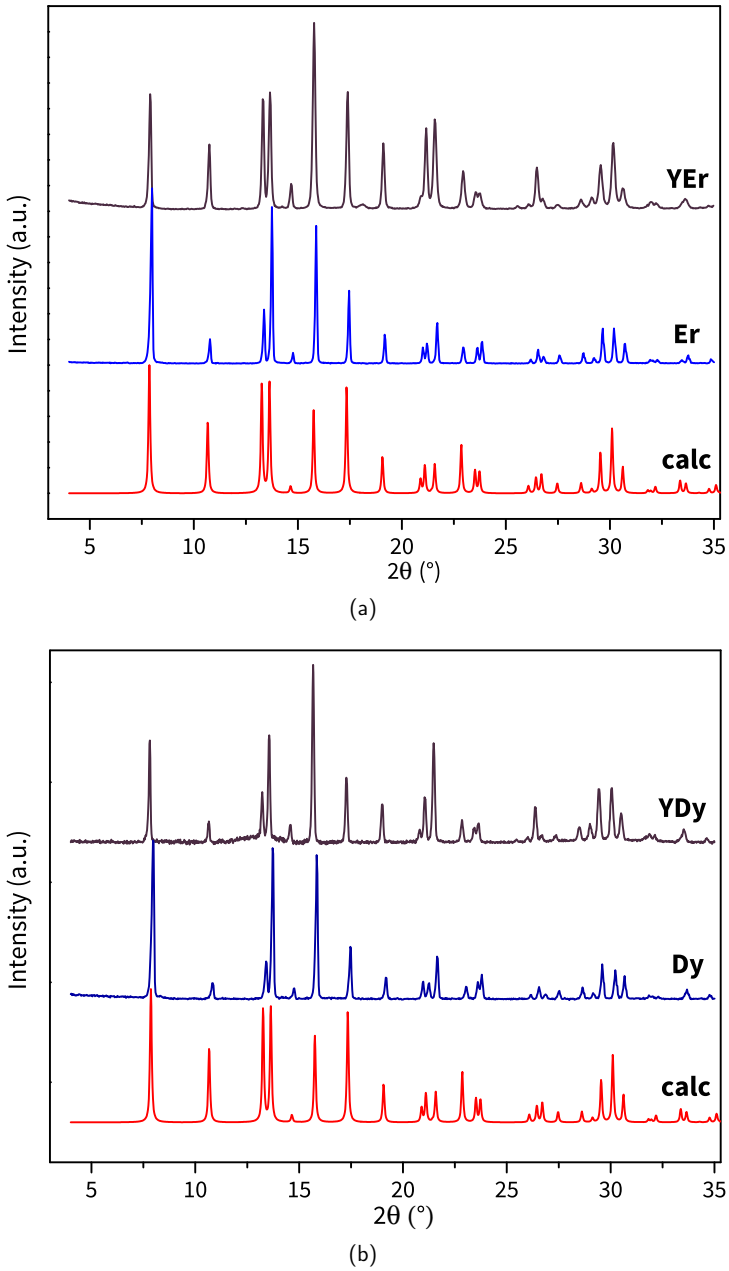

Figure S1: X-ray diffraction spectra of Er(trensal) and Dy(trensal) and of their Y-diluted samples. The red lines represent the calculated diffraction pattern for reported molecular structure (*2*).

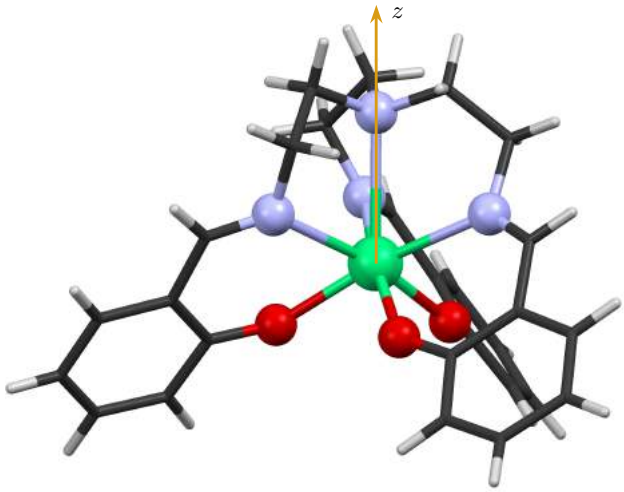

(a)

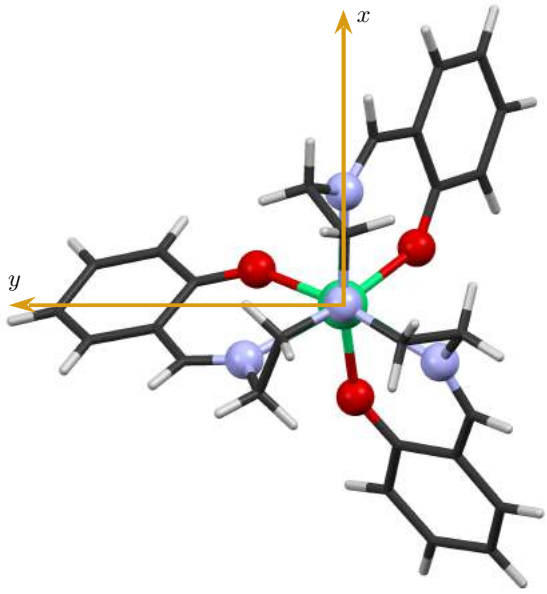

(b)

Figure S2: Molecular structure of Ln(trensal). The orientation of x and y axes is not defined *a priori* but it has been chosen in order to have a minimal set of CF parameters (*2*). The green colour identifies Ln, the red the oxygen, the light blue the nitrogen, the grey the carbon and the white the hydrogen.

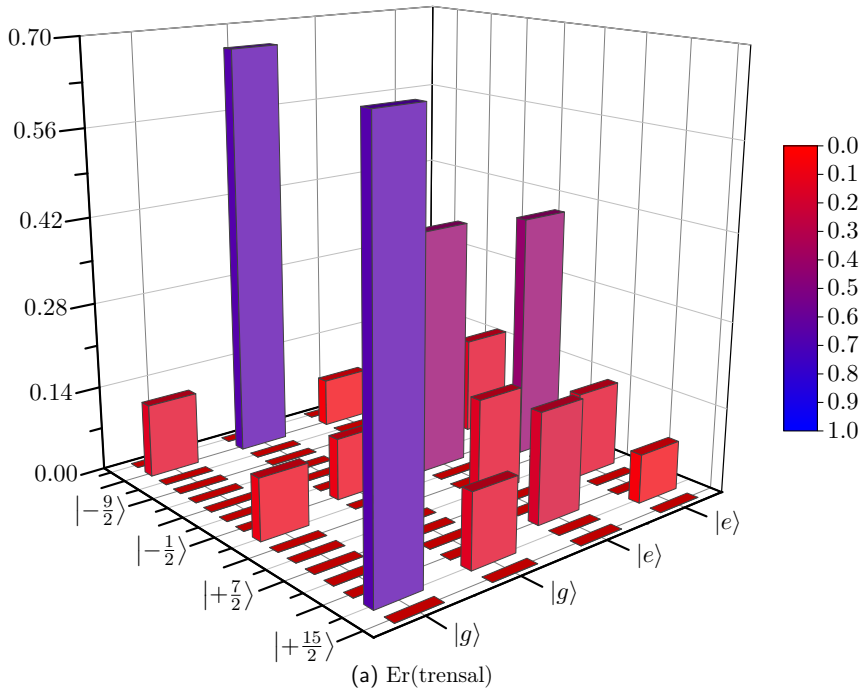

(a) Er(trensal)

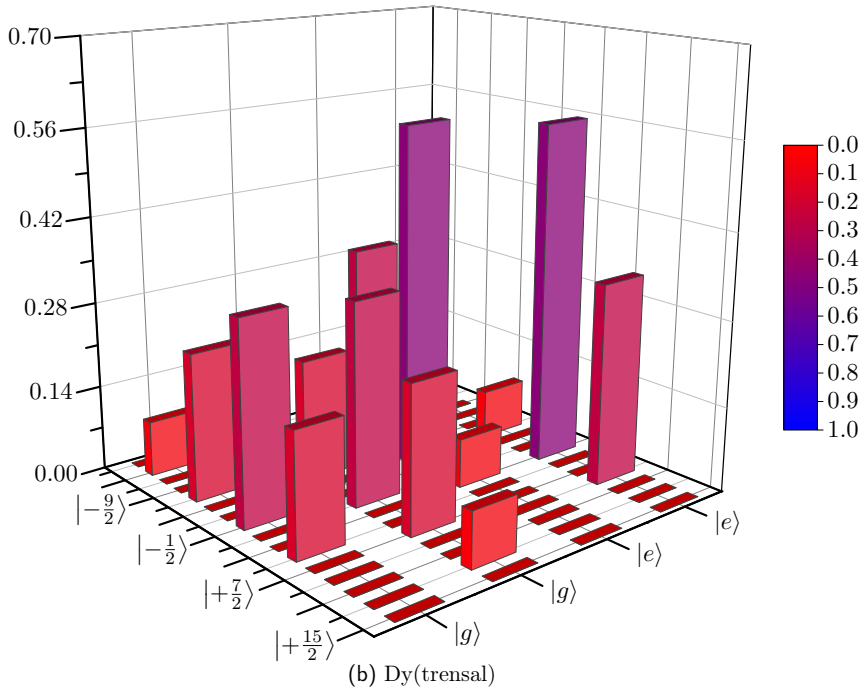

(b) Dy(trensal)

Figure S3: Composition of the ground doublet and of the first excited doublet for Er(trensal)(figure a) and Dy(trensal) (figure b). For clarity reasons contribution of M_J states less than 8 % are not included. More details can be found in tables S2 and S3.

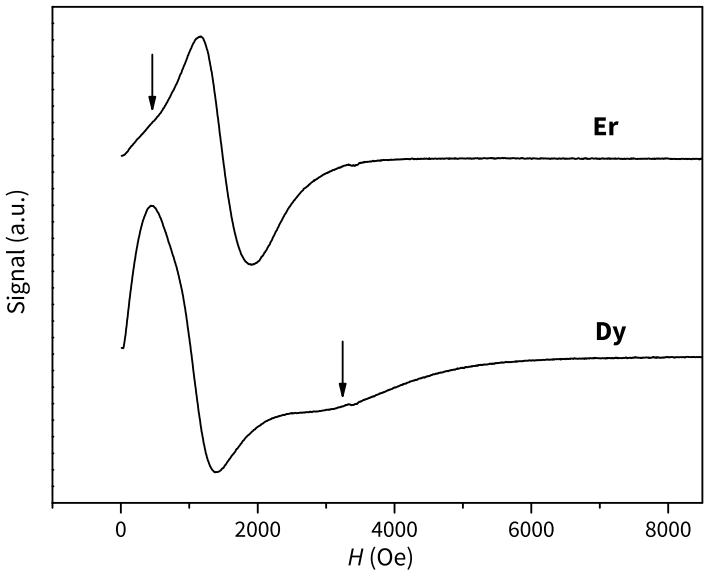

Figure S4: X band spectrum (9.4 GHz) of microcrystalline powder of Er(trensal) and Dy(trensal). The arrows evidence the parallel component of g_{eff} for the two compounds.

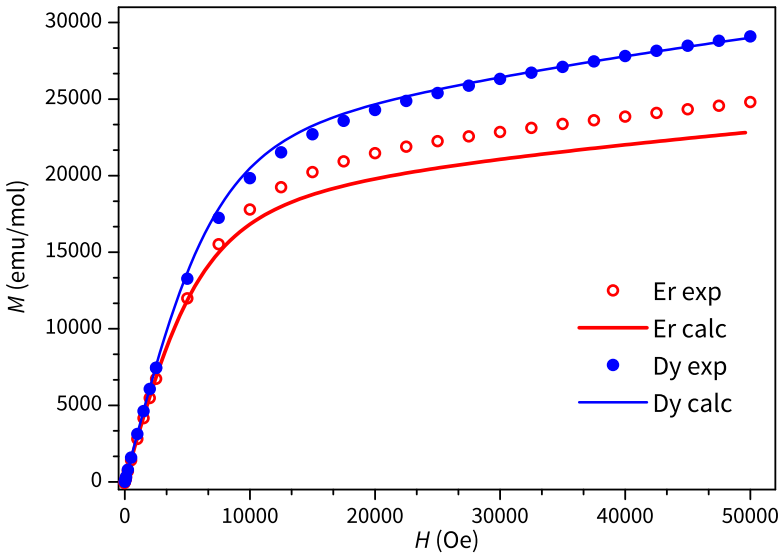

Figure S5: M vs H curves ($T = 1.9$ K): the circles represent the experimental data for Er(trensal) (empty) and for Dy(trensal) (full). The solid lines are the powder average magnetizations calculated using the CF parameters of reference (*2*) and a 55 points grid.

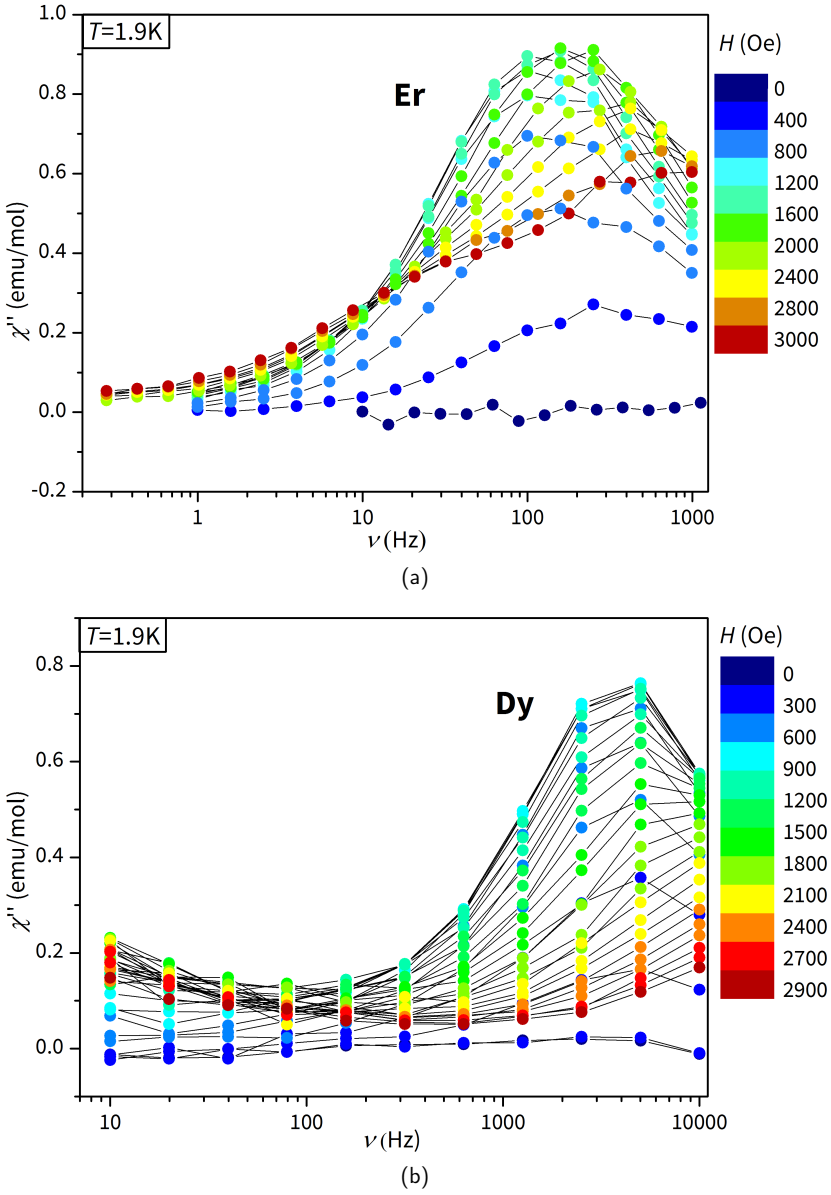

Figure S6: Imaginary susceptibility χ'' for different values of static dc field ($T = 1.9\,\mathrm{K}$).

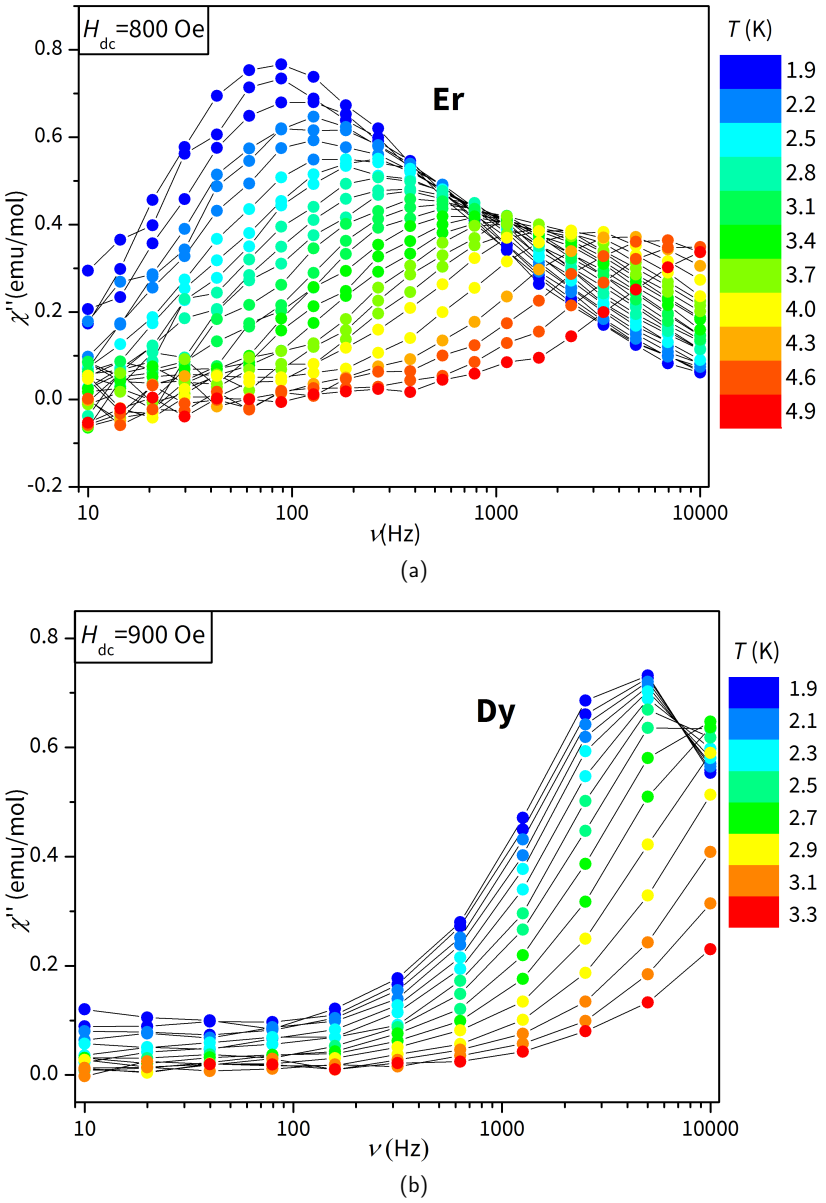

Figure S7: Imaginary susceptibility χ'' for different values of temperature T at the indicated static field.

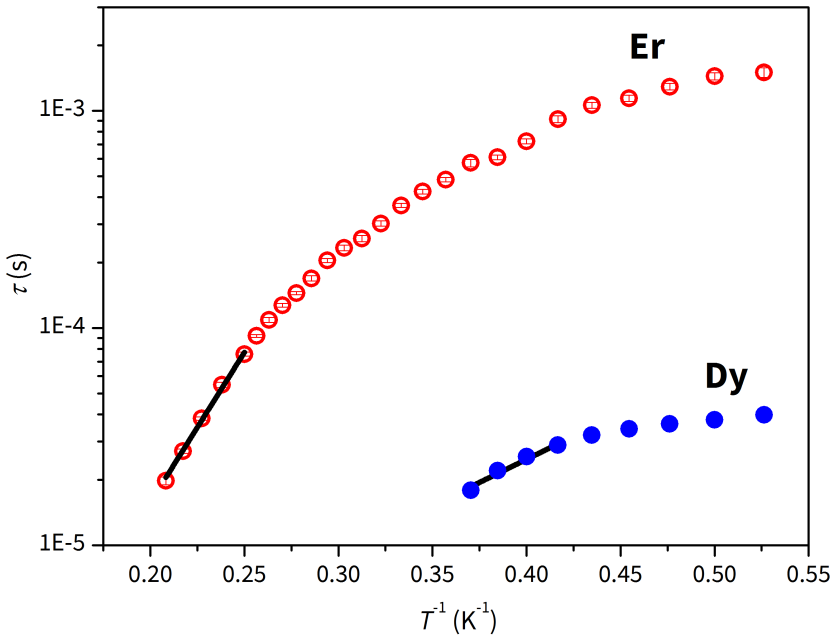

Figure S8: Arrhenius plot of temperature dependence of the relaxation rates of pure samples of Er(trensal) and Dy(trensal). Solid lines represent the best fit of the high temperature region using the Arrhenius formula $\tau = \tau_0 e^{\Delta E/k_B T}$ (see text for details).

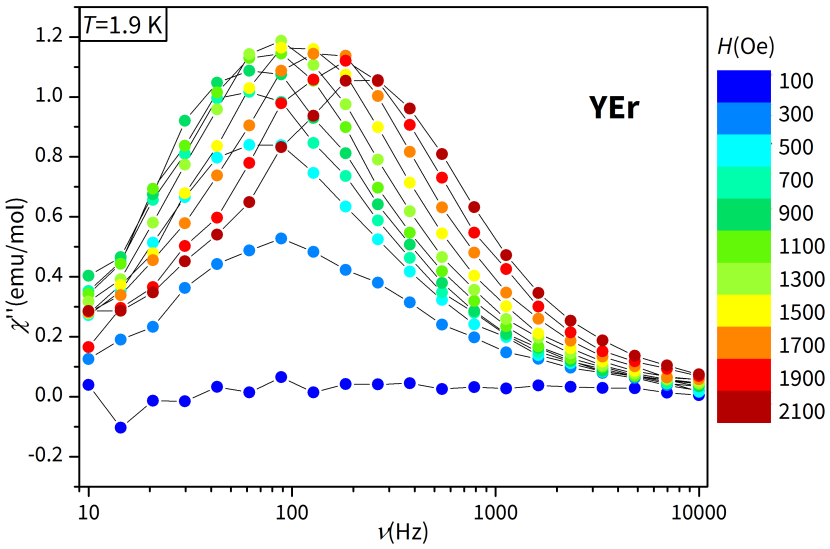

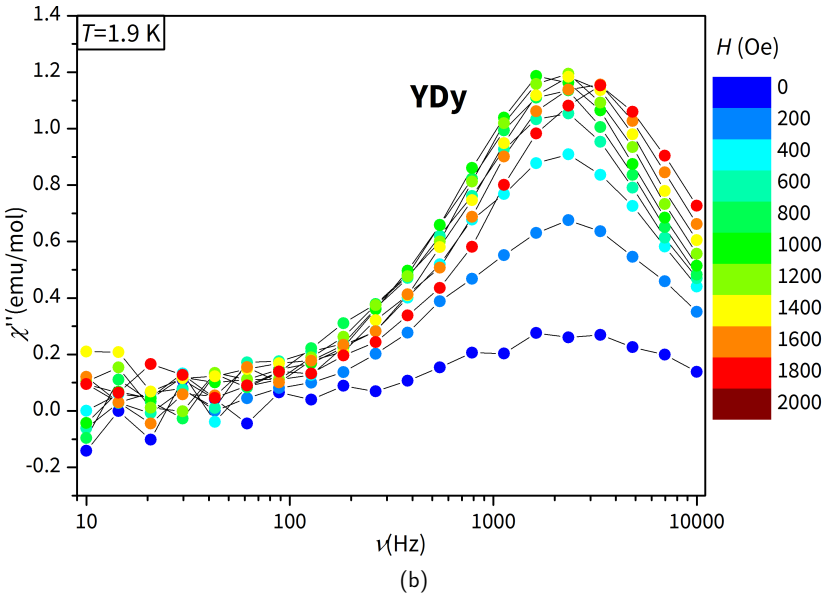

Figure S9: Imaginary susceptibility χ'' for Y-diluted samples at different values of static *dc* field. The dilutions are 5.8 % for Y:Er(trensal) and 3.1 % forY:Dy(trensal).

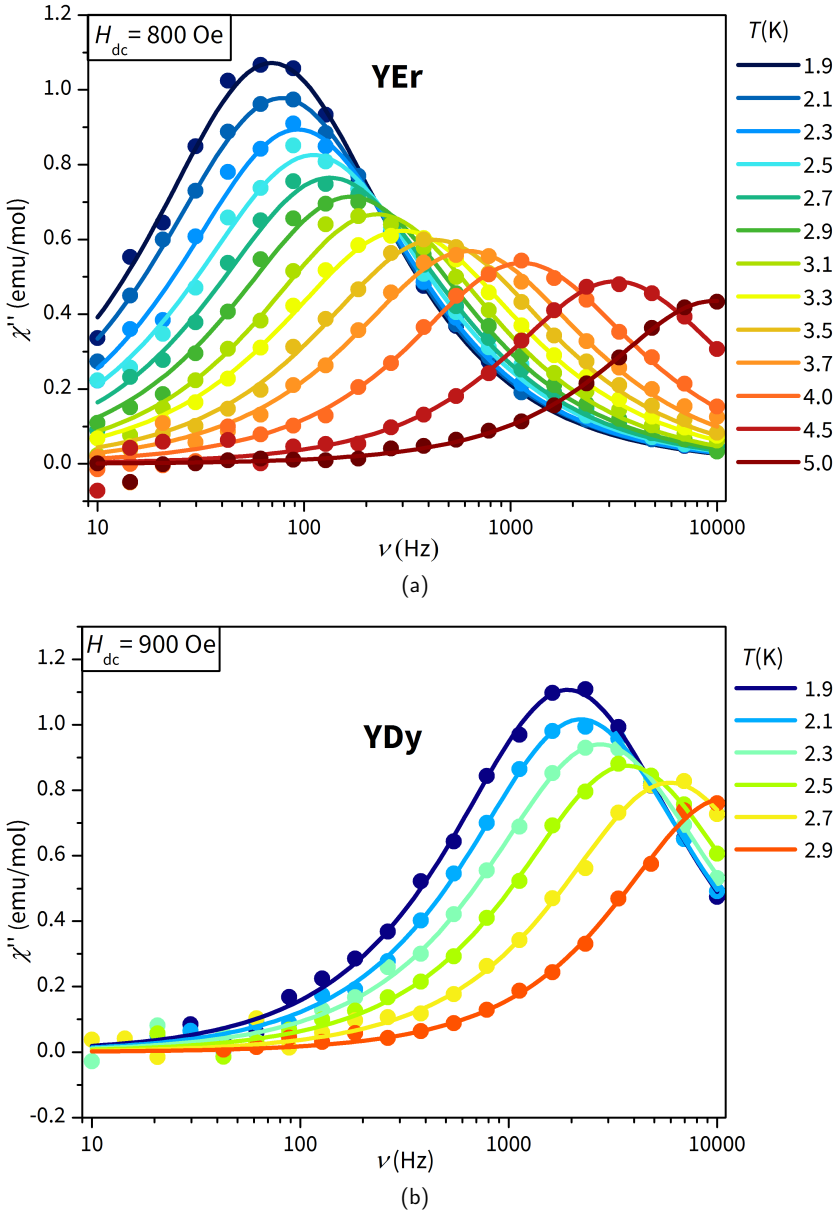

Figure S10: Imaginary susceptibility χ'' for Y-diluted samples at different values of temperature T. The solid lines are fits of the curves using the Debye formula (*3*).

Table S1: Crystal field parameters B_q^k for Dy(trensal) and Er(trensal). The values are expressed in cm^{-1} and the uncertainties are in brackets (*2*).

	Dy	Er
B_0^2	−671(39)	−720(59)
B_0^4	−186(77)	−44(106)
B_3^4	−2153(34)	−2121(83)
B'^4_3	0	0
B_0^6	1241(57)	988(36)
B_3^6	439(41)	353(49)
B'^6_3	−284(83)	92(53)
B_6^6	660(49)	545(34)
B'^6_6	145(137)	311(36)

Table S2: Composition of the ground doublet and of the first excited doublet for Er(trensal).

state	composition
ground state	68.4 % $\left\vert\pm\frac{13}{2}\right\rangle$, 11.6 % $\left\vert\mp\frac{13}{2}\right\rangle$, 10.4 % $\left\vert\pm\frac{1}{2}\right\rangle$, 5 % $\left\vert\pm\frac{7}{2}\right\rangle$
1° excited state	40 % $\left\vert\mp\frac{1}{2}\right\rangle$, 18 % $\left\vert\pm\frac{11}{2}\right\rangle$, 16 % $\left\vert\pm\frac{5}{2}\right\rangle$, 14 % $\left\vert\mp\frac{7}{2}\right\rangle$, 8 % $\left\vert\mp\frac{13}{2}\right\rangle$

Table S3: Composition of the ground doublet and of the first excited doublet for Dy(trensal).

state	composition
ground state	33.1 % $\left\vert\mp\frac{1}{2}\right\rangle$, 24.3 % $\left\vert\mp\frac{7}{2}\right\rangle$, 20.2 % $\left\vert\pm\frac{5}{2}\right\rangle$, 8.7 % $\left\vert\mp\frac{13}{2}\right\rangle$, 5.3 % $\left\vert\mp\frac{11}{2}\right\rangle$
1° excited state	56 % $\left\vert\mp\frac{3}{2}\right\rangle$, 33 % $\left\vert\mp\frac{9}{2}\right\rangle$, 8 % $\left\vert\pm\frac{3}{2}\right\rangle$

References

1. P. V Bernhardt *et al.*, *Australian Journal of Chemistry* **53**, 229–231 (2000).
2. B. M. Flanagan *et al.*, *Inorganic Chemistry* **41**, 5024–5033 (2002).
3. D. Gatteschi *et al.*, *Molecular Nanomagnets* (Oxford University Press, 2006).

Inorganic Chemistry

Communication

pubs.acs.org/IC

Determination of Magnetic Anisotropy in the LnTRENSAL Complexes (Ln = Tb, Dy, Er) by Torque Magnetometry

Mauro Perfetti,[†] Eva Lucaccini,[†] Lorenzo Sorace,[†] Jean Pierre Costes,[‡] and Roberta Sessoli*[,†]

[†]Dipartimento di Chimica "Ugo Schiff" and UdR INSTM, Università degli Studi di Firenze, Via della Lastruccia 3−13, 50019 Sesto Fiorentino, Italy

[‡]Laboratoire de Chimie de Coordination 205 route de Narbonne, 31077 Toulouse Cedex 4, France

Supporting Information

ABSTRACT: We report here a study about the magnetic anisotropy of the LnTRENSAL complexes (Ln = Tb, Dy, Er) performed by using cantilever torque magnetometry and electron paramagnetic resonance. For all of the compounds, we extracted a set of crystal-field parameters to obtain the energy-level splitting of the ground-state multiplet.

Magnetic anisotropy is a fundamental property that deeply affects the magnetic behavior of molecules that exhibit slow relaxation of magnetization, called single-molecule magnets (SMMs).[1] Among this class of systems, a central role is played by lanthanide-based SMMs. Indeed, the unquenched orbital momentum of these ions, caused by the partially filled f orbitals interacting with the electrostatic potential originated by the ligands, is often able to give rise to huge anisotropy barriers.[2,3] The magnetic anisotropy of SMMs containing lanthanide (Ln) ions is generally rationalized by modeling the effect of the ligands using approximate point-charge distributions;[4−7] however, deceptive results can be obtained, especially in low-symmetry compounds.[8,9] The correlation between the magnetic anisotropy and magnetization dynamics is also not always straightforward, as was recently shown for two isostructural compounds containing a central Er^{3+} or Dy^{3+} ion surrounded by the trianion of the heptadentate ligand 2,2′,2″-tris(salicylideneimino)triethylamine (H_3TRENSAL).[10] The LnTRENSAL family has been extensively studied in the literature to develop new synthetic strategies,[11,12] to investigate interaction with surfaces,[13] and to study the energy pattern and thus obtain a set of crystal-field (CF) parameters via magnetic[14] and luminescence[15,16] measurements.

Cantilever torque magnetometry (CTM) is a powerful tool to investigate magnetic anisotropy on single crystals of lanthanide complexes in a wide temperature range.[17,18] In this work, we have employed this technique to characterize in detail the magnetic anisotropy of three LnTRENSAL complexes (Ln = Tb, Dy, and Er, hereafter **Tb**, **Dy**, and **Er**, respectively).

In CTM, a sample is fixed on the cantilever acting as the upper plate of a capacitor.[19,20] The whole system can be rotated in an external magnetic field (**B**) and the magnetic torque ($\boldsymbol{\tau}$) experienced by the sample is directly proportional to the cantilever deflection detected as the change in the electric capacitance.

Hexagonally shaped single crystals belonging to the trigonal $P\bar{3}c1$ (No. 163) space group were grown for the three compounds as previously described.[10,11] The Ln ion lies on a special position (C_3 symmetry); thus, all molecules are isooriented. Crystals' faces were indexed on a single-crystal diffractometer to correlate the crystallographic reference frame (*abc*) with the laboratory one (*XYZ*), where torque is measured along *Y*, which is also the rotation axis of the cantilever (see Figures S1−S3 in the Supporting Information, SI).

The magnetic torque is defined as the vector product between the magnetization (**M**) and **B**.[1,19] Taking into account that experimentally only the *Y* component of $\boldsymbol{\tau}$ can be detected, it is possible to write τ_Y as

$$\tau_Y = M_Z B_X - M_X B_Z = B^2 \sin\theta \cos\theta(\chi_{ZZ} - \chi_{XX}) \qquad (1)$$

where θ is the angle between **B** and the *Z* axis and $\boldsymbol{\chi}$ is the susceptibility tensor. The additional term $B^2(2\sin^2\theta - 1)\chi_{XZ}$ has been omitted for sake of simplicity because χ_{XZ} can always be set to zero by a proper shift in the rotation. The second part of eq1 is only valid when **M** is linear with **B**, that is, in general, for weak fields or high temperatures. Following eq 1, the torque signal can be considered a direct measurement of the magnetic anisotropy of the molecule. Although CTM is able to detect magnetic anisotropy contributions even when arising from magnetically inequivalent molecules[17] and also from polynuclear clusters,[21−24] the present case is much more favorable because the macroscopic shape of the crystals easily permits identification of the *c* crystallographic axis, which is also a molecular symmetry axis.

Two rotations have been performed: the first (rot 1) has *Y* lying in the *ab* plane and *Z* coincident with $-c$ at $\theta = 0$, while the second (rot 2) scans the *ab* plane; hence, the rotation axis was the *c* crystallographic axis (see Figure S4 in the SI).

In Figure 1, we report the torque signals obtained in rot 1 for **Tb**, **Dy**, and **Er** at fixed temperature (5 K) and magnetic field (12 T). Fits of the torque curves obtained at different field and temperature values are reported in Figures S5−S7 in the SI. The data in Figure 1 were normalized for the different masses of the measured crystals. Beyond the trivial 180° periodicity, we first note that $\boldsymbol{\tau}$ has an opposite phase for **Er** compared to **Tb** and **Dy**. According to eq 1, this means that the term $\chi_{ZZ} - \chi_{XX} = \chi_c - \chi_{ab}$ is positive for **Er**, while it is negative for **Tb** and **Dy**, testifying that

Received: February 5, 2015
Published: March 10, 2015

DOI: 10.1021/acs.inorgchem.5b00288
Inorg. Chem. 2015, 54, 3090−3092

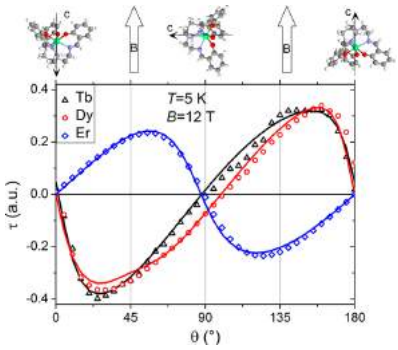

Figure 1. Torque signals for **Tb**, **Dy**, and **Er** obtained at 5 K and 12 T. The solid lines are the best-fit curves.

different distributions of the electronic density around the Ln ion are mirrored in diverse anisotropy features.[8,25,26] The shape of the torque profile, with the largest $|\partial\tau/\partial\theta|$ characteristic of the hard direction, indicates that $\theta = 0°$ corresponds to a hard axis for **Tb** and **Dy**, while it is an easy axis for **Er**. None of the compounds showed a detectable torque signal in the *ab* plane (rot 2), indicating that this plane has to be considered magnetically isotropic for our sensitivity (Figure S8 in the SI). We can then conclude that the anisotropy of **Er** is easy axis, while the one of **Dy** and **Tb** is easy plane. These results are in agreement with previous powder electron paramagnetic resonance (EPR) studies on **Er** and **Dy**[10] and are particularly interesting for **Tb**, a non-Kramers ion with no SMM behavior, for which the latter technique provides nonconclusive results. Indeed, the powder X-band EPR spectrum of **Tb** at 5 K showed a hyperfine split transition with isotropic line shape at about zero field, in both the perpendicular and parallel polarization modes (Figure S9 in the SI).

The sensitivity of CTM allowed us to measure the angular dependence of the torque at different fields even at high temperatures, where the first excited levels are also populated. These data can then be fit using an appropriate set of CF parameters. In favorable cases, like the LnTRENSAL family, a detailed description of the electronic structure of the complex can be obtained by luminescence measurements. However, while CTM provides direct information on the anisotropy of the ground-state Russell−Saunders multiplet, transitions that involve the ground-state multiplet may not be observed in luminescence spectra (as for **Tb** and **Dy**). In these cases, the electronic structure of the ground-state multiplet is obtained indirectly by the set of CF parameters needed to reproduce transitions to upper-lying multiplets. This may result in an incorrect prediction of the angular and field dependence of the magnetic anisotropy at low temperatures (see Figure S10 in the SI).

The CF Hamiltonian in Wybourne's notation for C_3 symmetry is[27]

$$\mathcal{H}_{CF} = B_0^2\mathbf{C}_0^2 + B_0^4\mathbf{C}_0^4 + B_0^6\mathbf{C}_0^6 + B_3^4(\mathbf{C}_{-3}^4 - \mathbf{C}_3^4) + B_3^6(\mathbf{C}_{-3}^6 - \mathbf{C}_3^6) + iB'^6_3(\mathbf{C}_{-3}^6 + \mathbf{C}_3^6) + B_6^6(\mathbf{C}_{-6}^6 + \mathbf{C}_6^6) + iB_6'^6(\mathbf{C}_{-6}^6 - \mathbf{C}_6^6) \quad (2)$$

where the *xyz* molecular reference frame was chosen to have $B'^4_3 = 0$ without any loss of generality.[14,15] All of the calculations took into account the Zeeman term and the Russell−Saunders ground state, which is the only one significantly populated in the investigated temperature range.[15] The fits were performed by projecting the Hamiltonian (2) onto the ground state *J* and using the corresponding set of Stevens' extended operators. In Table 1,

Table 1. CF Parameters According to Wybourne's Formalism, Obtained by Fitting the Torque Signals[a]

Parameter (cm^{-1})	Tb	Dy	Er
B_2^0	−562 (152)	−710 (38)	−726 (115)
B_4^0	40 (36)	−274 (80)	−81 (162)
B_6^0	−1410 (2115)	1309 (183)	952 (88)
B_4^3	1344 (520)	−1406 (98)	−2401 (233)
B_6^3	712 (498)	674 (69)	366 (69)
B'^3_6	420 (420)	−760 (334)	300 (900)
B_6^6	1137 (887)	935 (187)	490 (157)
B'^6_6	840 (840)	0 (−)	120 (360)

[a]Numbers in parentheses refer to the errors estimated with the *MINUIT* subroutine.

we report the obtained best-fit CF parameters (see also Tables S1 and S2 and eq S1 in the SI). The effective orientation of the crystals was taken into account by using two polar angles ($\delta = \widehat{Zc}$; $\alpha = \widehat{Ya}$). Because of the isotropy of the *ab* plane, α was fixed at the value obtained by the indexing, while δ was different from zero only for **Tb** [$\delta = 0.3(1)°$].

With the obtained CF parameters, we calculated the energies for all of the sublevels of the ground state for the three compounds and compared them with the results obtained using the parameters reported by Flanagan et al. (Figure 2).[15] The

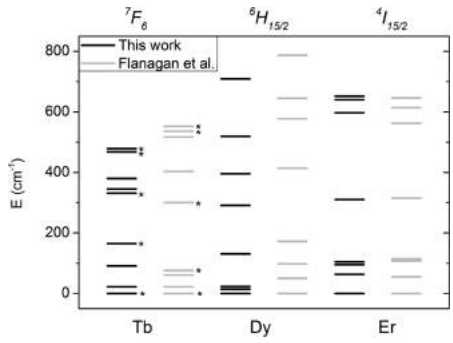

Figure 2. Energy patterns calculated using the CF parameters for the ground-state manifolds J = 6, $^{15}/_2$, and $^{15}/_2$ of **Tb**, **Dy**, and **Er**, respectively, obtained by CTM (black) and luminescence (gray). All of the levels are doublets, except for the ones indicated with black stars, which are singlets.

agreement between the levels calculated starting from the two techniques is particularly good for **Er**, for which luminescence provided a direct measure of the ground-state multiplet splitting (numerical results and details are reported in Tables S3−S5 in the SI). It is, however, worth noting that, because of the strong correlation between CF parameters, the uncertainty on some parameters is huge, as also occurs by using other techniques.[14,15] Interestingly, the χT versus T plot of **Tb**, **Dy**, and **Er** can be simulated with comparable agreement by using our parameters and those reported by Flanagan et al.[15] and by Dreiser et al.[14]

DOI: 10.1021/acs.inorgchem.5b00288
Inorg. Chem. 2015, 54, 3090−3092

(see Figure S11 in the SI). A good fit of the χT versus T curves is then a necessary but not a sufficient condition to extract the correct set of CF parameters.[28] In this sense a simple but anisotropy-sensitive technique is extremely helpful in obtaining an accurate description of low temperature magnetic anisotropy.

The obtained results also provide an important *caveat* about the interpretation of the EPR spectra of non-Kramers' Ln ions. As was already mentioned, the powder X-band EPR spectrum of **Tb** (Figure S9 in the SI) features a transition close to zero field. This is not compatible with the energy-level pattern calculated using the CF parameters derived either from CTM or luminescence,[15,16] both techniques indicating a singlet ground state well separated in energy from the first doublet excited state (Figure 2 and Table S3 in the SI). EPR spectra are also not compatible with a doublet ground state (strictly degenerate in trigonal symmetry), which may arise by a different choice of CF parameters. While a more detailed study might provide a definitive answer, we hypothesize that the observed EPR transition may be due to Tb^{3+} centers that experience a lower-symmetry CF, resulting in two low-lying singlets separated by about 0.3 cm^{-1} (the microwave energy in the X band). The situation is reminiscent of that reported for $[Tb(nicotinate)_3 \cdot 2H_2O]_2$, for which an EPR spectrum was observed despite magnetic and optical measurements indicating a singlet ground state: this was attributed either to defective sites or to the effect of residual solvent molecules in the lattice.[29] In the case of **Tb**, the powder X-ray diffraction (PXRD) pattern (Figure S12 in the SI) gave no evidence of the presence of other crystalline phases, so that the species responsible for the EPR signal should be less than 5%.

In conclusion, we studied the magnetic anisotropy of three derivatives of the LnTRENSAL family using CTM. The set of CF parameters used to correctly reproduce these data provided an energy pattern different from the one extracted by luminescence measurements, especially in the case of **Tb** and **Dy**, for which no direct luminescence information was available for their ground-state multiplet. The use of CTM can thus efficiently flank spectroscopic techniques to model the magnetic anisotropy of lanthanide-based SMMs.

■ ASSOCIATED CONTENT

Supporting Information

Experimental details, crystal orientations and reference frames, torque curves and fits, PXRD patterns, EPR spectra, and composition of the states. This material is available free of charge via the Internet at http://pubs.acs.org.

■ AUTHOR INFORMATION

Corresponding Author

*E-mail: roberta.sessoli@unifi.it.

Notes

The authors declare no competing financial interest.

■ ACKNOWLEDGMENTS

We acknowledge the financial support of EC through ERC-AdG MolNanoMas (Grant 267746) and of MIUR through the Project "Futuro in Ricerca 2012" (RBFR12RPD1).

■ REFERENCES

(1) Gatteschi, D.; Sessoli, R.; Villain, J. *Molecular nanomagnets*. Oxford University Press: Oxford, UK, 2006.

(2) Ishikawa, N. *Polyhedron* **2007**, *26*, 2147−2153.

(3) Jiang, S.-D.; Liu, S.-S.; Zhou, L.-N.; Wang, B.-W.; Wang, Z.-M.; Gao, S. *Inorg. Chem.* **2012**, *51*, 3079−3087.

(4) Chilton, N. F.; Collison, D.; McInnes, E. J.; Winpenny, R. E.; Soncini, A. *Nat. Commun.* **2013**, *4*, 2551.

(5) Aravena, D.; Ruiz, E. *Inorg. Chem.* **2013**, *52*, 13770−13778.

(6) Baldoví, J. J.; Cardona-Serra, S.; Clemente-Juan, J. M.; Coronado, E.; Gaita-Ariño, A.; Palii, A. *J. Comput. Chem.* **2013**, *34*, 1961−1967.

(7) Baldoví, J. J.; Clemente-Juan, J. M.; Coronado, E.; Gaita-Ariño, A.; Palii, A. *J. Comput. Chem.* **2014**, *35*, 1930−1934.

(8) Boulon, M. E.; Cucinotta, G.; Luzon, J.; Degl'Innocenti, C.; Perfetti, M.; Bernot, K.; Calvez, G.; Caneschi, A.; Sessoli, R. *Angew. Chem., Int. Ed.* **2013**, *125*, 368−372.

(9) Cucinotta, G.; Perfetti, M.; Luzon, J.; Etienne, M.; Car, P. E.; Caneschi, A.; Calvez, G.; Bernot, K.; Sessoli, R. *Angew. Chem., Int. Ed.* **2012**, *51*, 1606−1610.

(10) Lucaccini, E.; Sorace, L.; Perfetti, M.; Costes, J.-P.; Sessoli, R. *Chem. Commun.* **2014**, *50*, 1648−1651.

(11) Kanesato, M.; Yokoyama, T.; Itabashi, O.; Suzuki, T. M.; Shiro, M. *Bull. Chem. Soc. Jpn.* **1996**, *69*, 1297−1302.

(12) Bernhardt, P. V.; Flanagan, B. M.; Riley, M. J. *Aust. J. Chem.* **2000**, *53*, 229−231.

(13) Dreiser, J.; Wäckerlin, C.; Ali, M. E.; Piamonteze, C.; Donati, F.; Singha, A.; Pedersen, K. S.; Rusponi, S.; Bendix, J.; Oppeneer, P. M. *ACS Nano* **2014**, *8*, 4662−4671.

(14) Pedersen, K. S.; Ungur, L.; Sigrist, M.; Sundt, A.; Schau-Magnussen, M.; Vieru, V.; Mutka, H.; Rols, S.; Weihe, H.; Waldmann, O. *Chem. Sci.* **2014**, *5*, 1650−1660.

(15) Flanagan, B. M.; Bernhardt, P. V.; Krausz, E. R.; Lüthi, S. R.; Riley, M. J. *Inorg. Chem.* **2002**, *41*, 5024−5033.

(16) Flanagan, B. M.; Bernhardt, P. V.; Krausz, E. R.; Lüthi, S. R.; Riley, M. J. *Inorg. Chem.* **2001**, *40*, 5401−5407.

(17) Perfetti, M.; Cucinotta, G.; Boulon, M. E.; El Hallak, F.; Gao, S.; Sessoli, R. *Chem.—Eur. J.* **2014**, *20*, 14051−14056.

(18) Kuz'min, M. *J. Magn. Magn. Mater.* **1996**, *154*, 333−338.

(19) Cornia, A.; Gatteschi, D.; Sessoli, R. *Coord. Chem. Rev.* **2001**, *219*, 573−604.

(20) Godin, M.; Tabard-Cossa, V.; Miyahara, Y.; Monga, T.; Williams, P.; Beaulieu, L.; Lennox, R. B.; Grutter, P. *Nanotechnology* **2010**, *21*, 075501.

(21) Cornia, A.; Affronte, M.; Jansen, A. G. M.; Gatteschi, D.; Caneschi, A.; Sessoli, R. *Chem. Phys. Lett.* **2000**, *322*, 477−482.

(22) Cornia, A.; Affronte, M.; Jansen, A. G. M.; Abbati, G. L.; Gatteschi, D. *Angew. Chem., Int. Ed.* **1999**, *38*, 2264−2266.

(23) Rigamonti, L.; Cornia, A.; Nava, A.; Perfetti, M.; Boulon, M.-E.; Barra, A.-L.; Zhong, X.; Park, K.; Sessoli, R. *Phys. Chem. Chem. Phys.* **2014**.

(24) Cornia, A.; Jansen, A. G. M.; Affronte, M. *Phys. Rev. B* **1999**, *60*, 12177−12183.

(25) Sievers, J. *Z. Phys. B: Condens. Matter* **1982**, *45*, 289−296.

(26) Rinehart, J. D.; Long, J. R. *Chem. Sci.* **2011**, *2*, 2078−2085.

(27) Görller-Walrand, C.; Binnemans, K. *Handbook of Physics and Chemistry of Rare Earths* **1996**, *23*, 121−283.

(28) Marx, R.; Moro, F.; Dörfel, M.; Ungur, L.; Waters, M.; Jiang, S.; Orlita, M.; Taylor, J.; Frey, W.; Chibotaru, L. *Chem. Sci.* **2014**, *5*, 3287−3293.

(29) Baker, J.; Hutchison, C.; Leask, M.; Martineau, P.; Robinson, M. *Proc. R. Soc. London A* **1987**, *413*, 515−528.

DOI: 10.1021/acs.inorgchem.5b00288
Inorg. Chem. 2015, 54, 3090−3092

Determination of magnetic anisotropy in the LnTRENSAL complexes (Ln = Tb, Dy, Er) by torque magnetometry

Mauro Perfetti [†], Eva Lucaccini[†], Lorenzo Sorace[†], J. Pierre Costes[‡] and Roberta Sessoli[†]*

[†]Dipartimento di Chimica "Ugo Schiff" and UdR INSTM, Università degli Studi di Firenze, Via della Lastruccia 3-13, 50019 Sesto Fiorentino, Italy.

[‡]Laboratoire de Chimie de Coordination 205, route de Narbonne 31077 Toulouse, Cedex 4, France

SUPPORTING INFORMATION

Table of contents:

I. Synthesis and experimental setup

Crystalline samples of **Tb**, **Dy** and **Er** were obtained using a synthetic procedure previously reported.[1] Their structure was checked with a Single Crystal diffractometer Xcalibur3 with a Mo source (K_α, λ=0.71 Å). Xcalibur3 is a 4 cycles kappa geometry diffractometer equipped with a Sapphire 3 CCD detector.

DC magnetic measurement were performed by using a Quantum Design MPMS SQUID magnetometer on powders pressed in a pellet. The cantilever torque measurements were performed using a home made two-legs CuBe cantilever separated by 0.1 mm from a gold plate. The cantilever was inserted in an Oxford Instruments MAGLAB2000 platform with automated rotation of the cantilever chip in a vertical magnet. The capacitance of the cantilever was detected with a Andeen-Hegerling2500 A Ultra Precision Capacitance Bridge. EPR spectra of **Tb** were recorded at 5K with a E500 Bruker spectrometer for the X band, using a dual mode cavity ($\nu_\perp$~9.6 GHz, $\nu_{//}$~9.4 GHz).

II. Position of the crystals

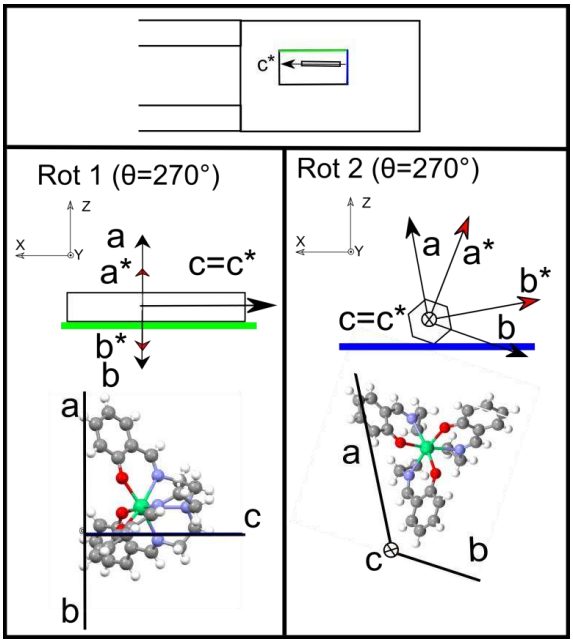

Fig. S1: Position of the **Tb** crystal.

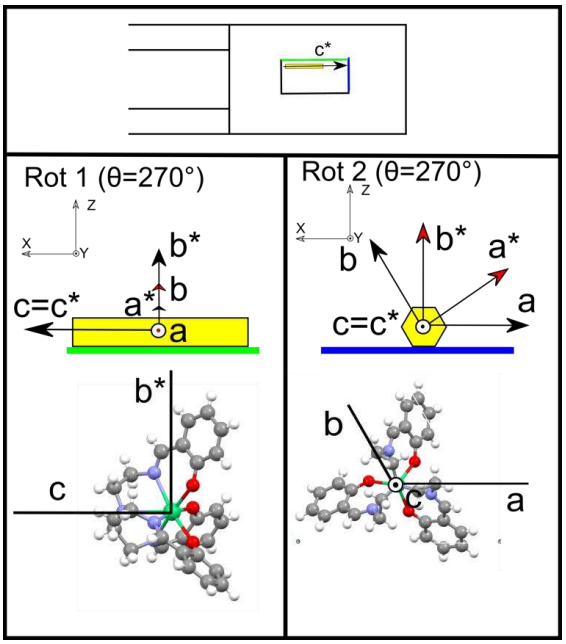

Fig. S2: Position of the **Dy** crystal.

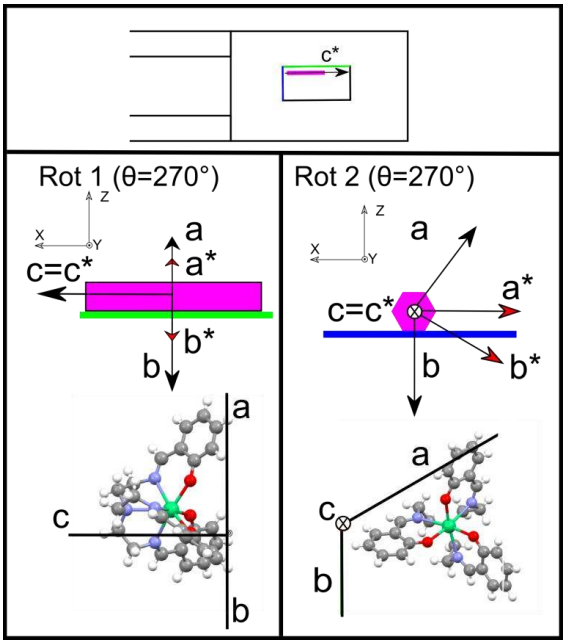

Fig. S3: Position of the **Er** crystal.

III. Reference frame for rotations

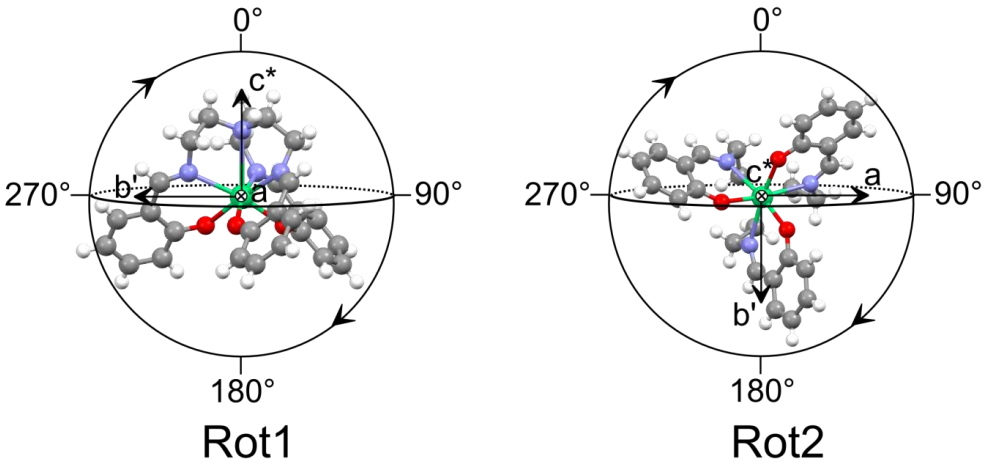

Fig. S4: Graphical representation of Rot1 (from C_3 axis to *xy* plane) and Rot2 (in-plane). The angle reported is θ.

IV. Torque data fit

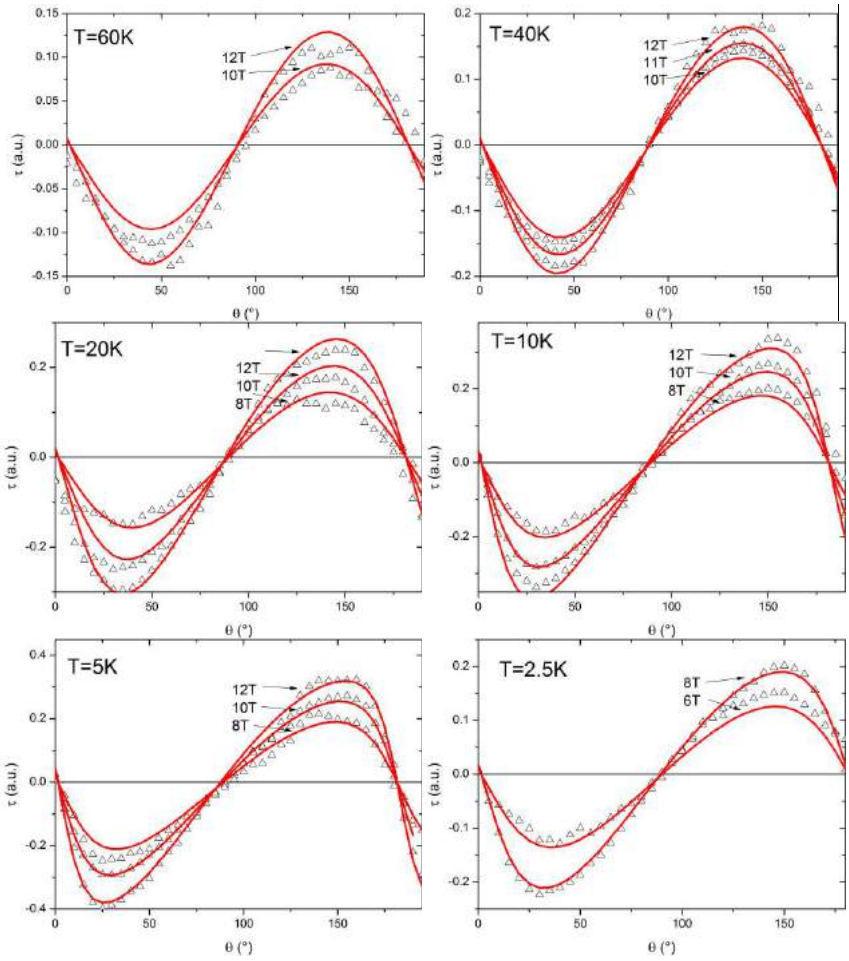

Fig. S5: Experimental (empty triangles) and best-fit (red lines) magnetic torque measured in rot1 for **Tb** at different fields and temperatures.

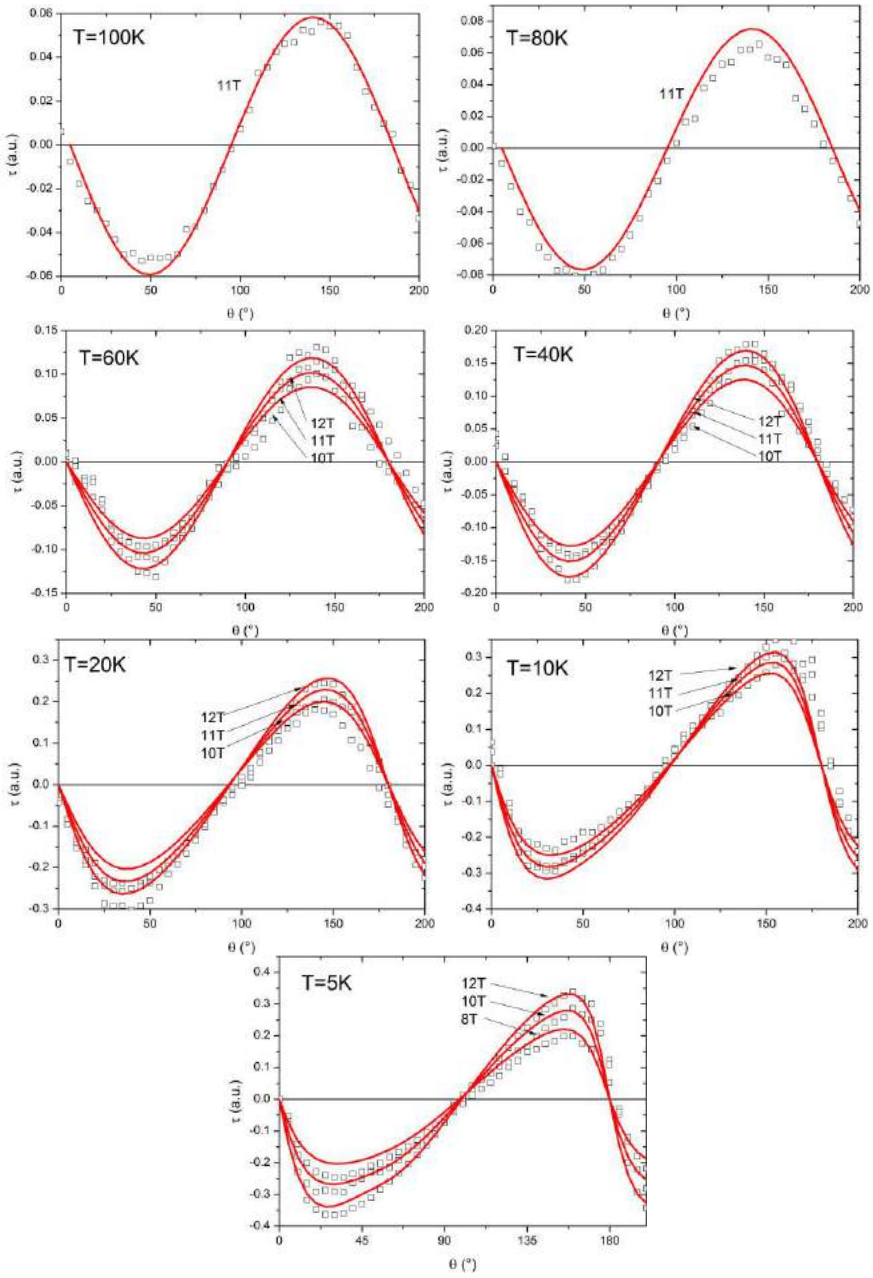

Fig. S6: Experimental (empty triangles) and best-fit (red lines) magnetic torque measured in rotı for **Dy** at different fields and temperatures.

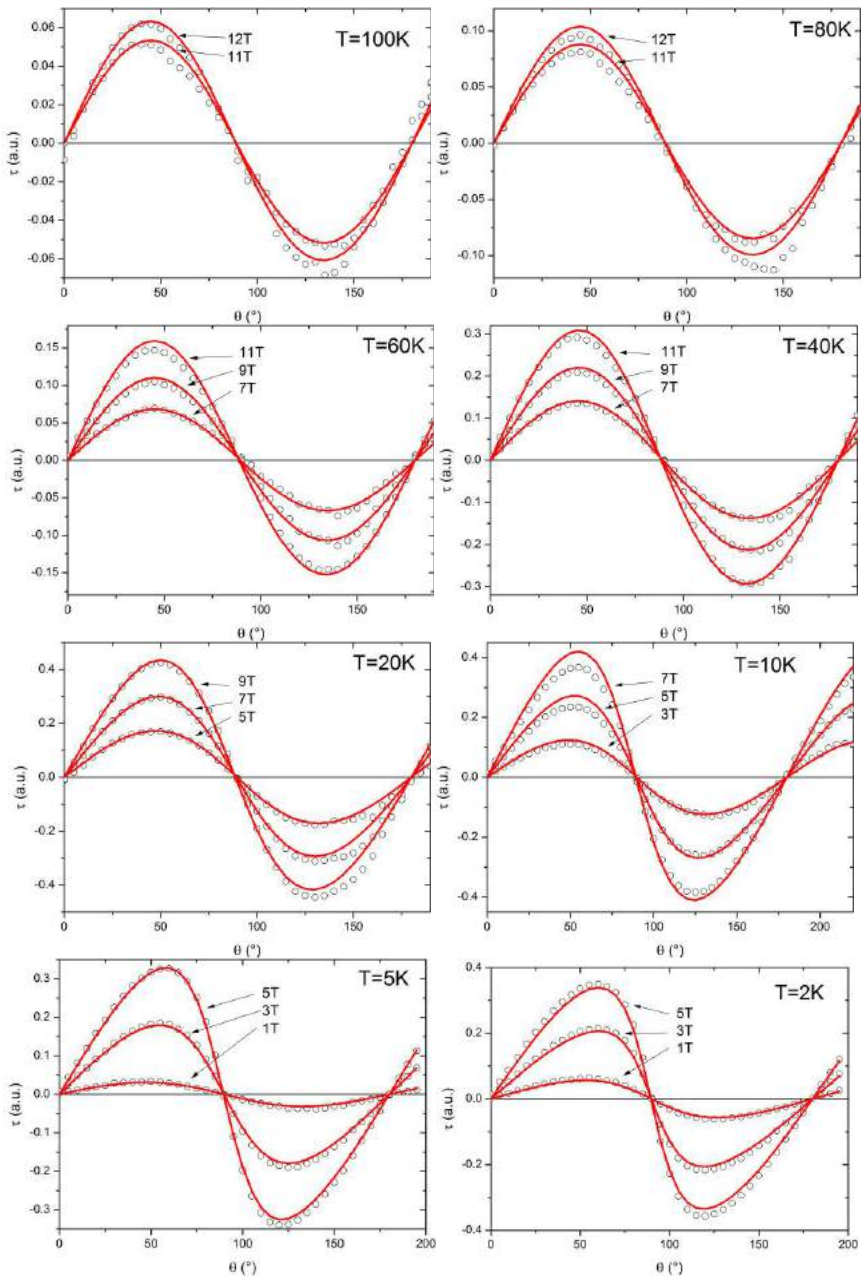

Fig. S7: Experimental (empty triangles) and best-fit (red lines) magnetic torque measured in rot1 for **Er** at different fields and temperatures.

V. In-plane rotation

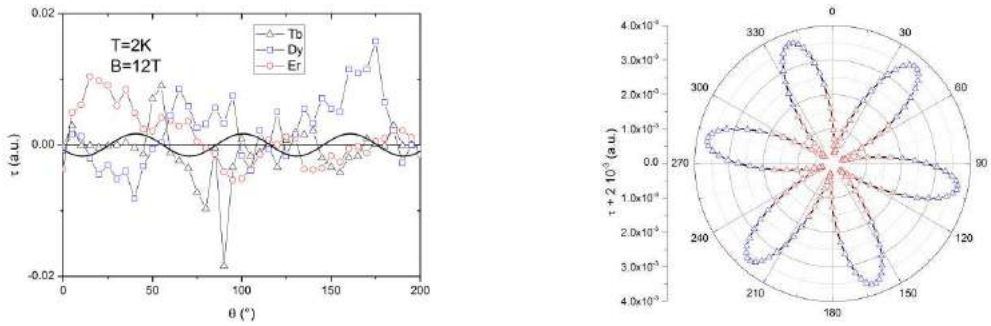

Fig. S8: Left: Angular dependence of torque measured at 2 K and 12 T for **Tb**, **Dy** and **Er** in rot2. Black line refers to the simulated curve for **Tb** (similar behavior is observed for **Dy** and **Er**). Right: Polar plot for the in-plane rotation of Tb. Blue triangles refer to positive values of τ while red triangles refer to negative values.

VI. EPR spectra

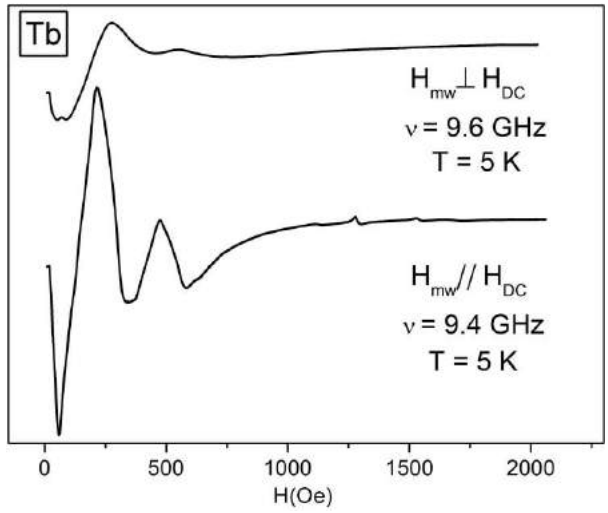

Fig. S9: EPR spectra of a microcrystalline powder spectrum of **Tb** in perpendicular (upper) and parallel (lower) polarization mode of the microwave.

VII. Comparison with Flanagan et al.

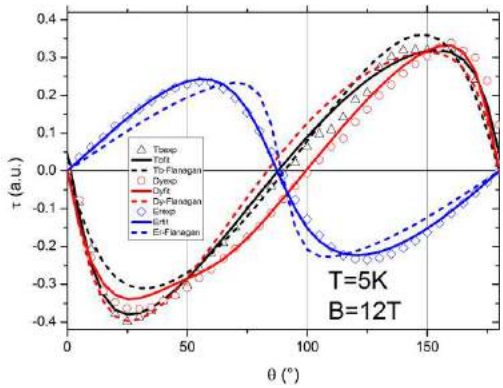

Fig. S10: Angular dependence of torque in rot1, for the three derivatives, measured at 5 K and 12 T: experimental data (empty symbols); simulated data using CF parameters of Flanagan *et al.*[2] (dashed lines); best fit curves obtained with parameters reported in Tab. 1 (continuous lines).

VIII. Fitting of χT vs T curves

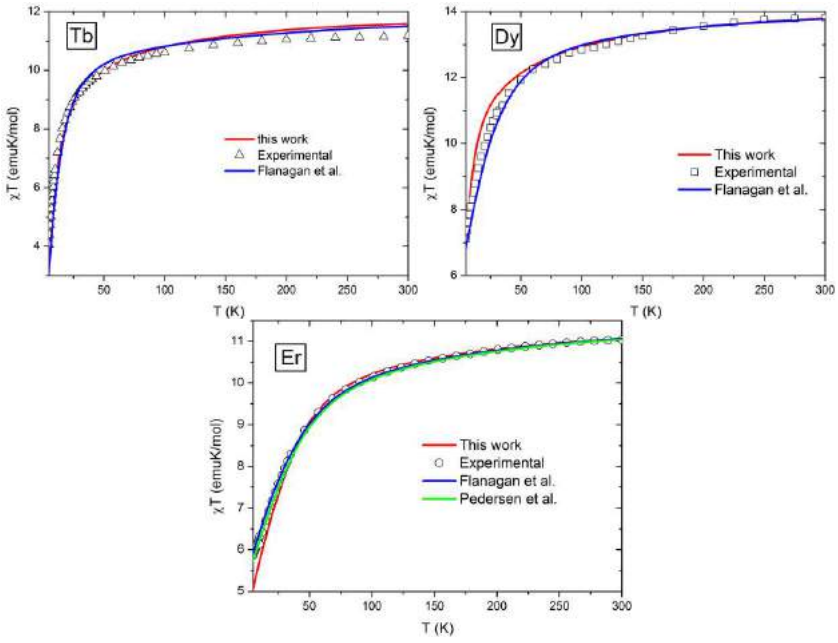

Fig. S11: χT vs T plot for **Tb**, **Dy** and **Er** (experimental=empty symbols, this work=red lines, Flanagan *et al.*[2]=blue lines, Pedersen *et al.*[3]=green line).

IX. XRD powder diffraction

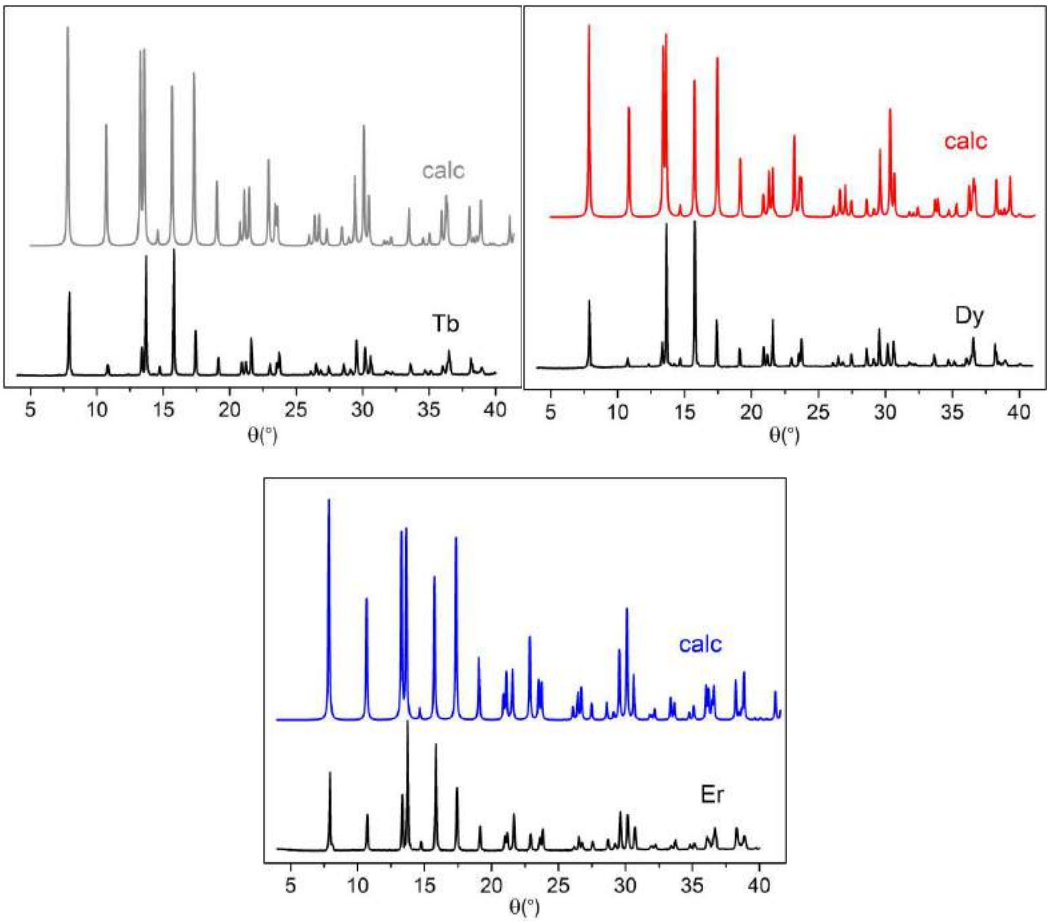

Fig. S12: XRPD pattern of **Tb**, **Dy** and **Er** and comparison to the corresponding ones calculated using the molecular structure obtained by single crystal x-ray diffractometry.

X. Details on formalism and conversions

Parameter	Tb	Dy	Er
α	$-\frac{1}{9\cdot 11}$	$-\frac{2}{9\cdot 5\cdot 7}$	$\frac{4}{9\cdot 25\cdot 7}$
β	$\frac{2}{27\cdot 5\cdot 121}$	$-\frac{8}{27\cdot 5\cdot 7\cdot 11\cdot 13}$	$\frac{2}{9\cdot 5\cdot 7\cdot 11\cdot 13}$
γ	$-\frac{1}{81\cdot 7\cdot 13\cdot 121}$	$\frac{4}{27\cdot 7\cdot 121\cdot 169}$	$\frac{8}{27\cdot 7\cdot 121\cdot 169}$

Tab. S1: Reduced matrix elements used for the conversion of Wybourne's parameters into Stevens' parameters[4].

$$\mathcal{H} = g_J \mu_B \boldsymbol{J}\cdot\boldsymbol{B} + b_2^0\boldsymbol{O_2^0} + b_4^0\boldsymbol{O_4^0} + b_6^0\boldsymbol{O_6^0} + b_4^3\boldsymbol{O_4^3} + b_6^3\boldsymbol{O_6^3} + b_6^{-3}\boldsymbol{O_6^{-3}} + b_6^6\boldsymbol{O_6^6} + b_6^{-6}\boldsymbol{O_6^{-6}}$$

Eq. S1: Spin Hamiltonian used for the fits, written according to Stevens' formalism.

Parameter (cm^{-1})	**Tb**	**Dy**	**Er**
b_2^o	2.84(0.77)	2.25(0.12)	-0.922(0.146)
b_4^o	6.1(5.0) 10^{-4}	2.03(0.59) 10^{-3}	-4.5(9.0) 10^{-4}
b_6^o	0.988(1.482) 10^{-4}	8.467(1.184) 10^{-5}	1.23(0.11) 10^{-4}
b_4^3	-0.4868(0.1883)	-0.2462(0.0172)	0.3153(0.0306)
b_6^3	-1.02(0.72) 10^{-4}	8.93(0.91) 10^{-4}	-9.70(1.83) 10^{-4}
b_6^{-3}	-6.03(6.03) 10^{-4}	-1.01(0.44) 10^{-3}	0.795(2.38) 10^{-3}
b_6^6	-1.211(0.945) 10^{-3}	9.19(1.84) 10^{-4}	9.63(3.08) 10^{-4}
b_6^{-6}	8.95(8.95) 10^{-4}	0.0(-)	-2.36(7.08) 10^{-4}

Tab. S2: Stevens' parameters providing the best fit to the torque data. The coefficients b_k^q contain the appropriate reduced matrix elements α, β, γ reported in Tab. S1. The relations used to convert the Wybourne's parameters into Stevens' can be found in literature[5]. The initial guesses for the fit were the CF parameters reported by Flanagan *et al.*.[6]

XI. Energy levels and composition of states

E (cm^{-1}) Flanagan *et al.*[6]	E (cm^{-1}) this work	Composition this work
552,s	479,s	$41\%\|+6\rangle, 9\%\|+3\rangle, 9\%\|-3\rangle, 41\%\|-6\rangle$
530,s	468,s	$46\%\|+6\rangle, 46\%\|-6\rangle$
517,d	380,d	$36\%\|\pm5\rangle, 23\%\|\pm2\rangle, 5\%\|\mp1\rangle, 5\%\|\mp2\rangle, 17\%\|\mp4\rangle, 8\%\|\mp5\rangle$
403,d	345,d	$29\%\|\pm5\rangle, 21\%\|\mp1\rangle, 47\%\|\mp4\rangle$
300,s	331,s	$9\%\|+6\rangle, 28\%\|+3\rangle, 25\%\|0\rangle, 28\%\|-3\rangle, 9\%\|-6\rangle$
76,s	165,s	$46\%\|+3\rangle, 46\%\|-3\rangle$
61,d	91,d	$11\%\|\pm4\rangle, 7\%\|\pm2\rangle, 5\%\|\pm1\rangle, 53\%\|\mp2\rangle, 19\%\|\mp5\rangle$
22,d	22,d	$19\%\|\pm4\rangle, 67\%\|\pm1\rangle, 9\%\|\mp2\rangle, 5\%\|\mp5\rangle$
0,s	0,s	$13\%\|+3\rangle, 72\%\|0\rangle, 13\%\|-3\rangle$

Tab. S3: Energies and composition of the m_j sublevels of the ground J=6 multiplet for **Tb** using best fit CF parameters (s= singlet, d= doublet).

E (cm^{-1}) Flanagan *et al.*[6]	E (cm^{-1}) this work	Composition this work
787	709	$77\%\left\|\pm\frac{15}{2}\right\rangle, 21\%\left\|\pm\frac{9}{2}\right\rangle$
645	519	$17\%\left\|\pm\frac{13}{2}\right\rangle, 28\%\left\|\pm\frac{7}{2}\right\rangle, 5\%\left\|\pm\frac{5}{2}\right\rangle, 7\%\left\|\mp\frac{5}{2}\right\rangle, 22\%\left\|\mp\frac{7}{2}\right\rangle, 14\%\left\|\mp\frac{13}{2}\right\rangle$
577	396	$49\%\left\|\pm\frac{11}{2}\right\rangle, 30\%\left\|\pm\frac{5}{2}\right\rangle, 5\%\left\|\mp\frac{1}{2}\right\rangle, 10\%\left\|\mp\frac{13}{2}\right\rangle$
414	291	$20\%\left\|\pm\frac{15}{2}\right\rangle, 48\%\left\|\pm\frac{9}{2}\right\rangle, 20\%\left\|\pm\frac{3}{2}\right\rangle, 10\%\left\|\mp\frac{3}{2}\right\rangle$
172	131	$21\%\left\|\pm\frac{11}{2}\right\rangle, 18\%\left\|\pm\frac{5}{2}\right\rangle, 9\%\left\|\mp\frac{1}{2}\right\rangle, 9\%\left\|\mp\frac{7}{2}\right\rangle, 34\%\left\|\mp\frac{13}{2}\right\rangle$
98	23	$13\%\left\|\pm\frac{9}{2}\right\rangle, 64\%\left\|\mp\frac{3}{2}\right\rangle, 17\%\left\|\mp\frac{9}{2}\right\rangle$
50	14	$5\%\left\|\pm\frac{13}{2}\right\rangle, 9\%\left\|\pm\frac{11}{2}\right\rangle, 8\%\left\|\pm\frac{7}{2}\right\rangle, 26\%\left\|\pm\frac{5}{2}\right\rangle, 5\%\left\|\mp\frac{1}{2}\right\rangle, 10\%\left\|\mp\frac{5}{2}\right\rangle, 20\%\left\|\mp\frac{7}{2}\right\rangle, 12\%\left\|\mp\frac{13}{2}\right\rangle$
0	0	$9\%\left\|\pm\frac{11}{2}\right\rangle, 10\%\left\|\pm\frac{1}{2}\right\rangle, 65\%\left\|\mp\frac{1}{2}\right\rangle, 7\%\left\|\mp\frac{7}{2}\right\rangle$

Tab. S4: Energies and composition of the m_j sublevels of the ground J=15/2 multiplet for **Dy** using best fit CF parameters.

E (cm^{-1}) Flanagan et al.[6]	E (cm^{-1}) this work	Composition this work
646	652	$61\%\left\|\pm\frac{7}{2}\right\rangle, 13\%\left\|\pm\frac{1}{2}\right\rangle, 17\%\left\|\mp\frac{5}{2}\right\rangle$
614	640	$58\%\left\|\pm\frac{9}{2}\right\rangle, 33\%\left\|\pm\frac{3}{2}\right\rangle$
562	597	$12\%\left\|\pm\frac{7}{2}\right\rangle, 17\%\left\|\pm\frac{1}{2}\right\rangle, 49\%\left\|\mp\frac{5}{2}\right\rangle, 20\%\left\|\mp\frac{11}{2}\right\rangle$
315	310	$70\%\left\|\pm\frac{15}{2}\right\rangle, 22\%\left\|\mp\frac{15}{2}\right\rangle, 5\%\left\|\mp\frac{3}{2}\right\rangle$
114	105	$67\%\left\|\pm\frac{11}{2}\right\rangle, 11\%\left\|\pm\frac{5}{2}\right\rangle, 17\%\left\|\mp\frac{1}{2}\right\rangle$
108	95	$6\%\left\|\pm\frac{3}{2}\right\rangle, 49\%\left\|\mp\frac{3}{2}\right\rangle, 40\%\left\|\mp\frac{9}{2}\right\rangle$
55	63	$9\%\left\|\pm\frac{13}{2}\right\rangle, 11\%\left\|\pm\frac{5}{2}\right\rangle, 14\%\left\|\pm\frac{1}{2}\right\rangle, 28\%\left\|\mp\frac{1}{2}\right\rangle, 6\%\left\|\mp\frac{5}{2}\right\rangle, 5\%\left\|\mp\frac{7}{2}\right\rangle, 18\%\left\|\mp\frac{13}{2}\right\rangle$
0	0	$6\%\left\|\pm\frac{5}{2}\right\rangle, 10\%\left\|\mp\frac{1}{2}\right\rangle, 15\%\left\|\mp\frac{7}{2}\right\rangle, 63\%\left\|\mp\frac{13}{2}\right\rangle$

Tab. S5: Energies and composition of the m_j sublevels of the ground J=15/2 multiplet for **Er** using best fit CF parameters.

XII. References

1. Kanesato, M.; Yokoyama, T.; Itabashi, O.; Suzuki, T. M.; Shiro, M., *Bull. Chem. Soc. Jpn.* **1996,** *69*, 1297-1302.
2. Flanagan, B. M.; Bernhardt, P. V.; Krausz, E. R.; Lüthi, S. R.; Riley, M. J., *Inorg. Chem.* **2002,** *41*, 5024-5033.
3. Pedersen, K. S.; Ungur, L.; Sigrist, M.; Sundt, A.; Schau-Magnussen, M.; Vieru, V.; Mutka, H.; Rols, S.; Weihe, H.; Waldmann, O., *Chemical Science* **2014,** 5, 1650-1660.
4. Abragam, A.; Bleaney, B., *Electron Paramagnetic Resonance of Transition Ions*. Dover: New York, 1986.
5. Stewart, G., *Hyperfine Interact.* **1985,** *23*, 1-16.
6. Flanagan, B. M.; Bernhardt, P. V.; Krausz, E. R.; Lüthi, S. R.; Riley, M. J., *Inorg. Chem.* **2001,** *40*, 5401-5407.

ChemPubSoc Europe

DOI: 10.1002/chem.201404218

CHEMISTRY A European Journal Full Paper

Magnetic Anisotropy

Angular-Resolved Magnetometry Beyond Triclinic Crystals Part II: Torque Magnetometry of Cp*ErCOT Single-Molecule Magnets**

Mauro Perfetti,[a] Giuseppe Cucinotta,[a] Marie-Emmanuelle Boulon,[a] Fadi El Hallak,[b] Song Gao,[c] and Roberta Sessoli*[a]

Dedicated to Professor Andrea Dei on the occasion of his retirement

Abstract: The experimental investigation of the molecular magnetic anisotropy in crystals in which the magnetic centers are symmetry related, but do not have a parallel orientation has been approached by using torque magnetometry. A single crystal of the orthorhombic organometallic Cp*ErCOT [Cp* = pentamethylcyclopentadiene anion ($C_5Me_5^-$); COT = cyclooctatetraenedianion ($C_8H_8^{2-}$)] single-molecule magnet, characterized by the presence of two nonparallel families of molecules in the crystal, has been investigated above its blocking temperature. The results confirm an Ising-type anisotropy with the easy direction pointing along the pseudo-symmetry axis of the complex, as previously suggested by out-of-equilibrium angular-resolved magnetometry. The use of torque magnetometry, not requiring the presence of magnetic hysteresis, proves to be even more powerful for these purposes than standard single-crystal magnetometry. Furthermore, exploiting the sensitivity and versatility of this technique, magnetic anisotropy has been investigated up to 150 K, providing additional information on the crystal-field splitting of the ground *J* multiplet of the Er^{III} ion.

Introduction

One of the key properties of magnetic materials is magnetic anisotropy because it governs the process of relaxation of the magnetization in traditional materials, as well as in molecules showing magnetic bistability of pure molecular origin, otherwise known as single-molecule magnets (SMMs).[1] Lanthanide ions, with their unquenched orbital contribution to the magnetic moment are largely exploited in both conventional and molecular materials, and current efforts are devoted to optimize the coordination environment to maximize magnetic anisotropy.[2] Several approaches are actually employed to correlate the magnetic anisotropy to the molecular structure.[3] The simplest ones are based on the spatial distribution of the electronic charges of the ligands,[3b] but it has been recently shown that misleading results can be obtained, as in the case of the complexes with the DOTA ligand (H_4DOTA = 1,4,7,10-tetraazacyclododecane-1,4,7,10-tetraacetic acid).[4] Although the validity of DFT approaches has still to be proven, encouraging results have been obtained with post Hartree–Fock methods, such as those implemented in the MOLCAS package.[5] However, a direct comparison with accurate experimental information on the strength and orientation of the magnetic anisotropy is mandatory to validate these predictive methods.[6] This is of particular relevance for molecular systems in which the low-symmetry environment does not allow one to make any prior assumptions.

A powerful experimental technique to extract the orientation of the magnetic anisotropy tensor and its correlation to the magnetic structure is angular-resolved magnetometry on single crystals.[4a,7] Several important results have been achieved with this technique, including the observation of chiral, or toroidal, arrangement of the spins in Dy^{III} triangles.[8] However, this technique provides unambiguous results only when the molecular system crystallizes in a triclinic space group or, generally, when the point symmetry of the crystal is not higher than the symmetry of the investigated magnetic site. Unfortunately, this occurs in only a minor fraction of the experimental situations. A key example we have recently reported is the case of the organometallic SMM Cp*ErCOT,[7a] in which Cp* is the pentamethylcyclopentadiene anion and COT is the cyclooctatetraene dianion (see Figure 1a), crystallizing in the orthorhombic space group *Pnma*.[9] Because the molecules lie on a mirror plane only two families of magnetically nonequivalent

[a] M. Perfetti, G. Cucinotta, Dr. M.-E. Boulon, Prof. R. Sessoli
Dipartimento di Chimica Ugo Schiff
Università degli Studi di Firenze
Via della Lastruccia 3-13, 50019 Sesto Fiorentino (Italy)
E-mail: roberta.sessoli@unifi.it

[b] Dr. F. El Hallak
1st Physikalisches Institut, Universitaet Stuttgart
Pfaffenwaldring 57, 70550 Stuttgart (Germany)

[c] Prof. S. Gao
Beijing National Laboratory of Molecular Science
State Key Laboratory of Rare Earth Materials Chemistry and Applications
College of Chemistry and Molecular Engineering, Peking University
Beijing 100871 (P. R. China)

[**] Cp* = pentamethylcyclopentadiene anion ($C_5Me_5^-$); COT = cyclooctatetraene dianion ($C_8H_8^{2-}$).

Supporting information for this article is available on the WWW under http://dx.doi.org/10.1002/chem.201404218.

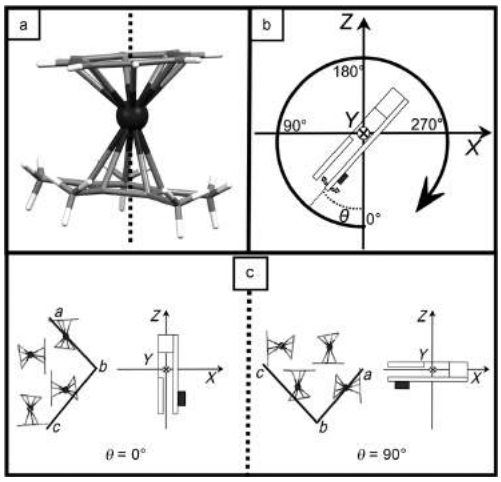

Figure 1. a) View of the molecular structure of Cp*ErCOT with the dotted line representing the orientation of the easy axis as estimated in ref. [7a]; b) schematic view of the CuBe cantilever; c) crystal packing and orientation of the molecules in the plane scanned by torque magnetometry at two different angles.

molecules, that is, with anisotropy tensors not parallel, are present in the crystal. The molecular pseudo symmetry axes of the two families are almost orthogonal to each other (see Figure 1 c). In our recent report we have exploited the SMM nature of the complex,[7a] and in particular the presence of magnetic hysteresis below 5 K, to extract information on the molecular anisotropy tensor by collecting out-of-equilibrium angular-resolved magnetization data. The results were supported by state of the art ab initio calculations[10] and confirmed the validity of the strategy based on the use of organometallic complexes of a single lanthanide ion.

Unfortunately, most investigated lanthanide complexes and SMMs do not show hysteresis at temperatures usually achievable with SQUID magnetometers and, though powerful, the developed protocol can be applied only in a limited number of cases. Herein, we demonstrate that magnetic anisotropy in molecules that are not in a parallel orientation can be assessed by employing angular-resolved torque magnetometry.[11] Despite being one of the first techniques used in magnetochemistry,[12] torque magnetometry's intrinsic superiority in the analysis of magnetic anisotropy has remained mostly unexploited, apart from few exceptions either among SMMs[13] or other types of magnetic molecules.[14] This superiority clearly emerges when addressing Cp*ErCOT SMM, which has been previously investigated by standard angular-resolved magnetometry.[7a]

Results and Discussion

Torque magnetometry is a very sensitive technique and suitable crystals for measurement are not larger than those commonly used in single-crystal X-ray diffractometry. Owing to the strong air sensitivity of the Cp*ErCOT compound, single crystals, grown from a cooled toluene solution as previously reported,[9b] were manipulated in a glove box, whereas the crystal faces indexing with an X-ray diffractometer and the installation on the cantilever were performed under nitrogen-gas flux. An indexed crystal (with mass of the order of a few μg) was mounted with its (1 0 1) face on a two-legged gold-plated CuBe cantilever acting as one plate of a capacitor. The deflection of the cantilever, owing to the torque exerted by the field on the magnetic sample, resulted in a change of the capacity. If the deflection is limited to a few percent, the response of the cantilever and the consequent change in capacity can be considered linear with the torque. The cantilever, having its plates parallel to the *Y* axis in the *XYZ* laboratory frame depicted in Figure 1 b, can be rotated in the *XZ* plane with the external field applied along the *Z* direction.

The crystal was placed on the cantilever so that the applied magnetic field scans the *ac* crystallographic plane as indicated in Figure 1 c. We focused our attention on this rotation, which corresponds to rot2 in ref. [7a], because it is characterized by an almost isotropic magnetic signal and thus is poorly informative when investigated by standard single-crystal magnetometry. The two symmetry-related families of molecules have in fact their easy axis almost perpendicular to each other (95°) and the magnetic anisotropy is nearly cancelled. Data were collected at variable temperature and magnetic field extending the angular range to 250° to provide some redundancy of data compared to the expected periodicity of 180°. At any investigated temperature the rotation was also performed in zero field to evaluate the contribution arising from the deflection of the cantilever owing to its own mass and that of the sample. This spurious contribution can be easily identified because it is characterized by a 360° periodicity.

In Figure 2 the capacity measured at 10 K and variable field is reported. The angle $\theta = 0°$ coincides to the cantilever being parallel to the vertical magnetic field (see Figure 1 c), and corresponds to one of the two families of molecules having their

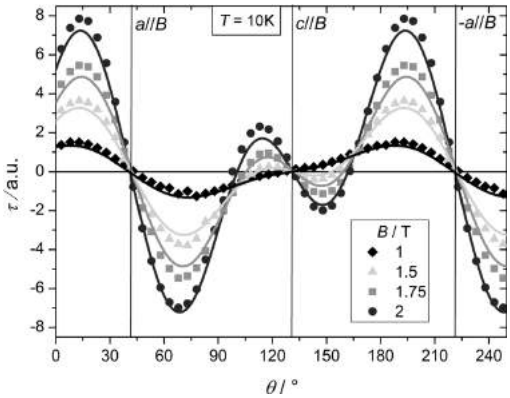

Figure 2. Angular dependence of the magnetic torque measured on a single crystal of Cp*ErCOT at $T = 10$ K at different applied magnetic fields. The lines correspond to the simulation using an effective $S = 1/2$ spin (Ising limit). See text for best fit parameters.

pseudo C_∞ symmetry axis roughly parallel to the applied field. The crystal symmetry also imposes that torque signal vanishes when the field is applied along the *a* and *c* crystallographic axes, as indeed observed for $\theta = 41$ and 131° (see also the Supporting Information, Figure S1). Beyond the intensity increase, the modification of the shape observed when increasing the magnetic field from 1 T to 2 T is remarkable, and is indeed the distinctive feature of the torque measurements providing the most important information.

Before entering in the details of the analysis we recall here some basic features of the technique that are essential to understand the obtained results.[11,12d,e] Starting from the definition of magnetic torque ($\boldsymbol{\tau} = \mathbf{M} \times \mathbf{B}$), where $\mathbf{M}$ is the magnetic moment and **B** the magnetic field. Taking into account that in our experimental setup only the *Y* component is measured, we have:

$$\tau_y = M_z B_x - M_x B_z \quad (1)$$

where the index *x* and *z* refer to the principal axes of the molecular anisotropy, assumed here for simplicity to lie in the *XZ* plane of the laboratory frame, that is, *y* and *Y* are coincident. In the case of a paramagnet, as well as of a SMM above its blocking temperature, when the field is weak enough to consider that the magnetization is linear with the field, equation (1) becomes:

$$\tau_y = \chi_z B_z B_x - \chi_x B_x B_x = B^2 \sin\varphi\cos\varphi(\chi_z - \chi_x) \quad (2)$$

in which φ is the angle formed by the field, applied along the the *Z* laboratory axis, with the *z* molecular axis, the latter corresponding to the easy axis. The angular dependence is significantly different from that observed in angle-resolved SQUID magnetometry:

$$M = B(\chi_z \cos^2\varphi + \chi_x \sin^2\varphi) \quad (3)$$

The torque in particular goes to zero when the field is applied along the principal axes of the magnetic anisotropy. For small enough magnetic fields, if two molecules are oriented exactly 90° one from each other, the sum of their contributions would result in zero torque. This is confirmed by calculations on a simplified model (see Figure 3a) taking into account two orthogonal strictly Ising molecules with an effective spin $S = 1/2$ and a $g_{eff} = Jg_L = 18$, in which $J = L + S = 15/2$ is the total angular momentum for the ground doublet and $g_L = 6/5$ is the Landé factor for Er^{III}. Therefore, the technique is not more informative than standard magnetometry, the latter providing also an isotropic response in a similar case. However, if the $g\mu_B B/k_B T$ ratio is large enough for the system to approach magnetic saturation, the situation changes dramatically, as shown in Figure 3b. In fact, close to saturation the curve becomes strongly asymmetric, with a steep variation when the field crosses the hard direction. This can be intuitively understood, saying that for low temperature it is sufficient that the field orientation deviates slightly from the hard (*x*) direction to get a small component along the easy axis (*z*) able to induce a significant magnetization. This makes the first term of equation (1) quite large and consequently a strong torque is observed. The same does not occur when the field is close to the easy axis (*z*) because the resulting small component of the field along the hard direction has little effect on the hard component of the magnetization, even at low temperature. A more gradual increase of the torque is thus observed around the easy axis.

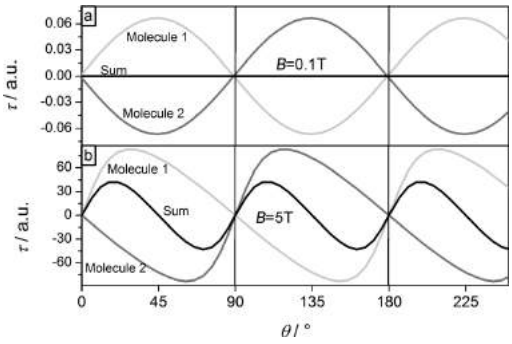

Figure 3. Calculated magnetic torque resulting from two orthogonal Ising spins at 10 K and at two different magnetic fields: a) 0.1 T and b) 5 T). The individual contributions are shown as light and medium gray, and the resultant signal is drawn in black.

It must also be said that in the case of standard SQUID magnetometry the application of a strong field induces deviation from equation (3) and additional features become visible in the angular dependence of the magnetic susceptibility. These, however, are superimposed to a strong isotropic signal, whereas torque measurements are insensitive to isotropic magnetization. Moreover, a small unavoidable misalignment of the crystal, resulting in rotating not along a principal axis, has no significant effect in torque measurements, but can induce a strong spurious modulation of the signal in angular-resolved magnetometry.

In Figure 2 the measured torque of Cp*ErCOT shows oscillations with different amplitude in contrast to the regular features of Figure 3b. This is a clear indication that the two families of molecules are not oriented with their easy axis exactly at 90°. The experimental data are in fact well reproduced (Figure 2, solid lines), with the previously described Ising model assuming the same angle between the two Ising directions, as in ref. [7a], and the g_{eff} factor free to adjust (more fits available in the Supporting Information, Figure S2). A scale factor has been introduced, given the incertitude on the mass of the sample and on the elastic constant of the cantilever. The latter has been assumed to be temperature independent because the Young modulus of CuBe varies only 6% over the entire investigated range.[15] The best fit of the effective *g* value at 10 K, $g_{eff} = 19.4 \pm 0.2$, is in reasonable agreement with the value expected for Er^{III} ions in the easy-axis limit.

One of the advantages of the use of torque magnetometers based on cantilevers is their high sensitivity. Combining this with the fact that only the anisotropic part of the magnetic re-

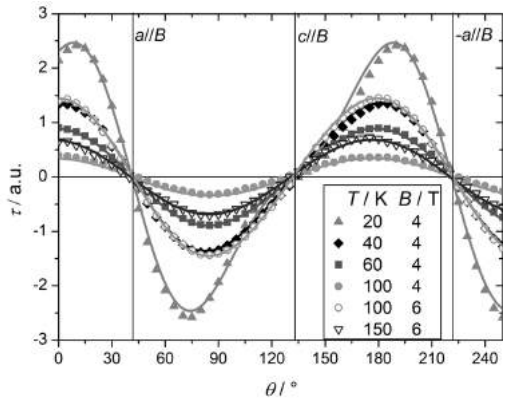

Figure 4. Angular dependence of the magnetic torque measured on a single crystal of Cp*ErCOT at variable temperature and applied fields. Filled symbols: $B=2$ T, empty symbols: $B=4$ T. The lines correspond to the simulations performed by using the spin Hamiltonian reported in equation (4). See text for best fit parameters.

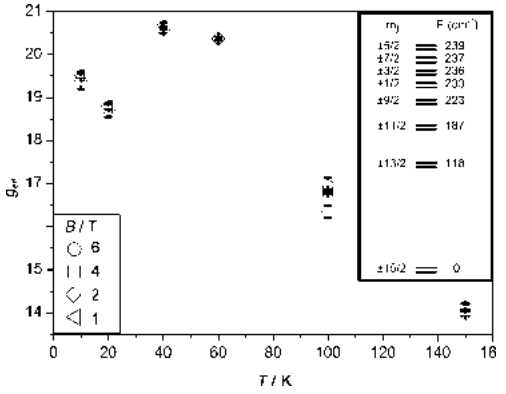

Figure 5. Values obtained for the g_{eff} factor at different temperatures and fields by fitting the data of Figures 4 and S2 with an Ising Hamiltonian. Inset shows the doublets pattern of the $J=15/2$ ground multiplet calculated with the best fit CF parameters, $B_2^0=-1.3\pm0.1$ cm^{-1} and $B_4^0=-3\pm1\times10^{-3}$ cm^{-1}, obtained in the simulation of the data of Figure 4 and S3.

sponse is measured allows the magnetic characterization to be easily extended to high temperatures. In Figure 4 the angular dependence of the torque measured for different temperatures is reported (more fields and temperatures available in the Supporting Information, Figure S3). It is clear that, on increasing the temperature, the curves become more sinusoidal-like as the effect of magnetic saturation becomes negligible.

By reproducing the curves by using the simple Ising model previously described, the experimental data can be fitted with g_{eff} values that progressively decrease above 60 K, as reported in Figure 5. This clearly indicates that at these temperatures other states beyond the ground doublet of the $J=15/2$ multiplet are thermally populated.

The same experimental data were also modeled by using a spin Hamiltonian describing the effects of the crystal field (CF) on the $J=15/2$ multiplet. Though the disorder of the COT ligand on two positions gives rise to two conformers exhibiting in principle different crystal field,[9] a unique set of CF parameters was assumed to avoid overparametrization problems. This appears justified by our previous study in which ab initio calculations showed only small differences between the energies of the two conformers.[7a] In principle one should also include many transverse terms of the CF because even small deviations from a perfect axial symmetry can produce non-negligible contributions. However, the small tilt angle between the organic rings that act as ligands suggests that transverse terms can be neglected at first approximation.

The experimental data were in fact successfully reproduced by using only axial terms (solid lines in Figure 4). Moreover, we found that the inclusion of the sixth-order term does not significantly improve the simulation and all calculations were carried out by using the spin Hamiltonian:

$$H = g_L\mu_B\mathbf{J}\cdot\mathbf{B} + B_2^0\hat{O}_2^0 + B_4^0\hat{O}_4^0 \qquad (4)$$

in which $\hat{O}_2^0$ and $\hat{O}_4^0$ are the Stevens operators commonly employed to describe the magnetic anisotropy.[16] The best fit parameters were: $B_2^0=-1.3\pm0.1$ cm^{-1} and $B_4^0=-3\pm1\times10^{-3}$ cm^{-1}. The tilt angle between the easy axis of the two families of molecules was also fitted and the resulting value (95 ± 1 °) agrees with previous estimations.[7a] Even if the strong correlation between CF parameters experienced reproducing thermodynamic properties does not allow to determine univocally the set of CF parameters, the calculated levels of the ground J manifold (see inset of Figure 5) provide an estimate of the energy separation between the ground and the first excited doublet, 118 cm^{-1}. This value is in good agreement with those obtained from ab initio calculations, which range between 85–135 cm^{-1} depending on the conformer and on structure optimization employed.[7a]

In our previous investigation of the magnetic anisotropy of Cp*ErCOT we exploited the magnetic hysteresis of this SMM to extract information on the molecular anisotropy. It is interesting to show here the information on magnetic bistability that can be provided by torque magnetometry.[13b] With this scope we recorded hysteresis loops at a fixed temperature and angular position, varying the sweeping rate of the applied magnetic field, as reported in Figure 6. Irreversibility is clearly observed at 5 K and the dynamic origin of the hysteresis is well evidenced by the differences upon changing the sweeping rate. A relevant feature to be stressed is that, according to equation (1), the magnetic torque always vanishes at zero applied field. Torque magnetometry is, therefore, unable to detect remnant magnetization. However, it is important to notice that, referring to a standard hysteresis loop, the magnetization curve goes through the II and IV quadrants if the remnant magnetization is not zero. In these regions the magnetization and the external field have different polarity and torque is expected to change sign in comparison with the I and III quadrants. In

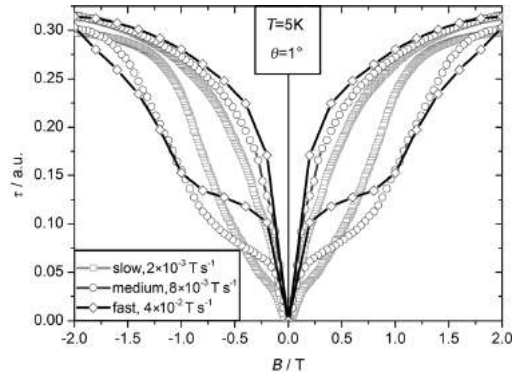

Figure 6. Hysteresis loops recorded at $T=5$ K and $\theta=1^\circ$. The legend refers to the velocity at which the magnetic field is varied.

Figure 6 the torque has the same sign over the entire loop, thus indicating that this system presents no remnant magnetization, and is actually characterized by a butterfly hysteresis cycle as observed by standard magnetometry.[7a]

Conclusion

In this work we have extended our investigation of the magnetic anisotropy of the Cp*ErCOT organometallic SMM, a textbook example of non collinearity of magnetic anisotropy axes in a nontriclinic crystal. We have previously shown[7a] that, notwithstanding the almost isotropic behavior of the angular-resolved magnetization, hints on the magnetic anisotropy can be provided by out-of-equilibrium experimental investigation. Torque magnetometry has been revealed to be equally powerful without requiring the presence of magnetic hysteresis. This makes the technique much more generally applicable than standard magnetometry. Moreover, its higher sensitivity and the selectivity to the anisotropic part of the magnetization allows the investigation of a much wider temperature range, thus providing an estimate of the energy separation of the first excited doublet from that of the ground one, a parameter that usually rules the magnetization dynamics. Even if magnetic torque intrinsically vanishes when no magnetic field is applied, and is therefore unable to detect remnant magnetization or zero field tunneling of the magnetization, it can equally provide information on the magnetic bistability of the system.

We foresee a renaissance of this simple and inexpensive technique given the key role played by magnetic anisotropy in molecular systems, such as SMMs, and the extensive efforts devoted to its optimization through rational chemical design.

Experimental Section

A crystal of Cp*ErCOT (volume $\approx 0.4\times0.3\times0.2$ mm^3), prepared as previously described, was attached to a square acetate foil (side ≈ 2 mm) with silicon vacuum grease and its faces were indexed by using an SCD Oxford Xcalibur3 X-Ray diffractometer. All manipulations were performed under inert atmosphere. The cantilever torque measurements were performed by using a home made two-legged CuBe cantilever separated by 0.1 mm from a gold plate. The cantilever was inserted into a Oxford Instruments MAGLAB2000 platform with automated rotation of the cantilever chip in a vertical magnet. The capacitance of the cantilever was detected with a Andeen-Hegerling 2500 A Ultra Precision Capacitance Bridge.

Acknowledgements

The financial support from the European Research Council, through the Advanced Grant "MolNanoMas" (Project no. 267746) is acknowledged. We thank Professor Andrea Cornia for the stimulating discussion.

Keywords: lanthanides · magnetic anisotropy · single-molecule magnets · torque magnetometry

[1] a) D. Gatteschi, R. Sessoli, J. Villain, *Molecular nanomagnets*, Oxford University Press, Oxford, **2006**; b) R. Winpenny, *Single-Molecule Magnets and Related Phenomena, Vol. 122*, Springer, Heidelberg, **2006**; c) J. Bartolomé, F. Luis, J. F. Fernández, *Molecular Magnets*, Springer, Heidelberg, **2014**.

[2] a) J. D. Rinehart, J. R. Long, *Chem. Sci.* **2011**, *2*, 2078 – 2085; b) J. J. Baldoví, S. Cardona-Serra, J. M. Clemente-Juan, E. Coronado, A. Gaita-Ariño, A. Palii, *Inorg. Chem.* **2012**, *51*, 12565 – 12574.

[3] a) J. J. Baldoví, S. Cardona-Serra, J. M. Clemente-Juan, E. Coronado, A. Gaita-Arino, A. Palii, *J. Comput. Chem.* **2013**, *34*, 1961 – 1967; b) N. F. Chilton, D. Collison, E. J. L. Mclnnes, R. E. P. Winpenny, A. Soncini, *Nat. Commun.* **2013**, *4*, 2551; c) D. Aravena, E. Ruiz, *Inorg. Chem.* **2013**, *52*, 13770 – 13778.

[4] a) M. E. Boulon, G. Cucinotta, J. Luzon, C. Degl'Innocenti, M. Perfetti, K. Bernot, G. Calvez, A. Caneschi, R. Sessoli, *Angew. Chem.* **2013**, *125*, 368 – 372; *Angew. Chem. Int. Ed.* **2013**, *52*, 350 – 354; b) G. Cucinotta, M. Perfetti, J. Luzon, M. Etienne, P. E. Car, A. Caneschi, G. Calvez, K. Bernot, R. Sessoli, *Angew. Chem.* **2012**, *124*, 1638 – 1642; *Angew. Chem. Int. Ed.* **2012**, *51*, 1606 – 1610.

[5] a) G. Karlström, R. Lindh, P. A. Malmqvist, B. O. Roos, U. Ryde, V. Veryazov, P. O. Widmark, M. Cossi, B. Schimmelpfennig, P. Neogrady, L. Seijo, *Comput. Mater. Sci.* **2003**, *28*, 222 – 239; b) F. Aquilante, L. De Vico, N. Ferré, G. Ghigo, P.-å. Malmqvist, P. Neogrády, T. B. Pedersen, M. Pitoňák, M. Reiher, B. O. Roos, L. Serrano-Andrés, M. Urban, V. Veryazov, R. Lindh, *J. Comput. Chem.* **2010**, *31*, 224 – 247; c) L. F. Chibotaru, L. Ungur, computer programmes SINGLE_ANISO and POLY_ANISO, University of Leuven, **2006**.

[6] J. Luzon, R. Sessoli, *Dalton Trans.* **2012**, *41*, 13556 – 13567.

[7] a) M. E. Boulon, G. Cucinotta, S. S. Liu, S. D. Jiang, L. Ungur, L. F. Chibotaru, S. Gao, R. Sessoli, *Chem. Eur. J.* **2013**, *19*, 13726 – 13731; b) P.-H. Guo, J.-L. Liu, Z.-M. Zhang, L. Ungur, L. F. Chibotaru, J.-D. Leng, F.-S. Guo, M.-L. Tong, *Inorg. Chem.* **2012**, *51*, 1233 – 1235.

[8] a) J. Luzon, K. Bernot, I. J. Hewitt, C. E. Anson, A. K. Powell, R. Sessoli, *Phys. Rev. Lett.* **2008**, *100*, 247205; b) J. K. Tang, I. Hewitt, N. T. Madhu, G. Chastanet, W. Wernsdorfer, C. E. Anson, C. Benelli, R. Sessoli, A. K. Powell, *Angew. Chem.* **2006**, *118*, 1761 – 1765; *Angew. Chem. Int. Ed.* **2006**, *45*, 1729 – 1733; c) L. F. Chibotaru, L. Ungur, A. Soncini, *Angew. Chem.* **2008**, *120*, 4194 – 4197; *Angew. Chem. Int. Ed.* **2008**, *47*, 4126 – 4129.

[9] a) W. J. Evans, M. A. Johnston, R. D. Clark, J. W. Ziller, *J. Chem. Soc. Dalton Trans.* **2000**, 1609 – 1612; b) B. W. Wang, S. J. Jiang, H. L. Sun, Z. M. Wang, S. Gao, *J. Am. Chem. Soc.* **2011**, *133*, 4730 – 4733.

[10] S. Carretta, P. Santini, E. Liviotti, N. Magnani, T. Guidi, R. Caciuffo, G. Amoretti, *J. Appl. Phys.* **2004**, *95*, 7348 – 7350.

[11] A. Cornia, D. Gatteschi, R. Sessoli, *Coord. Chem. Rev.* **2001**, *219*, 573 – 604.

[12] a) C. Rossel, P. Bauer, D. Zech, J. Hofer, M. Willemin, H. Keller, *J. Appl. Phys.* **1996**, *79*, 8166 – 8173; b) C. Rossel, M. Willemin, A. Gasser, H. Bo-

thuizen, G. I. Meijer, H. Keller, *Rev. Sci. Instrum.* **1998**, *69*, 3199 – 3203; c) S. A. J. Wiegers, A. S. Van Steenbergen, M. E. Jeuken, M. Bravin, P. E. Wolf, G. Remenyi, J. Perenboom, J. C. Maan, *Rev. Sci. Instrum.* **1998**, *69*, 2369 – 2374; d) W. J. De W. Horrocks, D. De W. Hall, *Coord. Chem. Rev.* **1971**, *6*, 147 – 186; e) S. Mitra, *Prog. Inorg. Chem.* **1977**, *22*, 309 – 408.

[13] a) A. Cornia, M. Affronte, A. G. M. Jansen, D. Gatteschi, A. Caneschi, R. Sessoli, *Chem. Phys. Lett.* **2000**, *322*, 477 – 482; b) J. A. A. J. Perenboom, J. S. Brooks, S. Hill, T. Hathaway, N. S. Dalal, *Phys. Rev. B* **1998**, *58*, 330 – 338.

[14] a) M. Affronte, A. Cornia, A. Lascialfari, F. Borsa, D. Gatteschi, J. Hinderer, M. Horvatic, A. G. M. Jansen, M. H. Julien, *Phys. Rev. Lett.* **2002**, *88*, 167201; b) A. Cornia, M. Affronte, A. G. M. Jansen, G. L. Abbati, D. Gatteschi, *Angew. Chem.* **1999**, *111*, 2409 – 2411; *Angew. Chem. Int. Ed.* **1999**, *38*, 2264 – 2266; c) A. Cornia, A. G. M. Jansen, M. Affronte, *Phys. Rev. B* **1999**, *60*, 12177 – 12183; d) J. van Slageren, R. Sessoli, D. Gatteschi, A. A. Smith, M. Helliwell, R. E. P. Winpenny, A. Cornia, A. L. Barra, A. G. M. Jansen, E. Rentschler, G. A. Timco, *Chem. Eur. J.* **2002**, *8*, 277 – 285; e) O. Waldmann, S. Carretta, P. Santini, R. Koch, A. G. M. Jansen, G. Amoretti, R. Caciuffo, L. Zhao, L. K. Thompson, *Phys. Rev. Lett.* **2004**, *92*, 096403; f) F. El Hallak, P. Rosa, P. Vidal, I. Sheikin, M. Dressel, J. v. Slageren, *Europhys. Lett.* **2011**, *95*, 57002; g) L. Rigamonti, A. Cornia, A. Nava, M. Perfetti, M.-E. Boulon, A.-L. Barra, X. Zhong, K. Park, R. Sessoli, *PCCP* **2014**, *16*, 17220 – 17230.

[15] S. W. Van Sciver, *Helium Cryogenics*, Springer, New York, **2012**.

[16] A. Abragam, B. Bleaney, *Electron Paramagnetic Resonance of Transition Ions*, Dover, New York, **1986**.

Received: July 2, 2014
Published online on September 11, 2014

CHEMISTRY
A European Journal

Supporting Information

Angular-Resolved Magnetometry Beyond Triclinic Crystals Part II: Torque Magnetometry of Cp*ErCOT Single-Molecule Magnets**

Mauro Perfetti,[a] Giuseppe Cucinotta,[a] Marie-Emmanuelle Boulon,[a] Fadi El Hallak,[b] Song Gao,[c] and Roberta Sessoli*[a]

chem_201404218_sm_miscellaneous_information.pdf

I. Zero-torque angles

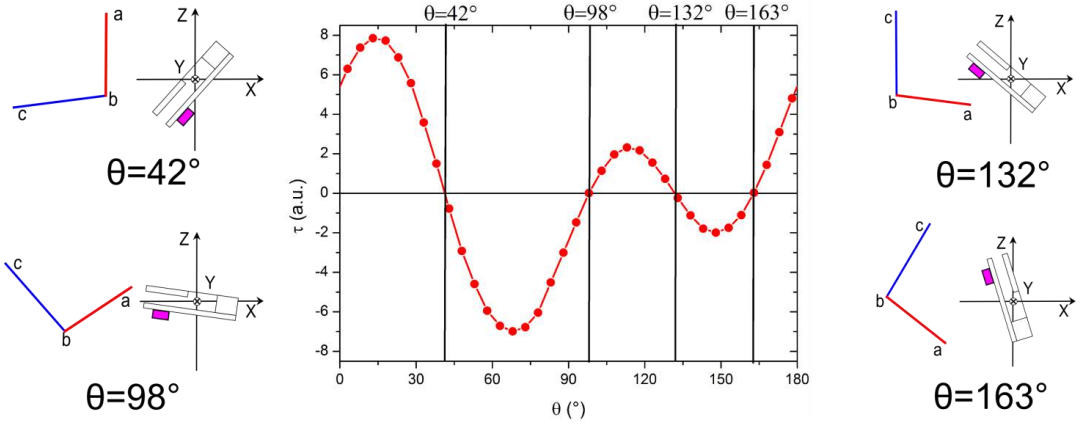

Figure S1: Rotation performed at *T*=10K and *B*=2T. In the left and right panels is evidenced the position of the crystal with respect to the vertical magnetic field. While θ=42° and 132° correspond to symmetry imposed zero torque, θ=98° and 163° correspond to accidental zero.

II. Fitting of low temperature experimental data using an Ising model

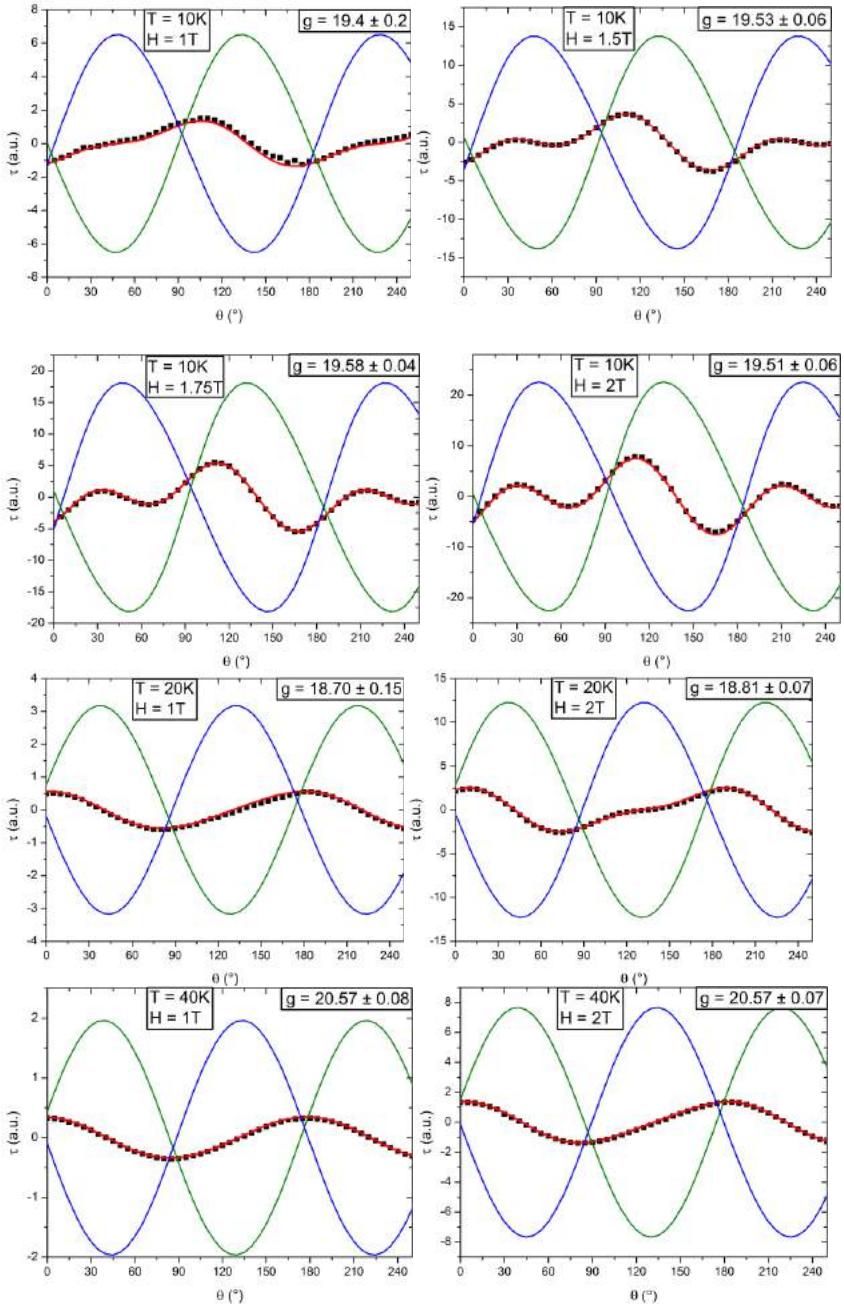

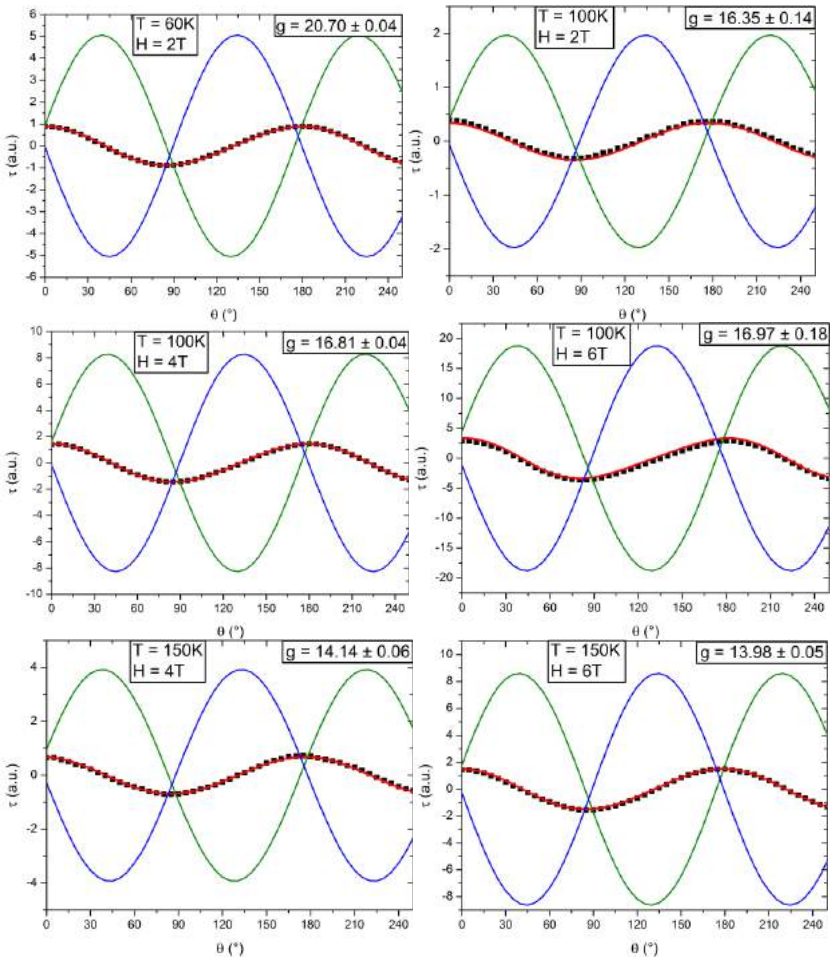

Figure S2: Simulation of experimental data using two Ising spins with *S*=1/2 and effective *g* free to adjust. Red lines represent the simulation, blue and green curves are the contribution of the two molecules tilted by 95°, while black symbols are the experimental data.

III. Fitting of experimental data using an axial Crystal Field Spin Hamiltonian

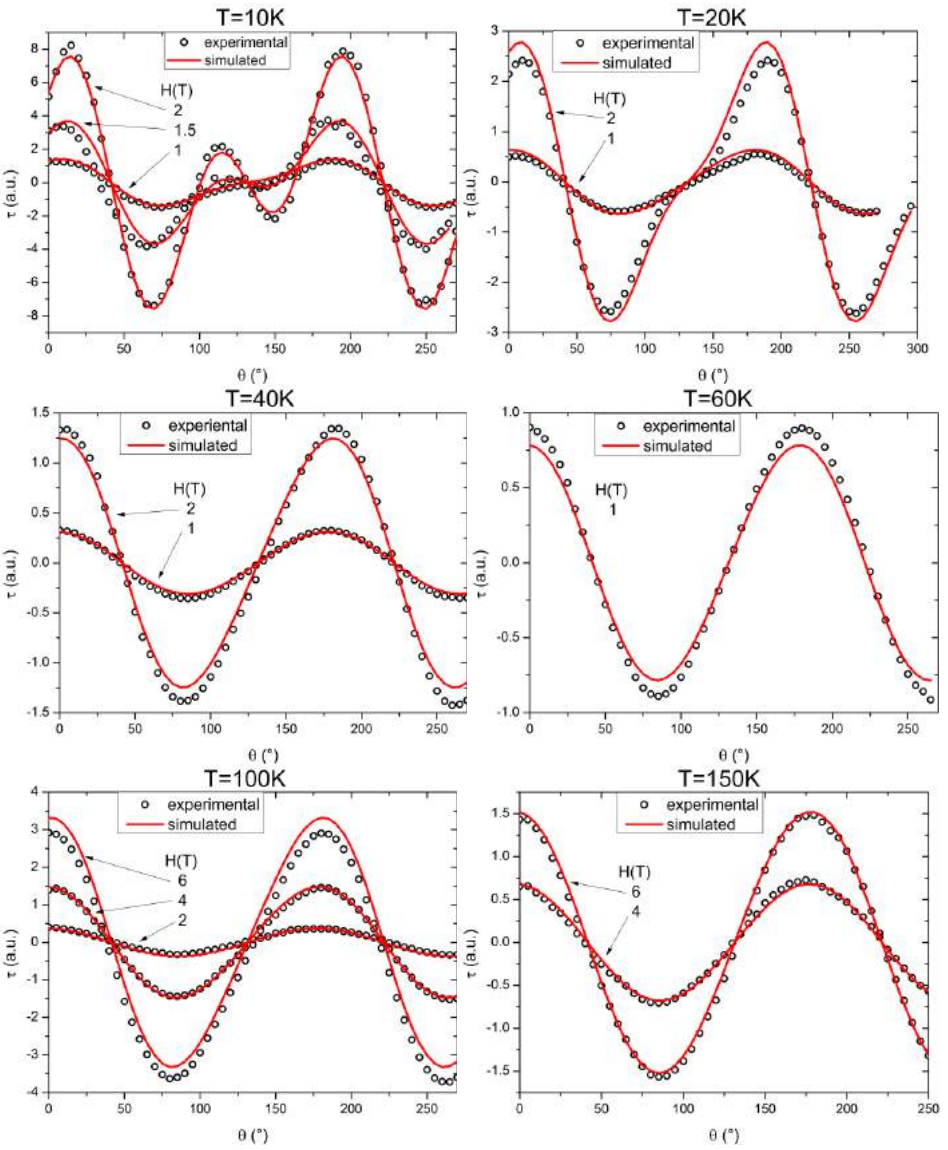

Figure S3: Fitting of experimental data using the spin Hamiltonian reported as eq (4) in the main text. Empty circles are the experimental measurements, while red lines are the calculated values.

PCCP

PAPER

View Article Online
View Journal

Cite this: DOI: 10.1039/c4cp02462a

Mapping of single-site magnetic anisotropy tensors in weakly coupled spin clusters by torque magnetometry†

Luca Rigamonti,[a] Andrea Cornia,*[a] Andrea Nava,[ab] Mauro Perfetti,[c] Marie-Emmanuelle Boulon,‡[c] Anne-Laure Barra,[d] Xiaoliang Zhong,[e] Kyungwha Park[e] and Roberta Sessoli[c]

Received 4th June 2014,
Accepted 30th June 2014

DOI: 10.1039/c4cp02462a

www.rsc.org/pccp

Single-crystal torque magnetometry performed on weakly-coupled polynuclear systems provides access to a complete description of single-site anisotropy tensors. Variable-temperature, variable-field torque magnetometry was used to investigate triiron(III) complex $[Fe_3La(tea)_2(dpm)_6]$ (**Fe_3La**), a lanthanum(III)-centred variant of tetrairon(III) single molecule magnets (Fe_4) (H_3tea = triethanolamine, Hdpm = dipivaloylmethane). Due to the presence of the diamagnetic lanthanoid, magnetic interactions among iron(III) ions (s_i = 5/2) are very weak (<0.1 cm^{-1}) and the magnetic response of **Fe_3La** is predominantly determined by single-site anisotropies. The local anisotropy tensors were found to have $D_i > 0$ and to be quasi-axial with $|E_i/D_i| \sim 0.05$. Their hard axes form an angle of approximately 70° with the threefold molecular axis, which therefore corresponds to an *easy* magnetic direction for the molecule. The resulting picture was supported by a High Frequency EPR investigation and by DFT calculations. Our study confirms that the array of peripheral iron(III) centres provides substantially noncollinear anisotropy contributions to the ground state of Fe_4 complexes, which are of current interest in molecular magnetism and spintronics.

Introduction

Noncollinear single-ion magnetic anisotropies play a central role in molecular magnetism, where they are responsible for exotic phenomena like the toroidal arrangement of magnetic moments in a triangular Dy_3 cluster.[1] They also often provide a leading contribution to the behaviour of Single Molecule Magnets (SMMs), a class of metal-ion based complexes of great current interest in molecular magnetism and spintronics by virtue of their directionally-bistable magnetic moment.[2,3] In these systems the ground spin state has an easy-axis-type anisotropy that generates an energy barrier to magnetic moment reversal. The origin of this ground-state anisotropy is most simply appreciated working in the so-called "strong-exchange" limit, *i.e.* assuming that isotropic superexchange interactions provide the leading contribution to the spin Hamiltonian while anisotropic terms act as perturbations. In this case, the spin states are grouped into multiplets with a well-defined value of the total spin (S). The magnetic anisotropy within each multiplet is then accurately described by a tensor $\mathbf{D}(S)$, which can be expressed as a linear combination of the different second-order contributions arising from single-site anisotropies ($\mathbf{D}_i$) and from spin–spin interactions ($\mathbf{D}_{i,j}$), as given by eqn (1).

$$\mathbf{D}(S) = \sum_i d_i(S)\mathbf{D}_i + \sum_{i<j} d_{i,j}(S)\mathbf{D}_{i,j} \quad (1)$$

[a] *Dipartimento di Scienze Chimiche e Geologiche, Università degli Studi di Modena e Reggio Emilia & INSTM RU of Modena and Reggio Emilia, via G. Campi 183, 41125 Modena, Italy. E-mail: andrea.cornia@unimore.it*
[b] *Dipartimento di Scienze Fisiche, Informatiche e Matematiche, Università degli Studi di Modena e Reggio Emilia, via G. Campi 183, 41125 Modena, Italy*
[c] *Laboratory of Molecular Magnetism (LaMM), Dipartimento di Chimica 'Ugo Schiff', Università degli Studi di Firenze & INSTM RU of Firenze, via della Lastruccia 3-13, 50019 Sesto Fiorentino (FI), Italy*
[d] *Laboratoire National des Champs Magnétiques Intenses, CNRS, BP166, 25 Avenue des Martyrs, 38042 Grenoble Cedex 9, France*
[e] *Department of Physics, Virginia Tech, Blacksburg, Virginia 24060, USA*

† Electronic supplementary information (ESI) available: Fig. S1: details of the geometry of the torque measurements. Fig. S2: infrared spectra of $[H_3La(tea)_2]$, **Fe_3La** and $[Fe_2(\mu\text{-OMe})_2(dpm)_4]$ as KBr disks. Fig. S3: structure of the ppp and sss isomers in crystals of **Fe_3La**. Fig. S4: Curie–Weiss plot for **Fe_3La**. Fig. S5: isothermal molar magnetization *vs.* H/T data for **Fe_3La**. Fig. S6: frequency dependence of the in-phase, χ'_M, and out-of-phase, χ''_M, AC susceptibilities for **Fe_3La** at zero and 1 kOe applied static fields and in the 1.9–3.5 K temperature range. Fig. S7: additional torque data measured on **Fe_3La** at 5.5 K and 30 kOe. Fig. S8–S10: calculated torque data for various sets of spin-Hamiltonian parameters. Fig. S11 and S12: internal energy and free energy surfaces of **Fe_3La** computed with the set of best-fit spin-Hamiltonian parameters. Fig. S13 and S14: EPR powder spectra of **Fe_3La** at 331.2 and 220.8 GHz and at 5 and 10 K. Fig. S15: details of the experimental and calculated EPR spectra of **Fe_3La** at 240.0 GHz and 5 K. Fig. S16: free energy surface of **Fe_4** computed using van Wüllen single-ion parameters. CCDC 1004458. For ESI and crystallographic data in CIF or other electronic format see DOI: 10.1039/c4cp02462a

‡ Present address: Photon Science Institute, EPSRC School of Chemistry, The University of Manchester, Oxford Road, Manchester M13 9PL, UK.

Here, $d_i(S)$ and $d_{i,j}(S)$ are projection coefficients that can be computed once the composition of the spin eigenfunctions is known.[4] In most SMMs investigated to date the $\mathbf{D}(S)$ tensor is dominated by single-site contributions and the second term in eqn (1) can be safely neglected. Owing to the tensorial nature of the above relation, an easy-axis $\mathbf{D}(S)$ tensor may arise in different ways, depending on the type (easy-axis or hard-axis) and orientation of local anisotropies. For instance, when combining easy-axis ions like tetragonally-elongated high-spin manganese(III), an easy-axis anisotropy results if the $\mathbf{D}_i$ tensors are approximately collinear, as found in the Mn_6[5] and Mn_{12}[6] families of SMMs. However, it is also possible to assemble *hard-axis* metal ions into *easy-axis* molecular structures, as long as the local anisotropy tensors are kept approximately perpendicular to a molecular axis. Such an arrangement finds practical realization in the family of Fe_4 propeller-like complexes, which have inspired the present work.[7]

As a second important effect, in the presence of noncollinear single-site anisotropies even rigorously axial structures can exhibit a nonisotropic in-plane response. In other words, the $\mathbf{D}(S)$ tensor does not provide an accurate description of magnetic anisotropy and higher-order transverse contributions have to be considered. To handle such contributions, the zero-field splitting Hamiltonian acting within the ground state is customarily expressed as a combination of extended Stevens operators, which are even-order (k) polynomials of the spin components:[6]

$$\hat{\mathcal{H}}_{\mathrm{zfs}} = \sum_{k=2}^{2S} \sum_{q=-k}^{k} B_k^q \hat{O}_k^q \qquad (2)$$

We anticipate here that for systems with D_3 point-group symmetry (Fig. 1) the only nonzero B_k^q coefficients (with k up to 6) are $B_2^0 = (1/3)D(S)$, B_4^0, B_4^3, B_6^0, B_6^3 and B_6^6.[8]

The transverse terms with $k > 2$ are important as they activate effective tunnelling pathways and have a profound influence on the spin dynamics.[9] However, they usually lead to only minor deviations from the static response predicted by eqn (1), so that spectroscopic methods, like single-crystal Electron Paramagnetic Resonance (EPR), are required for their evaluation.[6,8,9]

The effect of noncollinearities is expected to emerge in a clearer fashion as isotropic superexchange interactions are reduced and a "weak-exchange" regime is approached. Even the complete suppression of superexchange interactions is however not sufficient to reveal the orientation of single-site anisotropy tensors ($\mathbf{D}_i$) as long as investigations are performed in the high-temperature limit. In that case, the single-site contributions ($\mathbf{M}_i$) to the magnetization ($\mathbf{M}$) can be expressed as $\mathbf{M}_i = \boldsymbol{\chi}_i \cdot \mathbf{H}$, where $\boldsymbol{\chi}_i$ is the T-dependent single-site magnetic susceptibility tensor and $\mathbf{H}$ is the applied magnetic field. The magnetization is then linked to $\mathbf{H}$ as in eqn (3), where the sum of the $\boldsymbol{\chi}_i$'s is a tensor itself and describes the overall molecular susceptibility ($\boldsymbol{\chi}$).

$$\mathbf{M} = \sum_i \boldsymbol{\chi}_i \cdot \mathbf{H} = \boldsymbol{\chi} \cdot \mathbf{H} \qquad (3)$$

From eqn (3) it follows that any magnetic study carried out in the high-temperature limit will provide information on $\boldsymbol{\chi}$ but not on the underlying local responses, which remain hidden in the general case. To gain insight into single-site anisotropy tensors it is therefore essential to abandon the high-temperature regime so that the relationship $\mathbf{M}_i = \boldsymbol{\chi}_i \cdot \mathbf{H}$ breaks down.

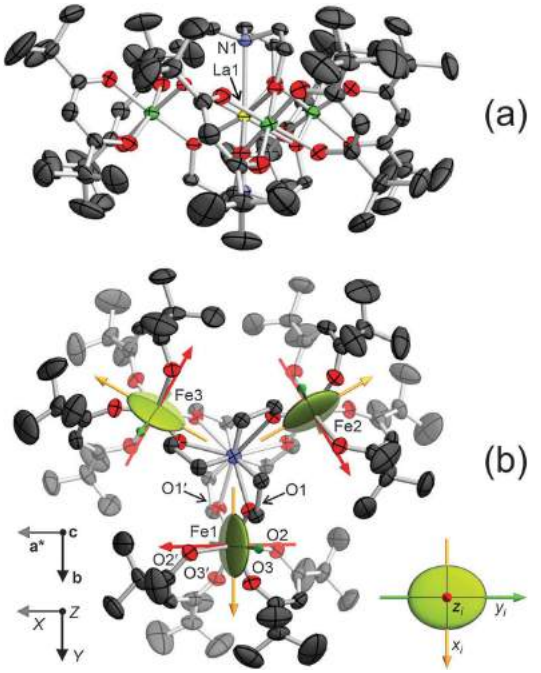

Fig. 1 Partially-labelled ORTEP-III[24] plot of the ppp isomer in $\mathbf{Fe_3La}$ viewed approximately perpendicular to the threefold molecular axis (a) and exactly along it (b). Thermal ellipsoids are drawn at the 40% probability level and hydrogen atoms are omitted for clarity. The three iron(III) ions are related by the three-fold symmetry axis along **c**. In (b) the iron thermal ellipsoids are replaced by single-site susceptibility tensors $\boldsymbol{\chi}_i$, calculated in the high temperature limit and drawn at an arbitrary scale. The hard, intermediate and easy magnetic directions are depicted using red, yellow and green arrows, respectively. A view of the susceptibility tensor along its hard axis is shown in the lower-right part of the figure. The plane of the metals is made partially transparent for a better rendering.

We herein apply such a simple idea to investigate the origin of magnetic anisotropy in a family of propeller-like tetrairon(III) complexes (Fe_4), which are among the simplest SMMs known to date.[10,11] In these robust and chemically-versatile molecules,[12] a central iron(II) ion is surrounded by three peripheral iron(III) centres at the vertices of an approximately equilateral triangle. The four ions are in a high-spin state (s_i = 5/2) and are antiferromagnetically coupled *via* the oxygen atoms of two tripodal ligands to give a ground state with S = 5. These molecules, which conform to either rigorous or idealized D_3 symmetry, exhibit an easy-axis anisotropy along their (idealized) threefold axis, *i.e.* the normal to the metal plane. There is now a growing body of experimental evidence that all four constituent ions contribute constructively to the observed anisotropy barrier, which amounts to about 15–17 K.[7,8,11,13] However, only the central ion has an easy-axis anisotropy. The three peripheral ions have a positive

zero-field splitting parameter, as clearly shown by magnetic dilution experiments.[13] Therefore, in order to properly combine to give the observed molecular anisotropy, their hard-axes must lie close to the molecular plane. This picture has been very recently confirmed by van Wüllen *et al.* using DFT calculations.[14]

With the aim of retrieving direct experimental information on such an arrangement, we have now designed and synthesized a variant of the Fe_4 propeller-type complexes, featuring a central diamagnetic ion. In octahedral coordination cobalt(III) and gallium(III) have ionic radii similar to high-spin iron(III)[15] and chemical routes to Fe_3Co or Fe_3Ga might be envisaged.[16] However, previous work by Murray and co-workers indicates that the replacement of the two tripods with two triethanolaminate ligands (tea^{3-}) affords a central pocket that quantitatively encapsulates an octacoordinated lanthanide.[17] The low-yield self-assembly procedure reported by the above authors was here developed into a sequential synthetic route that affords crystalline $[Fe_3La(tea)_2(dpm)_6]$ (**Fe_3La**) in high yield (Hdpm = dipivaloylmethane). The peripheral iron(III) centres in **Fe_3La** maintain the same coordination environment as in Fe_4 propellers, but magnetic communication between them becomes much weaker due to the presence of a central lanthanum(III) ion. The magnetic response of **Fe_3La** was indeed found to display pronounced in-plane modulations that reveal the type, magnitude and orientation of single-site anisotropies in unprecedented detail. The magnetic behaviour was studied on a single-crystal sample *via* torque magnetometry, a technique that probes the mechanical couple (τ) experienced by a magnetically-anisotropic substance in a uniform magnetic field (**B**).[18] The equation that provides the torque vector per unit sample volume is

$$\tau = \mathbf{M} \times \mathbf{B} \quad (4)$$

To detect the torque signal, the sample is fixed to a cantilever that works as the plate of a capacitor. Any deflection of the cantilever then results in a change of capacitance, which can be measured with high sensitivity. In the present study, torque measurements at 2.3 K for fields up to 70 kOe allowed the determination of the complete $\mathbf{D}_i$ tensors as well as of the residual superexchange interaction between iron(III) ions. In particular, the hard-axis nature of the local anisotropies was unequivocally established and the orientation of single-ion tensors was firmly related to the molecular structure.

Experimental

Materials and methods

All chemicals were of reagent grade and were used as received. Dry toluene ($H_2O \leq 0.005\%$) was stored over molecular sieves. Isopropanol and methanol were distilled over CaO and magnesium methoxide, respectively, and stored over 3 Å molecular sieves. Diethyl ether was predried over $CaCl_2$ overnight and distilled from its sodium benzophenone ketyl solution under N_2 before use. Elemental analyses were carried out on a Carlo Erba EA1110 CHNS-O automatic analyser. Infrared spectra were recorded as KBr disks using a Jasco FTIR-4200 spectrophotometer with a resolution of 2 cm^{-1}. $[La(AcO)_3]$[19] and $[Fe_2(\mu\text{-}OMe)_2(dpm)_4]$[11] were synthesised as reported in the literature.

Synthesis of $[H_3La(tea)_2]$[20]

The reaction was performed under a dinitrogen atmosphere using oven-dried glassware. Sodium (129.1 mg, 5.615 mmol) in small pieces was added to a suspension of $[La(AcO)_3]$ (578.9 mg, 1.832 mmol) in toluene (20 mL) and isopropanol (2 mL), and the resulting mixture was refluxed for 4 h. Upon cooling a white precipitate (NaOAc) formed; the colourless solution of $[La(O^iPr)_3]$ was syringed to a second flask under dinitrogen flow; the solid was further treated with toluene (2 × 5 mL) and the washings combined with the main organic phase. A solution of H_3tea (568.7 mg, 3.812 mmol) in isopropanol (3 mL) was added and the reaction mixture was left under stirring at room temperature for 24 h; it was then concentrated under vacuum until a white gelatinous precipitate was obtained; the product was collected, washed with isopropanol and dried in vacuum to give a white powder (586.2 mg, 73.76%). Elemental analysis found: C, 32.24; H, 6.40; N, 6.29. Calc. for $C_{12}H_{27}LaN_2O_6 \cdot 0.7H_2O$ (446.87): C, 32.25; H, 6.41; N, 6.27%. IR (KBr): ν_{max}/cm^{-1} 3353 (O–H), 2820 (C–H), 1098 and 1075 (C–O and C–N).

Synthesis of $[Fe_3La(tea)_2(dpm)_6]$ (Fe_3La)

A solution of $[Fe_2(\mu\text{-}OMe)_2(dpm)_4]$ (49.9 mg, 0.0550 mmol) in diethyl ether (10 mL) was layered over a solution of $[H_3La(tea)_2] \cdot 0.7H_2O$ (16.4 mg, 0.0367 mmol) in methanol (5 mL) in a cylindrical flask, with a *n*-hexane buffer (1 mL) between the two layers. The system was left undisturbed over a period of 2–4 weeks during which the formation of yellow crystals suitable for X-ray diffraction was observed. Once the diffusion was complete, the crystalline product was collected by filtration and dried in vacuum (36.8 mg, 59.1%). Elemental analysis found: C, 55.34; H, 7.92; N, 1.71. Calc. for $C_{78}H_{138}Fe_3LaN_2O_{18}$ (1698.36): C, 55.16; H, 8.19; N, 1.65%. IR (KBr): ν_{max}/cm^{-1} 2962, 2857 (C–H), 2811 ($C\text{–}H_{methine}$), 1592–1505 (C═O), 1403–1355 (C–H), 1080 (C–O).

X-ray crystallography

Single-crystal X-ray diffraction studies were carried out on compound **Fe_3La** using a four-circle Bruker X8-APEX diffractometer equipped with a Mo-Kα generator (λ = 0.71073 Å), an area detector and a Kryo-Flex cryostat, and controlled using the Bruker-Nonius X8APEX software. Crystal structure data for **Fe_3La**: $C_{78}H_{138}Fe_3LaN_2O_{18}$, M_r = 1698.36, crystal dimensions 0.48 × 0.34 × 0.13 mm^3, trigonal, space group: $R\bar{3}c$ (no. 167), $a = b$ = 16.8210(6) Å, c = 55.396(2) Å, $\alpha = \beta = 90°$, $\gamma = 120°$, V = 13574.3(9) $Å^3$, Z = 6, ρ_{calcd} = 1.247 g cm^{-3}, $2\theta_{max} = 58.01°$, T = 140(2) K, collected/independent reflections 51068/4023, R(int) = 0.0311, Final R indices: R_1 = 0.0375, wR_2 = 0.1010 [$I > 2\sigma(I)$], R_1 = 0.0477, wR_2 = 0.1101 [all data], goodness-of-fit = 1.075. The structure was solved by direct methods using the SIR92[21] program; full-matrix least-squares refinement on F_o^2 was performed using the SHELX-97[22] program with 191 parameters and 85 restraints; both programs are implemented in the WINGX[23] v1.80.05 package. The programs ORTEP-III for Windows[24] and

Mercury 3.3.1[25] were used for graphics. Two different arrangements of dpm^- ligands coordinated to Fe were observed, with resolved disorder on C but not on O atoms. In the first one (propeller-like, p) the two oxygen donors of dpm^- lie on opposite sides of the molecular plane; in the second one (sandwich-like, s) they lie on the same side of the molecular plane. Complementary occupancy factors were assigned to the carbon atoms of p and s, resulting in the highest occupancy for p (0.678(3)). The two components were restrained to have the same geometry within 0.01 Å for 1,2 distances and 0.02 Å for 1,3 distances. The C–C distances within each ^{t}Bu group were also restrained to be similar within 0.01 Å. All non-hydrogen atoms were refined anisotropically, with the exception of C atoms of dpm^- in the minority s arrangement. Due to the extensive overlap between the two components, the methyl carbons of ^{t}Bu groups in p arrangement had to be restrained to approximate isotropic behaviour within 0.015 Å^2. Within the s arrangement, two collective thermal parameters were refined, one for methyl carbons of ^{t}Bu groups and one for the remaining C atoms. Hydrogen atoms were added in idealized positions and assigned isotropic displacement parameters constrained to those of the attached carbon atoms. CCDC 1004458.

Magnetic measurements

Direct current (DC) magnetic data were recorded using a Quantum Design MPMS SQUID magnetometer. Magnetic susceptibilities (defined as M/H, with $M = |\mathbf{M}|$ and $H = |\mathbf{H}|$) were measured on a 15.37 mg powder sample of **Fe_3La**, packed in a Teflon pellet with applied fields of 1 kOe from 1.9 to 30 K and of 10 kOe from 30 to 240 K. Isothermal magnetization data were also registered at 1.9 and 4.5 K at fields up to 50 kOe. Data reduction was carried out by using -945.3×10^{-6} emu mol^{-1} as diamagnetic contribution, estimated from the Pascal's constants.[26] Alternating current (AC) magnetic data up to 10 kHz in the 1.9–3.5 K temperature range were recorded using a Quantum Design PPMS susceptometer on the same sample of **Fe_3La**.

Torque magnetometry measurements

The torque measurements were performed using a two-legs CuBe cantilever and a capacitive detection (Andeen Hegerling Ultra Precision Capacitance Bridge). A crystal of **Fe_3La** (*ca.* 0.5 × 0.3 × 0.2 mm^3) with rhombohedral habit was fixed on an acetate foil with vacuum grease and its faces were indexed (see Fig. S1, ESI†) by using an SCD Oxford Xcalibur3 diffractometer. The sample was bound by $(\bar{1}02)$, (012) and $(\bar{1}1\bar{2})$ faces and their Friedel equivalents. The (012) and $(\bar{1}1\bar{2})$ faces (as well as their Friedel equivalents) are related by the crystallographic twofold axis directed along **b**, while the (012), $(\bar{1}02)$ and $(1\bar{1}2)$ faces (as well as their Friedel equivalents) are related by the crystallographic threefold axis parallel to **c**. The latter forms an angle of 62.26° with the normal (**n**) to the $(\bar{1}02)$ face. The crystal was mounted with the $(10\bar{2})$ face lying on the cantilever surface to scan two different planes (see Fig. S1, ESI†). In the first rotation the magnetic field was applied in the **a*c** plane and the torque component along $-\mathbf{b}$ was detected. In its starting position (rot1 = 0°) the cantilever was parallel to the magnetic field and the **c** axis formed a nominal angle of 90° − 62.26° = 27.74° with **B**. Looking down the **b** axis, the torquemeter was rotated counterclockwise and at each setting the **c** axis formed a nominal angle of rot1 + 27.74° with the magnetic field (measured counterclockwise). In the course of this rotation the orientation of the magnetic field spanned from parallel to the threefold axis ($\mathbf{B}||\mathbf{c}$) to perpendicular to it ($\mathbf{B}||\mathbf{a}^*$). For constructive reasons the rotation angle could only range from 0° to 300°, which however already provides redundant angular data due to the 180° periodicity expected for any paramagnetic system. In the second rotation the magnetic field was applied in the **bn** plane. In its starting position (rot2 = 0°) the magnetic field was parallel to **b** and the rotation of the torquemeter was then carried out counterclockwise looking down $-\mathbf{b} \times \mathbf{n}$. By consequence, the angle between the magnetic field and the threefold axis ranged from 62.26° (rot2 = 270°) to 117.74° (rot2 = 90°) and the torque component along $\mathbf{b} \times \mathbf{n}$ was measured. Data have been collected at 2.3 and 5.5 K for fields up to 70 kOe. At each temperature the rotation was performed also at zero field in order to correct data for the deflection due to the mass of the sample and of the cantilever. The torquemeter was always operated in the linear response regime but we made no attempt to extract absolute torque values from the measured capacitance variation, since samples in the microgram range would anyway be impossible to weigh with due accuracy. By consequence all torque data are given in arbitrary units (a.u.). Information on spin-Hamiltonian parameters was then extracted from the angle- and field-dependence of the torque signal.

Computational studies

Spin-Hamiltonian calculations were carried out using an in-house developed software based on ZHEEV routine[27] for matrix diagonalization and MINUIT routine[28] for least-square fitting. The torque signal was computed from the three components of the magnetization using eqn (4). For each rotation (n = 1, 2) the calculated torque signal (in 10^8 erg mol^{-1}) was multiplied by an adjustable scale factor k_n to account for systematic errors, like those arising from differences in the position of the crystal or from a slightly different response of the cantilever. Helmholtz free energy (F) and internal energy (U) diagrams were drawn using the MESHLAB program.[29] F and U values were computed at field orientations corresponding to a 3074- or 770-point angular Lebedev–Laikov grid[30] for **Fe_3La** and **Fe_4**, respectively.

HF-EPR spectroscopy

High-Frequency EPR measurements were performed on a multi-frequency spectrometer operating in a double-pass configuration. Frequencies were generated with the help of multipliers (doubler or tripler) associated either to a 95 GHz Gunn-diode (Radiometer Physics), or to 110.4 GHz and 120 GHz frequencies (Virginia Diodes). The detection was performed using a hot electron InSb bolometer (QMC Instruments). The exciting light was propagated using a Quasi-Optical set-up (Thomas Keating) outside the cryostat and with the help of a corrugated waveguide inside it. The main magnetic field was provided by a 16 T superconducting magnet, and low temperatures were supplied by a VTI (Cryogenic). The measurements were done on powdered

samples of **Fe$_3$La** pressed into pellets in order to limit torqueing effects. However, discrepancies on the intensities between calculated spectra and experimental ones seem to indicate that some torqueing was still present. Calculated spectra were obtained using the SIM program from H. Weihe (Univ. of Copenhagen).[31]

Density-functional theory (DFT) calculation methods

The initial structure of the ppp **Fe$_3$La** molecule was taken from the X-ray crystallography data. To make calculations computationally affordable, all terminating methyl groups were replaced by hydrogen atoms, which would not affect the magnetic anisotropy properties of the compound. For the structural relaxation and electronic structure calculation, we used the Vienna *ab initio* Simulation Package (VASP).[32,33] The generalized gradient approximation (GGA) to exchange–correlation potential was applied (PBE functional)[34] with projector-augmented wave (PAW) pseudopotentials.[35] The electronic wavefunctions were represented by plane waves with a cut-off energy of 500 eV. For the geometric relaxation the maximum atomic residual force was set to 10^{-2} eV Å^{-1} and the D_3 symmetry was imposed. The total magnetic moment was set to 15 μ_B. The set up of the magnetic moment would not affect the structural properties of the molecule because it is experimentally known that the superexchange coupling between the Fe atoms in **Fe$_3$La** is extremely small. To calculate single-ion magnetic anisotropy parameters, we took the relaxed geometry obtained from VASP, and used the all-electron-based DFT code NRLMOL[36] with spin–orbit coupling.[37] In this calculation, we replaced the La atom (atomic number Z = 57) in the already relaxed geometry by In (Z = 49), which is non-magnetic and has three valence electrons just like La, because NRLMOL can deal with elements up to Ba (Z = 56), and not heavier elements.

Results and discussion

Synthesis and spectroscopic characterization

The synthesis of the tetranuclear cluster **Fe$_3$La** was achieved in two distinct steps: formation of the lanthanum(III) core [H$_3$La(tea)$_2$] and subsequent reaction with the dimeric species [Fe$_2$(μ-OMe)$_2$(dpm)$_4$].

Attempts to react La^{III} salts (chloride, nitrate, acetate, *etc.*) directly with triethanolamine to form [H$_3$La(tea)$_2$] always failed. By contrast, preparation of a tris-isopropoxido lanthanum derivative[19,20] allowed the subsequent exchange of the alkoxide ligands with the chelating tea^{3-}. Once formed by reaction of [La(AcO)$_3$] with Na^{i}PrO, [La(^{i}PrO)$_3$] was not isolated due to its very high reactivity towards humidity, but let to directly react with H$_3$tea in solution. The compound [H$_3$La(tea)$_2$] was then isolated by concentration of the reaction mixture as a white powder. The infrared spectrum represents a fingerprint of this compound (see Fig. S2a, ESI†).

Addition of solid [H$_3$La(tea)$_2$] to a solution of the dimeric compound [Fe$_2$(μ-OMe)$_2$(dpm)$_4$] in diethyl ether led to the precipitation of **Fe$_3$La** as a fine yellow powder, that revealed to be insoluble in the most common organic solvents (such as dichloromethane, acetone and dimethylformamide) and could not be recrystallized. By contrast, the product can be obtained in high yield as yellow X-ray quality crystals *via* liquid diffusion of a solution of the iron dimer in diethyl ether into a methanol solution of the lanthanum core [H$_3$La(tea)$_2$]. The infrared spectrum of **Fe$_3$La** is reported in the ESI† and compared with that of the dimer (Fig. S2b and S2c, ESI†), to highlight the ν(C–O) shift from 1049 to 1080 cm^{-1} upon formation of the tetranuclear complex.

X-ray crystal structure of Fe$_3$La

Crystals of **Fe$_3$La** belong to the trigonal space group $R\bar{3}c$, with six tetranuclear complexes per unit cell developing around D_3 symmetry sites. The three iron(III) ions are crystallographically equivalent and compose an equilateral triangle centred by the lanthanum ion, with all the metal centres lying on the same plane (Fig. 1). The La1···Fe(i) directions correspond to twofold crystallographic axes. The lanthanum(III) ion is coordinated by two deprotonated triethanolamine molecules, located one above and one below the plane of the metals, adopting the μ_4-η^2:η^2:η^2:η^1 bonding mode. The nitrogen donor atoms of tea^{3-} ligands are located on the trigonal axis and coordinate the lanthanum ion with a bond distance of 2.758(3) Å, longer than reported for compound [Nb$_3$La(tea)$_2$(^{i}PrO)$_{12}$] (2.680(7) Å),[20] while La–O bond lengths are very similar in the two compounds (2.4826(16) for **Fe$_3$La** and 2.499(6) Å for the niobium derivative). Even if they contain different lanthanide ions, a meaningful comparison can be done also with the molecular structures of compounds [Fe$_3$Ln(tea)$_2$(acac)$_6$][17] (Ln = Gd, Dy; acac$^-$ = acetylacetonate), in which Ln–N bond lengths are very similar to **Fe$_3$La** (mean values: Gd–N = 2.740(6) Å, Dy–N = 2.743(5) Å), while Ln–O bonds are much shorter (mean values: Gd–O = 2.360(6) Å, Dy–O = 2.344(5) Å), in accordance with the lanthanide ionic-radii contraction.

The coordination environment of the rare earth can be described as a bicapped (N$_2$) distorted trigonal prism (O$_6$). The three iron(III) centres are connected to the lanthanum core by the bridging oxygen atoms of tea^{3-} ligands, and two dpm$^-$ anions complete the coordination sphere of each iron(III) ion, giving a distorted octahedral coordination geometry. No solvent molecules are present in the crystal structure and no intermolecular contacts can be identified, beside weak aliphatic interactions. Other selected distances and angles are listed in Table 1.

The dpm$^-$ ligands coordinated to iron(III) display major disorder effects, as found in few other Fe$_4$ propellers.[10,11,38] In the first arrangement (propeller-like, p), the two oxygen donors of dpm$^-$ lie on opposite sides of the molecular plane,

Table 1 Selected interatomic distances (Å) and angles (°) in compound **Fe$_3$La**[a]

La1–O1	2.4826(16)	Fe1–O1	1.9462(18)
La1–N1	2.758(3)	Fe1–O2	2.0108(19)
La1···Fe1	3.5795(5)	Fe1–O3	2.0203(19)
Fe1···Fe2	6.1999(6)	La1–O1–Fe1	107.22(7)
O1–La1–N1	62.54(4)	O1–Fe1–O1′	82.98(10)
O1–La1–O1′	62.58(8)		

[a] Fe1 and Fe2 are related by a threefold rotation around **c**. Primed atoms are related to unprimed ones by the twofold axis directed along **b**.

while in the second arrangement (sandwich-like, s) they are found on the same side. The p and s components have relative occupancies close to 2 : 1. Assuming independent coordination environments for the three iron(III) ions, the crystal is expected to contain a mixture of ppp, pps, ssp and sss isomers, in 0.312 : 0.444 : 0.211 : 0.033 proportions. Views of the structures of ppp and sss isomers are also depicted in Fig. S3 (ESI†).

The pitch of the propeller structure, evaluated as the dihedral angle between the LaO_2Fe and Fe_3La planes, has a value of 62.62(8)°. It is thus very similar to that found in $[Fe_4(\mu\text{-}OMe)_6(dpm)_6]$ (63.2°[10]) and smaller than in Fe_4 clusters containing tripodal ligands, where it ranges from 65.9° to 70.8°.[7]

DC and AC magnetic studies

The temperature (T) dependence of the molar magnetic susceptibility, χ_M, at low fields (H = 1–10 kOe) was measured between 1.9 and 240 K on a polycrystalline sample of **Fe_3La**. The data are reported in Fig. 2 as a $\chi_M T$-*vs.*-T plot, together with the isothermal molar magnetization collected for fields up to 50 kOe at 1.9 and 4.5 K. The high temperature value of the $\chi_M T$ product, 13.2 emu K mol^{-1}, is close to the expectation for three independent s_i = 5/2 spins (13.13 emu K mol^{-1} with g = 2.00). Upon cooling, the $\chi_M T$ of the product remains approximately constant down to about 25 K and then rapidly decreases reaching 9.5 emu K mol^{-1} at 1.9 K. A plot of $\chi_M{}^{-1}$ *vs.* T is linear in the whole temperature range explored and affords a Curie constant C = 13.264(5) emu K mol^{-1} and a Curie–Weiss temperature $\theta = -0.90(3)$ K (Fig. S4, ESI†). These data are indicative of three substantially independent iron(III) centres exhibiting weak magnetic anisotropy and/or antiferromagnetic interactions among each other. This is confirmed by inspection of isothermal molar magnetization data at 1.9 and 4.5 K, which exhibit significant nesting when plotted against H/T (Fig. S5, ESI†).

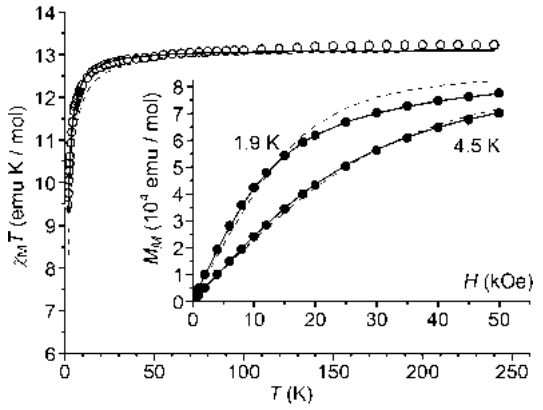

Fig. 2 Temperature dependence of the $\chi_M T$ product for compound **Fe_3La**. The inset shows the field dependence of the isothermal molar magnetization M_M measured at 1.9 and 4.5 K. The solid lines provide the best fit when including superexchange interactions and assuming axial $\mathbf{D}_1$ with β_1 = 90°. The dashed lines are the best simulation when single-ion anisotropies are neglected.

For a quantitative data analysis we assumed isotropic superexchange interactions among the metal centres, thereby disregarding anisotropic and antisymmetric exchange terms.[4] Such an assumption seem justified *a posteriori* by the fact that the single-site magnetic anisotropies so determined are much larger than isotropic coupling constants. The g factors were considered isotropic and equal to 2.00, while fourth-order single-ion anisotropy terms were neglected. Assuming D_3 symmetry the spin Hamiltonian takes the form

$$\hat{\mathcal{H}} = J(\hat{\mathbf{s}}_1 \cdot \hat{\mathbf{s}}_2 + \hat{\mathbf{s}}_2 \cdot \hat{\mathbf{s}}_3 + \hat{\mathbf{s}}_3 \cdot \hat{\mathbf{s}}_1) + g\mu_B \hat{\mathbf{S}} \cdot \mathbf{B} + \hat{\mathbf{s}}_1 \cdot \mathbf{D}_1 \cdot \hat{\mathbf{s}}_1 + \hat{\mathbf{s}}_2 \cdot \mathbf{D}_2 \cdot \hat{\mathbf{s}}_2 + \hat{\mathbf{s}}_3 \cdot \mathbf{D}_3 \cdot \hat{\mathbf{s}}_3 + \hat{\mathcal{H}}_{dip} \quad (5)$$

Here, $\mathbf{s}_i$ are the individual spin vectors for the high-spin iron(III) centres (s_i = 5/2), $\mathbf{S}$ is the total spin vector and $\hat{\mathcal{H}}_{dip}$ accounts for dipolar interactions. The molecular frame XYZ is defined with Z along the trigonal axis (**c**), Y along to the **b** axis, which is parallel to La1···Fe1 direction and coincides with a twofold symmetry axis, and X along **a*** (Fig. 1). Due to symmetry restrictions, the second-order anisotropy tensors $\mathbf{D}_i$ are related by a threefold rotation along Z and one of their principal axes (x_i, y_i or z_i) must coincide with the La1···Fe(i) direction. Referring to Fe1 for simplicity, this means that the $\mathbf{D}_1$ tensor expressed in the molecular XYZ frame contains four nonzero elements, *i.e.* $D_1(XX)$, $D_1(YY)$, $D_1(ZZ)$ and $D_1(XZ)$. However, since the tensor must be traceless, only two diagonal elements are independent, say $D_1(YY)$ and $D_1(ZZ)$, with $D_1(XX) = -[D_1(YY) + D_1(ZZ)]$. As an important feature, the magnetic energy surface resulting from Hamiltonian in eqn (5) has D_{3d} symmetry, *i.e.* the point-group symmetry of the molecule (D_3) *plus* an inversion centre. We want to emphasize here that only two of the four expected isomers in the crystal have rigorous D_3 symmetry, so that the spin-Hamiltonian parameters resulting from the present analysis have to be regarded as average values.

To obtain an upper-limit estimate of the J value, we have fixed single-site anisotropies to zero and simultaneously fitted $\chi_M T$-*vs.*-T and M_M-*vs.*-H data by a least-squares method on magnetization values (dipolar interactions were neglected for simplicity). The best-fit was achieved with J = 0.116(5) cm^{-1} although the quality of the fit was rather poor ($\chi^2 = 2.66 \times 10^{-2}$, see dashed lines in Fig. 2). A vastly improved reproduction of experimental data, with a more than hundred-fold decrease of χ^2, was possible by introducing single-site magnetic anisotropies. Using axial tensors for simplicity, the data were fitted with comparable accuracy for any angle (β_1) between z_1 and Z, affording D_1 and J values in the range 1.0–1.1 cm^{-1} and 0.05–0.07 cm^{-1}, respectively. With β_1 = 90°, for instance, the best-fit parameters are D_1 = 1.050(7) cm^{-1} and J = 0.0636(7) cm^{-1} ($\chi^2 = 1.66 \times 10^{-4}$, see continuous lines in Fig. 2). Although the available DC data do not allow a reliable determination of β_1, a much worse fit results when a negative D_1 is imposed, with $\chi^2 = 1.85 \times 10^{-3}$ at best. This strongly suggests that the single ion anisotropies are of the *hard-axis* type. To get further insight into molecular magnetic anisotropy, angular-resolved single-crystal SQUID magnetometry was attempted. However, due to

the weak anisotropy and the small crystal size, the data quality was not sufficient for a quantitative analysis.

In order to check SMM behaviour in comparison with Fe_4 clusters, AC magnetic measurements up to 10 kHz were also performed on **Fe_3La** at both zero and 1 kOe static applied fields (see Fig. S6, ESI†). Slow relaxation of the magnetization was not observed in the temperature range explored (1.9–3.5 K), showing that the compound behaves as a paramagnet.

Cantilever torque magnetometry

Cantilever torque data were collected at 2.3 and 5.5 K on a face-indexed single crystal of **Fe_3La** with mass of a few tens of μg. Fields up to 70 kOe were applied in two different planes. The field trajectory in the two rotations is shown in Fig. 3 along with the adopted **a*bc** reference frame and a sketch of the molecular structure. The direction in which the torque was measured for each rotation is indicated by an arrow and is always perpendicular to the field trajectory.

We start by considering the results of the first rotation (rot1), whose data at 2.3 K are presented in Fig. 4 for five different values of the applied field (10, 20, 30, 50 and 70 kOe). The measured torque component exhibits the 180°-periodicity expected for any paramagnetic system. At the beginning of the rotation (rot1 = 0°) the torque signal has a negative sign, which already indicates that the sample has a tendency to rotate so as to bring the **c** axis closer to the applied field, *i.e.* the trigonal axis corresponds to an easy magnetic direction. Zero torque is in fact measured at rot1 ∼ 155° (or, equivalently, at −25°), when the magnetic field lies close to the expected **c**-direction. However, the torque signal also vanishes at 51–63° and 231–243° (depending on applied field), meaning that zero-torque angles are *not evenly spaced*. This result demonstrates that single-site magnetic responses are nontensorial in nature and that the main requisite for our analysis is fulfilled. The key argument is that when the angular dependence of the magnetization follows eqn (3) and the field is scanned in a plane, as customarily done in torque magnetometry, the torque signal is proportional to sin(rot)cos(rot), where rot is the relevant rotation angle. Zero torque is thus expected every 90° (in other words, the magnetic free energy goes through extremes every 90°). We also notice that the torque curve detected in rot1 displays no additional symmetry properties beyond 180° periodicity, consistent with the molecular structure. The free energy surface is in fact expected to exhibit D_{3d} symmetry and a section along the mirror plane perpendicular to **b** will display *twofold* symmetry (plane point-group 2).

Turning now to the second rotation (rot2), the data recorded at 2.3 K at fields of 10, 30 and 50 kOe are shown in Fig. 5. The angular dependence of the torque is considerably more complex than for rot1. Beyond the trivial 180°-periodicity, the curve features additional oscillations and is *antisymmetric* with respect to rot2 ∼ 0° (mod 90). The reason is that a section of the free energy surface in a plane containing the **b** axis will in general display *2mm* point-group symmetry, with mirror lines

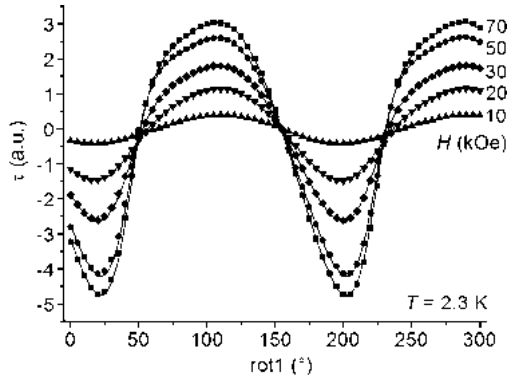

Fig. 4 Torque signal of **Fe_3La** measured at 2.3 K and for different values of the applied field during rot1. The cantilever was sensitive to the torque component along the green arrow in Fig. 3. The solid curves provide the best fit to experimental data.

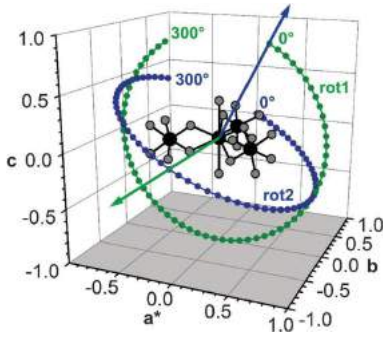

Fig. 3 Direction cosines of the magnetic field in the **a*bc** reference frame for the two performed rotations (rot1 and rot2), with the initial and final setting angles (0 and 300°). For each rotation, an arrow perpendicular to the field trajectory indicates the direction along which the torque signal has been measured. The molecular structure of **Fe_3La** is also included in the graph, omitting C and H atoms. Colour code: La, Fe = large black spheres, N, O = grey spheres.

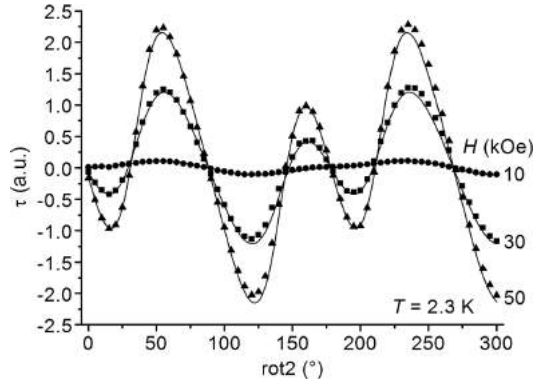

Fig. 5 Torque signal of **Fe_3La** measured at 2.3 K and for different values of the applied field during rot2. The cantilever was sensitive to the torque component along the blue arrow in Fig. 3. The solid curves provide the best fit to experimental data.

directed along **b** and normal to it. As a consequence, the setting angles rot2 = 0° (mod 90) correspond to free energy extremes and the torque component perpendicular to the section must then vanish at these specific angles. Furthermore, the torque must take opposite values at angles equidistant from rot2 = 0° (mod 90) as a result of the aforementioned mirror lines. All the described anomalies and the overall amplitude of the signal undergo considerable attenuation when the temperature is increased to 5.5 K, as shown in Fig. S7 (ESI†). At this temperature, the angular dependence detected in both rotations becomes closer to sin(rot)cos(rot), meaning that a behaviour described by eqn (3) is approached.

The observed departures from simple tensorial response at 2.3 K are consistent with dominant magnetic anisotropy effects over superexchange interactions, as found in the analysis of DC magnetization data. As a hint to the complex angular dependence of the measured torque signal, we have carried out detailed simulations of torque behaviour by neglecting dipolar and superexchange terms in eqn (5) and assuming $\mathbf{D}_1$ to be axial (Fig. S8 and S9, ESI†). Here, the value of β_1 becomes critical, as it determines whether a given sign of D_1 translates into an easy- or a hard-axis anisotropy along Z. More subtly, arranging $\mathbf{D}_1$ with its unique axis exactly perpendicular or parallel to **c** introduces an additional mirror plane normal to **c**, thereby raising the symmetry of the free energy surface from D_{3d} to D_{6h}. The section probed in rot1 would then display extra mirror lines parallel and perpendicular to **c**, causing the torque response to be antisymmetric with respect to rot1 = 0° (mod 90). Therefore, the observation of simple twofold symmetry in rot1 is a direct proof that, as far as rhombic distortion is weak or negligible, the single ion tensors are neither exactly parallel nor perpendicular to the trigonal axis. It is important to notice that adding isotropic superexchange interactions and/or dipolar couplings to the Hamiltonian does not change our conclusions, which are based on symmetry arguments.

Careful inspection of Fig. S8 and S9 (ESI†) suggests that for $D_1 = 1$ cm^{-1} the behaviour calculated with $\beta_1 = 70°$ is in reasonably close agreement with the sign and angular dependence of the torque signal observed in both rotations. When $D_1 = -1$ cm^{-1}, β_1 angles of 30°–40° also roughly reproduce the measured response, although the predicted behaviour in rot1 is more structured than observed. We have then carried out a least-squares fit of the whole set of experimental data recorded at 2.3 K as a function of applied field. The refined parameters were the three tensor elements $D_1(YY)$, $D_1(ZZ)$ and $D_1(XZ)$ (to allow local rhombicity) along with a scale factor (k_n) for each rotation (see Experimental section). Since at 5.5 K an approximately tensorial response is detected and Z remains an easy magnetic axis, the $D_1(ZZ)$ element must be negative. The space of the variables was then systematically sampled and two distinct χ^2 minima were found: $D_1(YY) = -0.340$ cm^{-1}, $D_1(ZZ) = -0.339$ cm^{-1}, $D_1(XZ) = 0.403$ cm^{-1} ($\chi^2 = 0.0200$) and $D_1(YY) = 0.900$ cm^{-1}, $D_1(ZZ) = -0.628$ cm^{-1}, $D_1(XZ) = -0.529$ cm^{-1} ($\chi^2 = 0.0358$). In a local frame $x_1y_1z_1$ with x_1 along Y, the two arrangements correspond to $D_1 = 1.23$ cm^{-1}, $E_1 = 0.070$ cm^{-1}, $\beta_1 = 70.8°$ and $D_1 = -1.51$ cm^{-1}, $E_1 = 0.396$ cm^{-1}, $\beta_1 = 35.7°$, respectively. Starting from the above findings, J and an angular offset (θ_n) for each rotation were introduced as further adjustable parameters. The complete model then comprised 488 datapoints and 8 adjustable parameters, namely $D_1(YY)$, $D_1(ZZ)$, $D_1(XZ)$ (or, alternatively, D_1, E_1, β_1), J, k_1, k_2, θ_1 and θ_2. Axial dipolar tensors were considered, with unique axis along the Fe···Fe directions and magnitude calculated using the point-dipolar approximation from the observed Fe···Fe distance (6.200 Å). Such an approach resulted in an extremely satisfactory reproduction of experimental data for both rotations ($\chi^2 = 2.62 \times 10^{-3}$) with $D_1 = 0.989(9)$ cm^{-1}, $E_1 = 0.0517(19)$ cm^{-1}, $J = 0.0783(19)$ cm^{-1}, $\beta_1 = 68.89(8)°$, $k_1 = 0.650(9)$, $k_2 = 0.696(9)$, $\theta_1 = -2.36(7)°$, $\theta_2 = 1.78(8)°$. We notice here that the angular offsets are comparable to the precision of visual crystal alignment and that the two scale factors differ by less than 7%. More important, J and θ_2 exhibit no correlation coefficients larger than 0.5 (in absolute value) with the other parameters, while β_1 and θ_1 display moderate reciprocal correlation (0.666). This parameter set also allows an accurate reproduction of the additional data collected at 5.5 K (see Fig. S7, ESI†). Imposing a negative D_1 parameter results in a much worse fit especially of the rot2 dataset (Fig. S10, ESI†), with a more than tenfold increased χ^2 and the requirement for a large rhombic distortion ($|E_1/D_1| = 0.23$).

Rewardingly, the best-fit D_1 and J values so obtained are close to those determined from the analysis of DC magnetic data (Fig. 2). Local anisotropies are not far from being axial, with $|E_1/D_1| = 0.05$ and the *intermediate* magnetic axis of $\mathbf{D}_1$ (x_1) directed along Y (Fig. 1b), in close agreement with previous work.[7,8,11,13] It is of interest that the angle β_1 between Z and the local hard axis z_1 is close to the helical pitch of the propeller-like structure (68.9 *vs.* 62.6°), indicating that the Fe anisotropy tensors are approximately perpendicular to the LaO_2Fe planes, which constitute the propeller "blades". From Fig. 1b it is also apparent that the hard axis of $\mathbf{D}_1$ is approximately directed along the O2–Fe1–O2′ axis.

The free energy surface computed with the best-fit spin-Hamiltonian parameters is presented in Fig. 6 for two different temperatures (2.3 and 5.5 K) and $H = 30$ kOe. As the temperature is raised, the D_{3d} symmetry is smeared out and the surface approaches cylindrical symmetry along **c**. Notice that when the field is scanned from **c** to **a*** in the **a*****c** plane, as done in rot1, the position of the free energy maximum at 2.3 K is close to the orientation of z_1. Therefore the shape of the free energy surface, which is probed by the torque method, directly discloses the arrangement of anisotropy tensors. Internal energy diagrams display similar features in an even clearer fashion, as do energy surfaces computed for very low temperature values (see Fig. S11 and S12, ESI†).

HF-EPR measurements

Powder EPR spectra of **Fe$_3$La** were recorded at 220.8, 240.0 and 331.2 GHz and two different temperatures (5 and 10 K). The 240.0 GHz spectra, presented in Fig. 7, exhibit signals in the 6–13.5 T region for the allowed transitions, and several groups of lines at lower fields associated to the so-called forbidden transitions (spectra at 331.2 and 220.8 GHz are available as Fig. S13 and S14, ESI,† respectively). Among the allowed transitions, at 5 K, we observed intense signals close to 6 T and much weaker ones close to 13.5 T. Thus, the EPR bands at the highest

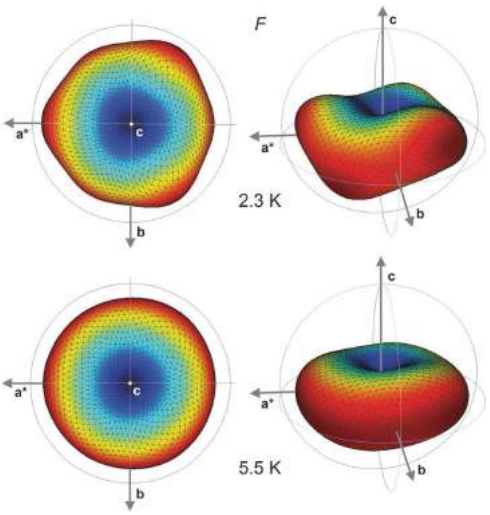

Fig. 6 Free energy surfaces computed with the set of best-fit spin-Hamiltonian parameters for different orientations of a 30 kOe magnetic field at 2.3 and 5.5 K. The distance from the centre of the diagram is proportional to $F - F_{min}$, where F_{min} is the minimum value of the free energy, which is found when the field is applied along **c**. The angular dependence of F is also displayed using a colour scale (from blue to red).

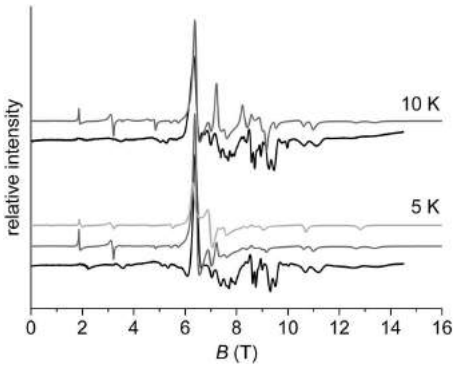

Fig. 7 Experimental EPR powder spectra (black lines) of **Fe_3La** at 240.0 GHz and 5 or 10 K. Best-fit spectra calculated at the same temperatures for independent (J = 0) iron(III) ions are shown in grey lines. The light grey line was calculated assuming three independent (J = 0) and equivalent iron(III) ions with D_i and E_i values that provide the best fit to torque data.

fields can be associated to parallel transitions whereas the ones close to 6 T come from perpendicular orientations, which means that the probed spin system has an hard axis anisotropy with $D_i > 0$. Another clear feature of the high field part of the spectrum is that the transitions are remarkably split, with a first pair of signals at 12.6 and 13.5 T and a second pair at 10.7 and 11.2 T. In addition, the intensity is larger for the highest field line in each pair, suggesting the presence of two inequivalent iron(III) sites in a $\sim$2 : 1 ratio. This result is in complete accordance with structural data, which indicate two different coordination environments (in $\sim$2 : 1 proportions) for the iron(III) ions. The spacing between these pairs of lines is close to 2.1 T (1.9 T for the lowest- and 2.3 T for the highest-field lines). Such a spacing should correspond to $2D_i$, indicating that $D_i \sim 1$ cm^{-1}. Since at 240.0 GHz the g = 2.00 signal is expected at 8.6 T, the lines observed at 10.7 T and 11.2 T can be assigned to transitions from $M_s = -3/2$ to $-1/2$ while the lines at 12.6 T and 13.5 T are due to transitions from $M_s = -5/2$ to $-3/2$. In a first approximation, the spectra can be described as a simple superposition of two s_i = 5/2 powder spectra with 2 : 1 intensity ratio, *i.e.* assuming magnetically-independent iron(III) centres (J = 0). A reasonable agreement (Fig. 7) between calculated and measured spectra is indeed obtained with the following parameters: $D_1 = 0.95$ cm^{-1}, $E_1 = 0.04$ cm^{-1}, and $D_2 = D_3 = 1.12$ cm^{-1}, $E_2 = E_3 = 0$, with an isotropic g = 2.00 in all cases. In order to reproduce the increase of the linewidth with increasing $|M_s|$ value, a Gaussian distribution of the D_i's was introduced characterized by $\Delta D_1 = 0.02$ cm^{-1} and by $\Delta D_2 = \Delta D_3 = 0.04$ cm^{-1}. The slightly higher anisotropy found for the majority iron(III) site (which features a p coordination environment) is in accordance with previous single-crystal EPR work on a Fe_4 complex exhibiting the same type of disorder.[38] In the same figure we also present the EPR spectrum calculated using three equivalent iron(III) sites with the D_i and E_i values that provide the best fit to torque data and J = 0. The agreement with the experimental spectra is of course poorer, as the splitting of parallel lines is not accounted for, but it plainly confirms that torque magnetometry gives a precise picture of the magnetic anisotropy of the constituent ions.

Even if spectra calculated for independent iron(III) centres are not far from experimental ones, the effect of a small super-exchange coupling between the iron(III) ions was also examined. In this case, it was not possible to look for an optimized set of parameters, since for $J \neq 0$ the relative orientation of single-site tensors and the existence of four possible isomers become relevant, leading to prohibitive calculation times. A few important results were nevertheless obtained from a sample calculation shown in Fig. S15 (ESI†), which was performed setting $\beta_i = 90°$ and $E_i = 0$ for simplicity. As a first consequence, the forbidden transitions are much better reproduced. Second, a small antiferromagnetic coupling leads to a slight shift of the whole spectrum towards higher fields. This means that the D_i values obtained from the calculation with J = 0 are slightly overestimated. Conversely, $|E_i|$'s are slightly underestimated.

DFT calculations and relation to the SMM properties of Fe_4 complexes

The experimental information on single-site anisotropies obtained from torque magnetometry was further compared with the results of DFT calculations. For simplicity, single-ion anisotropies were calculated for the ppp isomer only. From the relaxed geometry, we found the following structure information: La1$\cdots$Fe1 = 3.623 Å, Fe1$\cdots$Fe2 = 6.276 Å, La1–O1 = 2.511 Å, Fe1–O (average) = 2.039 Å and La1–O1–Fe1 = 107.04°. These structural results agree with the observed values listed in Table 1, considering that GGA is

known to give slightly overestimated bond lengths compared to experiment.[39]

The total magnetic anisotropy of the **Fe$_3$La** molecule was computed within DFT including spin–orbit coupling perturbatively, as discussed elsewhere.[36] The single-ion magnetic anisotropy was calculated using the same scheme as in ref. 36, by considering only the contribution arising from a single Fe atom in the **Fe$_3$La** molecule. Then we diagonalized the single-ion magnetic anisotropy matrix whose eigenvalues and eigenvectors provided magnetic anisotropy parameters and the hard, intermediate, and easy axes. We found hard-axis type anisotropies with $D_i = +1.094$ cm^{-1} and $E_i = 0.034$ cm^{-1}, the single-site intermediate axis (x_i) along the La1$\cdots$Fe(i) direction and the hard axis (z_i) at 72.7° from **c**. These parameters are very close to those experimentally determined and strongly support the picture of anisotropy tensors provided by torque magnetometry.

From the similarities in the coordination environment of peripheral ions, it can be expected that such an arrangement is largely preserved in Fe$_4$ SMMs. DFT calculations recently reported by van Wüllen and co-workers[14] on the trigonal compound [Fe$_4$(L)$_2$(dpm)$_6$] (**Fe$_4$**: H$_3$L = 1,1,1-tris(hydroxymethyl)ethane) lend considerable support to this picture by showing that the central iron(III) ion (Fe$_c$) has a negative zero-field splitting parameter with $D_c = -1.135$ cm^{-1} while the peripheral ions (Fe$_p$) have hard-axis tensors with $D_p = 0.621$ cm^{-1} and $E_p = 0.141$ cm^{-1}. The hard axes of the latter lie at 83.46° from Z and the Fe$_p\cdots$Fe$_c$ direction is the intermediate magnetic axis. These D_p and E_p values agree well with the results of magnetic dilution experiments (average over two sites: $D_p = 0.656$ cm^{-1} and $E_p = 0.089$ cm^{-1}).[13] Due to such an arrangement, and because dipolar– and spin–orbit contributions to anisotropic exchange roughly cancel out,[14] the triangle of peripheral iron(III) ions is found to be responsible for about 2/3 of the energy barrier in the ground $S = 5$ state of **Fe$_4$**.

The noncollinear single-site tensors of the peripheral ions are expected to generate high-order modulations of magnetic response which have been clearly detected by EPR spectroscopy on a related Cr-centred complex.[8] We used van Wüllen single-ion parameters to reconstruct the free energy surface of **Fe$_4$** at 2.3 K and 30 kOe while setting Fe–Fe superexchange interactions to the experimental values[11] and neglecting anisotropic exchange. The free energy surface was fitted to eqn (2) to determine the B_k^q parameters permitted by D_3 symmetry, which are given in the caption of Fig. S16 (ESI†). The values of $D(5)$ and B_4^0 (-0.433 and 1.51×10^{-5} cm^{-1}) are in remarkably good agreement with experimental ones (-0.445 and 1.0×10^{-5} cm^{-1}, respectively).[11] Of direct interest to the present work, however, are the high-order anisotropies introduced by $B_4^3\hat{O}_4^3$, $B_6^3\hat{O}_6^3$ and $B_6^6\hat{O}_6^6$, whose effect is displayed in Fig. S16 (ESI†), and bears strong resemblance to that found in **Fe$_3$La** (Fig. 6). This demonstrates that, although second-order contributions are overwhelmingly dominant, the orientation of single-site tensors determines a fine angular modulation of the magnetic response in the ground $S = 5$ spin state. Interestingly, all terms $B_4^3\hat{O}_4^3$, $B_6^3\hat{O}_6^3$ and $B_6^6\hat{O}_6^6$ were required for an accurate fitting of the free energy surface, with B_4^3, $B_6^6 > 0$ and $B_6^3 < 0$.[8]

Conclusions

The magnetic properties of weakly-coupled clusters of anisotropic spins, when investigated in the low-temperature regime on a single-crystal sample, display departures from simple tensorial response which can be used to map single-site anisotropy tensors. The angle- and field-dependence of the magnetization was studied on a lanthanum-centred triiron(III) complex with crystallographic D_3 symmetry, **Fe$_3$La**, where Fe–Fe interactions amount to less than 0.1 cm^{-1} while single-ion anisotropies are of the order of 1 cm^{-1}. Magnetic torque measurements at 2.3 K and at fields up to 70 kOe provided a complete picture of the local anisotropy tensors $\mathbf{D}_i$, including D_i and E_i parameters and the orientation of the principal axes in the molecular reference frame. The single-site tensors were found to be of the hard-axis type, as confirmed by HF-EPR spectra and DFT calculations. More importantly, they are strongly noncollinear and form an angle of $\sim$70° with the threefold molecular axis Z, which becomes an ''easy'' magnetic direction for the molecule. Although $\mathbf{D}_i$ tensors display only small rhombicity ($|E_i/D_i| \sim 0.05$), their intermediate axis coincides with the La1$\cdots$Fe(i) direction and the easy axis is found at $\sim$20° from Z. This description of single-site anisotropies in **Fe$_3$La** is fully consistent with a number of experimental and theoretical studies on the family of Fe$_4$ SMMs, which display a similar but iron(III)-centred structure. In particular, it confirms that the triangle of peripheral iron(III) ions contributes to the observed easy-axis anisotropy thanks to the strong noncollinearity of the single-site tensors, which are of the hard-axis type but approximately orthogonal to the (idealized) threefold molecular axis.

Finally, we notice that our approach based on low-temperature torque magnetometry might be easily extended to investigate weakly-interacting molecules embedded in a crystal and exhibiting noncollinear magnetic anisotropy axes, a very common situation in molecular magnetism.

Acknowledgements

Authors would like to thank the European Research Council and the italian MIUR for funding through the Advanced Grant MolNanoMaS (no. 267746) and a FIRB project (RBAP117RWN), respectively. X. Z. and K. P. were supported by U.S. National Science Foundation grant DMR-1206354. A.-L. B. would like to thank the Agence Nationale de la Recherche (project TEMAMA ANR-09-BLAN-0195-01) for financial support.

Notes and references

1 (*a*) J. Luzon, K. Bernot, I. J. Hewitt, C. E. Anson, A. K. Powell and R. Sessoli, *Phys. Rev. Lett.*, 2008, **100**, 247205; (*b*) L. F. Chibotaru, L. Ungur and A. Soncini, *Angew. Chem., Int. Ed.*, 2008, **47**, 4126–4129.
2 D. Gatteschi, R. Sessoli and J. Villain, *Molecular Nanomagnets*, Oxford University Press, 2006.

3 (*a*) D. N. Woodruff, R. E. P. Winpenny and R. A. Layfield, *Chem. Rev.*, 2013, **113**, 5110–5148; (*b*) T. Glaser, *Chem. Commun.*, 2011, **47**, 116–130.
4 A. Bencini and D. Gatteschi, *EPR of Exchange-coupled Systems*, Springer-Verlag, Berlin, 1990.
5 R. Inglis, C. J. Milios, L. F. Jones, S. Piligkos and E. K. Brechin, *Chem. Commun.*, 2012, **48**, 181–190.
6 (*a*) A.-L. Barra, A. Caneschi, A. Cornia, D. Gatteschi, L. Gorini, L.-P. Heiniger, R. Sessoli and L. Sorace, *J. Am. Chem. Soc.*, 2007, **129**, 10754–10762; (*b*) J. Liu and S. Hill, *Polyhedron*, 2013, **66**, 147–152; (*c*) S. Hill, *Polyhedron*, 2013, **64**, 128–135.
7 L. Gregoli, C. Danieli, A.-L. Barra, P. Neugebauer, G. Pellegrino, G. Poneti, R. Sessoli and A. Cornia, *Chem. – Eur. J.*, 2009, **15**, 6456–6467.
8 L. Sorace, M.-E. Boulon, P. Totaro, A. Cornia, J. F. Soares and R. Sessoli, *Phys. Rev. B: Condens. Matter Mater. Phys.*, 2013, **88**, 104407.
9 S. Hill, S. Datta, J. Liu, R. Inglis, C. J. Milios, P. L. Feng, J. J. Henderson, E. del Barco, E. K. Brechin and D. N. Hendrickson, *Dalton Trans.*, 2010, **39**, 4693–4707.
10 A.-L. Barra, A. Caneschi, A. Cornia, F. Fabrizi de Biani, D. Gatteschi, C. Sangregorio, R. Sessoli and L. Sorace, *J. Am. Chem. Soc.*, 1999, **121**, 5302–5310.
11 S. Accorsi, A.-L. Barra, A. Caneschi, G. Chastanet, A. Cornia, A. C. Fabretti, D. Gatteschi, C. Mortalo, E. Olivieri, F. Parenti, P. Rosa, R. Sessoli, L. Sorace, W. Wernsdorfer and L. Zobbi, *J. Am. Chem. Soc.*, 2006, **128**, 4742–4755.
12 L. Rigamonti, M. Piccioli, L. Malavolti, L. Poggini, M. Mannini, F. Totti, B. Cortigiani, A. Magnani, R. Sessoli and A. Cornia, *Inorg. Chem.*, 2013, **52**, 5897–5905.
13 E. Tancini, M. J. Rodriguez-Douton, L. Sorace, A.-L. Barra, R. Sessoli and A. Cornia, *Chem. – Eur. J.*, 2010, **16**, 10482–10493.
14 E. M. V. Kessler, S. Schmitt and C. van Wüllen, *J. Chem. Phys.*, 2013, **139**, 184110.
15 R. D. Shannon and C. T. Prewitt, *Acta Crystallogr., Sect. B: Struct. Crystallogr. Cryst. Chem.*, 1970, **26**, 1046–1048.
16 P. Totaro, K. C. M. Westrup, M.-E. Boulon, G. G. Nunes, D. F. Back, A. Barison, S. Ciattini, M. Mannini, L. Sorace, J. F. Soares, A. Cornia and R. Sessoli, *Dalton Trans.*, 2013, **42**, 4416–4426.
17 N. F. Chilton, S. K. Langley, B. Moubaraki and K. S. Murray, *Chem. Commun.*, 2010, **46**, 7787–7789.
18 (*a*) O. Waldmann, R. Koch, S. Schromm, J. Schülein, P. Müller, I. Bernt, R. W. Saalfrank, F. Hampel and E. Balthes, *Inorg. Chem.*, 2001, **40**, 2986–2995; (*b*) S. Carretta, P. Santini, G. Amoretti, M. Affronte, A. Ghirri, I. Sheikin, S. Piligkos, G. Timco and R. E. P. Winpenny, *Phys. Rev. B: Condens. Matter Mater. Phys.*, 2005, **72**, 06040(R); (*c*) F. El Hallak, P. Neugebauer, A.-L. Barra, J. van Slageren, M. Dressel and A. Cornia, *J. Magn. Reson.*, 2012, **223**, 55–60; (*d*) F. El Hallak, P. Rosa, P. Vidal, I. Sheikin, M. Dressel and J. van Slageren, *Europhys. Lett.*, 2011, **95**, 57002.
19 (*a*) J. R. Witt and E. I. Onstott, *J. Inorg. Nucl. Chem.*, 1962, **24**, 637–639; (*b*) X.-L. Zhu, G. Wu, Z.-C. Qiu, Y. Zhou, J. Gong, K.-K. Yang and Y.-Z. Wang, *J. Polym. Sci., Part A: Polym. Chem.*, 2008, **46**, 5214–5222.
20 V. G. Kessler, L. G. Hubert-Pfalzgraf, S. Halut and J.-C. Daran, *J. Chem. Soc., Chem. Commun.*, 1994, 705–706.
21 (*a*) A. Altomare, G. Cascarano, C. Giacovazzo and A. Guagliardi, *J. Appl. Crystallogr.*, 1993, **26**, 343–350; (*b*) A. Altomare, G. Cascarano, C. Giacovazzo, A. Guagliardi, M. C. Burla, G. Polidori and M. Camalli, *J. Appl. Crystallogr.*, 1994, **27**, 435–436.
22 (*a*) G. M. Sheldrick, *SHELX97, Programs for Crystal Structure Analysis*, University of Göttingen, Göttingen, 1997; (*b*) G. M. Sheldrick, *Acta Crystallogr., Sect. A: Found. Crystallogr.*, 2008, **64**, 112–122.
23 L. J. Farrugia, *J. Appl. Crystallogr.*, 2012, **45**, 849–854.
24 L. J. Farrugia, *J. Appl. Crystallogr.*, 1997, **30**, 565.
25 C. F. Macrae, I. J. Bruno, J. A. Chisholm, P. R. Edgington, P. McCabe, E. Pidcock, L. Rodriguez-Monge, R. Taylor, J. van de Streek and P. A. Wood, *J. Appl. Crystallogr.*, 2008, **41**, 466–470.
26 G. A. Bain and J. F. Berry, *J. Chem. Educ.*, 2008, **85**, 532–536.
27 ZHEEV LAPACK Driver Routine (version 2.0), Univ. of Tennessee, Univ. of California Berkeley, NAG Ltd., Courant Institute, Argonne National Lab, and Rice University, USA, 1994.
28 MINUIT Function Minimization and Error Analysis (version 94.1), CERN, Geneva, Switzerland, 1994–1998.
29 MESHLAB Visual Computing Lab, ISTI-CNR. http://meshlab.sourceforge.net/.
30 V. I. Lebedev and D. N. Laikov, *Dokl. Math.*, 1999, **59**, 477–481.
31 (*a*) C. J. H. Jacobsen, E. Pedersen, J. Villadsen and H. Weihe, *Inorg. Chem.*, 1993, **32**, 1216–1221; (*b*) S. Mossin, H. Weihe and A.-L. Barra, *J. Am. Chem. Soc.*, 2002, **124**, 8764–8765.
32 G. Kresse and J. Furthmüller, *Phys. Rev. B: Condens. Matter Mater. Phys.*, 1996, **54**, 11169–11186.
33 G. Kresse and J. Furthmüller, *Comput. Mater. Sci.*, 1996, **6**, 15–50.
34 J. P. Perdew, K. Burke and M. Ernzerhof, *Phys. Rev. Lett.*, 1996, **77**, 3865–3868.
35 G. Kresse and D. Joubert, *Phys. Rev. B: Condens. Matter Mater. Phys.*, 1999, **59**, 1758–1775.
36 (*a*) M. R. Pederson and K. A. Jackson, *Phys. Rev. B: Condens. Matter Mater. Phys.*, 1990, **41**, 7453–7461; (*b*) K. A. Jackson and M. R. Pederson, *Phys. Rev. B: Condens. Matter Mater. Phys.*, 1990, **42**, 3276–3281; (*c*) D. V. Porezag, PhD thesis, Chemnitz Technical Institute, 1997; (*d*) D. Porezag and M. R. Pederson, *Phys. Rev. A: At., Mol., Opt. Phys.*, 1999, **60**, 2840–2847.
37 M. R. Pederson and S. N. Khanna, *Phys. Rev. B: Condens. Matter Mater. Phys.*, 1999, **60**, 9566–9572.
38 A. Bouwen, A. Caneschi, D. Gatteschi, E. Goovaerts, D. Schoemaker, L. Sorace and M. Stefan, *J. Phys. Chem. B*, 2001, **105**, 2658–2663.
39 P. Haas, F. Tran, P. Blaha, K. Schwarz and R. Laskowski, *Phys. Rev. B: Condens. Matter Mater. Phys.*, 2009, **80**, 195109.

Mapping of single-site magnetic anisotropy tensors in weakly coupled spin clusters by torque magnetometry†

Luca Rigamonti,[a] Andrea Cornia,*[a] Andrea Nava,[a,b] Marie-Emmanuelle Boulon,[c,¶] Mauro Perfetti,[c] Anne-Laure Barra,[d] Xiaoliang Zhong,[e] Kyungwha Park,[e] and Roberta Sessoli[c]

[a] *Dipartimento di Scienze Chimiche e Geologiche, Università degli Studi di Modena e Reggio Emilia & INSTM RU of Modena and Reggio Emilia, via G. Campi 183, 41125 Modena, Italy. E-mail: andrea.cornia@unimore.it*

[b] *Dipartimento di Scienze Fisiche, Informatiche e Matematiche, Università degli Studi di Modena e Reggio Emilia, via G. Campi 183, 41125 Modena, Italy.*

[c] *Laboratory of Molecular Magnetism (LaMM), Dipartimento di Chimica 'Ugo Schiff', Università degli Studi di Firenze & INSTM RU of Firenze, via della Lastruccia 3-13, 50019 Sesto Fiorentino (FI), Italy.*

[d] *Laboratoire National des Champs Magnétiques Intenses, CNRS, BP166, 25 Avenue des Martyrs, 38042 Grenoble Cedex 9, France.*

[e] *Department of Physics, Virginia Tech, Blacksburg Virginia 24060, USA.*

¶ Present address: Photon Science Institute, EPSRC School of Chemistry, The University of Manchester, Oxford Road, Manchester M13 9PL, UK.

SUPPORTING INFORMATION

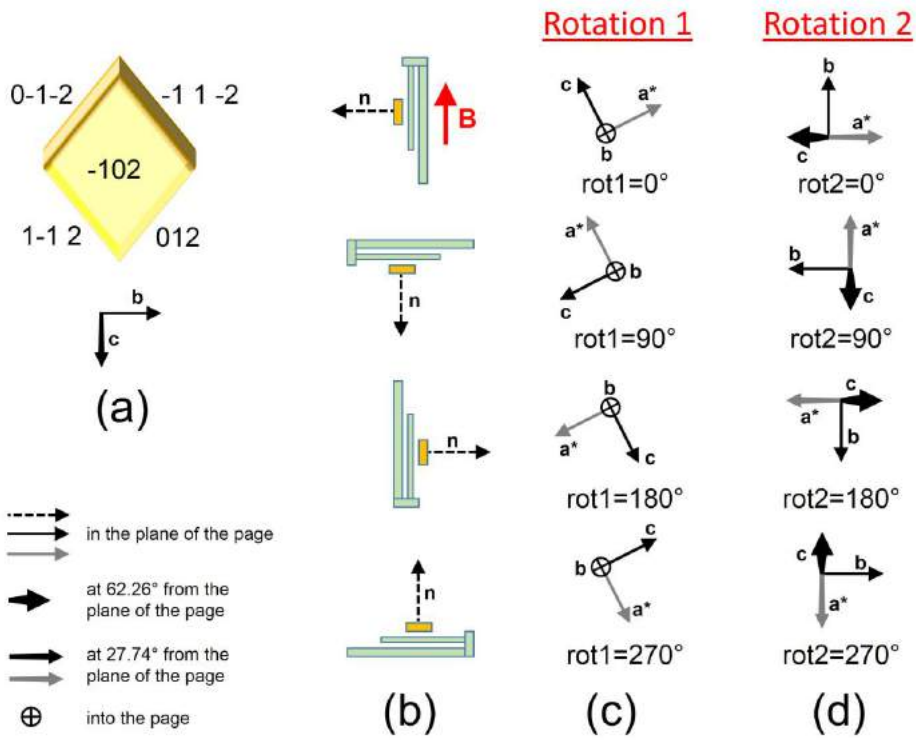

Fig. S1 Details on the geometry of torque measurements. In (a) we show face indices and the arrangement of the crystallographic axes, while in (b-d) we present the orientation of the cantilever (b) and of the crystallographic axes in the course of the two rotations for four different values of the setting angles (c, d).

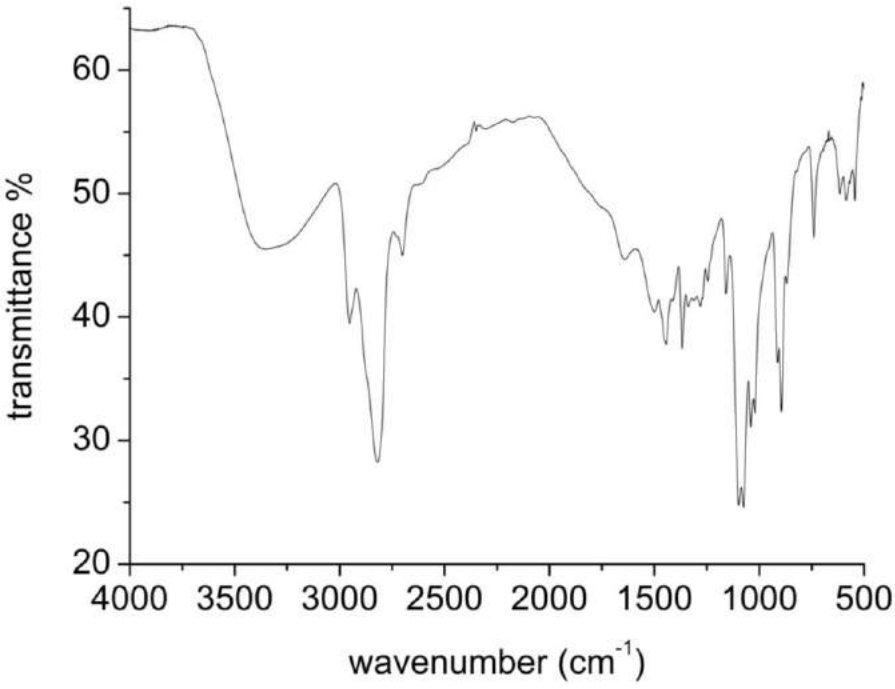
transmittance %
60
50
40
30
20
4000 3500 3000 2500 2000 1500 1000 500
wavenumber (cm-1)

(a)

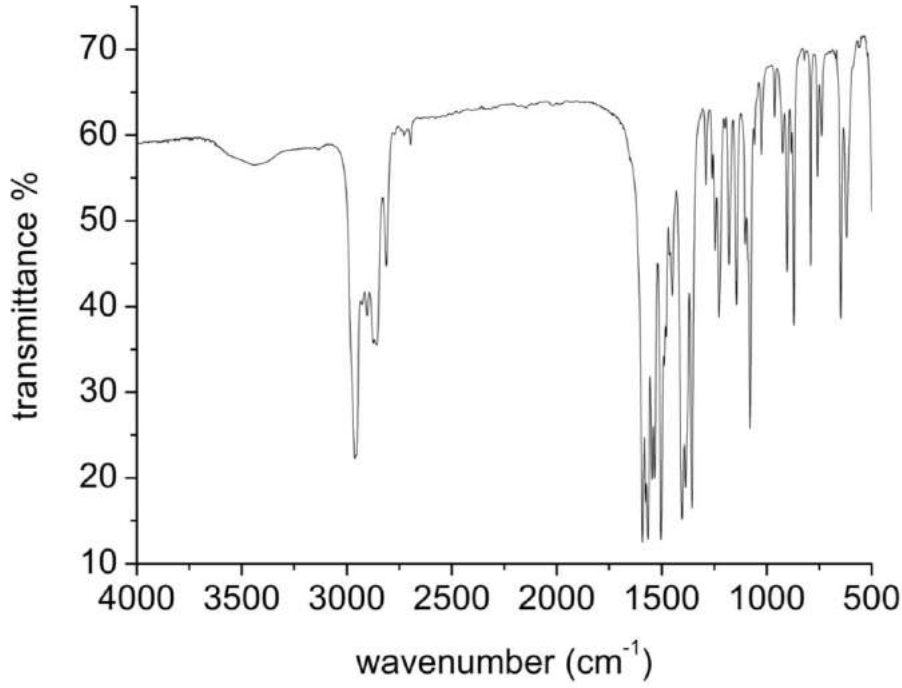
transmittance %
70
60
50
40
30
20
10
4000 3500 3000 2500 2000 1500 1000 500
wavenumber (cm-1)

(b)

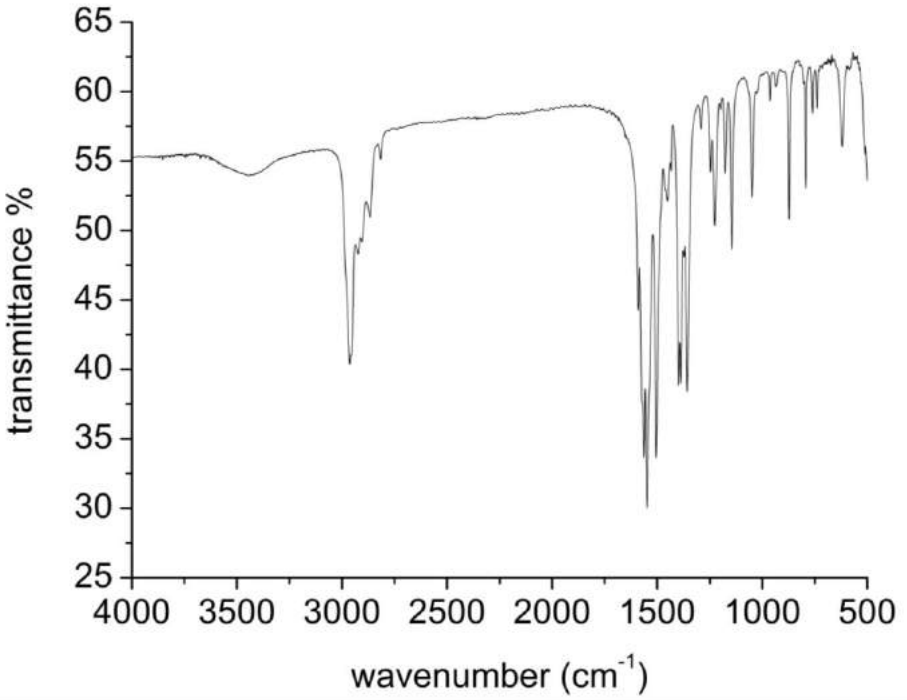

(c)

Fig. S2 Infrared spectra of $[H_3La(tea)_2]$ (a), **Fe_3La** (b), and $[Fe_2(\mu\text{-}OMe)_2(dpm)_4]$ (c) as KBr disks.

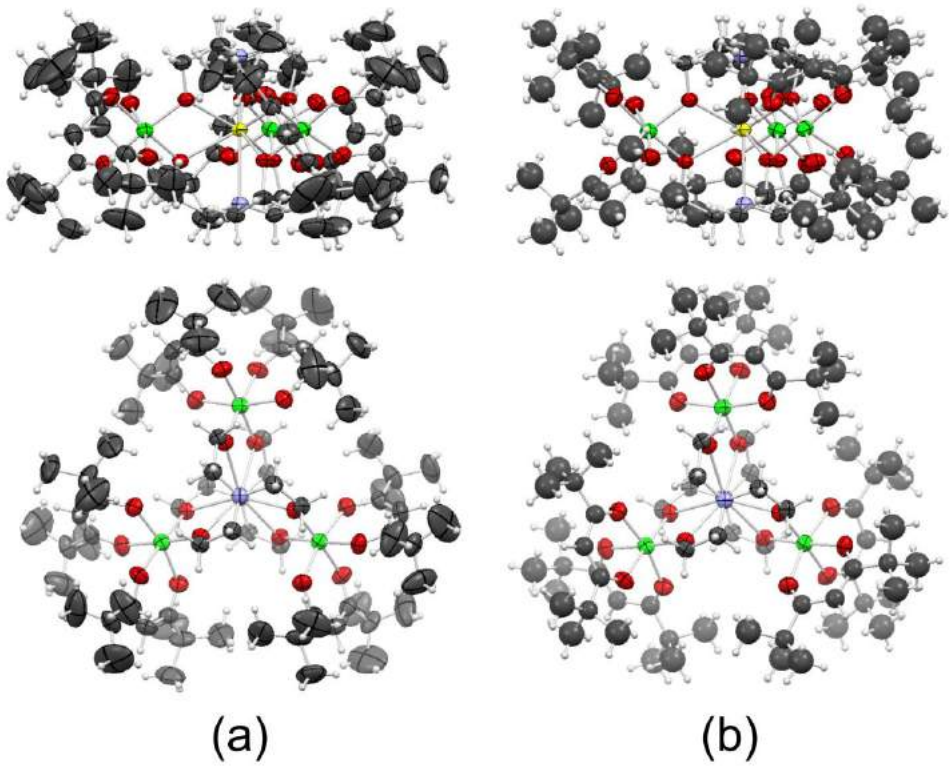

Fig. S3 Side and top views of the *ppp* (a) and *sss* (b) isomers in crystals of **Fe_3La** (La = yellow, Fe = green, O = red, N = blue, C = grey, H = white). Displacement ellipsoids are drawn at 40% probability level.

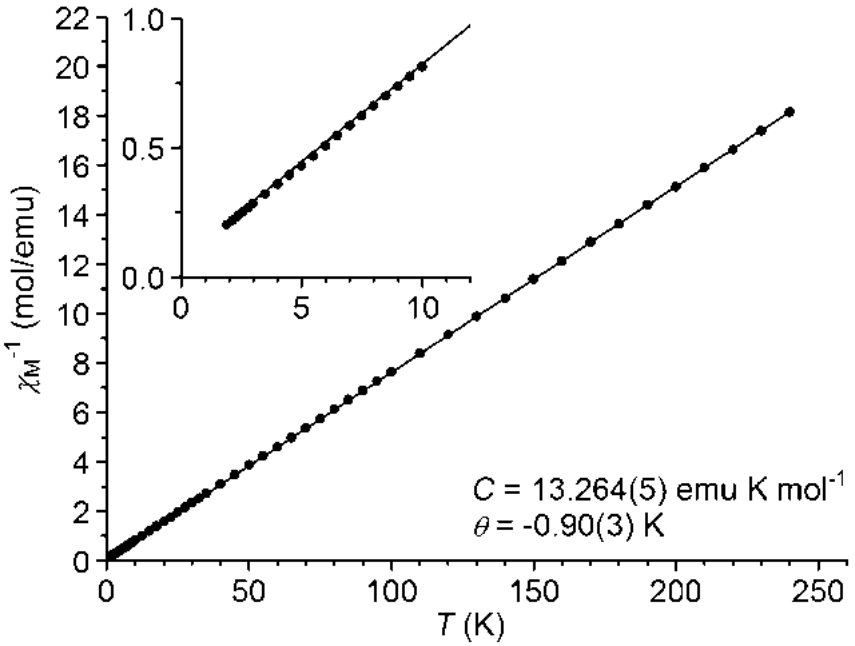

Fig. S4 Curie-Weiss plot for **Fe_3La**. The inset displays an enlargement of the low-temperature region.

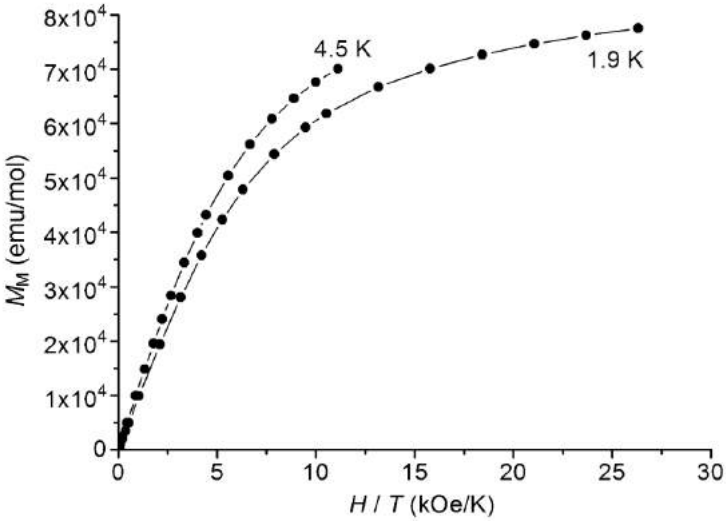

Fig. S5 Isothermal molar magnetization M_M vs. H/T data for **Fe_3La**. The nesting of curves recorded at different temperatures indicates departures from Brillouin function due to magnetic anisotropy and/or spin-spin interactions.

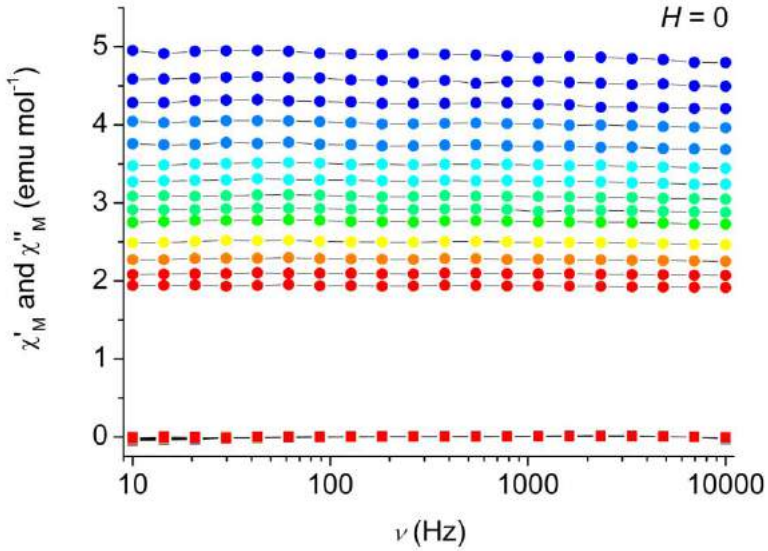

(a)

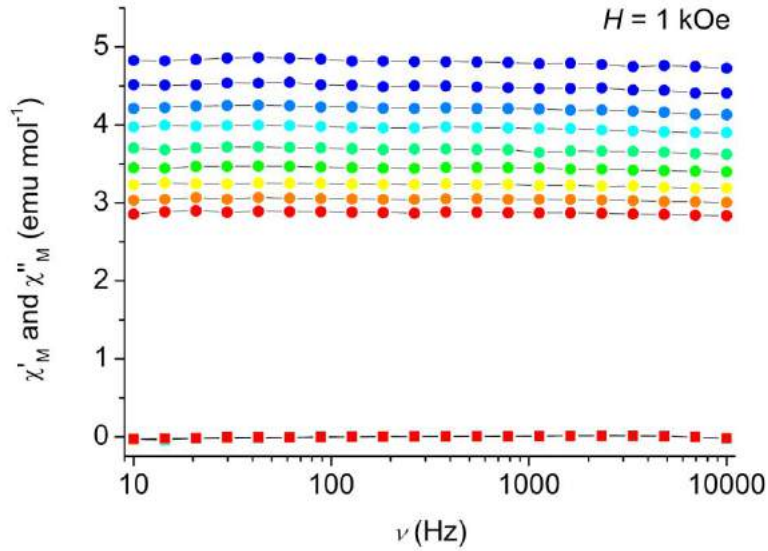

(b)

Fig. S6 Frequency dependence of the in-phase χ'_M (●) and out-of-phase χ''_M (■) AC susceptibilities of compound **Fe_3La** in zero (a) and 1-kOe (b) applied static fields and in the temperature range from 1.9 (red) to 3.5 K (blue).

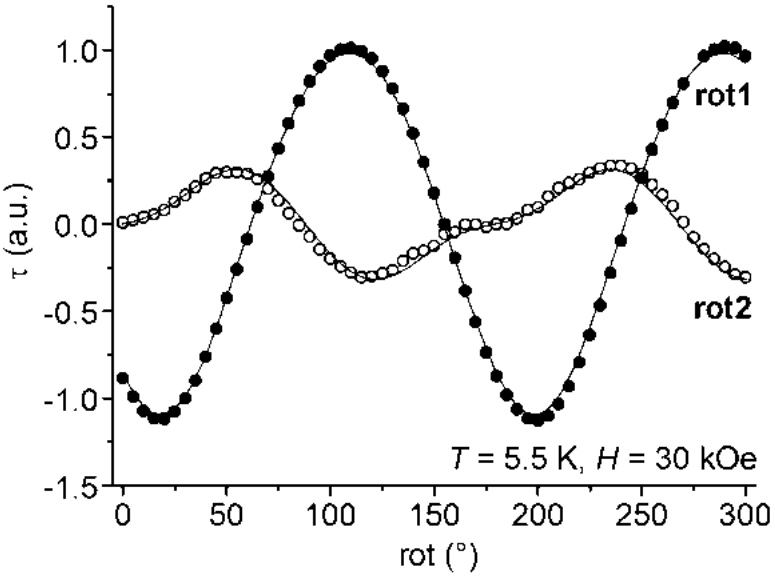

Figure S7. Torque signal for **rot1** and **rot2** at 5.5 K and 30 kOe. The cantilever was sensitive to the torque component along the green and blue arrows, respectively, in Fig. 3. The solid curves were calculated with the spin-Hamiltonian parameters, scale factors and angular offsets that provide the best fit to the 2.3 K data in Figs. 4 and 5.

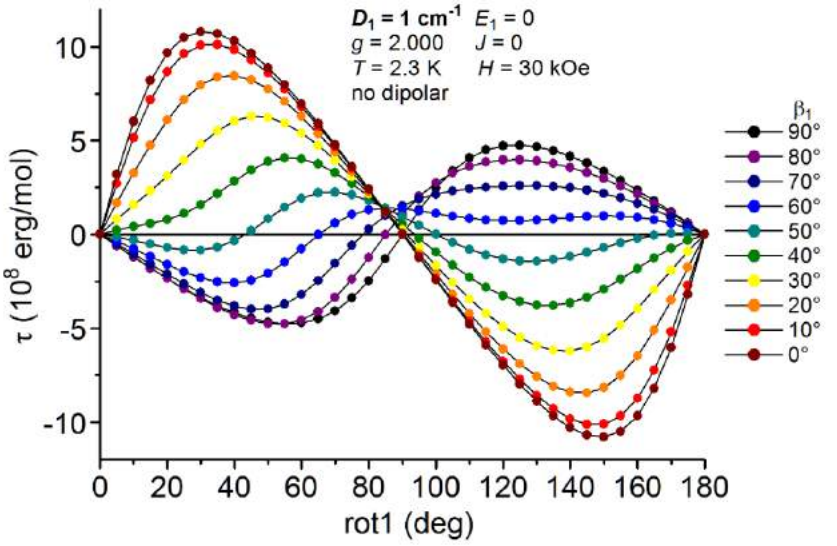
D_1 = 1 cm^{-1} E_1 = 0
g = 2.000 J = 0
T = 2.3 K H = 30 kOe
no dipolar
τ (10^8 erg/mol)
rot1 (deg)
β1
90°
80°
70°
60°
50°
40°
30°
20°
10°
0°

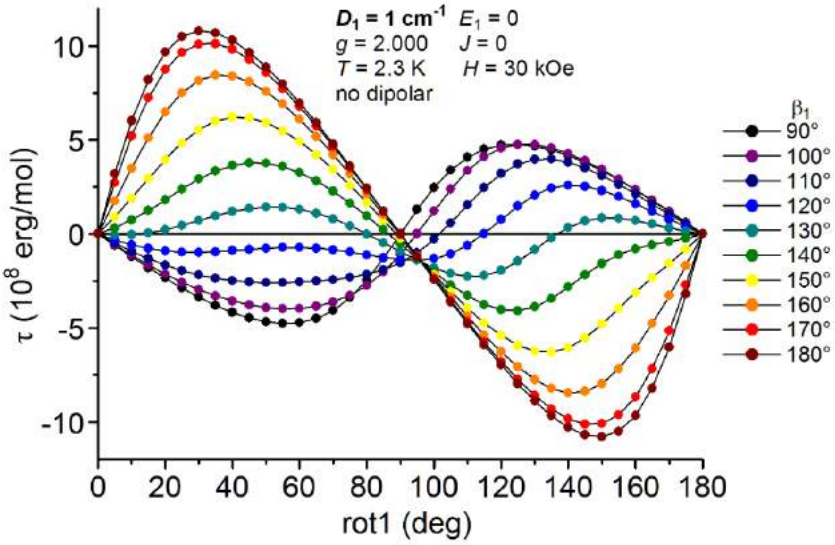
D_1 = 1 cm^{-1} E_1 = 0
g = 2.000 J = 0
T = 2.3 K H = 30 kOe
no dipolar
τ (10^8 erg/mol)
rot1 (deg)
β1
90°
100°
110°
120°
130°
140°
150°
160°
170°
180°

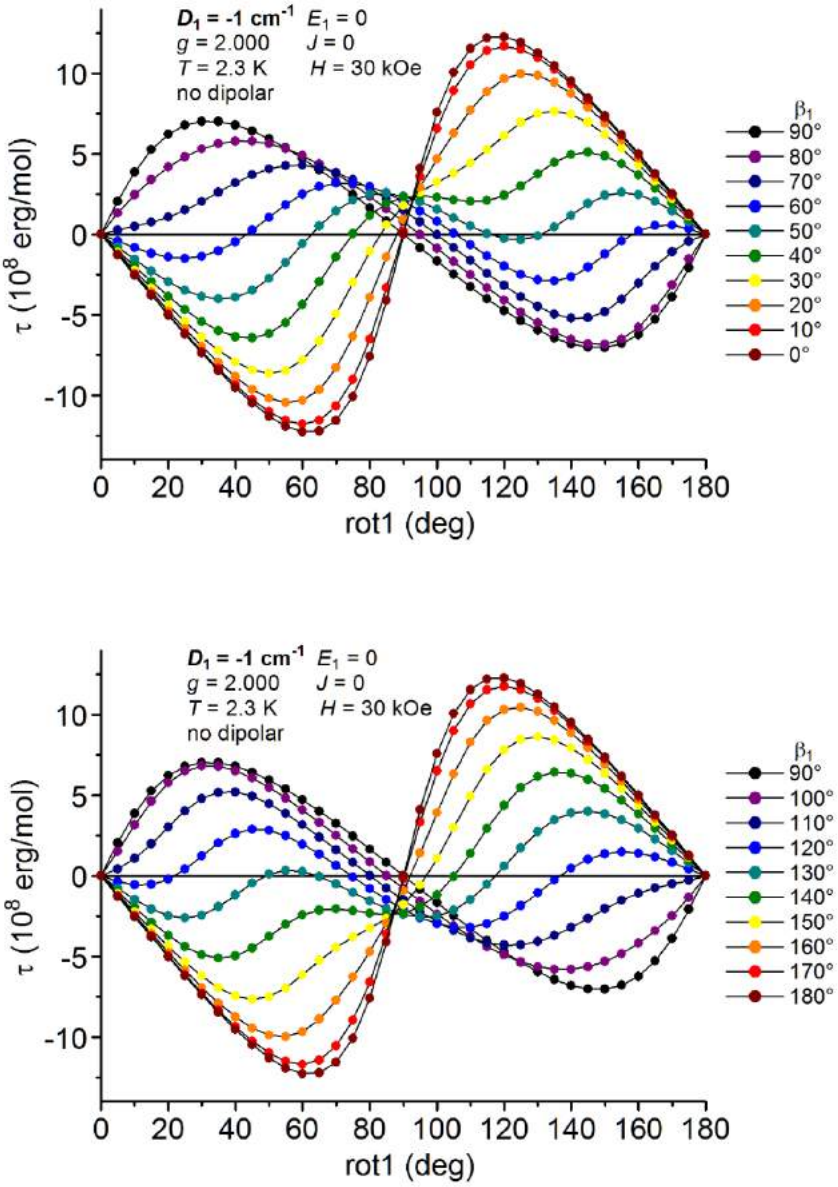

Fig. S8 Torque signal for **rot1** calculated with the indicated set of spin Hamiltonian parameters and for different values of the Euler angle β_1. Here, an offset of +27.74° was added to the rotation angle as defined in Fig. 3, so that at rot1 = 0 the magnetic field is directed along the **c** axis. The reported component of the torque is that along the green arrow in Fig. 3. Notice that curves are antisymmetric with respect to rot1 = 0 (mod 90) only for β_1 = 0, 90° and 180°.

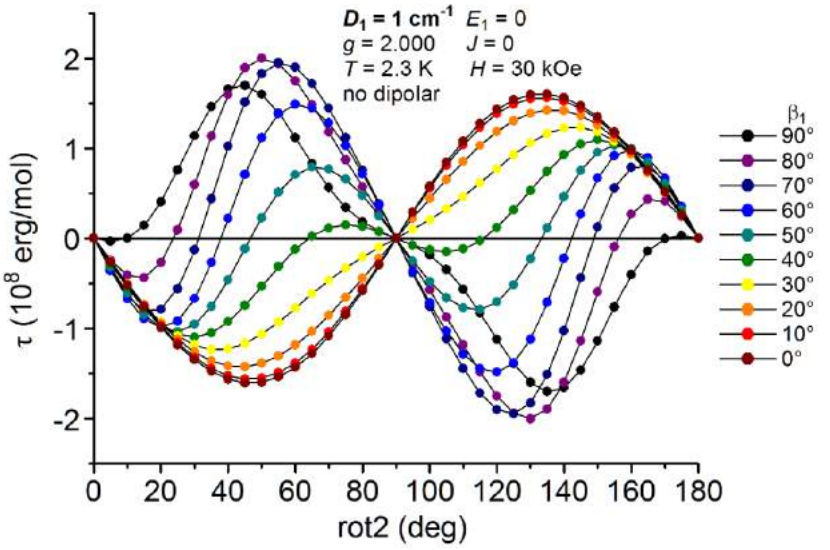
D_1 = 1 cm^{-1} E_1 = 0
g = 2.000 J = 0
T = 2.3 K H = 30 kOe
no dipolar
τ (10^8 erg/mol)
rot2 (deg)
β1
90°
80°
70°
60°
50°
40°
30°
20°
10°
0°

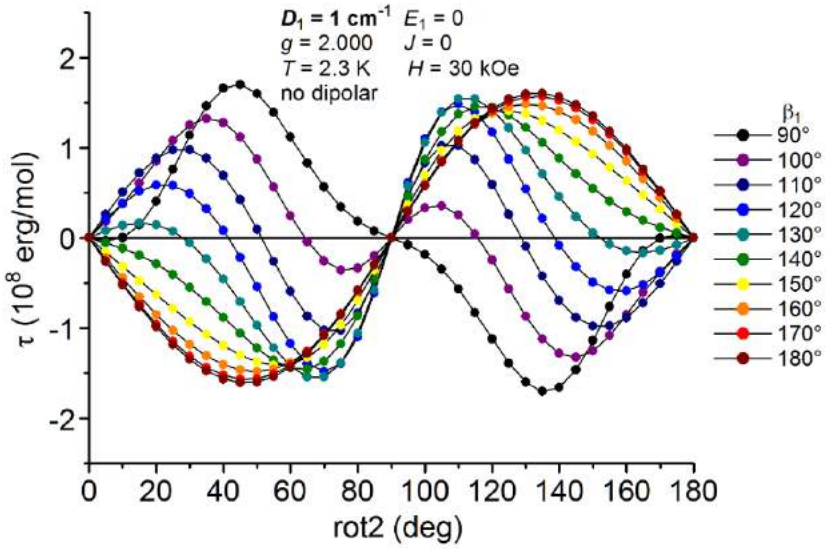
D_1 = 1 cm^{-1} E_1 = 0
g = 2.000 J = 0
T = 2.3 K H = 30 kOe
no dipolar
τ (10^8 erg/mol)
rot2 (deg)
β1
90°
100°
110°
120°
130°
140°
150°
160°
170°
180°

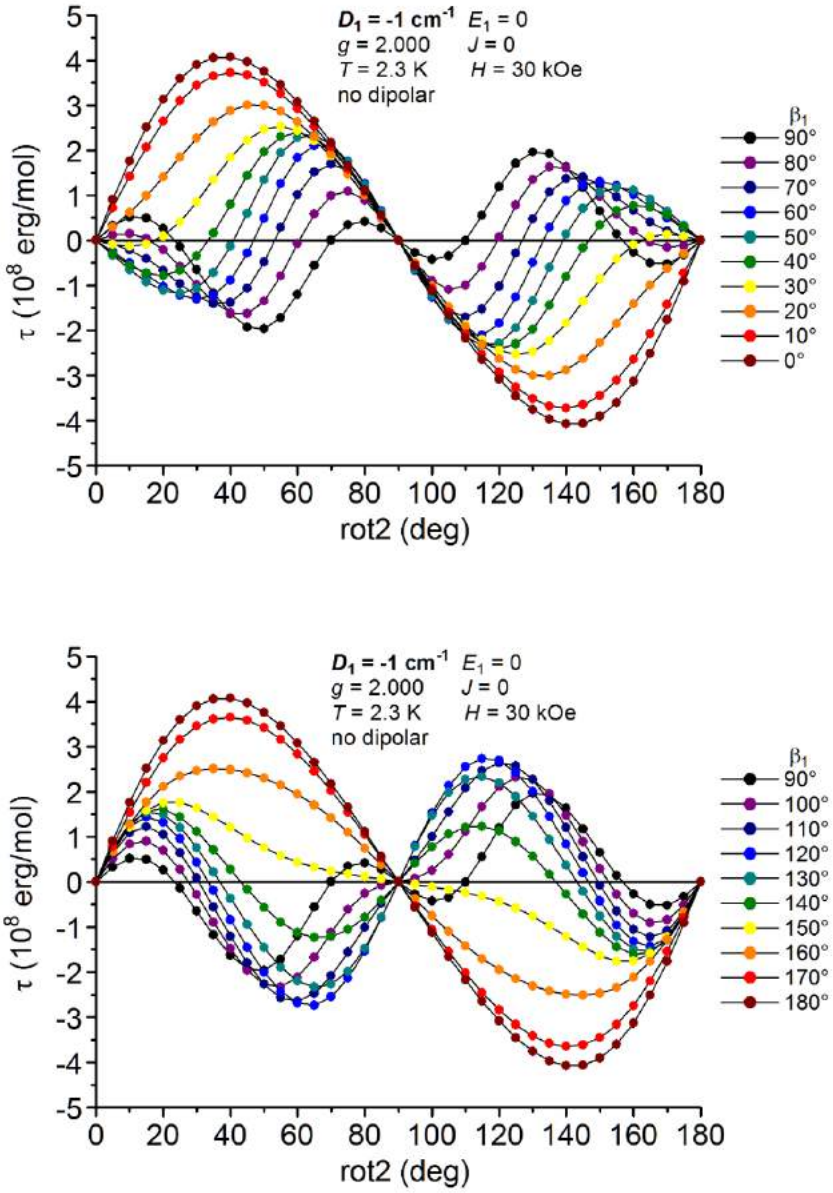

Fig. S9 Torque signal for **rot2** calculated with the indicated set of spin Hamiltonian parameters and for different values of the Euler angle β_1. Here, the rotation angle is the same as defined in Fig. 3, so that at rot2 = 0 the magnetic field is directed along the **b** axis. The reported component of the torque is that along the blue arrow in Fig. 3. Notice that all curves are antisymmetric with respect to rot2 = 0 (mod 90).

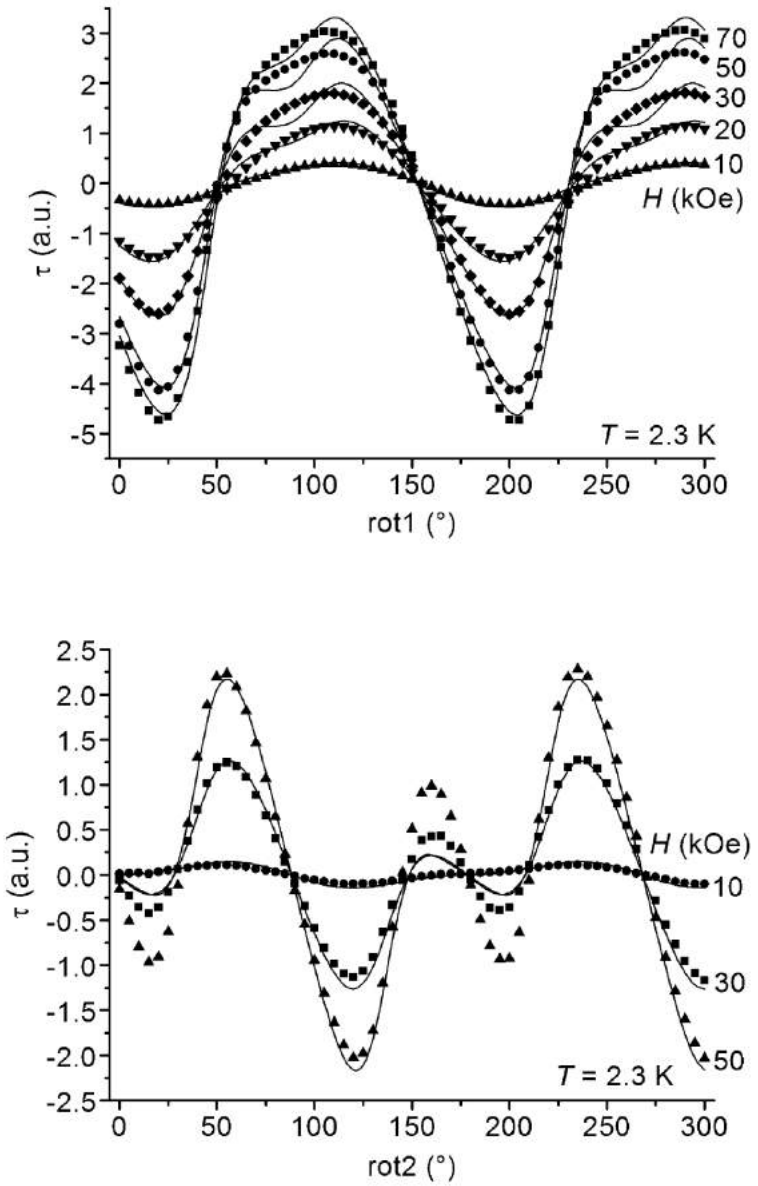

Fig. S10 Best-fit simulation of torque data at 2.3 K with $D_1 < 0$ (D_1 = –1.34(3) cm^{-1}, E_1 = –0.320(18) cm^{-1}, J = 0.066(7) cm^{-1}, β_1 = 35.1(4)°, k_1 = 0.304(7), k_2 = 0.368(10), θ_1 = –0.61(19)°, θ_2 = 1.8(3)°, $\chi^2 = 2.87 \times 10^{-2}$).

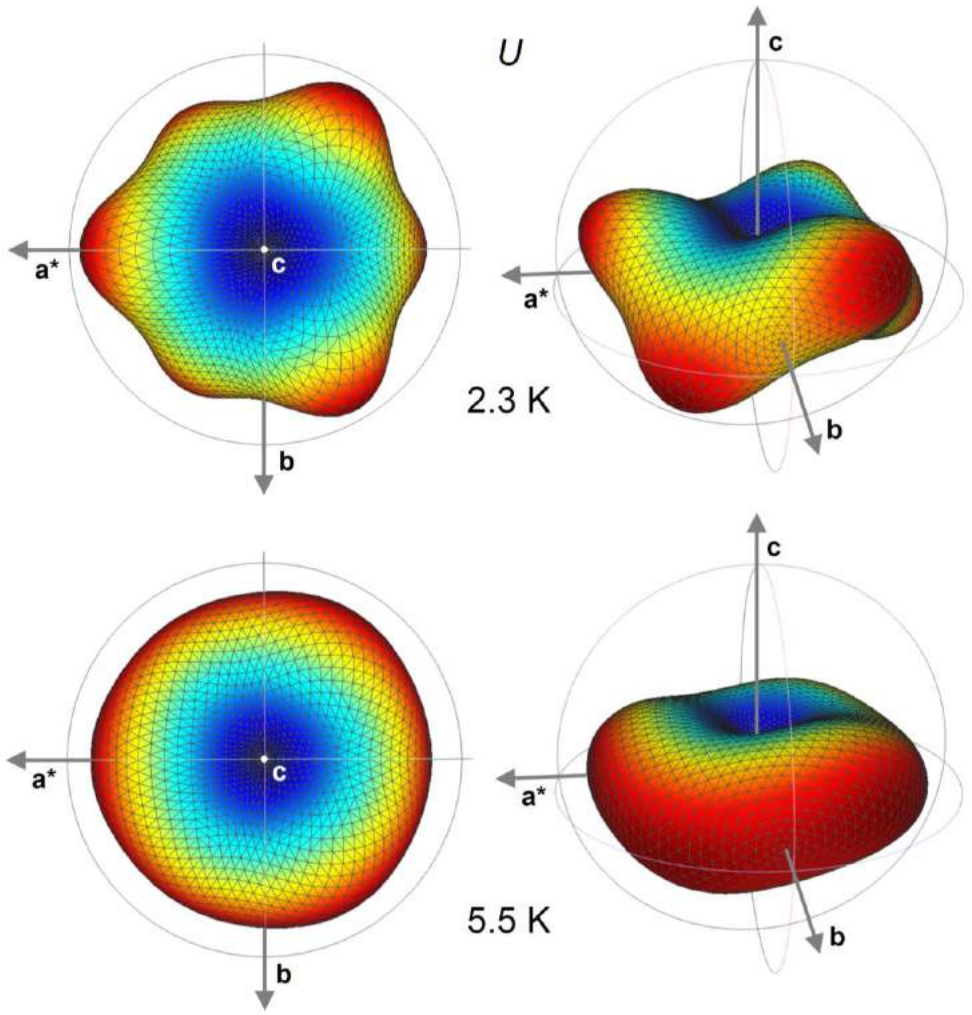

Fig. S11 Internal energy surfaces of **Fe_3La** computed with the set of best-fit spin Hamiltonian parameters for different orientations of a 30-kOe magnetic field at 2.3 and 5.5 K. The distance from the centre of the diagram is proportional to $U - U_{min}$, where U_{min} is the minimum value of the internal energy that is found when the field is applied along **c**. The angular dependence of U is also displayed using a colour scale (from blue to red).

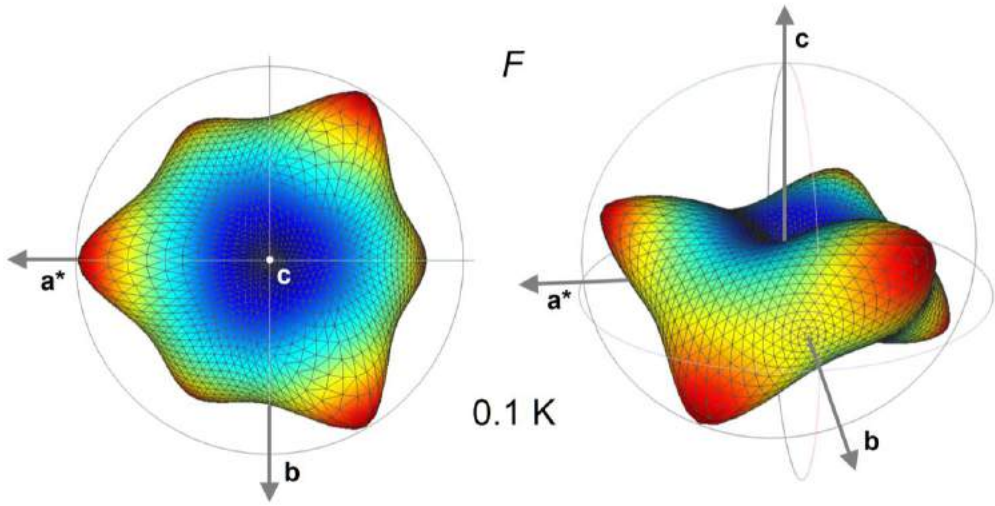

Fig. S12 Free energy surface of **Fe_3La** computed with the set of best-fit spin Hamiltonian parameters for different orientations of a 30-kOe magnetic field at 0.1 K. The distance from the centre of the diagram is proportional to $F - F_{min}$, where F_{min} is the minimum value of the free energy that is found when the field is applied along **c**. The angular dependence of F is also displayed using a colour scale (from blue to red).

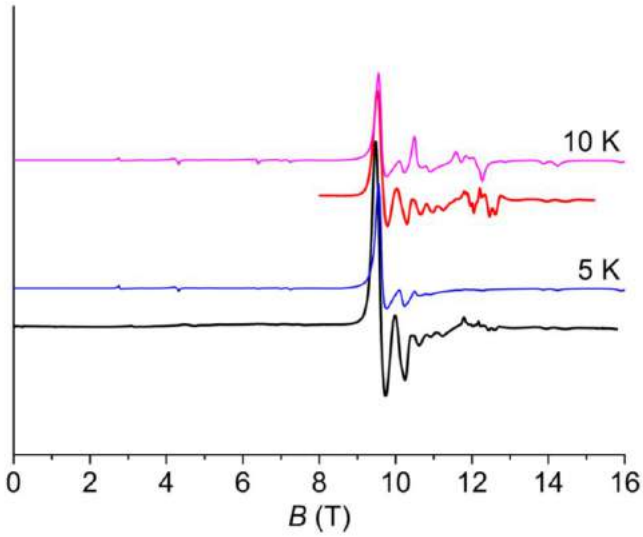

Fig. S13 EPR powder spectra (331.2 GHz) of **Fe_3La** at 5 and 10 K. Experimental spectra are drawn in black and red, while blue and pink curves are calculated spectra for independent (J = 0) iron(III) sites with D_1 = 0.95 cm^{-1}, E_1 = 0.04 cm^{-1}, $D_2 = D_3$ = 1.12 cm^{-1}, $E_2 = E_3$ = 0, ΔD_1 = 0.02 cm^{-1}, $\Delta D_2 = \Delta D_3$ = 0.04 cm^{-1} and an isotropic g = 2.00 in all cases.

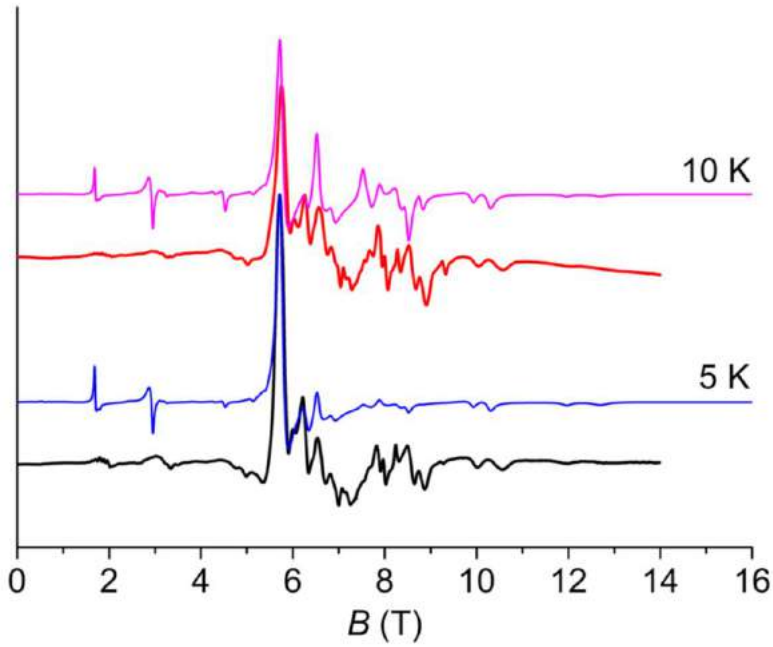

Fig. S14 EPR powder spectra (220.8 GHz) of **Fe_3La** at 5 and 10 K. Experimental spectra are drawn in black and red, while blue and pink curves are calculated spectra for independent (J = 0) iron(III) sites with D_1 = 0.95 cm^{-1}, E_1 = 0.04 cm^{-1}, $D_2 = D_3$ = 1.12 cm^{-1}, $E_2 = E_3$ = 0, ΔD_1 = 0.02 cm^{-1}, $\Delta D_2 = \Delta D_3$ = 0.04 cm^{-1} and an isotropic g = 2.00 in all cases.

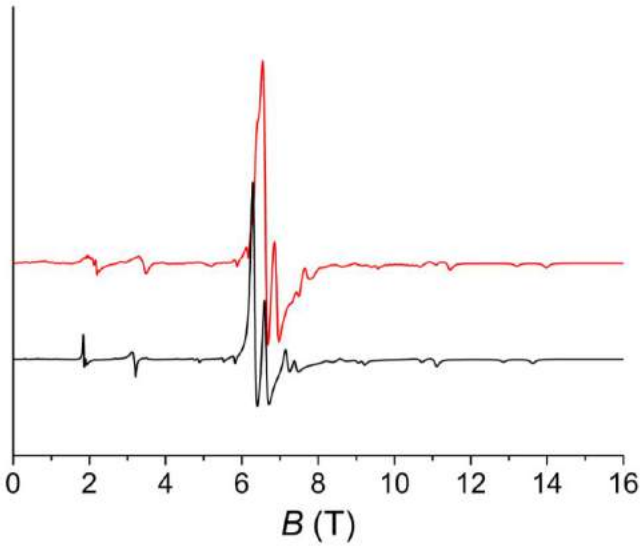

(a)

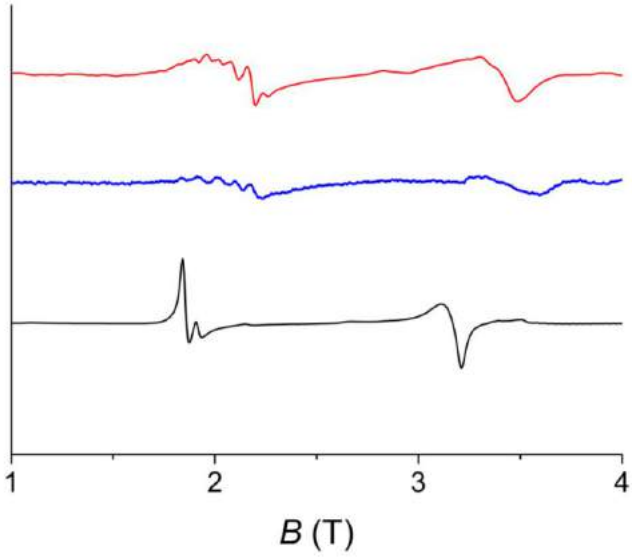

(b)

Fig. S15 (a) Calculated EPR powder spectra at 240.0 GHz and 5 K with D_1 = 1.00 cm^{-1}, $D_2 = D_3$ = 1.18 cm^{-1}, $E_1 = E_2 = E_3 = 0$, $\beta_1 = \beta_2 = \beta_3 = 90°$ and an isotropic g = 2.00. The black and red curves correspond to J = 0 and J = 0.064 cm^{-1}, respectively. (b) Zoom over the forbidden transitions together with the experimental spectrum of **Fe_3La** (blue curve).

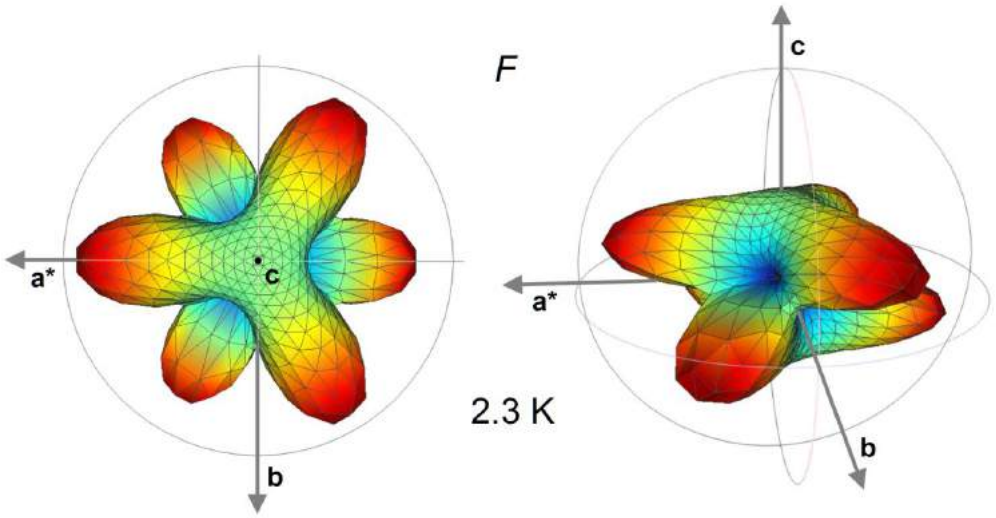

Fig. S16 Free energy surface of **Fe$_4$** computed using van Wüllen single-ion parameters for different orientations of a 30-kOe magnetic field at 2.3 K. The axial components $B_2^0\hat{O}_2^0$, $B_4^0\hat{O}_4^0$ and $B_6^0\hat{O}_6^0$ have been subtracted from the data to better display the high-order modulations arising from $B_4^3\hat{O}_4^3$, $B_6^3\hat{O}_6^3$ and $B_6^6\hat{O}_6^6$. The distance from the centre of the diagram is proportional to $F - F_{min}$, where F_{min} is the minimum value of the free energy that is found when the field is applied along **c**. The angular dependence of F is also displayed using a colour scale (from blue to red). The best-fit set of parameters required to reproduce the pristine free energy surface is: $D(5) = 3B_2^0 = -0.433$ cm^{-1}, $B_4^0 = 1.51 \times 10^{-5}$ cm^{-1}, $B_4^3 = 8.95 \times 10^{-5}$ cm^{-1}, $B_6^0 = 1.74 \times 10^{-8}$ cm^{-1}, $B_6^3 = -1.10 \times 10^{-7}$ cm^{-1} and $B_6^6 = 6.09 \times 10^{-8}$ cm^{-1}.

Bibliography

[1] B. D. Cullity and C. D. Graham. *Introduction to magnetic materials*. John Wiley & Sons, 2008.

[2] E. C. Stoner and E. Wohlfarth. "A mechanism of magnetic hysteresis in heterogeneous alloys". In: *Philosophical Transactions of the Royal Society of London A: Mathematical, Physical and Engineering Sciences* 240.826 (1948), p. 599.

[3] N. D. Mermin and H. Wagner. "Absence of ferromagnetism or antiferromagnetism in one-or two-dimensional isotropic Heisenberg models". In: *Physical Review Letters* 17.22 (1966), p. 1133.

[4] A. Kashuba and V. L. Pokrovsky. "Stripe domain structures in a thin ferromagnetic film". In: *Physical Review B* 48.14 (1993), p. 10335.

[5] Y. Wu et al. "Magnetic stripe domains in coupled magnetic sandwiches". In: *Physical review letters* 93.11 (2004), p. 117205.

[6] O Portmann et al. "An inverse transition of magnetic domain patterns in ultrathin films". In: *Nature* 422.6933 (2003), p. 701.

[7] J. H. van Vleck. "On the anisotropy of cubic ferromagnetic crystals". In: *Physical Review* 52.11 (1937), p. 1178.

[8] W Hübner and K. Bennemann. "Simple theory for spin-lattice relaxation in metallic rare-earth ferromagnets". In: *Physical Review B* 53.6 (1996), p. 3422.

[9] J Trygg et al. "Total Energy Calculation of the Magnetocrystalline Anisotropy Energy in the Ferromagnetic 3 d Metals". In: *Physical review letters* 75.15 (1995), p. 2871.

[10] S. Halilov et al. "Magnetocrystalline anisotropy energy in cubic Fe, Co, and Ni: Applicability of local-spin-density theory reexamined". In: *Physical Review B* 57.16 (1998), p. 9557.

[11] R. Sessoli et al. "Magnetic bistability in a metal-ion cluster". In: *Nature* 365 (1993), p. 141.

[12] N. Ishikawa et al. "Interaction between f-electronic systems in dinuclear lanthanide complexes with phthalocyanines". In: *Journal of the American Chemical Society* 124.38 (2002), p. 11440.

[13] D. Gatteschi et al. *Molecular Nanomagnets*. Oxford University Press, 2006.

[14] G. Christou et al. "Single-molecule magnets". In: *Mrs Bulletin* 25.11 (2000), p. 66.

[15] A. Abragam and B. Bleaney. *Electron Paramagnetic Resonance of Transition Ions*. Oxford University Press, 1970.

[16] E Bauer and M Rotter. "Magnetism of complex metallic alloys: crystalline electric field effects". In: *Script for a lecture given at CMA Euroschool* (2007).

[17] D. J. Newman and B. Ng. *Crystal field handbook*. Cambridge University Press, 2007.

[18] H. A. Kramers. "Théorie générale de la rotation paramagnétique dans les cristaux". In: *Proceedings of Amsterdam Academy* 33 (1930), p. 959.

[19] J Sievers. "Asphericity of 4f-shells in their Hund's rule ground states". In: *Zeitschrift für Physik B Condensed Matter* 45.4 (1982), p. 289.

[20] A. R. Edmonds. *Angular momentum in quantum mechanics*. Princeton University Press, 1996.

[21] J. D. Rinehart and J. R. Long. "Exploiting single-ion anisotropy in the design of f-element single-molecule magnets". In: *Chemical Science* 2.11 (2011), p. 2078.

[22] R Skomski and D. Sellmyer. "Anisotropy of rare-earth magnets". In: *Journal of Rare Earths* 27.4 (2009), p. 675.

[23] M. Boulon et al. "Magnetic Anisotropy and Spin-Parity Effect Along the Series of Lanthanide Complexes". In: *Angewandte Chemie-International Edition* 52 (2013), p. 350.

[24] C. E. Schäffer and C. K. Jörgensen. "The angular overlap model, an attempt to revive the ligand field approaches". In: *Molecular Physics* 9.5 (1965), p. 401.

[25] W Urland. "On the ligand-field potential for f electrons in the angular overlap model". In: *Chemical Physics* 14.3 (1976), p. 393.

[26] W Urland. "The application of the angular overlap model in the calculation of paramagnetic principal susceptibilities for f n-electron systems". In: *Chemical Physics Letters* 46.3 (1977), p. 457.

[27] K. C. M. Westrup et al. "Adding Remnant Magnetization and Anisotropic Exchange to Propeller-like Single-Molecule Magnets through Chemical Design". In: *Chemistry-A European Journal* 20.42 (2014), p. 13681.

[28] I. dzyaloshinskii. "A thermodynamic theory of "weak" ferromagnetism of antiferromagnetics". In: *Physics and Chemistry of Solids* 4.4 (1958), p. 241.

[29] T. Moriya. "Anisotropic superexchange interaction and weak ferromagnetism". In: *Physical Review* 120.1 (1960), p. 91.

[30] T. Moriya. "New mechanism of anisotropic superexchange interaction". In: *Physical Review Letters* 4.5 (1960), p. 228.

[31] P Erdös. "Theory of ion pairs coupled by exchange interaction". In: *Journal of Physics and Chemistry of Solids* 27.11 (1966), p. 1705.

[32] B. Tsukerblat et al. "Magnetochemistry and spectroscopy of transition metal exchange clusters". In: *Soviet Sci. Rev. B, Harwood Acad. Pub* (1987), p. 337.

[33] J. Schnack. "Effects of frustration on magnetic molecules: a survey from Olivier Kahn until today". In: *Dalton Transactions* 39.20 (2010), p. 4677.

[34] C. Lacroix et al. *Introduction to Frustrated Magnetism: Materials, Experiments, Theory*. Vol. 164. Springer Science & Business Media, 2011.

[35] H. Diep. *Frustrated spin systems*. 2005.

[36] G. Toulouse. "Theory of the frustration effect in spin glasses: I". In: *Commun. Phys* 2.4 (1977), p. 115.

[37] S. Kirkpatrick. "Frustration and ground-state degeneracy in spin glasses". In: *Physical Review B* 16.10 (1977), p. 4630.

[38] S. T. Bramwell and M. J. Gingras. "Spin ice state in frustrated magnetic pyrochlore materials". In: *Science* 294.5546 (2001), p. 1495.

[39] R Moessner. "Magnets with strong geometric frustration". In: *Canadian journal of physics* 79.11-12 (2001), p. 1283.

[40] A. P. Ramirez et al. "Zero-point entropy in 'spin ice'". In: *Nature* 399.6734 (1999), p. 333.

[41] M. Perfetti. "Commentary on: An intermediate state between the kagome-ice and the fully polarized state in $Dy_2Ti_2O_7$". In: *Papers in Physics* 7 (2015), p. 070010.

[42] M. L. Baker et al. "A classification of spin frustration in molecular magnets from a physical study of large odd-numbered-metal, odd electron rings". In: *Proceedings of the National Academy of Sciences* 109.47 (2012), p. 19113.

[43] C Benelli et al. "Structure and magnetic properties of linear-chain complexes of rare-earth ions (gadolinium, europium) with nitronyl nitroxides". In: *Inorganic Chemistry* 28.2 (1989), p. 275.

[44] C Benelli et al. "Gd (hfac) 3 NITEt molecular magnetic chain". In: *Journal of magnetism and magnetic materials* 140 (1995), p. 1649.

[45] J.-P. Costes et al. "A trinuclear gadolinium complex: structure and magnetic properties". In: *Inorganic chemistry* 40.20 (2001), p. 5285.

[46] G. Cucinotta et al. "Magnetic Anisotropy in a Dysprosium/DOTA Single-Molecule Magnet: Beyond Simple Magneto-Structural Correlations". In: *Angewandte Chemie-International Edition* 51 (2012), p. 1606.

[47] M. Perfetti et al. "Determination of Magnetic Anisotropy in the LnTRENSAL Complexes (Ln= Tb, Dy, Er) by Torque Magnetometry". In: *Inorganic chemistry* 54.7 (2015), p. 3090.

[48] D. N. Woodruff et al. "Lanthanide single-molecule magnets". In: *Chemical reviews* 113.7 (2013), p. 5110.

[49] G. Ventura and M. Perfetti. *Thermal Properties of Solids at Room and Cryogenic Temperatures*. Springer, 2014.

[50] W. Radcliffe et al. "A microwave method for thermal expansion measurement". In: *Journal of Physics E: Scientific Instruments* 16.12 (1983), p. 1200.

[51] G. Meyer and N. M. Amer. "Novel optical approach to atomic force microscopy". In: *Applied physics letters* 53.12 (1988), p. 1045.

[52] S. Alexander et al. "An atomic-resolution atomic-force microscope implemented using an optical lever". In: *Journal of Applied Physics* 65.1 (1989), p. 164.

[53] F. Giessibl and B. Trafas. "Piezoresistive cantilevers utilized for scanning tunneling and scanning force microscope in ultrahigh vacuum". In: *Review of scientific instruments* 65.6 (1994), p. 1923.

[54] C Rossel et al. "Active microlevers as miniature torque magnetometers". In: *Journal of applied physics* 79.11 (1996), p. 8166.

[55] C. Lee et al. "Self-excited piezoelectric PZT microcantilevers for dynamic SFM—with inherent sensing and actuating capabilities". In: *Sensors and Actuators A: Physical* 72.2 (1999), p. 179.

[56] R Griessen. "A capacitance torquemeter for de Haas-van Alphen measurements". In: *Cryogenics* 13.6 (1973), p. 375.

[57] M Qvarford et al. "Microtorquemeter for magnetization measurements on small superconducting samples". In: *Review of scientific instruments* 63.12 (1992), p. 5726.

[58] M Weber et al. "UHV cantilever beam technique for quantitative measurements of magnetization, magnetostriction, and intrinsic stress of ultrathin magnetic films". In: *Physical review letters* 73.8 (1994), p. 1166.

[59] F. El Hallak. "Magnetic Anisotropy of Molecular Nanomagnets". PhD thesis. University of Stuttgart, 2009.

[60] N. F. Chilton et al. "An electrostatic model for the determination of magnetic anisotropy in dysprosium complexes". In: *Nature communications* 4 (2013).

[61] J. J. Baldoví et al. "Rational design of single-ion magnets and spin qubits based on mononuclear lanthanoid complexes". In: *Inorganic chemistry* 51.22 (2012), p. 12565.

[62] B. M. Flanagan et al. "A Ligand-Field Analysis of the trensal Ligand. An Application of Angilar Overlap Model to Lanthanides". In: *Inorganic Chemistry* 41 (2002), p. 5024.

[63] P. V. Bernhardt et al. "Rapid communication: completion of the isomorphous Ln (trensal) series". In: *Australian Journal of Chemistry* 54.4 (2001), p. 229.

[64] M. Kanesato and T. Yokoyama. "Synthesis and Structural Characterization of Ln (III) Complexes (Ln= Eu, Gd, Tb, Er, Tm, Lu) of Tripodal Tris (2-(salicylideneamino) ethyl) amine." In: *Chemistry Letters* 2 (1999), p. 137.

[65] M. Kanesato et al. "Synthesis and Structural Characterization of Praseodymium (III) and Neodymium (III) Complexes of Tripodal Tris (2-(salicylideneamino) ethyl) amine." In: *Bulletin of the Chemical Society of Japan* 69.5 (1996), p. 1297.

[66] M. Kanesato and T. Yokoyama. "Crystal Structures of Dysprosium (III) and Holmium (III) Complexes of Tripodal Tris [2-(salicylideneamino) ethyl] amine." In: *Analytical sciences* 16.3 (2000), p. 335.

[67] M. Kanesato et al. "Comparison of the bond lengths for the lanthanide complexes of tripodal heptadentate ligands". In: *Journal of alloys and compounds* 374.1 (2004), p. 307.

[68] K. S. Pedersen et al. "Modifying the properties of 4f single-ion magnets by peripheral ligand functionalisation". In: *Chemical Science* 5.4 (2014), p. 1650.

[69] J. Dreiser et al. "Exchange interaction of strongly anisotropic tripodal erbium single-ion magnets with metallic surfaces". In: *ACS nano* 8.5 (2014), p. 4662.

[70] A Fort et al. "Mixed quantum-thermal relaxation in Mn 12 acetate molecules". In: *Physical review letters* 80.3 (1998), p. 612.

[71] E. Lucaccini et al. "Beyond the anisotropy barrier: slow relaxation of the magnetization in both easy-axis and easy-plane Ln (trensal) complexes". In: *Chemical Communications* 50.14 (2014), p. 1648.

[72] B. M. Flanagan et al. "Ligand-Field Analysis of an Er(III) Complex with a Heptadentate Tripodal N_4O_3 Ligand". In: *Inorganic Chemistry* 40 (2001), p. 5401.

[73] N. Viola-Villegas and R. P. Doyle. "The coordination chemistry of 1,4,7,10-tetraazacyclododecane-N,N',N",N"'-tetraacetic acid (H_4DOTA): Structural overview and analyses on structure–stability relationships". In: *Coordination Chemistry Reviews* 253.13 (2009), p. 1906.

[74] M. Bottrill et al. "Lanthanides in magnetic resonance imaging". In: *Chemical Society Reviews* 35.6 (2006), p. 557.

[75] N. Cakić et al. "Synthetic strategies for preparation of cyclen-based MRI contrast agents". In: *Tetrahedron Letters* 56.6 (2015), p. 759.

[76] F Benetollo et al. "Structural variations across the lanthanide series of macrocyclic DOTA complexes: insights into the design of contrast agents for magnetic resonance imaging". In: *Inorganic chemistry* 42.1 (2003), p. 148.

[77] L Armelao et al. "Design of luminescent lanthanide complexes: from molecules to highly efficient photo-emitting materials". In: *Coordination Chemistry Reviews* 254.5 (2010), p. 487.

[78] D. Lawson et al. "Optimizing the high-field relaxivity by self-assembling of macrocyclic Gd (III) complexes". In: *Dalton Transactions* 44.11 (2015), p. 4910.

[79] P. Å. Malmqvist et al. "The restricted active space (RAS) state interaction approach with spin–orbit coupling". In: *Chemical physics letters* 357.3 (2002), p. 230.

[80] W. J. Evans. "Organometallic lanthanide chemistry". In: *Adv Organometal Chem* 24 (1985), p. 131.

[81] D. P. Mills et al. "A delocalized arene-bridged diuranium single-molecule magnet". In: *Nature chemistry* 3.6 (2011), p. 454.

[82] N. Magnani et al. "Magnetic memory effect in a transuranic mononuclear complex". In: *Angewandte Chemie International Edition* 50.7 (2011), p. 1696.

[83] S.-D. Jiang et al. "An organometallic single-ion magnet". In: *Journal of the American Chemical Society* 133.13 (2011), p. 4730.

[84] S. Jiang et al. "An Organometallic Single-Ion Magnet". In: *Journal of American Chemical Society* 133 (2011), p. 4730.

[85] M.-E. Boulon et al. "Angular-Resolved Magnetometry Beyond Triclinic Crystals: Out-of-Equilibrium Studies of Cp* ErCOT Single-Molecule Magnet". In: *Chemistry-A European Journal* 19.41 (2013), p. 13726.

[86] J. Perenboom et al. "Relaxation of the magnetization of Mn 12 acetate". In: *Physical Review B* 58.1 (1998), p. 330.

[87] S. W. Van Sciver. *Helium cryogenics*. Springer Science & Business Media, 2012.

[88] P. E. Car et al. "Giant field dependence of the low temperature relaxation of the magnetization in a dysprosium(III)-DORA complex". In: *Chemical Communication* 47 (2011), p. 3571.

[89] R. Ruamps et al. "Giant Ising-Type Magnetic Anisotropy in Trigonal Bipyramidal Ni (II) Complexes: Experiment and Theory". In: *Journal of the American Chemical Society* 135.8 (2013), p. 3017.

[90] F. Shao et al. "Tuning the Ising-type anisotropy in trigonal bipyramidal Co (ii) complexes". In: *Chemical Communications* 51.92 (2015), p. 16475.

[91] R. Ruamps et al. "Ising-type magnetic anisotropy and single molecule magnet behaviour in mononuclear trigonal bipyramidal Co (II) complexes". In: *Chemical Science* 5.9 (2014), p. 3418.

[92] M. D'Aniello Jr et al. "Structure of a square pyrimidal pentacoordinate complex of nickel (N-tetramethylcyclam) 2+. Kinetically determined ligand stereochemistry". In: *Journal of the American Chemical Society* 97.1 (1975), p. 192.

[93] S Reimer et al. "Structure of azido (1, 4, 8, 11-tetramethyl-1, 4, 8, 11-tetraazacyclotetradecane) cobalt (II) perchlorate". In: *Acta Crystallographica Section C: Crystal Structure Communications* 45.11 (1989), p. 1694.

[94] R. Inglis et al. "Twisted molecular magnets". In: *Chemical Communications* 48.2 (2012), p. 181.

[95] A.-L. Barra et al. "The origin of transverse anisotropy in axially symmetric single molecule magnets". In: *Journal of the American Chemical Society* 129.35 (2007), p. 10754.

[96] S. Hill. "Magnetization tunneling in high-symmetry Mn 12 single-molecule magnets". In: *Polyhedron* 64 (2013), p. 128.

[97] J. Liu and S. Hill. "Magnetization quantum tunneling and improper rotational symmetry". In: *Polyhedron* 66 (2013), p. 147.

[98] L. Gregoli et al. "Magnetostructural Correlations in Tetrairon (III) Single-Molecule Magnets". In: *Chemistry-A European Journal* 15.26 (2009), p. 6456.

[99] L Sorace et al. "Origin and spectroscopic determination of trigonal anisotropy in a heteronuclear single-molecule magnet". In: *Physical Review B* 88.10 (2013), p. 104407.

[100] S. Accorsi et al. "Tuning anisotropy barriers in a family of tetrairon (III) single-molecule magnets with an S= 5 ground state". In: *Journal of the American Chemical Society* 128.14 (2006), p. 4742.

[101] E. Tancini et al. "Slow Magnetic Relaxation from Hard-Axis Metal Ions in Tetranuclear Single-Molecule Magnets". In: *Chemistry-A European Journal* 16.34 (2010), p. 10482.

[102] A. Lunghi and F. Totti. "DFT magnetic characterization of a Fe 4 SMMs series: from isotropic exchange interactions to multi-spin zero field splitting". In: *Journal of Materials Chemistry C* 2.39 (2014), p. 8333.

[103] E. M. Kessler et al. "Broken symmetry approach to density functional calculation of zero field splittings including anisotropic exchange interactions". In: *The Journal of chemical physics* 139.18 (2013), p. 184110.

[104] A. Bencini and D. Gatteschi. *EPR of Exchange-coupled Systems*. Springer, 1990.

[105] J. Luzon et al. "Spin chirality in a molecular dysprosium triangle: The archetype of the noncollinear ising model". In: *Physical review letters* 100.24 (2008), p. 247205.

[106] L. F. Chibotaru et al. "The origin of nonmagnetic Kramers doublets in the ground state of dysprosium triangles: Evidence for a toroidal magnetic moment". In: *Angewandte Chemie* 120.22 (2008), p. 4194.

[107] A Caneschi et al. "Ising-Type Magnetic Anisotropy in a Cobalt (II) Nitronyl Nitroxide Compound: A Key to Understanding the Formation of Molecular Magnetic Nanowires". In: *Chemistry-A European Journal* 8.1 (2002), p. 286.

[108] N. Ishii et al. "Giant coercivity in a one-dimensional cobalt-radical coordination magnet". In: *Journal of the American Chemical Society* 130.1 (2008), p. 24.

[109] J. Lee et al. "Metal–organic framework materials as catalysts". In: *Chemical Society Reviews* 38.5 (2009), p. 1450.

[110] J.-R. Li et al. "Selective gas adsorption and separation in metal–organic frameworks". In: *Chemical Society Reviews* 38.5 (2009), p. 1477.

[111] R. B. Getman et al. "Review and analysis of molecular simulations of methane, hydrogen, and acetylene storage in metal–organic frameworks". In: *Chemical reviews* 112.2 (2011), p. 703.

[112] Z.-Y. Gu et al. "Metal–organic frameworks as biomimetic catalysts". In: *ChemCatChem* 6.1 (2014), p. 67.

[113] C. G. Silva et al. "Metal–organic frameworks as semiconductors". In: *Journal of Materials Chemistry* 20.16 (2010), p. 3141.

[114] R Tiron et al. "Quantum tunneling in a three-dimensional network of exchange-coupled single-molecule magnets". In: *Physical Review B* 68.14 (2003), p. 140407.

[115] E.-C. Yang et al. "Exchange bias in Ni 4 single-molecule magnets". In: *Polyhedron* 22.14 (2003), p. 1727.

[116] E.-C. Yang et al. "Fast magnetization tunneling in tetranickel (II) single-molecule magnets". In: *Inorganic chemistry* 45.2 (2006), p. 529.

[117] R. Inglis et al. "Ground Spin State Changes and 3 D Networks of Exchange Coupled [MnIII3] Single-Molecule Magnets". In: *Chemistry-A European Journal* 14.30 (2008), p. 9117.

[118] R. Inglis et al. "Twisting, bending, stretching: strategies for making ferromagnetic [Mn III 3] triangles". In: *Dalton Transactions* 42 (2009), p. 9157.

[119] A. Das et al. "Reversible solvatomagnetic effect in novel tetranuclear cubane-type Ni4 complexes and magnetostructural correlations for the [Ni4 (μ3-O) 4] core". In: *Inorganic chemistry* 51.15 (2012), p. 8141.

[120] A. Nava et al. "Redox-Controlled Exchange Bias in a Supramolecular Chain of Fe4 Single-Molecule Magnets". In: *Angewandte Chemie* 127.30 (2015), p. 8901.

[121] L. Rigamonti et al. "Mapping of single-site magnetic anisotropy tensors in weakly coupled spin clusters by torque magnetometry". In: *Physical Chemistry Chemical Physics* 16.32 (2014), p. 17220.

[122] H. B. G. Casimir and F. K. Du Pré. "Note on the thermodynamic interpretation of paramagnetic relaxation phenomena". In: *Physica* 5 (1938), p. 507.

[123] A.-L. Barra et al. "New Single-Molecule Magnets by Site-Specific Substitution: Incorporation of "Alligator Clips" into Fe4 Complexes". In: *European Journal of Inorganic Chemistry* 2007.26 (2007), p. 4145.

[124] M. Perfetti et al. "Grafting single molecule magnets on gold nanoparticles". In: *Small* 10.2 (2014), p. 323.

[125] C. Coulon et al. "Single-chain magnets: theoretical approach and experimental systems". In: *Single-molecule magnets and related phenomena*. Springer, 2006, p. 163.

[126] C. Benelli and D. Gatteschi. "Single Chain Magnets (SCM) and More". In: *Introducton to Molecular Magnetism: from Transition Metals to Lanthanides*. Wiley, 2015. Chap. 15, p. 251.

[127] L Pasteur. "La dissymétrie moléculaire. Conférence faite le 22 décembre 1883". In: *Rev. Sci* 7 (1884), p. 2.

[128] S. Bordacs et al. "Chirality of matter shows up via spin excitations". In: *Nature Physics* 8.10 (2012), p. 734.

[129] F. Pop et al. "Electrical magnetochiral anisotropy in a bulk chiral molecular conductor". In: *Nature communications* 5 (2014).

[130] N. Romming et al. "Writing and deleting single magnetic skyrmions". In: *Science* 341.6146 (2013), p. 636.

[131] A. Fert et al. "Skyrmions on the track". In: *Nature nanotechnology* 8.3 (2013), p. 152.

[132] S.-W. Cheong and M. Mostovoy. "Multiferroics: a magnetic twist for ferroelectricity". In: *Nature materials* 6.1 (2007), p. 13.

[133] D. Khomskii. "Trend: Classifying multiferroics: Mechanisms and effects". In: *Physics* 2 (2009), p. 20.

[134] M Kubota et al. "X-ray directional dichroism of a polar ferrimagnet". In: *Physical review letters* 92.13 (2004), p. 137401.

[135] C. Train et al. "Strong magneto-chiral dichroism in enantiopure chiral ferromagnets". In: *Nature materials* 7.9 (2008), p. 729.

[136] M. Ceolín et al. "Strong Hard X-ray Magnetochiral Dichroism in Paramagnetic Enantiopure Molecules". In: *Advanced Materials* 24.23 (2012), p. 3120.

[137] Y. Kitagawa et al. "Magneto-Chiral Dichroism of Organic Compounds". In: *Angewandte Chemie* 123.39 (2011), p. 9299.

[138] R. Sessoli et al. "Strong magneto-chiral dichroism in a paramagnetic molecular helix observed by hard X-rays". In: *Nature physics* (2014).

[139] J.-P. Costes et al. "Unprecedented ferromagnetic interaction in homobinuclear erbium and gadolinium complexes: structural and magnetic studies". In: *Angewandte Chemie International Edition* 41.2 (2002), p. 323.

[140] L. Bogani et al. "Molecular Engineering for Single-Chain-Magnet Behavior in a One-Dimensional Dysprosium–Nitronyl Nitroxide Compound". In: *Angewandte Chemie International Edition* 44.36 (2005), p. 5817.

[141] K. Bernot et al. "Magnetic anisotropy of dysprosium (III) in a low-symmetry environment: a theoretical and experimental investigation". In: *Journal of the American Chemical Society* 131.15 (2009), p. 5573.

[142] K. Bernot et al. "A family of rare-earth-based single chain magnets: playing with anisotropy". In: *Journal of the American Chemical Society* 128.24 (2006), p. 7947.

[143] K. Bernot et al. "[Tm III (hfac) 3 (NITPhOPh)]∞: A new member of a lanthanide-based Single Chain Magnets family". In: *Inorganica Chimica Acta* 360.13 (2007), p. 3807.

[144] J.-X. Xu et al. "Four New Lanthanide- Nitronyl Nitroxide (LnIII= PrIII, SmIII, EuIII, TmIII) Complexes and a TbIII Complex Exhibiting Single-Molecule Magnet Behavior". In: *Inorganic chemistry* 48.18 (2009), p. 8890.

[145] A. Okazawa et al. "Exchange coupling and energy-level crossing in a magnetic chain [Dy2Cu2] n evaluated by high-frequency electron paramagnetic resonance". In: *Chemistry of Materials* 20.9 (2008), p. 3110.

[146] H. Zhao et al. "Lanthanide–3d cyanometalate chains Ln (III)–M (III)(Ln= Pr, Nd, Sm, Eu, Gd, Tb; M= Fe) with the tridentate ligand 2, 4, 6-tri (2-pyridyl)-1, 3, 5-triazine (tptz): evidence of ferromagnetic interactions for the Sm (III)–M (III) compounds (M= Fe, Cr)". In: *Dalton Transactions* 8 (2007), p. 878.

[147] P. Hu et al. "A new family of Ln–radical chains (Ln= Nd, Sm, Gd, Tb and Dy): synthesis, structure, and magnetic properties". In: *Dalton Transactions* 43.5 (2014), p. 2234.

[148] I. Mihalcea et al. "Spontaneous Resolution in Homochiral Helical [Ln (nic) 2 (Hnic)(NO3)] Coordination Polymers Constructed from a Rigid Non-chiral Organic Ligand". In: *Crystal Growth & Design* 14.9 (2014), p. 4729.

[149] H. Zabrodsky et al. "Continuous symmetry measures". In: *Journal of the American Chemical Society* 114.20 (1992), p. 7843.

[150] S. Liu et al. "Slow magnetic relaxation in a lanthanide helix chain compound [Dy (HNA)(NA) 2 (NO 3)] n (HNA= nicotinic acid)". In: *Dalton Transactions* 44.13 (2015), p. 6169.

[151] N. Ishikawa et al. "Determination of ligand-field parameters and f-electronic structures of double-decker bis (phthalocyaninato) lanthanide complexes". In: *Inorganic chemistry* 42.7 (2003), p. 2440.

[152] D. P. Arnold and J. Jiang. "Distinction between Light and Heavy Lanthanide (III) Ions Based on the 1H NMR Spectra of Heteroleptic Triple-Decker Phthalocyaninato Sandwich Complexes". In: *The Journal of Physical Chemistry A* 105.32 (2001), p. 7525.

[153] K. M. Kadish et al. "Electrochemistry of a double-decker lutetium (III) phthalocyanine in aqueous media. The first evidence for five reductions". In: *The Journal of Physical Chemistry B* 105.40 (2001), p. 9817.

[154] N. Ishikawa et al. "Upward temperature shift of the intrinsic phase lag of the magnetization of bis (phthalocyaninato) terbium by ligand oxidation creating an S= 1/2 spin". In: *Inorganic chemistry* 43.18 (2004), p. 5498.

[155] M. Urdampilleta et al. "Supramolecular spin valves". In: *Nature materials* 10.7 (2011), p. 502.

[156] L. Malavolti et al. "Erratic magnetic hysteresis of TbPc 2 molecular nanomagnets". In: *Journal of Materials Chemistry C* 1.16 (2013), p. 2935.

[157] L. Margheriti et al. "X-Ray Detected Magnetic Hysteresis of Thermally Evaporated Terbium Double-Decker Oriented Films". In: *Advanced Materials* 22.48 (2010), p. 5488.

[158] L Malavolti et al. "Magnetism of TbPc 2 SMMs on ferromagnetic electrodes used in organic spintronics". In: *Chemical Communications* 49.98 (2013), p. 11506.

[159] M. Gonidec et al. "Surface supramolecular organization of a terbium (III) double-decker complex on graphite and its single molecule magnet behavior". In: *Journal of the American Chemical Society* 133.17 (2011), p. 6603.

[160] S. Mauthoor. "Structural analysis of molecular nanostructures and thin films". Imperial College London, 2010.

[161] A. Scarfato et al. "Scanning tunneling microscope study of iron (II) phthalocyanine growth on metals and insulating surfaces". In: *Surface Science* 602.3 (2008), p. 677.

[162] M. Warner et al. "Spin-based diagnostic of nanostructure in copper phthalocyanine–C60 solar cell blends". In: *ACS nano* 6.12 (2012), p. 10808.

[163] B. L. Henke et al. "Soft-x-ray-induced secondary-electron emission from semiconductors and insulators: Models and measurements". In: *Physical review B* 19.6 (1979), p. 3004.

[164] R. Marx et al. "Spectroscopic determination of crystal field splittings in lanthanide double deckers". In: *Chemical Science* 5.8 (2014), p. 3287.

[165] C. Barraclough et al. "Paramagnetic Anisotropy, Low Temperature Magnetization, and Electronic Structure of Iron (II) Phthalocyanine". In: *The Journal of Chemical Physics* 53.5 (1970), p. 1643.

Acknowledgements

This Thesis is the outcome of three years of hard work of many people. Because of that, I want to sincerely acknowledge all the people involved in the collaborations. From a professional point of view I really own almost all my knowledge to Roberta, that was a tireless teacher in explaining me all the theoretical concepts as well as the experimental methods to understand and measure magnetic anisotropy. Nevertheless, I think that the most important lesson I have learned from her is the love for science, that I share with Eva, Lorenzo S., Elisabetta, Lorenzo T. and all the other people of the LaMM staff. I really enjoyed my PhD due to many people that I would like to sincerely acknowledge. My family (Sergio, Sandro and Antonella) deserves a special thanks because they always support me (they even pretend that I am not boring or nerd!). Great thanks should go to Bianca, Alessandro e Lorenzo, my assiduous lunch partners, that encouraged me every time I failed a calculation or a measurement (quite often, actually...). Thanks to all the friends that helps me to remember that friendship makes life wonderful, in particular during the holidays time (Ciume, Sere, Nico, Simo, Marco, Giulia, Silvia, Betta, Lore B., Pacio, Carlo, Carde)... and of course the Sunday evenings playing endless Catan games (Anto, Eva, Lore P.). I must also acknowledge my old friends (Peo, Fede, Elena) that shared with me tons of good (and bad!) experiences. A special thanks goes, as always, to Paola, because I know that we can stay miles away but we will always be together. Like in all the *Acknowledgement* sections of a PhD Thesis I surely forgot someone, that however will forgive me, or so I hope.

Mauro